

**Charles University**

**Faculty of Science**

Department of Physical and Macromolecular Chemistry

Physical Chemistry



RNDr. Radka Heydová

**Theoretical study of spin–orbit coupling on spectra and photophysics  
of rhenium complexes**

**Teoretická studie vlivu spin–orbitální interakce na spektra a fotofyziku  
rheniových komplexů**

**Doctoral thesis**

Jaroslav Heyrovsky Institute of Physical Chemistry AS CR, v.v.i.  
Department of Biophysical Chemistry

Supervisor: Ing. Stanislav Záliš, CSc.

**Prague, 2017**

**Prohlášení:**

Prohlašuji, že jsem závěrečnou práci zpracovala samostatně a že jsem uvedla všechny použité informační zdroje a literaturu. Tato práce ani její podstatná část nebyla předložena k získání jiného nebo stejného akademického titulu.

V Praze, květen 2017

Radka Heydová

Hereby and with all my love I would like to express my thousand thanks to my husband Honza – for his endless patience and all the help, motivating and generous support, fruitful discussions and his trust in me that I am able to finish my Ph.D. studies in spite of a long time which has elapsed since I started to study. It is also him whom I owe a lot, because he managed without any difficulty to take care of our beloved children Dominik and Karolína when I needed to concentrate myself on the doctoral thesis. Without him my Ph.D. thesis would not have come into existence.

I wish to express my deepest gratitude to my dear mother without whom I would not have been able to complete the thesis. Without a slightest problem she coped with her role as a full-time grandmother. She dedicated her spare time to looking after our children, so as I could engage in writing. I am aware how strenuous the last months before the submission must have been for her, and I sincerely appreciate what my mother has done for me.

I would like to thank my supervisor, Dr. Stanislav Záliš, for all he did for me, for his patience, kindly guidance and useful help and assistance. Above all he gave me several times during my studies the chance to decide freely on my own how to approach to my studies and whether it makes sense for me to graduate. Despite my immense hesitancy in making the first step in beginning working on my thesis he has not lost his hope and optimism, regardless of my despair. I also wish to acknowledge the chance to use the computational resources at J. Heyrovský Institute of Physical Chemistry AS CR, v.v.i.

Many thanks ought to be expressed to Professor Antonín Vlček Jr. for his valuable comments to the text and to Professor Chantal Daniel from Université de Strasbourg (Laboratoire de Chimie Quantique, Institut de Chimie de Strasbourg, UMR7177), where I have been given the opportunity to spend two weeks and to benefit from the presence of experts on employing the Molcas suite of programs in actual applications.

Last but not least I truly thank my immediate family not only for the fact that they have stood and still stand by me under all circumstances and they will always be here for me. My thanks belong also to our children – although, due to their young age, they were not capable of grasping the reality that his mother did not so often devote her time exclusively to them, they tolerated it, accepted it as a fact and thus they enabled me to work on my writing.

Regarding the English language I would like to thank my friend Honza for helpful advice and comments.

Finally I am grateful for many useful remarks and corrections from the aforementioned people.

Title: Theoretical study of spin–orbit coupling on spectra and photophysics of rhenium complexes

Author: RNDr. Radka Heydová

Department: Physical and Macromolecular Chemistry

Supervisor: Ing. Stanislav Zális, CSc., JHI AS CR, v.v.i.

Supervisor's e-mail address: stanislav.zalis@jh.inst-cas.cz

**Abstract:** Relativistic effects, especially spin–orbit coupling (SOC), play an essential role in transition metal chemistry and SOC treatment is indispensable for a correct theoretical description. To demonstrate the importance of SOC, the energies and oscillator strengths of vertical transitions for a series of  $[\text{ReX}(\text{CO})_3(2,2'\text{-bipyridine})]$  ( $\text{X} = \text{Cl}, \text{Br}, \text{I}$ ) and  $[\text{Re}(\text{imidazole})(\text{CO})_3(1,10\text{-phenanthroline})]^+$  complexes were calculated in the spin-free (SF) and spin–orbit (SO) conceptual frameworks. Two different computational approaches were adopted: SO-MS-CASPT2 where SOC was added a posteriori using a configuration interaction model (SO-RASSI), and the approximate perturbative SO-TD-DFT method. Relativistic effects were included via the two-component Douglas–Kroll–Hess transformation and the zeroth-order regular approximation in the former and the latter technique, respectively. The SF (i.e. accounting only for the scalar relativistic effects) and SO results from both methods were compared with each other and to available experiments. The character of charge-transfer transitions was used to describe the SF states. The SO states were characterized by their parentages in terms of the SF states and double-group symmetries. In case of complexes with a halide ligand, several observed spectral trends, mainly on going from Cl to I, were studied. We have proven that the SO model is able to interpret absorption spectra, emission characteristics and excited-state behaviour correctly and it improves a quantitative agreement with the experiment. Moreover, only the inclusion of SOC can explain some of spectroscopic features (temperature-dependent emission decay, various picosecond relaxation times, enormous broadness of emission bands etc.) that cannot be captured by the SF model. The photophysical SO excited-state model was developed in order to elucidate ultrafast spectroscopic experimental data – the principal observations (emission, the presence of an intermediate emissive state, electronic/vibrational relaxation, nonradiative transitions, equilibration among the lowest SO states) and detected time constants can be associated with particular processes and SO states.

Several generalizations can be extracted from the SO model, which are applicable to many other closed-shell transition metal complexes, such as high excited-state density, highly spin-mixed character of SO states, and multiple electronic and vibrational excitation and relaxation pathways (occurring after optical excitation). When strong SOC is introduced, the assignment of spin multiplicity is no longer appropriate and hence a unified point of view should be adopted. To sum up, our calculations are capable of providing an insight into the excited-state dynamics of rhenium(I) tricarbonyl complexes, which can be utilized in many photonic applications, e.g. organic light-emitting diodes.

**Keywords:** rhenium, carbonyl, diimine, spin–orbit coupling, excited states, ultrafast intersystem crossing, luminescence, spectroscopy, photophysics, CASSCF, MS-CASPT2, TD-DFT

Název práce: Teoretická studie vlivu spin–orbitální interakce na spektra a fotofyziku rheniových komplexů

Autor: RNDr. Radka Heydová

Katedra: Fyzikální a makromolekulární chemie

Školitel: Ing. Stanislav Zális, CSc., ÚFCH JH AV ČR, v.v.i.

E-mail školitele: stanislav.zalis@jh.inst-cas.cz

**Abstrakt:** Předkládaná práce poukazuje na důležitost relativistických efektů, obzvláště spin–orbitální interakce (SOI), jež hrají zásadní roli v chemii komplexů přechodných kovů. Zahrnutí SOI je tak nezbytné pro jejich správný teoretický popis. Za účelem prokázání významu SOI byly pro komplexy  $[\text{ReX}(\text{CO})_3(2,2'\text{-bipyridin})]$  ( $\text{X} = \text{Cl}, \text{Br}, \text{I}$ ) a  $[\text{Re}(\text{imidazol})(\text{CO})_3(1,10\text{-fenantrolin})]^+$  napočítány energie a oscilátorové síly vertikálních přechodů v bez-spinovém (spin-free, SF) a spin–orbitálním (SO) konceptuálním rámci. Byly použity dva různé výpočetní přístupy: SO-MS-CASPT2, kde byla SOI přidána *a posteriori* pomocí konfiguračního stavového modelu (SO-RASSI), a přibližná poruchová metoda SO-TD-DFT. Relativistické efekty byly zohledněny prostřednictvím dvoukomponentní Douglas–Kroll–Hessovy transformace a regulární aproximace nultého řádu (ZORA) v prvním, resp. druhém případě. SF (tj. obsahující pouze skalární relativistické efekty) a SO výsledky z obou metod byly porovnány navzájem a s dostupnými experimenty. Charakter přenosových (charge-transfer) přechodů byl použit k popisu SF stavů. SO stavy byly charakterizovány svým složením z původních SF stavů a označeny podle dvojité grupy symetrie. V případě komplexů s halogenidovým ligandem bylo studováno několik trendů pozorovaných ve spektru, zejména v závislosti na aktuálním halogenidu. Dokázali jsme, že spin–orbitální model umožňuje správně interpretovat absorpční spektra, emisní charakteristiky a problematiku excitovaných stavů a dosahuje lepší kvantitativní shody s experimentem. Mimo to některé spektroskopické jevy mohou být objasněny pouze s uvažováním SOI, jako např. teplotní závislost vyhasínání emise, různé pikosekundové relaxační časy, enormně široké emisní pásy apod., které nemohou být vysvětleny s použitím SF modelu. S cílem detailněji prozkoumat experimentální data z ultrarychlých spektroskopií byl vyvinut fotofyzikální model SO excitovaných stavů – jednotlivá pozorování (emise, přítomnost intermediárního emisivního stavu, elektronická/vibrační relaxace, nezářivé přechody, ustanovení rovnováhy mezi nejnižšími SO stavy) a detekované časové konstanty tak mohou být identifikovány s konkrétními procesy a SO stavy.

Z SO modelu lze vyvodit několik zobecnění, jež se dají aplikovat i na další komplexy přechodných kovů s konfigurací uzavřených slupek, jako je vysoká hustota excitovaných SO stavů s výrazně spinově smíšeným charakterem, a velké množství elektronických a vibračních excitačních a relaxačních dějů (probíhajících po optické excitaci). V případě silné SOI není již klasifikace stavů podle spinové multiplicity korektní a je třeba použít obecnější SO přístup. Závěrem můžeme konstatovat, že naše výpočty umožňují lépe porozumět dynamice excitovaných stavů trikarbonyl rhenných komplexů, které mohou být využity v mnoha fotonických aplikacích, např. v organických luminiscenčních diodách.

**Klíčová slova:** rhenium, karbonyl, diimin, spin–orbitální interakce, excitované stavy, ultrarychlý mezisystémový přechod, luminiscence, spektroskopie, fotofyzika, CASSCF, MS-CASPT2, TD-DFT

# Contents

LIST OF TABLES .....	vii
LIST OF FIGURES .....	ix
LIST OF ABBREVIATIONS .....	xi
LIST OF SYMBOLS AND UNITS .....	xiv
Chapter 1: INTRODUCTION .....	1
Chapter 2: THEORETICAL OVERVIEW .....	4
2.1 Heavy-metal complexes .....	4
2.1.1 Electronic excited states and their mixing .....	5
2.2 Relativistic effects .....	6
2.2.1 The Dirac equation and its approximations .....	6
2.2.2 Scalar relativistic effects .....	12
2.2.3 Spin-orbit coupling .....	13
2.2.4 Jablonski diagram .....	17
2.3 Experimental overview .....	20
2.3.1 Overview of relevant experimental techniques .....	20
2.3.2 Theoretical aspects of spectra .....	21
2.4 Computational methods .....	22
2.4.1 System initialization: HF/DFT .....	23
2.4.2 CASSCF .....	25
2.4.3 CASPT2 .....	28
2.4.4 Spin-orbit coupling calculations: SO-RASSI .....	34
2.4.5 TD-DFT .....	36
Chapter 3: INDIVIDUAL PROJECTS .....	43
3.1 Rhenium tricarbonyl complexes with halide ligands .....	43
3.1.1 Introduction .....	43
3.1.2 Computational details .....	47
3.1.3 Results and discussion .....	50
3.2 Rhenium tricarbonyl complex with imidazole .....	74
3.2.1 Introduction .....	74
3.2.2 Computational details .....	75
3.2.3 Results and discussion .....	76
Chapter 4: CONCLUSION .....	97
BIBLIOGRAPHY .....	101
LIST OF ATTACHED PUBLICATIONS .....	117
ATTACHED PUBLICATIONS .....	118

## LIST OF TABLES

Table 3.1. The contraction schemes for ANO-RCC basis sets used for rhenium(I) tricarbonyl complexes with halide ligands. ....	47
Table 3.2. The experimental UV–vis absorption spectra of $[\text{ReX}(\text{CO})_3(\text{bpy})]$ ( $\text{X} = \text{Cl}, \text{Br}, \text{I}$ ) in acetonitrile, dichloromethane and toluene. ....	52
Table 3.3. The spin-free MS-CASPT2 transition energies and oscillator strengths $f$ of $[\text{ReCl}(\text{CO})_3(\text{bpy})]$ calculated in vacuo. ....	53
Table 3.4. The spin-free MS-CASPT2 transition energies and oscillator strengths $f$ of $[\text{ReBr}(\text{CO})_3(\text{bpy})]$ calculated in vacuo. ....	54
Table 3.5. The spin-free MS-CASPT2 transition energies and oscillator strengths $f$ of $[\text{ReI}(\text{CO})_3(\text{bpy})]$ calculated in vacuo. ....	55
Table 3.6. The solvent-corrected (COSMO) spin-free TD-DFT transition energies and oscillator strengths $f$ of $[\text{ReCl}(\text{CO})_3(\text{bpy})]$ calculated in dichloromethane. ....	56
Table 3.7. The solvent-corrected (COSMO) spin-free TD-DFT transition energies and oscillator strengths $f$ of $[\text{ReBr}(\text{CO})_3(\text{bpy})]$ calculated in dichloromethane. ....	57
Table 3.8. The solvent-corrected (COSMO) spin-free TD-DFT transition energies and oscillator strengths $f$ of $[\text{ReI}(\text{CO})_3(\text{bpy})]$ calculated in dichloromethane. ....	58
Table 3.9. The spin-orbit MS-CASPT2 transition energies and oscillator strengths $f$ of $[\text{ReCl}(\text{CO})_3(\text{bpy})]$ calculated in vacuo. ....	61
Table 3.10. The spin-orbit MS-CASPT2 transition energies and oscillator strengths $f$ of $[\text{ReBr}(\text{CO})_3(\text{bpy})]$ calculated in vacuo. ....	62
Table 3.11. The spin-orbit MS-CASPT2 transition energies and oscillator strengths $f$ of $[\text{ReI}(\text{CO})_3(\text{bpy})]$ calculated in vacuo. ....	63
Table 3.12. The spin-orbit TD-DFT transition energies and oscillator strengths $f$ of $[\text{ReX}(\text{CO})_3(\text{bpy})]$ ( $\text{X} = \text{Cl}, \text{Br}, \text{I}$ ) calculated in dichloromethane (COSMO). ....	64
Table 3.13. The solvent-corrected (COSMO/MeCN) spin-orbit TD-DFT transition energies to the low-lying excited states and oscillator strengths $f$ of $[\text{ReX}(\text{CO})_3(\text{bpy})]$ calculated at the optimized $a^3A''$ state geometry. ....	72
Table 3.14. The contraction schemes for ANO-RCC basis sets used for $[\text{Re}(\text{imH})(\text{CO})_3(\text{phen})]^+$ . ....	75
Table 3.15. The spin-free MS-CASPT2 transition energies and oscillator strengths $f$ of $[\text{Re}(\text{imH})(\text{CO})_3(\text{phen})]^+$ calculated in vacuo. ....	78

Table 3.16. The spin-free lowest TD-DFT transition energies and oscillator strengths $f$ of $[\text{Re}(\text{imH})(\text{CO}_3(\text{phen}))]^+$ calculated in DMF (COSMO).....	79
Table 3.17. The spin-orbit MS-CASPT2 transition energies and oscillator strengths $f$ of $[\text{Re}(\text{ImH})(\text{CO})_3(\text{phen})]^+$ calculated in vacuo. ....	82
Table 3.18. The spin-orbit TD-DFT transition energies and oscillator strengths $f$ of $[\text{Re}(\text{imH})(\text{CO})_3(\text{phen})]^+$ calculated in DMF. ....	83
Table 3.19. The solvent-corrected (COSMO/DMF) spin-orbit TD-DFT transition energies to the low-lying excited states and oscillator strengths $f$ of $[\text{Re}(\text{imH})(\text{CO})_3(\text{phen})]^+$ calculated at the optimized $b^1A'$ geometry. ....	88
Table 3.20. The solvent-corrected (COSMO/DMF) spin-orbit TD-DFT transition energies to the low-lying excited states and oscillator strengths $f$ of $[\text{Re}(\text{imH})(\text{CO})_3(\text{phen})]^+$ calculated at the optimized $a^3A''$ geometry. ....	89



## LIST OF FIGURES

Figure 2.1. The schematic structure of <i>fac</i> -[Re(L)(CO) <sub>3</sub> ( $\alpha$ -diimine)] <sup>0/+</sup> complexes. ....	5
Figure 2.2. Jablonski diagram. ....	18
Figure 3.1. The general molecular structure of rhenium(I) tricarbonyl complexes with a halide. ....	43
Figure 3.2. The geometries of rhenium(I) tricarbonyl complexes with halide ligands. ....	43
Figure 3.3. The schematic molecular diagram of the pseudo-octahedral [ReX(CO) <sub>3</sub> (bpy)] complex. ....	44
Figure 3.4. The frontier occupied and virtual molecular orbitals included in the active space at the CASSCF stage of the calculation of [ReCl(CO) <sub>3</sub> (bpy)]. ....	48
Figure 3.5. The experimental UV–vis absorption spectra of [ReX(CO) <sub>3</sub> (bpy)] (X = Cl, Br, I) in acetonitrile (MeCN) and dichloromethane (DCM). ....	51
Figure 3.6. The theoretical UV–vis absorption spectra of [ReX(CO) <sub>3</sub> (bpy)] calculated by means of spin-free TD-DFT (PBE0, COSMO/CH <sub>2</sub> Cl <sub>2</sub> ) (fwhm = 4000 cm <sup>-1</sup> ). ....	59
Figure 3.7. The experimental spectra recorded in toluene. ....	60
Figure 3.8. The correlation of the low-lying TD-DFT spin-free singlet (left column) and triplet (right column) states with the resulting spin–orbit states (in the middle) of [ReI(CO) <sub>3</sub> (bpy)] in toluene. ....	65
Figure 3.9. The correlation of the low-lying MS-CASPT2 spin-free singlet (left column) and triplet (right column) states with the resulting spin–orbit states (in the middle) of [ReI(CO) <sub>3</sub> (bpy)] in vacuo. ....	66
Figure 3.10. The theoretical UV–vis absorption spectra of [ReX(CO) <sub>3</sub> (bpy)] calculated by means of SO-TD-DFT (COSMO/CH <sub>2</sub> Cl <sub>2</sub> ) (fwhm = 4000 cm <sup>-1</sup> ). ....	68
Figure 3.11. The comparison of calculated low-lying spin-free (top) and spin–orbit (bottom) transitions of [ReI(CO) <sub>3</sub> (bpy)] by means of TD-DFT/toluene (left) and MS-CASPT2/vacuum (right). ....	70
Figure 3.12. The molecular structure of the [Re(imH)(CO) <sub>3</sub> (phen)] <sup>+</sup> complex. ....	74
Figure 3.13. The frontier occupied and virtual molecular orbitals included in the active space at the CASSCF stage of the calculation of [Re(imH)(CO) <sub>3</sub> (phen)] <sup>+</sup> . ....	76
Figure 3.14. The spin-free model of [Re(imH)(CO) <sub>3</sub> (phen)] <sup>+</sup> . ....	80

Figure 3.15. The theoretical UV–vis absorption spectra of $[\text{Re}(\text{imH})(\text{CO})_3(\text{phen})]^+$ in DMF (COSMO) simulated by means of a) SF- (top) and b) SO-TD-DFT (bottom). .....	84
Figure 3.16. The correlation of MS-CASPT2 spin-free singlet (left column) and triplet (right column) states with the resulting spin–orbit states (in the middle) of $[\text{Re}(\text{imH})(\text{CO})_3(\text{phen})]^+$ in vacuo. ....	85
Figure 3.17. The correlation of TD-DFT spin-free singlet (left column) and triplet (right column) states with the resulting spin–orbit states (in the middle) of $[\text{Re}(\text{imH})(\text{CO})_3(\text{phen})]^+$ in DMF. ....	86
Figure 3.18. The comparison of individual SO states of $[\text{Re}(\text{imH})(\text{CO})_3(\text{phen})]^+$ calculated at three different optimized geometries: the spin-free ground $a^1A'$ (left), $b^1A'$ (middle) and $a^3A''$ (right) states. ....	90
Figure 3.19. The spin–orbit model of $[\text{Re}(\text{imH})(\text{CO})_3(\text{phen})]^+$ . ....	92

## LIST OF ABBREVIATIONS

<b>ADF</b>	– Amsterdam Density Functional (quantum chemistry software)
<b>AMFI</b>	– Atomic Mean Field Integral
<b>ANO-RCC</b>	– Atomic Natural Orbital Relativistic Consistent Correlated (basis set)
<b>bpy</b>	– 2,2'-bipyridine
<b>br</b>	– broad
<b>B3LYP</b>	– Becke, Lee, Yang, Perdew exchange and correlation functional
<b>CASPT2</b>	– Multiconfigurational Second-Order Perturbation Theory
<b>CASSCF</b>	– Complete Active Space Self-Consistent Field
<b>CBS</b>	– Complete Basis Set
<b>CC</b>	– Coupled Cluster (techniques)
<b>DCM</b>	– dichloromethane/methylene chloride ( $\text{CH}_2\text{Cl}_2$ )
<b>MeCN</b>	– acetonitrile ( $\text{CH}_3\text{CN}$ )
<b>CI</b>	– Configuration Interaction
<b>CIS</b>	– Configuration Interaction Singles Method
<b>COSMO</b>	– Conductor-like Screening Model
<b>CPU</b>	– Central Processor Unit
<b>CSF</b>	– Configuration State Function
<b>CT</b>	– Charge Transfer
<b>DFT</b>	– Density Functional Theory
<b>DK(H)</b>	– Douglas–Kroll(–Hess) Transformation
<b>DMF</b>	– N,N-dimethylformamide
<b>EA</b>	– Electron Affinity
<b>ECP</b>	– Effective Core Pseudopotential
<b>EOM-CC</b>	– Equation-of-Motion Coupled Cluster
<b>ES</b>	– Excited State
<b>FT</b>	– Fourier Transform
<b>Full CI</b>	– Full Configuration Interaction
<b>FW</b>	– Foldy–Wouthuysen Transformation
<b>fwhm</b>	– Full Width at Half Maximum
<b>GGA</b>	– Generalized Gradient Approximation
<b>GS</b>	– Ground State
<b>GUGA</b>	– Graphical Unitary Group Approach
<b>H-dab</b>	– 1,4-diaza-1,3-butadiene
<b>HF</b>	– Hartree–Fock
<b>HK</b>	– Hohenberg–Kohn
<b>HOMO</b>	– Highest Occupied Molecular Orbital
<b>IC</b>	– Internal Conversion
<b>IL</b>	– Intra-Ligand Transition
<b>imH</b>	– imidazole
<b>IP</b>	– Ionization Potential
<b>ISC</b>	– Intersystem Crossing

<b>IUPAC</b>	– International Union of Pure and Applied Chemistry
<b>IVR</b>	– Intramolecular Vibrational Reorganization
<b>KS</b>	– Kohn–Sham
<b>LC</b>	– Ligand-Centred
<b>LDA</b>	– Local Density Approximation
<b>LF</b>	– Ligand Field
<b>LFT</b>	– Ligand Field Theory
<b>LLCT</b>	– Ligand-to-Ligand Charge Transfer
<b>LR</b>	– Linear Response
<b>LS</b>	– Level Shift
<b>LUMO</b>	– Lowest Unoccupied Molecular Orbital
<b>MBPT</b>	– Many-Body Perturbation Theory
<b>MC</b>	– Metal-Centred
<b>MCSCF</b>	– Multiconfigurational Self-Consistent Field
<b>MLCT</b>	– Metal-to-Ligand Charge Transfer
<b>MO</b>	– Molecular Orbital
<b>MO-LCAO</b>	– Molecular Orbital with a Linear Combination of Atomic Orbitals
<b>MP</b>	– Møller–Plesset
<b>MR-CC</b>	– Multireference Coupled Cluster
<b>MR-CCI</b>	– Multireference Contracted Configuration Interaction
<b>MR-CI</b>	– Multireference Configuration Interaction
<b>MS-CASPT2</b>	– Multi-State CASPT2
<b>N<sup>^</sup>N</b>	– $\alpha$ -diimine ligands (usually polypyridines)
<b>NIR</b>	– Near Infrared (Absorption Spectra)
<b>OLED</b>	– Organic Light-Emitting Diode
<b>PBE0</b>	– Perdew, Burke, Ernzerhof exchange and correlation functional
<b>PCM</b>	– Polarizable Conductor Calculation Model
<b>PES</b>	– Potential Energy Surface
<b>phen</b>	– 1,10-phenanthroline
<b>PT</b>	– Perturbation Theory
<b>RAS</b>	– Restricted Active Space
<b>RASSCF</b>	– Restricted Active Space Self-Consistent Field
<b>RASSI</b>	– Restricted Active Space State Interaction
<b>RSH</b>	– Range Separated Hybrids
<b>SA</b>	– State-Averaged
<b>SALC</b>	– Symmetry Adapted Linear Combination
<b>SD</b>	– Slater Determinant
<b>SF</b>	– Spin-Free
<b>SGUGA</b>	– Split Graphical Unitary Group Approach
<b>sh</b>	– shoulder
<b>SO</b>	– Spin-orbit
<b>SOC</b>	– Spin-orbit Coupling
<b>SO-MS-CASPT2</b>	– CASSCF/MS-CASPT2/SO-RASSI
<b>SO-RASSI</b>	– Restricted Active Space State Interaction including SOC

<b>SO-TD-DFT</b>	– Spin–orbit Time-Dependent Density Functional Theory
<b>SR</b>	– Scalar Relativistic (Effects)
<b>STO</b>	– Slater Type Orbital
<b>TD-DFRT</b>	– Time-Dependent Density-Functional Response Theory
<b>TD-DFT</b>	– Time-Dependent Density Functional Theory
<b>TRIR</b>	– Time-Resolved Infrared Spectroscopy
<b>UKS-DFT</b>	– Unrestricted Kohn–Sham Density Functional Theory
<b>UV–vis</b>	– Ultraviolet – Visible (Absorption Spectra)
<b>VR</b>	– Vibrational Relaxation
<b>XC</b>	– Exchange-Correlation (Functional)
<b>XLCT</b>	– X Ligand-to-Ligand Charge Transfer (Halide-to-Ligand CT)
<b>ZFS</b>	– Zero-Field Splitting
<b>ZORA</b>	– Zeroth-Order Regular Approximation
<b>ZPE</b>	– Zero-Point Energy
<b>1-S</b>	– Single-State

**Abbreviations are arranged in alphabetical order.**

## LIST OF SYMBOLS AND UNITS

Reduced Planck constant (Dirac constant)	$\hbar = h/2\pi = 1.05457267 \cdot 10^{-34} \text{ J}\cdot\text{s}$
Mass of electron	$m_e = 9.1093897 \cdot 10^{-31} \text{ kg}$
Charge of electron	$e = 1.60217662 \cdot 10^{-19} \text{ C}$
Speed of light	$c = 299\,792\,458 \text{ m}\cdot\text{s}^{-1}$
Vacuum permittivity	$\varepsilon_0 = 8.854187817 \cdot 10^{-12} \text{ F}\cdot\text{m}^{-1}$
Vacuum permeability	$\mu_0 = 1.2566370614 \cdot 10^{-6} \text{ H}\cdot\text{m}^{-1}$
Bohr radius	$a_0 = 4\pi\varepsilon_0\hbar^2/m_e e^2$

$$1 \text{ hartree} = 27.211396 \text{ eV} = 219\,474.6305 \text{ cm}^{-1}$$

$$1 \text{ eV} = 3.67493095 \cdot 10^{-2} \text{ hartree} = 8\,065.54 \text{ cm}^{-1}$$

$$1 \text{ \AA} = 10^{-10} \text{ m}$$

$$1 \text{ bohr} = 0.52917726 \text{ \AA}$$

Conversion of SI units into cgs-Gaussian units:  $q_{\text{cgs}} = \frac{q_{\text{SI}}}{\sqrt{4\pi\varepsilon_0}}$ ,  $\mathbf{E}_{\text{cgs}} = \sqrt{4\pi\varepsilon_0}\mathbf{E}_{\text{SI}}$  and  $\mathbf{B}_{\text{cgs}} = \sqrt{4\pi/\mu_0}\mathbf{B}_{\text{SI}}$

Hartree atomic units (a.u.):  $m_e = e = \hbar = \frac{1}{4\pi\varepsilon_0} = 1$ ;  $c \text{ (a.u.)} \approx 137$

**All vectors and vector operators are written as boldface symbols (without arrows). Conventionally they have three Cartesian components  $x, y, z$ .**

**Constants mentioned in the following text are described and quantified only in this part in order not to make the thesis more extensive than necessary.**

**Unless otherwise stated, standard SI units will be used in this thesis.**

## Chapter 1: INTRODUCTION

Transition metal complexes are attractive systems not only from a practical and industrial, but also from a computational and experimental perspective.<sup>1</sup> They still represent a bit of a mystery and a great challenge for theoretical scientists, partially due to the size and complexity of these systems and partially due to the necessity to account properly for relativistic effects caused by the presence of heavy atoms. The effects of relativity can be divided into the scalar and spin-orbit coupling parts and both have to be included for a reasonable description. The latter plays a central role in this doctoral thesis – nowadays spin-orbit coupling (SOC) treatment is considered indispensable for high-precision quantum chemical calculations. The significance of SOC was recognized in the scientific community almost 50 years ago<sup>2-4</sup> and since then it has been gradually taken into account in more and more fields of physical chemistry. The first spin-orbit (SO) computational studies of metal complexes showed up in the 1980s, proposing SOC models of  $[M(\text{bpy})_3]^{2+}$  ( $M = \text{Fe}, \text{Ru}, \text{Os}$ ) for interpreting their electronic structures and spectra.<sup>5-7</sup> In 1994  $[\text{Ru}(\text{bpy})_3]^{2+}$  was calculated at a density functional level of theory with the inclusion of SOC and the results were found promising, yielding a reasonable agreement with experimental spectra.<sup>8</sup> Over the decades, this inorganic photosensitizer has become one of the most investigated systems, both experimentally and theoretically. Despite these efforts, its excited-state structure still cannot be regarded as fully revealed, which suggests that transition metal chemistry requires indeed an immensely complex and sophisticated treatment.

Generally, the SOC influence is getting stronger with the increasing atomic number. By light atoms or molecules its inclusion can lead to overall improvement in accuracy without changing the fundamental characteristics of a system, whereas for heavy-metal complexes SOC becomes an essential factor in any comprehensive theoretical study. In fact, the neglect of SOC could often result in inadequate or completely wrong conclusions – some relevant photophysical aspects might be misinterpreted or even missed. Based on these findings it is obvious that heavy transition metal chemistry is unthinkable without taking SOC into consideration. Therefore in this thesis I focus on SOC and its implications for photophysics of heavy-metal complexes.

One of the most important and at the same time fashionable SOC effects is the ultrafast population of the lowest triplet state(s), mainly via intersystem crossing (ISC), followed by the emission to the electronic singlet ground state, traditionally known as phosphorescence.<sup>9</sup> From a formal point of view, these transitions are strictly forbidden according to the spin selection rule, but when SOC comes into play, the transitions become allowed and display non-zero intensities, which indeed corresponds to the observed reality. A number of complexes are thus able to exhibit intense phosphorescence in a spectral region different from fluorescence which is often virtually absent due to an extremely efficient population of the triplet emissive states after irradiation. Many applications and inventions have made use of

these interesting features and a wide range of utilizations has been proposed up to now. Luminophores (phosphorescent dyes) in organic light-emitting diodes<sup>10–13</sup> (OLEDs), which are found, for instance, in modern types of displays, represent one of the most principal technical progresses which have been accomplished with the use of heavy-metal compounds. Many other practical implementations of transition metal complexes can be named, e.g. sensitizers of solar-energy conversion<sup>14,15</sup> (photovoltaic cells), phosphorescent biological (DNA, protein, cellular) probes and labels,<sup>16–18</sup> photosensitizers and phototriggers of electron transfer in biomolecules,<sup>19,20</sup> luminescence-based sensors,<sup>21,22</sup> non-linear optical materials, photocatalysts (e.g. carbon dioxide reduction<sup>23,24</sup>) etc. Transition metal complexes can be employed also in molecular devices<sup>25</sup> (moletronics), supramolecular chemistry or as photoimaging agents. Not only the phosphorescence, but also other phenomena are typical of heavy-metal complexes and I would like to extend this topic in the result section on chosen examples.

Our motivation to perform exact calculations on below presented systems is thus encouraged by the need for answering unresolved questions arising from a heavy metal presence and by rapid industrial development in this area. To this end, we have utilized advanced capabilities of current computational chemistry and concentrated our efforts on developing relativistic spin–orbit models which can provide a satisfactory interpretation of experimental observations, sometimes even qualitatively different from the counterpart based on the spin-free (SF) concept.

In this doctoral thesis a few representative complexes of a broad class of rhenium(I) tricarbonyl complexes  $[\text{Re}(\text{L})(\text{CO})_3(\alpha\text{-diimine})]^n$  (L being an axial ligand) have been investigated. There are several main reasons why we have decided for these complexes. Firstly, there are available experimental data, e.g. absorption (UV–vis) and emission spectra (under low temperatures), and data from ultrafast spectroscopies<sup>26–29</sup> – our goal is to explain these experiments on the basis of our theoretical results.

Secondly, *ab initio* calculations of heavy-metal compounds still pose a significant challenge to scientists and especially SO computational studies are scarce in literature. The SO treatment thus introduces a fairly novel approach to these molecules. Moreover, to the best of our knowledge some of these systems have not been computed in the SO framework.

Thirdly, the extensive research is prompted and driven by the ambition to accelerate the development of photonic applications and to exploit recent advances in optoelectronics. The rich diversity of photophysical behaviour observed in this family of rhenium complexes is connected to the character of their lowest excited states, which depends profoundly on a particular structure of a complex. Therefore one of the aims of this thesis is to analyze the influence of a ligand substitution in the coordination sphere of the rhenium metal centre on physical and optical properties of a complex.<sup>21,30</sup> Four different axial ligands (chloride, bromide, iodide and imidazole) and two  $\alpha$ -diimine ligands (bipyridine or phenanthroline derivatives) were varied in order to examine qualitatively and quantitatively how molecular orbitals and the resulting energies are affected by changing the coordination surroundings. These findings might be helpful in tailoring and tuning systems with the potential for OLED (and other) applications according to concrete requirements.

It is self-evident that the motivation for calculating these heavy-metal complexes goes hand in hand also with the ongoing improvements of experimental techniques. At present,



experimentalists are achieving not only high spectral and spatial resolution, but they are also able to measure on short time scales (of the picosecond/femtosecond order, which corresponds with ISC rates and lifetimes<sup>31,32</sup> of low-lying states) etc. Clearly, it is particularly interesting and useful to simulate experiments via theoretical computations and thus obtain information about the strengths and limitations of a chosen theoretical method in order to assess its quality and area of its applicability.

Recently, the conjunction of different quantum chemical calculations and experimental measurements has enabled a successful characterization of heavy-metal complexes and related photophysical processes in many projects.<sup>1,33,34</sup> It has been proven that such a way of investigation is able to bring a reasonable depiction of these complexes, and is highly promising.<sup>28,35–38</sup> For instance, theory might help to identify the origin of radiationless transitions not directly observable in an experiment or to discover excited states which take part in emissive processes. Furthermore, a mutual agreement between calculated and measured spectroscopic properties gives evidence in the sense that we are undoubtedly closer to a better understanding of these complicated systems.

On the whole, the synergy of theory and experiment has turned out to be of great benefit in gaining a deeper insight into electronic structures, molecular spectra and underlying photophysics of heavy-metal complexes. On the theoretical side, we have used two distinct computational techniques, namely spin–orbit multiconfigurational second-order perturbation theory (SO-MS-CASPT2) and spin–orbit time-dependent density functional theory (SO-TD-DFT) and compared the obtained results with available experimental data which have primarily originated from the laboratory of Professor Antonín Vlček Jr. and his co-workers.

## Chapter 2: THEORETICAL OVERVIEW

### 2.1 Heavy-metal complexes

Transition metal chemistry is not only colourful, but also quite challenging because of many special characteristics that can be attributed to the presence of the heavy metal atom, for example a possibility of long-range charge separation, strong SOC that manifests itself in ultrafast ISC to triplet states and their intense radiative decay, and a high density of electronic states, i.e. energy differences between two neighbouring states are small, which can lead to near-degeneracy effects. All that implies that transition metal complexes are remarkable systems, but at the same time it dramatically complicates their theoretical description.

Coordination compounds are typically characterized in terms of a number of ligands donating a pair of electrons to a metal centre. The coordination number typically exceeds the oxidation number of the metal centre. As the title of my doctoral thesis suggests, transition metals (especially rhenium) are in the centre of our attention. The standard definition according to the International Union of Pure and Applied Chemistry (IUPAC) says that transition metals have a partially filled  $(n-1)d$ -subshell. These  $d$  orbitals are responsible for many characteristic features of these metals and derived complexes. For example, magnetic properties or colour can be explained based on the actual un/occupancy of molecular orbitals (MOs) originating from  $(n-1)d$  orbitals or transitions from these MOs to higher orbitals, respectively. Depending on a geometry of a complex with a metal ion surrounded by a field of neighbouring ligands, the original degeneracy of metal  $d$  orbitals is broken and they are split accordingly (an illustrative example of the MO diagram will be given in Chapter 3.1.1). Two fundamental and semi-empirical theories have been formulated in order to describe transition metal complexes, the loss of degeneracy of  $d$  orbitals being at the heart of both these approaches: (1) crystal field theory which represents a relatively simple model grounded on pure electrostatic interactions between a metal centre and its ligands, and (2) an extension of the previous concept – ligand field theory<sup>39</sup> (LFT). The latter one attempts to interpret the orbital arrangement and chemical bonding. Thus LFT is able to provide valuable information about the electronic structure, spectroscopy and photochemistry of transition metal complexes and it could serve as a useful guide to investigating experimental and theoretical data.

Since we have focused on rhenium(I) complexes in the studies presented in this work, the further text will be almost exclusively devoted to these molecules. However, some of general findings and our conclusions can also be applied to heavy-atom compounds containing other transition metals, such as ruthenium, platinum, iridium etc.

### 2.1.1 Electronic excited states and their mixing

Several different types of electronic transitions can be distinguished in transition metal chemistry. In our studies we have mainly dealt with charge-transfer (CT) transitions – what decides about the character of a CT state is an origin of the site from which charge density shifts away (the so-called donor) and of the site where charge density increases (the acceptor). Among excited states generated by five most typical transitions in transition metal complexes we rank: (1) metal-centred (MC) states, also known under the label “metal-localised”,  $dd$  states (due to  $d \rightarrow d^*$  excitations) or ligand-field (LF) excited states, (2) intraligand (IL) states (also called ligand-centred (LC)), for which electronic redistribution occurs within the same ligand, (3) metal-to-ligand charge-transfer (MLCT) states, (4) ligand-to-metal CT (LMCT) states, and (5) ligand-to-ligand CT (LLCT) states, where the donor and acceptor are two different ligands of a transition metal complex (in case of a halide donating ligand X, we talk about XLCT). Many other, usually special cases of CT states can be recognized and defined, for example specifying that the charge is transferred from sigma bonds of metal/ligands etc.

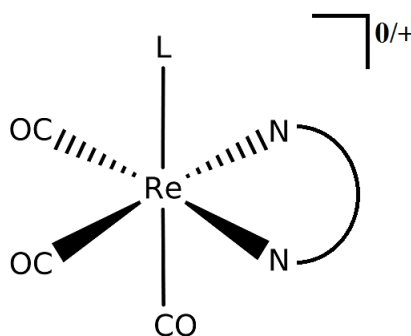


**Figure 2.1.** The schematic structure of  $fac\text{-[Re(L)(CO)}_3(\alpha\text{-diimine)]}^{0/+}$  complexes.

Regarding a broad class of rhenium(I) tricarbonyl-diimine complexes of the  $fac\text{-[Re(L)(CO)}_3(\text{N}^{\wedge}\text{N})]^n$  type, electronic states of great interest to spectroscopy and photophysics are those low-lying excited states that arise from a mixing of MLCT, LLCT and IL characters.<sup>30,40</sup> It is the origin of the orbital mixing that decides about their excited-state behaviour, and in this sense two types of that mixing should be pointed out, MLCT–LLCT and MLCT–IL mixing.

The former usually occurs in the lowest excited states which have a predominant MLCT character involving an equatorial diimine ligand with a LLCT contribution from the occupied axial ligand (L)  $\pi$  orbitals. In addition, a LLCT from  $\pi$ -antibonding carbonyl orbitals is present, which is caused by the fact that rhenium  $d$  orbitals are mixed with carbonyl  $\pi^*$  in the final molecular orbitals. Therefore a MLCT state is always accompanied by the  $\pi^*(\text{CO})$  electronic depopulation, which is confirmed in spectra by blue shifts of  $\nu(\text{CO})$  vibrations upon excitation.<sup>35,41,42</sup> A significant mixing of MLCT and LLCT ( $\text{L} \rightarrow \text{N}^{\wedge}\text{N}$ ) characters is noted when an axial ligand L acts as  $\pi$ -donor, e.g. halides, imidazole, amides, phosphides etc.<sup>19,28,37,43</sup> Then the best description of such excited states is delocalized  $\text{ReL(CO)}_3 \rightarrow \text{N}^{\wedge}\text{N}$  CT.

The latter one mostly takes place in triplet states and its detailed character is structurally and environmentally dependent.<sup>30,40</sup> Low-lying excited states are influenced by the fact that

the amount of charge transferred from a metal upon excitation is lower in contrast to a pure MLCT state. The extent of decrease of MLCT participation in a particular state is related to an actual solvent.<sup>29,44,45</sup> For illustration, a typical example of IL is a charge transfer from  $\pi$  to  $\pi^*$  orbitals on a bipyridine ligand of  $[\text{ReX}(\text{CO})_3(\text{bpy})]$  (see Chapter 3.1).

MC states are of little photophysical importance for our study, since they lie at too high energies in  $\text{Re}^{\text{I}}$  tricarbonyl-diimines (or generally in third row transition metal complexes) to participate in the excited-state dynamics after optical excitation. In contrast, in photophysics of  $\text{Ru}^{\text{II}}$  polypyridines<sup>46</sup> or complexes containing 3d metals such as  $\text{Fe}^{31,47}$  and  $\text{Cr}^{48}$  MC states play a significant role.

## 2.2 Relativistic effects

We may follow a widespread belief that Einstein's special theory of relativity must be applied only to situations when velocities of objects are approaching the speed of light. Indeed, many chemical processes and properties could be described and obtained at a reasonable level of accuracy without recourse to relativistic treatment. Nevertheless, when we intend to perform electronic structure calculations to high precision, the theory of relativity is recommended for a qualitatively and quantitatively correct characterization even of lighter atoms, let alone heavy metals and molecules involving them, for which the inclusion of relativistic corrections is obligatory. The effect of relativity can be observed to a different extent across the entire periodic table, having many dramatic consequences especially for heavier elements such as 5d transition metals, lanthanides and actinides.<sup>2,3,49</sup> It influences their electronic structures by splitting originally degenerate components of multiplets, by mixing nonrelativistically obtained electronic excited states and changing thus substantially their origin and energy. This naturally increases the density of electronic states, which is relevant to reactivity, photophysics and spectroscopy. As a result of SOC, electrons of heavy atoms occupying atomic  $p$  orbitals (and similarly  $d$  and higher orbitals) are no longer equivalent, since these orbitals are split into  $p_{1/2}$  and  $p_{3/2}$  (or  $d_{3/2}$  and  $d_{5/2}$  etc.) components which differ in their energy and shape. Basically, in atoms SOC increases with the increasing nuclear charge and decreases in the order  $p > d > f$  within a shell. In molecules, the relativity can markedly affect bond energies as well as bond lengths and strengths, to name just a few important impacts. The yellow colour of gold or the liquidity of mercury belong to the well-known examples of relativity manifestation which have been the subject of many publications.<sup>2,4</sup>

### 2.2.1 The Dirac equation and its approximations

The relativistic effects are conventionally divided into the scalar (spin-independent, spin-free) and spin-orbit (spin-dependent) relativistic effects. However, the separation into these two distinct categories is not unambiguously defined and is in fact arbitrary, since it depends on a particular formalism and an employed approximation of the Dirac Hamiltonian.<sup>50</sup> Thus both effects can be handled at once within a chosen approximation. All the exact and approximate theories proceed from the fully relativistic one-electron, four-component Dirac equation<sup>51,52</sup> which replaces the time-dependent Schrödinger equation used in nonrelativistic

quantum chemistry. To generalize the one-electron Dirac equation to a many-electron problem, electron–electron interaction must be accounted for. At the simplest level, it can be achieved by adding the nonrelativistic Coulomb potential two-electron operator to the Dirac Hamiltonian, resulting in the Dirac-Coulomb Hamiltonian. The Dirac equation for an electron that is described by a wave function  $\psi$  and is moving in an external potential  $V(x, y, z)$  can be written in the form

$$\left[ -ic\hbar \left( \alpha_x \frac{\partial}{\partial x} + \alpha_y \frac{\partial}{\partial y} + \alpha_z \frac{\partial}{\partial z} \right) + \beta m_e c^2 + V(x, y, z) \right] \psi = i\hbar \frac{\partial \psi}{\partial t} \quad (2.1)$$

where  $\alpha_x$ ,  $\alpha_y$ ,  $\alpha_z$  and  $\beta$  are four-by-four matrices that must obey three conditions:  $\alpha_i \alpha_j = -\alpha_j \alpha_i$  ( $i \neq j$ ),  $\alpha_i \beta = -\beta \alpha_i$  and  $\alpha_i^2 = \beta^2 = 1$ . In the standard representation these quantities are

$$\beta = \begin{pmatrix} \mathbf{I}_2 & \mathbf{0}_2 \\ \mathbf{0}_2 & -\mathbf{I}_2 \end{pmatrix}, \alpha_x = \begin{pmatrix} \mathbf{0}_2 & \boldsymbol{\sigma}_x \\ \boldsymbol{\sigma}_x & \mathbf{0}_2 \end{pmatrix}, \alpha_y = \begin{pmatrix} \mathbf{0}_2 & \boldsymbol{\sigma}_y \\ \boldsymbol{\sigma}_y & \mathbf{0}_2 \end{pmatrix}, \alpha_z = \begin{pmatrix} \mathbf{0}_2 & \boldsymbol{\sigma}_z \\ \boldsymbol{\sigma}_z & \mathbf{0}_2 \end{pmatrix} \quad (2.2)$$

where the elements of  $\alpha_x$ ,  $\alpha_y$ ,  $\alpha_z$  and  $\beta$  matrices are two-by-two matrices (denoted by the bold font),  $\mathbf{I}_2$  and  $\mathbf{0}_2$  being the 2x2 identity and null matrices, respectively, and  $\boldsymbol{\sigma}_x$ ,  $\boldsymbol{\sigma}_y$ ,  $\boldsymbol{\sigma}_z$  are the 2x2 Pauli spin matrices:

$$\boldsymbol{\sigma}_x = \begin{pmatrix} 0 & 1 \\ 1 & 0 \end{pmatrix}, \quad \boldsymbol{\sigma}_y = \begin{pmatrix} 0 & -i \\ i & 0 \end{pmatrix}, \quad \boldsymbol{\sigma}_z = \begin{pmatrix} 1 & 0 \\ 0 & 1 \end{pmatrix} \quad (2.3)$$

Therefore  $\psi$  has to be a four-component column vector

$$\psi = \begin{pmatrix} \psi_1 \\ \psi_2 \\ \psi_3 \\ \psi_4 \end{pmatrix} \quad (2.4)$$

where each component depends on three spatial coordinates  $x, y, z$  and time  $t$ . The expression  $m_e c^2$  represents the rest mass energy of the electron. For the sake of clarity, but without going into more details, the potential  $V$  replaces  $-e\phi$ ;  $\phi$  being the scalar potential and at the same time one component of a four-potential  $\mathbf{A} = (\mathbf{A}, i\phi/c)$ . The vector potential  $\mathbf{A}$  is assumed to be zero. In contrast to the Schrödinger equation where second-order partial derivatives in the spatial coordinates and only a first-order derivative in the time occur, the Dirac equation treats  $x, y, z$  and  $t$  on an equal footing (first derivatives) in accordance with requirements of the theory of relativity (i.e. the relativistic principle of equivalence of spatial and temporal variables).

Four solutions to Eq. (2.1) correspond to two possible spin states of the electron (the positive-energy solution) and its antiparticle, the positron (the negative-energy solution), which differ only in the sign of their charge. The wave function  $\psi$  can be decomposed into the large  $\psi^L$  and small  $\psi^S$  two-component parts

$$\psi = \begin{pmatrix} \psi^L \\ \psi^S \end{pmatrix}, \quad \psi^L = \begin{pmatrix} \psi_1 \\ \psi_2 \end{pmatrix}, \quad \psi^S = \begin{pmatrix} \psi_3 \\ \psi_4 \end{pmatrix}. \quad (2.5)$$

If  $V$  is a electrostatic potential generated by a molecular field (in the form of Coulomb interaction with nuclei) within the Born-Oppenheimer approximation (where the vector potential  $\mathbf{A} = 0$ ) and we rewrite Eq. (2.1) into the time-independent electronic Dirac equation where additionally the rest energy  $m_e c^2$  has been subtracted, we get Eq. (2.6) on matrix form convenient for subsequent sections:

$$\begin{pmatrix} V - E & c(\boldsymbol{\sigma} \cdot \mathbf{p}) \\ c(\boldsymbol{\sigma} \cdot \mathbf{p}) & V - E - 2m_e c^2 \end{pmatrix} \begin{pmatrix} \psi^L \\ \psi^S \end{pmatrix} = 0 \quad (2.6)$$

where  $\boldsymbol{\sigma} = (\sigma_x, \sigma_y, \sigma_z)$ ,  $\mathbf{p} = -i\hbar\nabla$  is the canonical momentum operator and the energy  $E$  does not include the rest energy  $m_e c^2$ . For our purposes, we choose the positive-energy solutions corresponding to electrons. The large and small components are coupled in the following way:

$$\psi^S = R\psi^L \quad (2.7)$$

$$R = (2m_e c^2 - V + E)^{-1} c(\boldsymbol{\sigma} \cdot \mathbf{p}) = \frac{1}{2m_e c} \left[ 1 - \frac{V - E}{2m_e c^2} \right]^{-1} (\boldsymbol{\sigma} \cdot \mathbf{p}) \quad (2.8)$$

where  $R$  represents the energy-dependent exact coupling operator between  $\psi^S$  and  $\psi^L$ . It can be shown that in the nonrelativistic limit (i.e.  $c \rightarrow \infty$ ) the small component and relativistic corrections vanish and we return back to the Schrödinger equation.<sup>53</sup>

Nowadays the advances in computational quantum chemistry allow for accurate calculations of small molecules within the fully relativistic four-component theory.<sup>54</sup> For electronic excited-state calculations in large transition metal compounds, however, it is necessary to reduce the formalism to a two-component scheme (or even into a one-component form whereas SOC is treated afterwards, for instance by perturbation theory (PT)) in order to keep the computational costs at a feasible level. In this respect various simplifying approximations have been proposed,<sup>53,55</sup> some of them being outlined below.

In fact, the inclusion of relativistic effects is realized by the choice of Hamiltonian – most of widely used two-component relativistic Hamiltonians are based on decoupling/separating the large- and small-component blocks of the fully relativistic four-component Dirac Hamiltonian and projecting out the negative-energy solutions. This can be performed in either an exact or approximate way,<sup>55,56</sup> where the energy-dependent coupling  $R$  (Eq. (2.8)) of the large and small component is calculated either exactly or is approximated, respectively. We further limit ourselves to the latter option, since only the approximate relativistic Hamiltonians were employed in this thesis.

One of the oldest and simplest approximate methods of a four-to-two-component transformation was introduced by Pauli. The construction of the Pauli Hamiltonian is usually based on the elimination of the small component through a combination of Eq. (2.6), (2.7) and (2.8) and the subsequent expansion of the term  $\left[ 1 - \frac{V - E}{2m_e c^2} \right]^{-1}$  in Eq. (2.8) in powers of the denominator  $2m_e c^2$  (or generally in  $1/c$ ), which is valid only when  $|V - E| \ll 2m_e c^2$ . Only the first-order corrections (i.e. those including  $1/c^2$ ) are retained. Without a further derivation the Pauli Hamiltonian reads:

$$\hat{H}^{Pauli} = V + \frac{\mathbf{p}^2}{2m_e} - \frac{\mathbf{p}^4}{8m_e^3c^2} + \frac{\hbar^2}{8m_e^2c^2}(\nabla^2 V) + \frac{\hbar}{4m_e^2c^2} \boldsymbol{\sigma} \cdot (\nabla V) \times \mathbf{p} \quad (2.9)$$

where the terms from the left are the nonrelativistic kinetic energy operator, the external (nuclear) potential, the mass–velocity term that represents a relativistic correction to the kinetic energy, the fourth term is the Darwin operator (a relativistic correction to the potential) and the last term corresponds to the one-electron spin–orbit operator (see Chapter 2.2.3). The mass–velocity and Darwin terms are the scalar relativistic corrections to the nonrelativistic one-electron Hamiltonian.

The applicability of this approach is, however, rather limited. Firstly, the problem is that the Pauli Hamiltonian is not bounded from below due to the presence of the mass–velocity operator (powers of the momentum operator higher than 2 are not bounded), which in consequence excludes this Hamiltonian from the variational use. Thus this relativistic Hamiltonian must be employed in perturbation theory only. Secondly, a serious obstacle to using this method lies in the highly singular nature of the operators in the expansion caused by the invalidity of the expansion in the vicinity of the nuclei. Despite serious shortcomings of the Pauli Hamiltonian, it is worth mentioning for illustrative reasons due to its relative transparency. Moreover, the development of many other methods has aimed to correct the deficiencies of the Pauli Hamiltonian by designing a better decoupling transformation and expansion scheme.

To introduce an principal idea behind a decoupling method, the unitary Foldy–Wouthuysen (FW) transformation<sup>53,57</sup> will be briefly described. Its goal is to separate the large- and small-component parts of the one-electron Dirac Hamiltonian and to define an energy-independent two-component Hamiltonian reproducing the positive-energy branch. We follow from Eq. (2.6) – for the Dirac Hamiltonian  $\hat{H}^D$  in this equation a unitary transformation  $\mathcal{U}$  is sought so that this Hamiltonian is diagonalized with respect to the large- and small-component spinor spaces

$$\mathcal{U}\hat{H}^D\mathcal{U}^{-1} = \begin{pmatrix} \hat{H}_+ & \mathbf{0} \\ \mathbf{0} & \hat{H}_- \end{pmatrix} \quad (2.10)$$

and so that a four-component wave function is transformed into a two-component form by eliminating the small component. The Foldy–Wouthuysen transformation is found to be

$$\mathcal{U} = \begin{pmatrix} \Omega_+ & \Omega_+ R^\dagger \\ -\Omega_- R & \Omega_- \end{pmatrix}; \quad \Omega_+ = \frac{1}{\sqrt{1+R^\dagger R}}, \quad \Omega_- = \frac{1}{\sqrt{1+RR^\dagger}}, \quad (2.11)$$

$R$  and its Hermitian conjugate  $R^\dagger$  being known from Eq. (2.8). This transformation can be expressed as two successive steps,  $\mathcal{U} = W_1 W_2$ , whereby  $W_1$  is responsible for decoupling the large and small components and  $W_2$  ensures renormalization. The Foldy–Wouthuysen two-component wave function is then given as

$$\psi^{FW} = \sqrt{1 + R^\dagger R} \psi^L. \quad (2.12)$$

Nevertheless,  $R$  is energy- and potential-dependent, the associated equations are hard to solve and the transformed Hamiltonian is much more complicated than the original Dirac Hamiltonian. Therefore one has to proceed to various approximations – one usually resorts to decoupling to some order in a particular coupling/expansion parameter (thus in fact adopting perturbation theory).

In this thesis two different approximations to the Dirac equation were used: (1) the Douglas–Kroll(–Hess) (DK(H)) transformation,<sup>58–62</sup> and (2) the zeroth-order regular approximation<sup>63–65</sup> (ZORA).

The Douglas–Kroll(–Hess) transformation is based on eliminating the coupling between the large and small components to a certain order by a sequence of unitary transformations. As the first step the free-particle FW transformation  $\mathcal{U}_0$  to the free-field Dirac Hamiltonian  $\hat{H}_0 = c\boldsymbol{\alpha} \cdot \mathbf{p} + \beta m_e c^2$  (i.e. without the term  $V$ ) is carried out

$$\mathcal{U}_0 = \sqrt{\frac{\hat{E}_p + m_e c^2}{2\hat{E}_p}} \left( \mathbf{I}_4 + \frac{c\beta\boldsymbol{\alpha} \cdot \mathbf{p}}{\hat{E}_p + m_e c^2} \right) \quad (2.13)$$

where  $\boldsymbol{\alpha} = (\alpha_x, \alpha_y, \alpha_z)$ ,  $\mathbf{I}_4$  denotes the identity matrix and  $\hat{E}_p = \sqrt{m_e^2 c^4 + c^2 p^2}$  is the free-particle Dirac energy operator and  $\mathbf{p}$  is linear momentum. Note that here we do not subtract the rest mass energy. The transformed lowest-order free-field Dirac Hamiltonian  $\hat{H}_0$  has the following simple and diagonal form:

$$\mathcal{U}_0 \hat{H}_0 \mathcal{U}_0^{-1} = \beta \hat{E}_p = \begin{pmatrix} \hat{E}_p & \mathbf{0} \\ \mathbf{0} & -\hat{E}_p \end{pmatrix} \quad (2.14)$$

If we now assume the external potential  $V$  in the Dirac Hamiltonian, after transforming additional terms (relativistic corrections) would appear in Eq. (2.14). These terms include the potential, where singularities are prevented by the presence of so-called kinematic factors. When the positive-energy block of the transformed Hamiltonian is taken, we achieve the so-called DK1 Hamiltonian (to the first order). However, this operator is still insufficient for relativistic purposes and a further transformation is required. Therefore the approximate decoupling through several transformations ( $\mathcal{U} = \mathcal{U}_0 \mathcal{U}_1 \mathcal{U}_2 \dots$ ) is applied by using an approximate expansion procedure, i.e. by a unitary transformation which is expanded in orders of the one-electron external potential  $V$ .<sup>58</sup> This is usually generated up to the second order ( $\mathcal{U} = \mathcal{U}_0 \mathcal{U}_1$ , DKH2), as was originally proposed by Hess<sup>62</sup> – the DKH2 scheme is widely used in many quantum chemistry programs. Later, also higher-order DK Hamiltonians were derived.<sup>66</sup> We end up with the two-component approximate relativistic Douglas–Kroll Hamiltonian that involves both the scalar and spin–orbit effects. The no-pair approximation is invoked, i.e. the Hamiltonian in the positive-energy two-component subspace is employed. In contrast to the Pauli Hamiltonian, the DK Hamiltonian is bounded from below and can be used variationally. Another advantage is that all these Hamiltonians are gauge-invariant.

The zeroth-order regular approximation to the Dirac equation adopts a different approach to transformation into a two-component form. It was first formulated by Chang, Pélissier, and Durand,<sup>67</sup> and elaborated by van Lenthe et al.,<sup>63,65</sup> who came with the term “regular



approximation". Such an approximation employs an alternative expansion scheme to the Pauli Hamiltonian and the suitably rearranged exact coupling  $R$  is:

$$R = \frac{c}{2m_e c^2 - V} \left[ 1 + \frac{E}{2m_e c^2 - V} \right]^{-1} (\boldsymbol{\sigma} \cdot \mathbf{p}) \quad (2.15)$$

Comparing to Eq. (2.8) we see that now the expansion is performed in powers of the denominator  $2m_e c^2 - V$  (instead of  $2m_e c^2$  in the Pauli Hamiltonian), which explicitly involves the potential and is valid under the condition  $|E| < 2m_e c^2$  (since the minimum of potential is zero). Importantly, the presence of  $V$  in the denominator regularizes the expansion (at the nucleus) and we are able to describe correctly the complicated behaviour close to the nuclei (where the potential becomes large). Thus the regular expression for the Hamiltonian and the resulting energy avoids singularity and divergence problems encountered with the Pauli Hamiltonian and it is possible to use the ZORA method in variational treatment. The ZORA Hamiltonian reads:

$$\hat{H}^{ZORA} = V + T^{ZORA}; \quad T^{ZORA} = \frac{1}{2m_e} (\boldsymbol{\sigma} \cdot \mathbf{p}) \frac{2m_e c^2}{2m_e c^2 - V} (\boldsymbol{\sigma} \cdot \mathbf{p}) \quad (2.16)$$

For  $V \rightarrow 0$  far from the nuclei we get the nonrelativistic expression of kinetic energy operator. Expanding  $(2m_e c^2 - V)^{-1}$  in a series and comparing to the Pauli Hamiltonian (Eq. (2.9)), it is found out that the ZORA Hamiltonian includes only a part of the Darwin term and no mass-velocity term, while the full one-electron spin-orbit contribution is present in both Hamiltonians.

It can be shown that the decoupling transformation  $W_1$  (as described above for the FW transformation) gives the ZORA and the subsequent renormalizing transformation  $W_2$  provides the extension to the infinite-order<sup>68</sup> (IORA).

Unfortunately, the ZORA Hamiltonian in its original formulation (due to the potential term in the denominator) suffers from the disadvantage that it is not invariant to the choice of electric gauge (i.e. where the zero of the potential is set). In other words, when a constant is added to the potential, it does not lead to the energies that are shifted also by this constant. It turns out that the energy errors of the valence electrons are not so serious. However, especially the core electrons are much affected by this deficiency and within ZORA their core-orbital energies are too low when compared to the Dirac equation. Therefore the scaled ZORA<sup>65</sup> has been implemented in order to remedy the gauge-dependence. It is usual to employ ZORA within DFT rather than the wave function formalism and the integral evaluation is performed easily by 3D numerical integration techniques (the potentials being tabulated on a grid), resulting in an efficient and computationally convenient scheme.

Complete derivations of these two-component approximate relativistic Hamiltonians and more details about issues sketched above can be found elsewhere.<sup>53,55</sup>

To conclude, all these Hamiltonians account both for the scalar and spin-orbit relativistic effects. The separation of the spin-free and spin-dependent terms in these Hamiltonians leads to a further simplification of calculations, since we can treat these categories separately. Therefore in next two sections we will examine some of the approximate Hamiltonians

described in this Chapter independently from a perspective of the scalar relativistic (SR) effects and spin–orbit coupling, respectively.

### 2.2.2 Scalar relativistic effects

The SR effects (e.g. the mass–velocity and Darwin corrections in the Pauli Hamiltonian, Eq. (2.9)) have their origin in the balance between kinetic and potential energies of electrons affected by the fact that velocity of electrons in the vicinity of nucleus is close to the speed of light in heavy atoms. Based on the principles of the special theory of relativity the relativistic mass  $m$  of these electrons increases with their velocity  $v$  according to a well-known relation ( $m_e$  being the rest mass of the electron):

$$m = \frac{m_e}{\sqrt{1 - (v/c)^2}} \quad (2.17)$$

Thus the mass of the electrons can no longer be considered constant. The average radial velocity  $\langle v_{rad} \rangle$  of the  $1s$  electrons in a hydrogenlike atom with the atomic number  $Z$  can be roughly approximated by  $Z$  (in atomic units) and the average relativistic mass increase of the electrons is estimated to be  $m \sim m_e / \sqrt{1 - (Z/c)^2}$ . Inspecting Bohr radius  $a_0 \sim 1/m$  (see List of symbols and units) it is obvious that the high speed of the inner electrons has a direct impact on the most probable radial distance between the center of nucleus and these electrons. Namely, it is smaller when compared to its nonrelativistic counterpart. This leads to the direct relativistic contraction of  $s$  and  $p$  orbitals and to the stabilization of their orbital energies. This effect is profound mainly for the deep-lying  $s$  and  $p$  orbitals, but affects to a certain extent also the valence shells. Consequently  $d$  and  $f$  orbitals expand and their energies are destabilized (owing to the so-called indirect relativistic orbital expansion), since electrons from these orbitals feel a less attraction to the nucleus that is more effectively shielded by the contracted  $s$  and  $p$  orbitals.

The scalar relativistic effects do not cause any splitting or mixing of electronic states – their main influence consists in shifting final energies. In systems containing atoms starting from third row of the periodic table they can significantly change molecular properties such as bond distances and bond energies; in case of lighter atoms the SR effects are not so important. In molecules SOC tends to be quenched in contrast to original atoms. In addition, it can be shown that in closed-shell systems spin-dependent terms do not emerge in a perturbation expansion based on the nonrelativistic wave function earlier than in second order, whereas the SR terms contribute already in first order. Based on these findings it seems adequate to calculate a system with the full inclusion of only the SR effects at first and to handle the spin-dependent effects perturbatively afterwards, as was performed in this thesis.

Luckily, the implementation of the SR effects is often technically simple, as the scalar terms usually modify only the one-electron Hamiltonian. Provided that the spin-dependent terms have been separated from a two-component Hamiltonian, which is equivalent to ignoring SOC at this level of theory, a spin-free Hamiltonian within a one-component approximation is obtained. This suggests that we can compute the scalar relativity in the usual nonrelativistic regime, only with slight adaptations (modified one- and two-electron

integrals). The resulting relativistic spin-free wave function may be employed in the subsequent SO calculations.

In our projects three different computational options to account for the SR effects were chosen: (1) relativistic effective core pseudopotentials<sup>69,70</sup> (ECPs), (2) the DKH Hamiltonian,<sup>59,61</sup> and (3) the SR ZORA.<sup>65,71</sup>

The ECPs take into account the SR effects by replacing the transition metal core electrons by an effective potential which was generated on the footing of atomic relativistic calculations. The remainder of a heavy metal atom is described by an appropriately adjusted and optimized valence basis set, i.e. only heavy metal valence electrons are treated explicitly. This originally very popular and frequently used method was found worse in quality than the other two approaches which adopt all-electron scheme and so we abandoned ECPs after a few preliminary calculations. More details about relativistic pseudopotentials could be found in the literature.<sup>72</sup>

The DK Hamiltonian (based on the DKH transformation) can be partitioned into the SF and SO parts. The common practice (as it is adopted in the SO-MS-CASPT2 approach) is to use them separately and as a first step the spin-free Douglas–Kroll-transformed Hamiltonian is employed. When the bare Coulomb operator is included in this spin-free DK-transformed Hamiltonian, we talk about the Douglas–Kroll–Hess Hamiltonian.<sup>\* 59,61</sup> We are thus able to introduce the SR effects into a calculation by adding the corresponding spin-free terms (by averaging over spin) of the DKH Hamiltonian to the one-electron integrals, which is ensured by using the atomic natural orbital relativistic consistent correlated (ANO-RCC) type of basis set.<sup>73–75</sup> In other words, this basis set has been contracted using the DKH Hamiltonian. It has been shown that the ANO-RCC basis set is the best affordable and the most accurate one for our purposes. The two-electron integrals are left untransformed in the DKH scheme, which turns out to be a reasonable approximation.

The third alternative is the ZORA treatment of the scalar relativistic effects. As with the DKH transformation, in principle the full ZORA accounts for both spin-free and spin–orbit effects and only the SR ZORA can be defined by separating and neglecting the spin-dependent parts.

### 2.2.3 Spin–orbit coupling

The spin–orbit interaction represents the most important and frequently observed fine effect causing the fine structure of atomic and molecular spectra. In comparison to other fine and hyperfine effects its magnitude ranks it among the most pronounced ones. SOC can induce a crossing between different potential energy surfaces (PESs) or change the shape of a single PES. For that reason its influence cannot be neglected and is experimentally measurable, although in relatively low energies ( $\sim 1\text{--}100\text{ cm}^{-1}$ ), however it can reach even greater values in case of very strong SOC. Spin–orbit coupling is noticeable even by light

---

\* However, there is some inconsistency in labelling this transformation and associated Hamiltonians in literature. Both DK and DKH abbreviations frequently appear in books and articles, regardless of the precise meaning and authorship, probably indicating the equal importance of contributions of all three main authors, Douglas, Kroll and Hess. For clarity, I decided to use terms the DKH transformation and mostly the DK Hamiltonian.

molecules consisting of the first- and second-row atoms. Not surprisingly, SOC is of extreme importance for transition metal complexes.

Spin–orbit coupling denotes the interaction between the magnetic moments associated with the electron spin and orbital angular momenta (owing to orbital motion of electrons) in the form of scalar product. Spin–orbit coupling<sup>3,76</sup> follows inherently from the very essence of the Dirac equation, as well as the spin magnetic moment which was correctly predicted by Dirac,<sup>51,52</sup> whereas in nonrelativistic treatment the existence of electron spin is just phenomenologically postulated. The spin–orbit Hamiltonian can have many forms depending on the level of desired accuracy and the applied approximation. The well-known *ab initio* formulation is that of Breit and Pauli<sup>77,78</sup> (Eq. (2.18)), on which individual terms contributing to SOC will be explained. The full Breit–Pauli Hamiltonian operator is defined as a difference between the total relativistic and nonrelativistic electronic Hamiltonian and can be written as a sum of six types of relativistic corrections. The five of them will be listed without a further description: (1) spin–spin dipole interaction (Fermi contact interaction), (2) Dirac correction for electron spin, (3) orbit–orbit interaction between the magnetic dipole moments of electrons arising from the orbital motion, (4) the relativistic mass variation of electron due to the dependence of mass on velocity, and (5) the interaction between spin and orbital magnetic moments in the presence of external magnetic or electric fields. The sixth term in the Breit–Pauli Hamiltonian is responsible for spin–orbit coupling and only this part will be given explicitly. In polyatomic molecules the spin–orbit Hamiltonian reads

$$\hat{H}_{BP}^{SO} = \frac{e^2 \hbar}{2m_e^2 c^2} \left\{ \sum_i \sum_A \frac{Z_A}{r_{iA}^3} (\mathbf{r}_{iA} \times \mathbf{p}_i) \cdot \mathbf{s}_i - \sum_{i \neq j} \left( \frac{\mathbf{r}_{ij}}{r_{ij}^3} \times \mathbf{p}_i \right) \cdot (\mathbf{s}_i + 2\mathbf{s}_j) \right\} \quad (2.18)$$

and consists of one-electron and two-electron contributions (operators). The former represents the interaction of the spin of electron  $i$  with its own orbital angular momentum relative to the nucleus  $A$  at the position  $\mathbf{R}_A$ . The latter is composed of the so-called “spin-same-orbit” and “spin-other-orbit” parts, which can be interpreted as the coupling between the spin momentum of the  $i$ -th electron and the orbital angular momentum of the same electron induced by its motion in the field of the  $j$ -th electron, and as the coupling between the spin momentum of the  $i$ -th electron and the orbital angular momentum of the  $j$ -th electron around the  $i$ -th electron, respectively.  $Z_A$  stands for the atomic number (the bare nuclear charge of the  $A$ -th nucleus),  $\mathbf{r}_{iA} = \mathbf{r}_i - \mathbf{R}_A$ ,  $r_{iA} = |\mathbf{r}_i - \mathbf{R}_A|$  are the vector and distance between the  $i$ -th electron and  $A$ -th nucleus, respectively. Likewise,  $r_{ij} = |\mathbf{r}_i - \mathbf{r}_j|$  denotes the distance between the  $i$ -th and  $j$ -th electron.  $\mathbf{p}_i$  and  $\mathbf{s}_i$  are the canonical momentum and the spin momentum operators of the  $i$ -th electron, respectively. The orbital angular momentum of the  $i$ -th electron with respect to the position of the  $j$ -th electron is defined as  $\mathbf{l}_{ij} = \mathbf{r}_{ij} \times \mathbf{p}_i$ . All constants are evaluated in the section List of symbols and units.

It should be mentioned that the microscopic SOC operators used within the ZORA and DKH formalism are more complicated than Eq. (2.18), but the basic idea behind the SO operator remains the same. Eq. (2.18) could be easily simplified by ignoring two-electron operators, which is justified by the fact that the one-electron term usually contributes considerably more to SOC than two-electron ones. In addition, because of its dependence on

the atomic number, the one-electron term becomes even more dominant for heavy elements. Nevertheless, the neglect of the two-electron terms can result in erroneous overestimation of SO splitting, and therefore better strategies to tackle the computationally demanding two-electron terms are sought. One of the successful and efficient techniques was developed by Hess et al.<sup>79</sup> and is pursued in the SO-MS-CASPT2 method, namely in the restricted active space state interaction including SOC (SO-RASSI) procedure. For more details see Chapter 2.4.4.

It is widely accepted among quantum chemists that the spin selection rule postulates a condition  $\Delta S = 0$  for allowed electronic transitions, where  $S$  is the total spin quantum number of a particular state in a system. That means transitions between states with different spin multiplicity ( $2S + 1$ ) are traditionally strictly forbidden – for example between singlet ( $S = 0$ ,  $M_S = 0$ ) and triplet ( $S = 1$ ,  $M_S = -1, 0, 1$ ) electronic states.  $M_S = \sum_i (m_s)_i$  is the total spin-projection quantum number (where the index  $i$  represents all unpaired electrons in a system) with values ranging from  $-S$  to  $+S$  and  $m_s = \pm \frac{1}{2}$  is the (spin-projection) quantum number of the  $z$ -component of the spin angular momentum for a single electron.<sup>†</sup> However, the validity of this rule is broken in relativistic treatment when the spin–orbit interaction is no longer negligible.  $S$  and  $M_S$  cannot be then called good quantum numbers. Due to SOC of heavy atoms in complexes, originally degenerate  $S$  multiplet is split in  $M_S$  components and states with different spin multiplicity are mixed. Consequently, it is useful to discriminate in quantum chemical terminology between spin-free and spin–orbit states. As their name already suggests, the former represent states without and the latter with the inclusion of SOC, respectively. With SF states we work on the CASSCF/CASPT2 level of theory and spin–orbit states are the output of SO-RASSI calculations (see Chapter 2.4.4). It can be said that spin-free states serve us as a useful tool for computational purposes. Moreover, already within the spin-free model we are able to describe reasonably an absorption spectrum. Nevertheless, in fact the spin–orbit interaction is present, which changes the whole situation dramatically, and what exists and is observed in reality are spin–orbit states. SOC induces a mixing of original spin-free states, which causes that spin–orbit states are comprised of various spin contributions (for illustration, in case of  $[\text{ReCl}(\text{CO})_3(\text{bpy})]$  the lowest excited SO state is composed of 79%  $a^3A''$  (SF triplet) and 18%  $b^1A'$  (SF singlet) as calculated by SO-MS-CASPT2). While spin multiplicity can be attributed to spin-free states without any difficulty, in the latter case it becomes ill-defined, since in the SO model we usually do not deal with pure singlets, triplets etc. any more.

It is an important aspect of relativistic SOC treatment that symmetry representations of a system must be extended accordingly. The SO states are thus characterized by their double-group symmetries without assigning any spin label, as electron spin is already naturally

<sup>†</sup> For the sake of clarity it should be noted that there are two different coupling schemes for the description of SOC in atoms: (1)  $LS$ -coupling (the so-called Russell–Saunders) which is accurate enough for most of atoms, especially light ones ( $Z \leq 30$ ), and (2)  $jj$ -coupling which is relevant for heavy atoms with strong SOC (i.e. when the spin–orbit effects are greater than other electronic effects). For transition metals the quantum numbers  $S$  and  $M_S$  etc. are then not well-defined and instead we ought to work with the quantum numbers  $J$ ,  $M_J$  and  $\vec{J} = \vec{L} + \vec{S}$ . However, for most of heavy atoms the description is somewhat intermediate between  $LS$ - and  $jj$ -coupling. The situation is even more complicated in case of molecules containing heavy atoms. For simplicity reasons the above text deals with the atomistic simplified picture.

incorporated in the SO scheme described by using the double-point-group symmetry labels.<sup>76,80,81</sup> Double groups can be regarded as the relativistic SO counterparts to the normal symmetry point groups, otherwise known as single groups. The main difference lies in the fact that single groups concern only spatial symmetries of a system and the information about electron spin is handled separately (i.e. nonrelativistic spatial atomic and molecular orbitals can be occupied simultaneously by up- and down-spin electrons in line with the Pauli exclusion principle). In contrast, double point groups take into account the spin of electron inherently, which has consequences for the composition of these groups and for the final relativistic spin-orbitals. Since a rotation by  $360^\circ$  does not return a system to its original position (for non-integral angular momentum values  $j$ ), it cannot be considered as the identity operation, but it still belongs to the group and it is denoted by the symbol  $R$ . From the designation “double groups” it can be inferred that they consist of twice as many symmetry operations as single groups. Hence double groups must also include new symmetry operations created by multiplying all elements of the single group by the symmetry operation  $R$ . A rotation by  $720^\circ$  then acts as the standard identity operation  $E$ . The double-group symmetry must be employed whenever electronic states are characterized by half-integer values of angular momentum instead of integer values.

The multiplet splitting occurs even in the absence of external magnetic field. We talk about the so-called zero-field splitting (ZFS) – each triplet state then splits into three SO sublevels. The ZFS concept usually concerns the splitting of the lowest spin-free triplet state. The energy gaps between the resulting three lowest SO states can be obtained experimentally from high-resolution emission spectra at low temperatures or temperature-dependent emission lifetimes.<sup>10,12</sup> The ZFS is thus a useful experimental parameter which may help to identify strongly phosphorescent complexes with the potential for OLED applications. The larger magnitude of ZFS is associated with greater SOC and the increased MLCT character in the emitting triplet (given by the increasing  $d$  orbital participation). For higher triplet states, the ZFS parameter is impossible to evaluate, since higher states are involved in so many SO interactions and state mixings that the parent spin-free triplet and its three components cannot be found in practice.

The effect of SO splitting is ordinarily much smaller than energy differences between electronic states, and thus SOC is often treated as a weak perturbation that is additionally included to the electronic Hamiltonian. This is a relatively reliable approach for atoms up to the 4-th row of the periodic table. Such an assumption is, however, a bit questionable in case of strong SOC in transition metal compounds. It can be considered as a reasonable approximation at least for a description of the intense phosphorescence from the lowest triplet state (the above mentioned ZFS concept). SOC splits this state into its three spin sublevels and mixes some of them with spectroscopically allowed singlet states, which makes these components emissive.

In this thesis three different approaches towards treating spin-orbit coupling were employed. In case of SO-MS-CASPT2, the spin-orbit interaction is added a posteriori by calculating the matrix elements of the spin-orbit Hamiltonian over the set of spin-free states which result from the preceding spin-independent method (including only the scalar relativistic effects), as implemented in the Molcas<sup>82–84</sup> package. The no-pair spin-orbit Hamiltonian originating from the DKH transformation is used. More details about this SO

method are presented in Chapter 2.4.4. On the other hand, it is possible to include spin–orbit coupling already from the start of a calculation by means of a two-component approximation, which has been performed in TD-DFT based on the relativistic two-component ZORA.<sup>85</sup> However, due to the large computational effort only a few test calculations have been done, so that the results could be compared to a computationally significantly cheaper perturbative technique,<sup>64,86</sup> further referred to as SO-TD-DFT. Finally, it was this approximate SO-TD-DFT method which was adopted for the generation of our SO results. Both of these spin–orbit TD-DFT methods are available in the Amsterdam Density Functional (ADF) software<sup>87–89</sup> and further details will be given at the end of Chapter 2.4.5.

The cost-effective alternative to theoretical quantum chemical calculations is the qualitative approach to SOC based on computing the coupling between spin-free singlet  $S_n$  and triplet  $T_n$  states of interest, usually between the lowest spin-free triplet state  $T_1$  and other states.<sup>10,12</sup> The energies  $E_i$  of its three SO substates  $T_{1(i)}$  are obtained by means of simple PT (SOC taken as a small perturbation) from the following equation:

$$E_i = E_{T_1} + \sum_{S_n} \frac{|\langle S_n | \hat{H}_{SO} | T_{1(i)} \rangle|^2}{E_{T_1} - E_{S_n}} + \sum_{T_n} \frac{|\langle T_{n(j)} | \hat{H}_{SO} | T_{1(i)} \rangle|^2}{E_{T_1} - E_{T_n}} \quad (2.19)$$

where  $E_{T_1}$  denotes the unperturbed energy of the lowest spin-free state  $T_1$ .  $T_{n(j)}$  and  $E_{T_n}$  represent the SO sublevel wave functions of higher spin-free triplet states  $T_n$  and their unperturbed energies, respectively. Likewise,  $E_{S_n}$  are the unperturbed energies of spin-free singlet states. Only the non-zero terms with respect to symmetry rules have to be evaluated. The form of the SO Hamiltonian used in Eq. (2.19) is obtained by several simplifications and approximate assumptions, for example only the one-electron terms and in addition only those originating from heavier atoms are considered. This convenient approach is instrumental in gaining first insights into SO interactions between the lowest excited states and may provide a quick identification of strongly SO-coupled states which possibly participate in intense emission or fast ISC pathways.<sup>28,90,91</sup> The SOC estimates can be combined with empirical knowledge of the characteristics of MLCT and IL excited states – the resulting information is helpful in a qualitative classification of transition metal complexes and can assess their applicability in OLEDs. Important findings and practical design rules deduced and derived from this procedure are discussed in more detail in Reference [92].

### 2.2.4 Jablonski diagram

To conclude this part of theory and to set the scene for the next section concerning spectroscopic aspects, we describe the popular and widely used Jablonski diagram<sup>93</sup> (Figure 2.2) in order to shed light on photophysical processes occurring in a molecule.<sup>9</sup>

It should be noted that for simplicity reasons it is usual and convenient to interpret the photophysics of a system at the level of pure singlet and triplet states and to label processes by traditionally used designations (see the legend of Figure 2.2). However, as will be demonstrated later (e.g. in Chapter 3.2.3), when strong SOC is included explicitly, the assignment of spin multiplicity is not appropriate with potential consequences for the origin of photophysical processes.

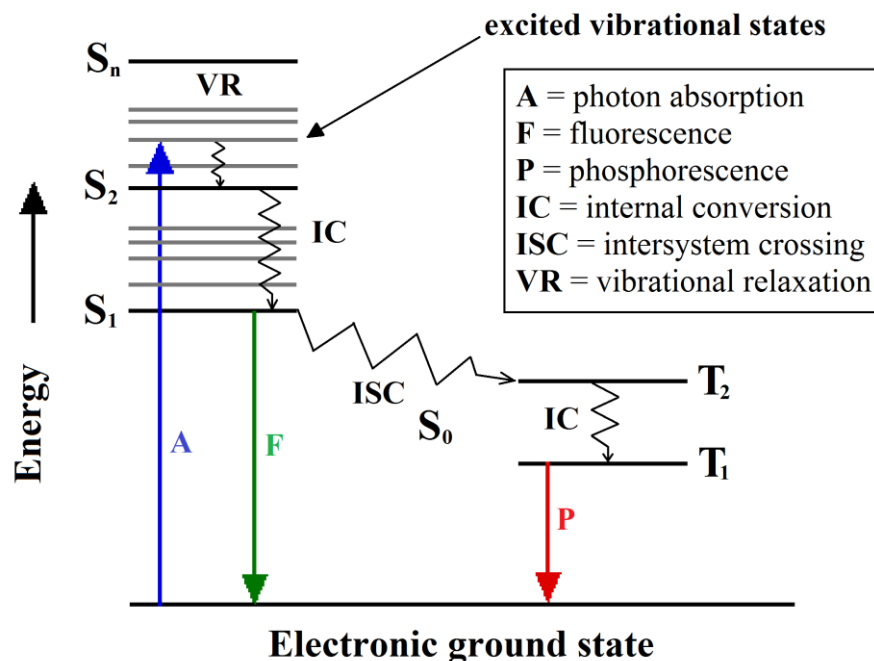


**Figure 2.2.** Jablonski diagram. A diagram with an electronic singlet ground state (GS) showing radiative and nonradiative processes in a system as described in the legend. Black horizontal lines represent electronic states, grey multiple lines within an electronic state represent vibrational levels. For more details see the text. (adopted from Reference [94] and modified)

Jablonski diagram schematically summarizes which processes are activated in a molecule by the absorption of excitation light energy. We will consider a system in its singlet ground state  $S_0$ . If a molecule absorbs energy in the form of electromagnetic radiation (which is an extremely fast action – it may only take a femtosecond), a system can be raised to a higher energy level (typically to higher singlet states  $S_1$ ,  $S_2$  etc. – in Figure 2.2 indicated by the blue upward pointing arrow). Subsequently, various decay pathways (with a different degree of probability) by which a molecule loses energy and returns back to the ground state are possible.

First of all, we will list these fundamental processes and afterwards they will be discussed in more detail. They can be divided into two groups – on the one hand there are nonradiative deactivation routes that include vibrational relaxation (VR), internal conversion (IC) and intersystem crossing (ISC), and on the other hand radiative transitions such as fluorescence and phosphorescence are noted (in Figure 2.2 depicted by the red and green arrow, respectively).

Upon the absorption of a photon, it is usual that higher vibrational levels are more populated at the excited state (ES), in contrast with a situation prior to excitation, when dominantly the zeroth vibrational level is populated at room temperature. The falling back from the upper to lower vibrational levels and finally relaxing to the zeroth vibrational level within a particular excited state is termed vibrational relaxation. If a deactivating includes also a nonradiative transition between states of the same spin multiplicity, such a process is known as internal conversion. The time of both VR and IC does not usually exceed a picosecond.



Compared to IC and ISC, VR is the most common way to release energy. VR also includes situations when the energy is distributed into remote parts of a molecule, i.e. into other normal modes through which a system relaxes. Actually, VR is intensified by collisions of an excited molecule with particles in its vicinity (a solvent in liquid phase, other gas molecules in gas phase). The absorbed energy is thus dissipated in the surroundings of a molecule (in this case we talk about solvational relaxation), before other photophysical events can happen.

A nonradiative transition from a singlet to a triplet state, or conversely a passage from a triplet to a singlet state is called intersystem crossing. Generally we can speak about a radiationless transition between states differing in their spin multiplicity. Its essence is based on a spin conversion of the excited electron, which is normally forbidden. However, if SOC is significant (such as in heavy-metal complexes), the probability of ISC is rapidly increased. This is illuminated by the fact that due to SOC the density of excited states is high and thus the vibrational levels of these two excited states can overlap, making a change in spin more favourable.

Concerning luminescence, experimentalists can observe the emission from the lowest excited singlet  $S_1$  to the singlet GS  $S_0$ , which is known as fluorescence, or the emission from the lowest triplet  $T_1$  to the singlet GS  $S_0$ , which is termed phosphorescence. Both processes are similar, except that prior to phosphorescence the excited electron has to undergo a spin conversion into a "forbidden" triplet state (ISC). From that it follows that fluorescence is the spin-allowed transition (both initial and final states have the same spin multiplicity) and for molecules containing no heavy atoms it is a statistically much more likely process than phosphorescence. In contrast, phosphorescence is formally forbidden, since a transition between two states of different spin multiplicity does not fulfil the spin selection rule. Nevertheless, owing to SOC induced by the presence of a heavy atom ISC is more probable and phosphorescence does not have to be treated as a spin-forbidden process any longer. Fluorescent states typically do not live longer than  $10^{-5}$  to  $10^{-8}$  s, phosphorescence occurs in timeframes ranging up to minutes or even hours. In case of our complexes, both radiative and nonradiative processes are usually ultrafast, e.g. fluorescence and long-lived phosphorescence decay on a femtosecond and nanosecond time scales, respectively.<sup>26,95</sup> Comparing energies of transitions, phosphorescence lies in lower energies (i.e. in longer wavelengths) relative to fluorescence. In transition metal complexes, it can sometimes happen that fluorescence exhibits low intensity or is even virtually missing. This is caused by ultrafast ISC that efficiently depopulates the excited singlet states in favour of triplet emissive states and thus only intense phosphorescence is present in a spectrum.

Comparing an emission ( $S_1$  to  $S_0$ ) and absorption ( $S_0$  to  $S_1$ ) spectra of a fluorescent chemical compound (the so-called fluorophore), we would notice that they create a mirror image of each other and they display similar, but reversed vibrational structures. The explanation is based on the fact that electronic excitations are instantaneous in nature. Therefore the geometry of nuclei is more or less preserved during fluorescent (and also phosphorescent) events and the spacing of excited-state vibrational levels resembles that of the ground state.

In photophysics we usually distinguish three categories of excited states. Firstly, there are "ordinary" valence excited states which arise from the excitation of an electron from valence orbitals. Secondly, we talk about Rydberg states which stem from the excitation from

Rydberg orbitals. So we call highly excited molecular orbitals with a dominant contribution of originally unoccupied atomic orbitals of a heavier atom in a molecule. Thirdly, charge transfer is a type of an excited state typical of heavy-metal complexes – this feature has been discussed in more detail in Chapter 2.1.

## 2.3 Experimental overview

### 2.3.1 Overview of relevant experimental techniques

Considering the complexity and intricacies of transition metal complexes, it is obvious that the interplay between theory and experiment is crucial for comprehensive understanding of their electronic structure and associated photophysics. The continuing development of various ps–fs time-resolved spectroscopies has enabled experimentalists to detect elementary processes such as ISC/IC or luminescence within a few tens of femtoseconds. The valuable information about the excited-state behaviour can thus be obtained from the combination of experimental and calculated data, which can complement each other and may help us to confirm or disprove our initial hypotheses concerning the radiative and nonradiative decay pathways and relaxation dynamics in transition metal compounds.

In this section I will briefly introduce experimental techniques used in transition metal chemistry which are relevant to our quantum chemical calculations. The UV–vis or near infrared (NIR) absorption and emission spectroscopies belong to the fundamental measurements. They inform us about energies and intensities of allowed electronic transitions and can be straightforwardly compared with theory. The ZFS parameter and the equilibration rate of the lowest SO states can be measured by time-resolved spectroscopy in fluid solutions at ambient temperature. Generally, time-resolved spectroscopies cover different time scales (up to picoseconds and even femtoseconds) and domains, such as resonance Raman, Fourier transform (FT)-Infra-Red, FT-electron paramagnetic resonance etc. By means of time-resolved laser techniques we can investigate particularly lower-lying triplet states, since ultrafast ( $\sim$ fs) ISCs usually depopulate the optically populated (singlet) states. For some complexes it is thus extremely hard to observe fluorescence – in this respect femtosecond fluorescence up-conversion techniques have proven to be very successful, as they are able to detect prompt fluorescence.<sup>32,91,96</sup> As will be shown, these spectroscopic methods have been applied also to our systems.<sup>26,28</sup> Time-resolved UV–vis absorption spectroscopy could give a useful insight into excited-state kinetics, but is less informative about the structure of transition metal complexes. For this purpose time-resolved IR absorption (TRIR) and resonance Raman spectroscopy are found to be more suitable methods. They exploit relations between the changes in structure characteristics and vibrational frequencies.<sup>97–99</sup> Moreover, from resonance Raman spectra the characters of Franck–Condon (i.e. optically populated) excited states can be extracted (based on solvatochromism). Relatively new two-dimensional TRIR techniques provide information on changes in the composition of vibrational normal modes and their coupling after irradiation.<sup>100</sup> For a more thorough overview of experimental methods the reader is referred to the above cited publications and other literature.

In this doctoral thesis the calculated SF and SO results are compared to available experimental data, thus providing a critical assessment of SF vs. SO treatment. As will be

shown later, the spin-free concept is able to interpret absorption spectra with a reasonable accuracy, however, there are issues which cannot be explained unless the spin-orbit model is adopted. Moreover, regarding emission spectra, the spin-free results fail to reproduce emission characteristics, not even qualitatively. The manifestations of SO-state dynamics can be seen in ultrafast spectroscopic experiments in which time constants connected to various processes are identified.

### 2.3.2 Theoretical aspects of spectra

Molecular spectroscopy gives a qualitative and quantitative description of the interaction between matter (a molecule) and electromagnetic radiation, which consists of two components: an electric and a magnetic field. Consider the Lorentz force (in cgs-Gaussian units – relations for conversion from SI units can be found in the section List of symbols and units)

$$\mathbf{F} = q_{\text{cgs}}\mathbf{E}_{\text{cgs}} + \frac{q_{\text{cgs}}}{c}(\mathbf{v} \times \mathbf{B}_{\text{cgs}}) \quad (2.20)$$

where two terms represent the electric and magnetic contribution, respectively.  $q$  is electric charge and  $\mathbf{v}$  is velocity of a particle moving in the presence of electromagnetic field described by electric  $\mathbf{E}$  and magnetic  $\mathbf{B}$  field. Since electric force (the first term) is dominant over magnetic force (the second term) (e.g. for the electron in a hydrogen atom the ratio  $\langle v^2 \rangle^{1/2}/c$  is around 1/137, which is a small number), the approximation in which magnetic effects are neglected (including magnetic dipole transitions as well) is thus justified and often used in the calculation of electronic excitation spectra.

The transition from an initial state  $\Psi_i$  to a set of final states  $\Psi_f$  caused by the perturbation  $\Delta$  due to the photon field (to the first order) can be characterized by the constant transition rate (transition probability  $\mathcal{P}$  per unit time) which is formulated by Fermi's golden rule:

$$\mathcal{P} = \frac{2\pi}{\hbar} \sum_f |\langle \Psi_f | \Delta | \Psi_i \rangle|^2 \delta(E_f - E_i) \quad (2.21)$$

where  $E_i$  and  $E_f$  are respective energies of the initial and final states. Depending on the measurement, absorption (typically,  $\Psi_i$  being the ground state) or emission can be studied, whereby one-photon or multiphoton processes can be assumed.

An electronic absorption spectrum can be constructed theoretically based on calculated information including excitation energies (describing the position of a band) and oscillator strengths (determining the intensity of a band). In our case we calculated Franck–Condon vertical transition energies without the inclusion of zero-point-energy (ZPE) corrections, whereas in a spectrum we observe adiabatic energies with ZPE. However, these differences may be considered insignificant in the overall computational context. Owing to the dependence on the transition dipole moment, oscillator strengths  $f_n$  indicate which transitions are spectroscopically allowed or forbidden. The magnitude of  $f_n$  is proportional to the absorption band intensity and can be written as

$$f_n = \left( \frac{4\pi m_e}{3e^2 \hbar} \right) \nu_n |\mu_n|^2 = \left( \frac{2m_e}{3e^2 \hbar^2} \right) E_n |\mu_n|^2 \quad (2.22)$$

where  $\mu_n = \langle \Psi_n | e\hat{\mathbf{r}} | \Psi_0 \rangle$  is the transition dipole moment of the electronic vertical transition from the GS ( $\Psi_0$ ) to the  $n$ -th excited state ( $\Psi_n$ ) and  $E_n = h\nu_n$  are the corresponding energy and frequency. Due to the presence of  $E_n$  in Eq. (2.22) it directly follows that the band with a given value of  $\mu_n$  will be more intense in higher energy regions. The relation between the integrated absorption band area  $A$  and the associated oscillator strength is given by

$$f_n = 6.257 \cdot 10^{-19} A, \text{ for } A \text{ in } [\text{m}^2 \cdot \text{mol}^{-1} \cdot \text{s}^{-1}]. \quad (2.23)$$

Eq. (2.23) has been used in a theoretical modelling of an absorption spectrum in this thesis, whereby the Gaussian shape of bands centred at  $E_n$  values has been assumed. The bandwidth is typically estimated by a value of around 0.4 eV which has been chosen on experimental grounds.<sup>1,14</sup> In the further text, it is referred to as full-width at half-maximum (fwhm) (see e.g. Figures 3.6, 3.10 or 3.15).

Intensities of individual bands in an emission spectrum can be evaluated by means of Einstein coefficients of spontaneous emission. In the SO model, the radiative rate constant of emission  $k_r(n)$  from an excited spin-orbit state  $SO_n$  to the ground state  $SO_0$  can be expressed as:<sup>92</sup>

$$k_r(n) \cong \text{const} \times \tilde{\nu}^3 \times \langle SO_n | e\hat{\mathbf{r}} | SO_0 \rangle^2 \times \text{FC} \quad (2.24)$$

where FC denotes the vibrational overlap (the so-called Franck–Condon factor),  $\tilde{\nu}$  is the wavenumber of the transition from the  $SO_n$  to the  $SO_0$  state and  $\langle SO_n | e\hat{\mathbf{r}} | SO_0 \rangle$  is the associated transition dipole moment which decides about the emission probability. As seen from Eq. (2.22), the transition dipole moment determines also the absorption probability in case of oscillator strengths.

## 2.4 Computational methods

The rigorous treatment of electronic excited states represents a non-trivial and quite a difficult task in quantum chemistry. To achieve a description with satisfactory accuracy one has to include both static and dynamic electron correlation. Several approaches have been devised to tackle excited states, among others we can name multireference configuration interaction<sup>101</sup> (MR-CI), CASPT2,<sup>102</sup> equation-of-motion coupled cluster (EOM-CC) methods,<sup>103</sup> TD-DFT, quantum Monte-Carlo or the Bethe-Salpeter equation<sup>104</sup> (stemming from many-body perturbation theory (MBPT) and based on a set of Green's function equations).

In this doctoral thesis the final energies of the ground and excited states of several chosen transition metal complexes were calculated by means of a four-step procedure. First of all, the GS geometries were optimized in Gaussian<sup>105,106</sup> at the density functional theory (DFT) level of approximation with a well-chosen functional. The obtained geometric structures were used as the input geometry for all states including excited states (unless otherwise stated in the result sections). We started with the Hartree–Fock (HF) method/DFT, by which starting

orbitals were generated. Then the complete active space self-consistent field (CASSCF) method<sup>107</sup> was utilized and subsequently we applied multiconfigurational second-order perturbation theory<sup>108</sup> (otherwise called multi-state complete active space second-order perturbation theory) (MS-CASPT2). Up to this point, the approach is spin-free, i.e. only the SR effects were included at this stage of calculation. This was achieved by employing the scalar relativistic DKH Hamiltonian,<sup>58,59,61</sup> which is realized by using a proper relativistic ANO-RCC basis set.<sup>73,74</sup> Finally, spin-orbit coupling and related characteristics were evaluated in the restricted active space state interaction<sup>109</sup> (SO-RASSI) procedure. All the steps were computed with the Molcas<sup>82–84</sup> package.

In addition, spin-orbit time-dependent density functional theory<sup>86</sup> (SO-TD-DFT) using the Amsterdam Density Functional<sup>87–89</sup> software was applied to our systems in parallel with the CASSCF/MS-CASPT2/SO-RASSI calculations (further referred to as SO-MS-CASPT2), in order to compare these different computational techniques with respect to available experimental results.

### 2.4.1 System initialization: HF/DFT

To launch an exact quantum chemical calculation, an initial guess of wave function is needed. To this end, it is convenient to employ a computationally cheap calculation such as the HF<sup>110,111</sup> theory or DFT.<sup>112,113</sup>

HF is a variational method exploiting a variational principle which states that any trial wave function  $\Phi$  will lead to an energy expectation value greater than or equal to the true GS energy  $E_0$ . The derivation of the HF equations is accomplished by employing the method of Lagrange multipliers. It follows from the other formulation of a variational principle: the variation of energy functional of a trial wave function  $\Phi$  differing from the exact ground-state wave function  $\Psi$  only by the first-order variation is zero (i.e. the term representing the second-order variation is neglected)

$$\delta E[\Phi] = E[\Phi] - E[\Psi] = \frac{\langle \Phi | \hat{H} | \Phi \rangle}{\langle \Phi | \Phi \rangle} - E_0 = 0 \quad (2.25)$$

where  $\hat{H}$  is a time-independent Hamiltonian operator. In the HF conception the assumption that the exact  $N$ -electron wave function can be approximated by a single Slater determinant (SD) is accepted. Each electron is thus described by its own one-electron function (spin-orbital), which corresponds to the independent particle model (electrons move independently of each other in the field of the nuclei and the mean field potential created by other electrons). The HF approximation neglects intrinsic electron repulsions and thereby does not account for correlation among electrons. Therefore it is not capable of providing correlation energy in a calculation – we talk about the so-called correlation error, which may amount even to several per cent of the exact nonrelativistic energy. Unfortunately, this is significant when compared to energy changes occurring for example during chemical reactions. The electron correlation can be divided into a static and dynamic part. For the static part we need to include those configurations into a wave function which are supposed to interact with each other (e.g. near-degeneracy effects should be taken into account in case of transition metal complexes). The more flexible the wave function is (i.e. the more parameters we optimize), the more precise

final solution is obtained. For instance, we are thus able to describe correctly bond dissociation/formation processes and any other situation where electrons rearrange substantially and the single determinantal HF description fails. The dynamic part is brought by the instantaneous interaction between electrons and relates to a nature of individual states – in fact, energies of different states contain different shares of correlation energy. The dynamic correlation effects in transition metal complexes play a very important role and they could not be ignored. For the sake of completeness, it should be noted that within the HF approach the Born-Oppenheimer approximation is inherently assumed and no relativistic effects are taken into account, hence the HF energy, in the limit of the complete basis set (CBS), gives an upper bound of the true nonrelativistic GS energy of a system when compared to other post-HF methods.

Another option to get a starting point for further excited-state calculations cost-effectively is to use the density functional method. (Not only) among quantum chemists it has gained enormous popularity, since it represents a computationally cheap and yet formally rigorous concept. It should be emphasized that unlike the HF approximation, DFT leads, in principle, to the exact GS energy and charge density. However, this is true only in the limit of the exact exchange-correlation (XC) functional. The idea behind the DFT method is based on a different approach to a choice of a fundamental carrier of physical information. Instead of a complicated multidimensional wave function  $\Psi$ , DFT employs electron density  $\rho(\mathbf{r})$  as a basic variable where  $\mathbf{r}$  is the spatial position. It takes advantage of the fact that electron density is a function only of three space coordinates  $x, y, z$  in total, whereas a wave function depends on  $4N$  variables ( $x, y, z$  and spin variable), where  $N$  is the total number of electrons in a system and each electron is described by a spin-orbital depending on  $x, y, z$  and spin.

In 1964 Hohenberg and Kohn postulated two theorems,<sup>113</sup> which together with Kohn–Sham (KS) equations<sup>112</sup> form cornerstones of DFT. The first Hohenberg–Kohn (HK) theorem states that the external potential  $v(\mathbf{r})$  is determined uniquely (up to a trivial additive constant) by the  $v$ -representable electron density  $\rho(\mathbf{r})$  (i.e. electron density which corresponds to the antisymmetric GS wave function of a Hamiltonian with some external potential  $v(\mathbf{r})$ ). Under the constraint  $\int \rho(\mathbf{r})d\mathbf{r} = N$  and from the fact that  $\rho(\mathbf{r})$  exhibits singularities in the vicinity of the nuclei, it follows that  $\rho(\mathbf{r})$  determines the GS wave function  $\Psi$ . In other words, a one-to-one mapping  $\Psi \leftrightarrow \rho(\mathbf{r})$  exists for the GS  $\Psi$  and  $v$ -representable  $\rho(\mathbf{r})$ . Consequently, the total energy of a system in the ground state is a functional of its GS electron density  $E = E[\rho]$ , defined for all  $v$ -representable densities. The second HK theorem, known as the energy variational principle, says that the exact electron density minimizes the functional of system energy. To proceed to actual implementations of DFT the Kohn–Sham equations were formulated in order to deliver a practical tool for more precise results than those given by Thomas-Fermi and related models. These models are based on a direct approach, i.e. energy functionals are written explicitly involving electron density alone – unfortunately they entail a great loss in accuracy. For that reason Kohn and Sham<sup>112</sup> introduced orbitals into the formula for the kinetic energy functional again – they exploited the fact that the GS kinetic energy can be expressed exactly by means of Laplace operator, natural (one-electron) spin-orbitals  $\psi_i$  and their occupation numbers  $n_i$ . Further, they cleverly designed a reference system (labelled by index “s”) of  $N$  noninteracting electrons, with the Hamiltonian (Eq. (2.26)) including the

kinetic part (constructed such that  $n_i = 1$  for  $N$  spin-orbitals and  $n_i = 0$  for the rest) and no electron–electron repulsion terms

$$\hat{H}_s = \sum_i^N \left( -\frac{\hbar^2}{2m_e} \nabla_i^2 \right) + \sum_i^N v_s(\mathbf{r}) \quad (2.26)$$

such that the GS electron density of the physical (interacting) system is equal to  $\rho$  of the reference system placed in the external KS effective potential  $v_{\text{eff}}^{\text{KS}}(\mathbf{r})$

$$v_s(\mathbf{r}) = v_{\text{eff}}^{\text{KS}}(\mathbf{r}) = v(\mathbf{r}) + \frac{\delta J[\rho]}{\delta \rho(\mathbf{r})} + \frac{\delta E_{\text{xc}}[\rho]}{\delta \rho(\mathbf{r})}. \quad (2.27)$$

$J[\rho]$  represents classical Coulombic repulsion (repulsion energy) and the XC functional  $E_{\text{xc}}[\rho]$  encompasses a small residual correction to the exact kinetic energy and the nonclassical part of electron–electron interaction energy. After some derivation we can finally arrive at a set of  $N$  Kohn–Sham orbital equations

$$\left[ -\frac{\hbar^2}{2m_e} \nabla^2 + v_{\text{eff}}^{\text{KS}}(\mathbf{r}) \right] \psi_i = \varepsilon_i \psi_i. \quad (2.28)$$

The exact electron density

$$\rho(\mathbf{r}) = \sum_i^N \sum_s |\psi_i(\mathbf{r}, s)|^2 \quad (2.29)$$

is resolved into  $N$  single-particle components  $\psi_i(\mathbf{r}, s)$  fulfilling the Kohn–Sham one-electron equations with eigenvalues  $\varepsilon_i$ ,  $s$  representing the spin variable. Up to this point, DFT could be viewed as an exact *ab initio* method. Nevertheless, the HK theorems and the KS method guarantee uniqueness of the solution, but not the recipe how to obtain that solution for the desired exact electron density. Therefore in practical applications some approximations must be adopted. From the beginning of DFT the greatest challenge has been posed by the search for an expression of the exact XC functional, which constitutes the unknown part of the total energy. In order to yield an agreement between calculations and experiments the effort is concentrated on seeking after physically sound and more and more accurate approximations of this part of energy by exploiting experimental and/or theoretical findings, introducing various empirical parameters. This is the task of the modern DFT development and systematic improvements are still needed. Due to these reasons, DFT is frequently not regarded as an *ab initio* method. However, it is extensively used in many kinds of calculations nowadays, since the possibility of customizing DFT by a proper choice of XC functionals to certain requirements makes this method universally applicable to a wide range of systems. More details can be found in the literature.<sup>114</sup>

## 2.4.2 CASSCF

As the second step, in order to account for the static part of correlation energy we need to apply one of the post-HF methods. We have chosen the CASSCF method, which has become

since its introduction<sup>107</sup> in 1980 very popular and has gained a widespread use.<sup>115</sup> In particular, it represents a very efficient and useful method that is flexible enough to cope with a diversity of chemical problems, ranging from excited states to molecules with weak bonds. Moreover, with a suitable selection of active orbitals it has proven to be a feasible method even for challenging systems, such as transition metal complexes.<sup>33,34,36,38</sup>

CASSCF belongs to variational methods and follows the configuration-interaction (CI) approach, which is based on the minimization of energy with respect to expansion coefficients of a trial many-body wave function, constructed as a linear combination of determinants. CASSCF is a special and clever variant of multiconfigurational self-consistent field (MCSCF).<sup>116</sup> The CASSCF wave function contains all possible SDs or rather configuration state functions (CSFs) within the active space described by a given number of electrons in the a-priori specified number of orbitals with respect to the spin and the symmetry of the wave function. In other words, the wave function is constructed as a full CI expansion in an active subset of the orbital space.<sup>107</sup> Speaking in a simplified way, at first the expansion coefficients characterizing contributions of particular SDs/CSFs to the total wave function are varied and subsequently fixed (macro iteration), secondly the MO-LCAO (molecular orbital with a linear combination of atomic orbitals) coefficients are optimized (micro iteration) – the both steps are repeated, until the convergence criterion is reached.

The CASSCF method is based on a partitioning of orbitals into three general groups, namely there are **core** (frozen) orbitals (doubly occupied in all CSFs, not being correlated during the calculation), **valence** (active) orbitals (creating the so-called active space) and **secondary** (external) orbitals (always unoccupied). To ensure that a calculation does not exceed currently achievable computational resources, one has to limit oneself only to a certain subspace from all the electrons and orbitals when constructing the wave function. The main essence of the CASSCF principle is that only all possible excitations within the selected active space (with a given number of electrons and active orbitals) are taken into account. With the use of the complete CI wave function in the active space, the otherwise difficult selection of the “dominant” configurations in the MCSCF method can be avoided and is replaced by a determination of active orbitals.

Although the above explained theory may sound conceptually simple, it is clear that a crucial and non-trivial part of the input preparation lies in the appropriate choice of the active space that plays the alpha and omega of any CASSCF calculations. For many-electron systems only a limited number of correlated electrons in a limited number of active orbitals is computationally tractable, which imposes high restrictions on calculations of large molecules, such as metal-ligand complexes with hundreds of orbitals (counting also unoccupied orbitals, whose number is given by the size of a chosen basis set). For illustration, the current upper limit for calculations in the Molcas package is around 16 electrons in 16 orbitals (in ~2010), i.e. this is equal or less than 5 million CSFs. That means we are allowed to correlate only a very small fraction of all orbitals and the rest has to be kept with fixed coefficients. In cases when the active space is severely restricted, the results (i.e. energies) have a tendency to be sensitive to its choice, therefore making extremely hard to anticipate in advance which orbitals should be inevitably added into the active space. Chemical intuition and advanced experience with transition metal specifics, charge transfer, orbital shapes etc. is needed to select those orbitals which have to be necessarily included in the active space, still



guaranteeing the feasibility of the calculation itself on the one hand and the physically and chemically correct description of a system on the other hand. If any of significant orbitals is omitted, the calculation might lead to completely wrong results. Also different active spaces by the same complex may unfortunately provide fairly inconsistent numbers. To avoid misleading and confusing data, the common procedure involves an iterative series of calculations with various active spaces – first the selection and later decomposition of the active space depending on actual results. Such an approach helps us to gain a better perception of a system electronic structure. Then we are able to determine which orbitals are obligatory in the active space and which can be left out. Thus we can eliminate some of apparent mistakes and to obtain a stable result. Regarding transition metal complexes, one has to be very cautious, for instance, about *d* orbitals on a metal centre and those ligand orbitals that play a role in CT states in which we are interested.

We used the CASSCF program which has been implemented in the RASSCF code (Restricted Active Space SCF) in the Molcas package. The restricted active space (RAS) concept can be regarded as an extension of the complete active space (CAS) approach.<sup>117</sup> In comparison to the above described CASSCF orbital classification into the **core**, **valence**, **secondary** subspaces, the RAS formalism tackles the orbital division issue in a slightly different way. Namely, it divides the total orbital space into the **primary** and **secondary** space. The **primary** space comprises **inactive** orbitals which are doubly occupied in all configurations (in practice it means that their occupation numbers are close to two and they should not participate in a studied chemical process) and **active** orbitals which are expected to take part in the chemical process of our interest. The latter ones are subsequently subdivided into three groups:

(1) orbitals that are doubly occupied except for a maximum number of holes allowed in this subspace (RAS1);

(2) actual active orbitals where all possible distributions of *N* electrons among *M* active orbitals (satisfying all possible spin-couplings in relation to a desired total spin quantum number *S*) are allowed (RAS2);

(3) orbitals that are unoccupied except of a maximum number of electrons allowed in this subspace (RAS3).

Additionally, **frozen (core)** orbitals can be specified – as expected those orbitals will not be modified in a calculation. The remaining not occupied and not optimized orbital space (arising from a choice of the basis set size) is termed **secondary** as in CASSCF. Its main function is to improve the primary space during the optimization. The employment of the first (RAS1) and the third (RAS3) subspaces requires a previous deeper insight into a studied system and their incorrect use might introduce undesirable errors. For these reasons, this feature was not utilized in our calculations and only the standard active space (RAS2) was applied. Obviously, the defined RASSCF **primary** space (taking RAS1 and RAS3 not into account) corresponds to the **valence** subspace in the above described CASSCF method with the difference that there are no restrictions imposed on occupation numbers in the **valence**

subspace. For the sake of clarity, when we refer to CASSCF in the following text, the actual implementation of CASSCF in the RASSCF program will be considered.

Further theoretical details and technical aspects (e.g. a super-CI approach, Davidson technique, direct CI etc.) of the CASSCF method are described in the literature.<sup>107,118</sup>

If the information about spectroscopic constants and other single-state characteristics are needed, usually the single-state (1-S) calculations are preferred. Here each electronic state is treated independently of the others and its CASSCF wave function is obtained by using individually optimized orbitals for this separate state. Not surprisingly, such an approach may sometimes lead to a set of active orbitals which substantially change their character from one state to another. Since we took an interest in the whole ensemble of states – the ground, as well as excited ones, we performed state-averaged (SA) calculations, which tend to be more suitable and convenient for a mutual comparison of excitation energies. SA computations also converge more efficiently when a near-degeneracy problem is encountered (i.e. several excited states are close in energy, a situation typical of transition metal compounds), whereas 1-S calculations can have difficulty in convergence in such a case. As discussed later, SA calculations are also required for the subsequent MS-CASPT2 method. All desired states were thus sorted out into groups on the basis of their spin multiplicity and spatial symmetry representation. Then only one SA-CASSCF calculation per a group (characterized by the combination of a certain spin multiplicity and irreducible representation) needs to be performed – the states within the same group were given the equal weight. As exemplified with calculations on electronic spectra of organic molecules, such an procedure provides results not significantly different from the results obtained with CASSCF orbitals optimized for each state separately.<sup>102,119</sup>

### 2.4.3 CASPT2

It still remains a great challenge in quantum chemical computations to reach a chemical accuracy (spectral data within a few reciprocal centimeters). Therefore, in an attempt to recover correlation energy with good precision and to reduce energy error as much as possible, we have to choose a powerful tool for electronic structure calculations; in our case a suitable method which is feasible even for transition metal compounds. As already mentioned, the description of heavy atoms must account not only for correlation effects, but also for the scalar and spin–orbit relativistic effects. At the CASSCF level of approximation we managed to encompass only the static part of correlation energy – the dynamic correlation is lost, since this would necessitate an exceedingly large active space. Nevertheless, an energy error caused by omitting of dynamic correlation energy is non-negligible for heavy-metal complexes and it is evident that dynamic electron correlation has to be evaluated. In this respect, the CASSCF represents an excellent zeroth-order reference for a subsequent step. Although it is theoretically possible to include the dynamic correlation through MR-CI calculations and other highly correlated methods (full CI, MR coupled cluster methods (MR-CC)), the applicability of these approaches to our complexes is severely limited due to their enormous computational expenses, with respect to the size of a system and a basis set. On the other hand, it has been shown<sup>102,119</sup> that one of the convenient and probably yet the best affordable

options for these purposes is multiconfigurational second-order perturbation theory (CASPT2).<sup>120,121</sup>

Perturbation theory applications (the second-order or higher MBPTs) have been well established and used routinely for nondegenerate closed-shell systems over the decades. However, the strict condition must be fulfilled in order to apply MBPT. It is essential that a system can be described by a single SD, i.e. the HF wave function could be regarded as a reasonable representation of the zeroth-order reference function, otherwise the reliability of MBPT is questionable and good convergence behaviour is not guaranteed. It is therefore obvious that excited states, bond breaking, transition state structures and degenerate or near-degenerate states were for a long time excluded from the applicability of PT correlation methods. Several attempts to derive an effective formulation of second-order PT in conjunction with a wave function of the CASSCF type were made.<sup>122–124</sup> Unfortunately the outcomes of particular applications were more or less unsatisfactory.

In the presented studies we used a current implementation of the CASPT2<sup>120,121</sup> program in the Molcas package. As the zeroth-order reference function  $\Psi_0$ , a multiconfigurational wave function generated from the preceding CASSCF calculation is employed and all potential near-degeneracy effects are supposed to have been already handled at the CASSCF stage of calculation. The CASPT2 method only has to account for dynamic correlation effects. This perturbation approach calculates the first-order wave function  $\Psi_1$  and provides us with the second-order estimate of the energy difference between the CASSCF and the full CI energy, in other words the second-order correction to the CASSCF energy. In this sense, no approximations are adopted and CASPT2 is a true ab-initio method.

In CASPT2 the first-order wave function has been expanded into the configuration space that can be subdivided into four subspaces: (1)  $V_0$  – the zeroth-order wave function  $|\Psi_0\rangle$  itself, (2)  $V_K$  – the orthogonal complement to  $|\Psi_0\rangle$  in the limited full CI subspace used for constructing the reference function, (3)  $V_{SD}$  – the space containing all single and double replacement states out of the reference function, i.e. states generated by applying single or double excitation operators to the CASSCF wave function, and (4)  $V_{TQ..}$  – the space spanned by all higher-order excitations not included in  $V_0$ ,  $V_K$ , and  $V_{SD}$ . Since the total (spin-free) Hamiltonian  $\hat{H}$  includes only one- and two-particle operators,  $V_0$ ,  $V_K$  and  $V_{TQ..}$  do not have to be considered in the expansion. Accordingly, no other functions except for the ones from  $V_{SD}$  interact with the zeroth-order function by means of the total Hamiltonian. Next, we notice that the single replacements from  $V_{SD}$  do not contribute due to the extended Brillouin theorem<sup>125,126</sup> and the completeness of the wave function in the active subspace. To sum up, only double replacements need to be taken into account.  $V_{SD}$  consists of internal, semiinternal and external functions, having 0, 1 or 2 orbitals in the secondary subspace, respectively. Finally, the first-order wave function is expressed as an expansion into the full interacting space  $V_{SD}$ :

$$|\Psi_1\rangle = \sum_{j=1}^M C_j |j\rangle, \quad |j\rangle \in V_{SD} \quad (2.30)$$

where  $M \geq \dim V_{SD}$  and  $C_j$  are the expansion coefficients of the first-order wave function. The three groups of functions are mutually orthogonal. However, the basis functions  $|j\rangle$  within one subspace do not necessarily fulfil the orthogonality condition and linear dependence may occur among them, but both of these imperfections can be easily resolved by a subsequent orthogonalization procedure and unitary transformation into an orthonormal system. In earlier work<sup>124</sup> only the external functions of  $V_{SD}$  were employed. However, this turned out to be insufficient with respect to accuracy.

Generally, in accordance with the principles of time-independent (Møller–Plesset (MP)) second-order perturbation theory<sup>127</sup> the first-order wave function in the CASPT2 method is determined by Eq. (2.31):

$$(\hat{H}_0 - E_0)\Psi_1 = -(\hat{H}_1 - E_1)\Psi_0 \quad (2.31)$$

where  $\hat{H}_0$  is the zeroth-order Hamiltonian,  $E_0 = \langle \Psi_0 | \hat{H}_0 | \Psi_0 \rangle$  is the zeroth-order energy,  $E_1$  is the first-order energy and  $\hat{H}_1$  is the perturbation defined as  $(\hat{H} - \hat{H}_0)$ .

Applying Eq. (2.30) to Eq. (2.31) and multiplying it with  $\langle i |$  from the left side we arrive at a set of linear equations for the coefficients  $C_j$ :

$$\sum_{j=1}^M C_j \langle i | \hat{H}_0 - E_0 | j \rangle = -\langle i | \hat{H}_1 | \Psi_0 \rangle, \quad i = 1, \dots, M \quad (2.32)$$

The coefficients obtained by solving Eq. (2.32) are used to construct the first-order wave function, which is thereafter needed for the evaluation of the second-order energy  $E_2$  and the total second-order perturbation energy  $E_{CASPT2}$ :

$$E_{CASPT2} = E_{CASSCF} + E_2; \quad E_2 = \langle \Psi_0 | \hat{H}_1 | \Psi_1 \rangle \quad (2.33)$$

The form of the unperturbed (zeroth-order) Hamiltonian  $\hat{H}_0$  plays a fundamental and decisive role in PT. It is desirable to formulate  $\hat{H}_0$  in such a way that three requirements are met: (1) a perturbation expansion is required to converge efficiently, (2) if no active orbitals are present (the zeroth-order reference is described by a single closed-shell SD), it should reduce to the MP2 Hamiltonian, and (3) it ought to be easy to implement and simple to evaluate. To this end,  $\hat{H}_0$  is defined in terms of a one-electron Fock-type operator  $\hat{F}$  (the generalized Fock operator):

$$\hat{H}_0 = \hat{P}_0 \hat{F} \hat{P}_0 + \hat{P}_K \hat{F} \hat{P}_K + \hat{P}_{SD} \hat{F} \hat{P}_{SD} + \hat{P}_{TQ..} \hat{F} \hat{P}_{TQ..} \quad (2.34)$$

where  $\hat{P}_0 = |\Psi_0\rangle\langle\Psi_0|$  is the projection operator onto the zeroth-order function and  $\hat{P}_K, \hat{P}_{SD}, \hat{P}_{TQ..}$  are the projection operators onto the remaining three subspaces of interacting space. Such a definition guarantees that only functions from  $V_{SD}$  will have a contribution to  $\Psi_1$  and the second-order energy. The matrix elements of the generalized Fock operator  $\hat{F}$  have the following form:

$$F_{pq} = h_{pq} + \sum_{r,s} D_{rs} \left[ (pq|rs) - \frac{1}{2}(ps|rq) \right] \quad (2.35)$$

where the indices  $q, s$  refer to inactive or active orbitals and  $p, r$  to active or secondary orbitals and  $D_{rs}$  is an element of density matrix. Actually, there are two different choices how to implement the Fock operator: (1) Only the diagonal part of the Fock matrix is utilized (off-diagonal terms are set to zero), which leads to a computationally easier and much cheaper calculation. This simplified procedure is usually satisfactory enough and suffices to provide reasonable energies and structural data. Strictly speaking, however, such a formulation is not invariant to rotations of the molecular orbitals, which can cause a problem in specific situations (e.g. if an active orbital is close to being doubly occupied, it can easily rotate with inactive orbitals when a perturbing field is present or a change in geometry occurs). Thus for these cases the results obtained with neglecting of non-diagonal elements are to a certain extent unreliable. (2) Another option is to use the full Fock operator with non-zero elements also in off-diagonal matrix blocks, which should be adopted to avoid a discontinuous change in  $\hat{H}_0$ . The price to be paid for a more rigorous approach is that the first-order equation (Eq. (2.32)) has to be solved iteratively, which is CPU (central processor unit) time-consuming.

The explicit expressions for the second-order energy etc. and further details of the method sketched above can be found elsewhere.<sup>120,121</sup>

A thorough test consisting of geometry and binding energy calculations on a large class of benchmark molecules containing first-row atoms revealed that the early implementations of the CASPT2 method unintentionally underestimated bond energies by 3–6 kcal/mol for each new electron pair formed in a molecule. This was a consequence of an inherent error in the former formulation of the program.<sup>128</sup> Moreover, due to this deficiency the correlation energy of open shell systems was relatively overestimated when compared to closed-shell structures. However, it has been found out that the error is clearly systematic and its magnitude depends linearly on the difference between the number of paired electrons in a molecule and atoms. Upon introducing a level shift into  $\hat{H}_0$ , which modifies the diagonal elements of the Fock matrix, the error has been to a large extent corrected and the problem resolved.<sup>129</sup> It uses the fact that the diagonal elements  $F_{pp}$  of the Fock matrix for inactive, secondary and half-occupied orbitals are equal to a negative value of ionization potential (IP), a negative value of electron affinity (EA) and a negative average value of IP and EA, respectively. For an active orbital (i.e. partially occupied) the situation is unclear and thus a negative weighted average of IP and EA is assumed. The level shift (the so-called ionization potential-electron affinity (IPEA) shift) is responsible for adjusting the energies of active orbitals as follows: regarding excitations into the active orbitals, their energy is shifted towards  $-EA$  and conversely, regarding excitations out of the active orbitals, their energy is modified to be closer to  $-IP$ . As a consequence of the introduced shift, the denominators in the expression for the second-order energy are increased, and so is the total energy (by reducing the correlation energy). CASPT2 with the new IPEA modified  $\hat{H}_0$  leads to overall improvement in the achieved accuracy of predicted binding, excitation, dissociation and ionization energies. By comparing with experimental data, the optimal value of the shift parameter  $\epsilon = ((IP)_p - (EA)_p)$  was found out

to be 0.25 a.u. Notably, this is very close to the average value of differences between experimental atomic IP and EA.

Another serious issue frequently arises in calculations mainly on excited states and compounds with heavy atoms – if the denominator in the second order energy expression becomes too small or even negative, potential curves exhibit undesirable singularities and results cannot be trusted. Such a situation is caused by the presence of intruder states that can be described in a simplified way as states in the first-order interacting space whose eigenvalues of the zeroth-order Hamiltonian accidentally almost coincide with the eigenvalue of the zeroth-order wave function. In these cases the physically most sensible solution is to extend the active orbital space and to include the intruding orbitals (often Rydberg orbitals), whose omitting causes the intruder state problem. Unfortunately, this procedure is not always computationally feasible. Such a treatment is also recommended when intruder states interact strongly with the reference function – in this case the intruder state effect on the correlation energy cannot be neglected and due to the near-degeneracy with the zeroth-order wave function the perturbation approach cannot be employed. Instead, the interaction should be handled variationally at the CASSCF level by increasing the active space.

By contrast, for weakly coupling intruder states the so-called level shift (LS) technique<sup>130,131</sup> has been additionally developed and tested in order to avoid the intruder state problem. It adds a level shift parameter to the zeroth-order Hamiltonian and removes singularities by separating the eigenvalues. Afterwards, the second-order energy is corrected by a back transformation (LS correction) to the unshifted value, so that the final impact of the LS technique on the total energy etc. is minimized and the effect of intruder states disappears at the same time. The advantage of this procedure is that the influence of the level shift is negligible when no intruder states are present in the first-order wave function. Nevertheless, a value of the level shift remains to be determined. Since it cannot be chosen on any physical grounds, it has been shown that a reasonable option is to employ a minimal, but sufficiently large value (by trial and error) that removes the intruder states. Naturally, a particular choice of the value is system-dependent and cannot be predicted in advance. It should be, however, noted that the LS technique cannot be applied universally to all systems. The intruder states can arise not only as a result of the presence of diffuse orbitals from the next shells, but also as a consequence of leaving ligand orbitals which are involved in CT excitations out of the active space.

To ensure validity of (CAS)PT2, the perturbation must be defined in such a way that it is sufficiently small. Since the zeroth-order wave function originates from the previous CASSCF calculation, it is advisable to pay utmost attention to the selection of inactive and active orbitals so as to obtain as a good reference function as possible.

It may, however, happen that it is impossible to find a reasonable CASSCF zeroth-order wave function. Such cases involve avoided crossings, conical intersections etc. where various CASSCF states interact and mix strongly with each other and the CASSCF/CASPT2 method is thereby not able to cope with this problem adequately. This failure was demonstrated on a simple system of lithium fluoride – the CASPT2 curves for ionic and neutral dissociation of LiF exhibit a double crossing instead of an avoided crossing.<sup>132</sup> Another example, for which the CASSCF/CASPT2 approach can break down, is valence-Rydberg mixing of excited states that cannot be described at the CASSCF stage of calculation appropriately. In order to remedy

these deficiencies an extension to the CASPT2 method, entitled multi-state CASPT2 (MS-CASPT2), has been designed.<sup>108</sup> In this sense, the original CASPT2 program can be also referred to as single-state CASPT2 (SS-CASPT2), since it uses only a single reference function (one-dimensional reference space). In contrast to this, MS-CASPT2 operates on a multi-dimensional reference space – it is based on treating several different CASPT2 wave functions (of interest) simultaneously in one calculation. This is achieved by employing a second-order effective Hamiltonian that is constructed in the following way: diagonal elements (virtually) correspond to the SS-CASPT2 energies and off-diagonal elements introduce mutual interactions between these states. To compute final second-order energies, the effective Hamiltonian is diagonalized within the multi-dimensional reference space. The new effective zeroth-order wave functions are simply linear combinations of the original CASSCF ones. The straightforwardness of this procedure is ensured by using multiple partitioning of the total Hamiltonian<sup>133</sup> so that each reference function has its own zeroth-order Hamiltonian (defined identically to  $\hat{H}_0$  from the SS-CASPT2). More information can be obtained in the literature.<sup>108,133</sup> It is recommended that one should use MS-CASPT2 whenever the CASSCF electronic states are substantially influenced by dynamic correlation effects. Once states of the same symmetry are expected to be close in energy, the successful usage of CASPT2 may be problematic and MS-CASPT2 ought to be adopted. This situation occurs very often for transition metal compounds where the energy level spacing between states is quite small. Also for that reason the MS-CASPT2 method was utilized in all our calculations. As was already mentioned, the zeroth-order wave functions have to stem from the preceding SA-CASSCF calculation.

To summarize this section, CASPT2 possesses many distinct advantages that make this method generally applicable to a diverse spectrum of systems, from conjugated organic molecules to third row transition metal compounds. All atoms in the periodic table can be treated and the method is size extensive. In essence, as long as a valid CASSCF function is achievable, there are no further severe restrictions on the use of CASPT2. As a matter of fact, the bottleneck that decides whether the CASSCF/CASPT2 approach is tractable for a given system is the quality and feasibility of the CASSCF stage of calculation. One of the real benefits is that in CASPT2 excited states can be handled at the same level as ground states and all three types of excited states (see Chapter 2.2.4) can be treated with reasonable accuracy. CASPT2 has thus proved to be especially valuable for calculations of excitation energies. It is also useful for evaluating dissociation and ionization energies, spectroscopic constants etc.<sup>129</sup> Moreover, currently the relativistic DK Hamiltonian (see Chapter 2.2.1) can be employed in the CASPT2 procedure, enabling calculations on compounds with heavy atoms (among others). The CASSCF/CASPT2, SA-CASSCF/MS-CASPT2 approach have been applied over the past decade in transition metal, organic, inorganic chemistry and biochemistry. It has been successfully tested in a number of chemical problems and the usage for our systems can be exemplified and justified on the following case studies and reviews.<sup>33,34,36,38,102,119–121</sup>

#### 2.4.4 Spin–orbit coupling calculations: SO-RASSI

Once we have calculated the spin-free electronic states and their energies on the CASSCF/(MS-)CASPT2 level of theory, we are ready to employ the RASSI module, as implemented in the Molcas suite of programs in order to obtain the spin–orbit splittings, the spin–orbit states, their final energies and spin-free components (expressed as a percentage), dipole oscillator strengths of individual electronic excitations etc.

The RASSI method provides a highly efficient and straightforward way of evaluating transition densities, matrix elements and expectation values of one- and two-electron operators in a basis formed by individually optimized CASSCF wave functions in the previous calculation steps. Whereas CASSCF has proven to be good at obtaining characteristics only of isolated electronic eigenstates, RASSI, on the other hand, is able to describe also properties associated to several states at once, such as transition moments. It was devised by Malmqvist and Roos<sup>134</sup> in 1989 as a part of the Molcas package, based on the successful and relatively simple algorithm of Malmqvist<sup>135</sup> and since then it has been used primarily for calculations in molecular spectroscopy (e.g. for a prediction of electronic spectra).<sup>136</sup> Among other potential applications we can mention calculations of intermolecular forces or charge-transfer processes, for instance electron transfer between  $\text{Fe}^{2+}$  and  $\text{Fe}^{3+}$  ions in water etc.<sup>137</sup> RASSI can also help in localizing avoided crossings in transition metals, since a mutual interaction among states enabled by this procedure is necessary for a correct description. It is caused by the fact that different occupancies of *s* and *d* orbitals in transition metals have a strong influence on their shapes and energies. Especially, the RASSI program is well-suited for spin–orbit calculations.<sup>138</sup> The applicability and validity of this method has been verified in a number of tests counting molecules and atoms across the entire periodic system.<sup>109,138</sup> It can be concluded that the SO-RASSI code is able to describe reasonably well relativistic effects in all elements of the periodic table except for heavier sixth row main group atoms and superheavy atoms. It can be thus used for systems involving the third series of transition metals, as is the matter of this Ph.D. thesis.

In our case we utilized the RASSI module for the calculation of spin–orbit coupling between electronic states (the so-called SO-RASSI calculations) – the whole procedure is executed in the following manner. The chosen ground and excited spin-free states of interest calculated on the CASSCF/CASPT2 level of theory (in a state-averaged calculation) are put together to create a matrix and they are allowed to interact by means of the spin–orbit Hamiltonian. The spin-free Hamiltonian and then the total Hamiltonian is diagonalized in this basis (i.e. the secular problem is solved). The final spin–orbit states are eigenstates of the sum of the spin-free and the spin–orbit Hamiltonian and they can be described as mixtures of the original CASSCF functions of different spin and space symmetry entering the calculation. In our case we calculated a set of spin-free singlet and triplet states. The number of resulting spin–orbit states is given by a sum of spin-free singlets and three components for each spin-free triplet state.

It should be noted that the CASSCF and RASSI methods are de facto spinless, i.e. they utilize a spin-free formalism known as the split graphical unitary group approach<sup>117</sup> (SGUGA) which is a modified version of the original GUGA formalism.<sup>139,140</sup> That means the CASSCF wave functions are classified according to the total quantum number *S*, but not according to



the  $M_S$  quantum number, which virtually does not exist in this concept. The whole  $S$  multiplet (at this level  $(2S + 1)$ -fold degenerate) is thus handled together regardless of the spin projection and the CASSCF wave functions are invariant to rotations in the spin space. At first the so-called reduced matrix elements of the spin-orbit Hamiltonian are calculated over the basis of spin-free states. To obtain the final spin-orbit matrix elements over the  $(2S + 1)(2S' + 1)$  pairs of spin components from two multiplets ( $S$  and  $S'$ ) one applies the Wigner-Eckart theorem at the last stage of the SO-RASSI calculation. The relationships for the evaluation of individual matrix elements can be found elsewhere.<sup>109</sup>

SO-RASSI uses an effective one-electron Fock-type spin-orbit Hamiltonian formulated by Hess et al.<sup>79</sup> In analogy to the HF method where the exact electron-electron repulsion is replaced by the mean-field approximation, the spin-orbit mean-field operator is devised to treat the two-electron terms. It is based on averaging two-electron contributions to the spin-orbit matrix element over the valence (and core<sup>141</sup>) shell. It has been successfully tested that such an approximation considerably reduces the computational expenses of a SOC calculation without a substantial loss of accuracy and can be applied to transition metal complexes. In addition, in the SO-RASSI method the atomic mean field integrals<sup>142</sup> (AMFI) are employed which introduce further approximations. In contrast to the approach developed by Hess et al. where only multi-centre two-electron spin-orbit terms are discarded, in the AMFI program also multi-centre one-electron SO terms are disregarded. Thus only one-centre integrals are calculated, i.e. SOC induced by the nuclear charge of a particular atom interacts only with the electron density localized at this atom. Such an approach takes advantage of the short-range character of the SO interaction in order to simplify the integral evaluation, still maintaining the precision at the reasonable level.<sup>143</sup>

To account for dynamic correlation, the shift of the diagonal Hamiltonian elements (obtained in CASPT2) could be added

$$\Delta H_{IJ} = 0.5(\Delta E_I + \Delta E_J)S_{IJ} \quad (2.36)$$

where  $\Delta E_I, \Delta E_J$  are the shifts for state  $I$  and  $J$ , respectively, and  $S_{IJ}$  denotes the overlap between the states  $I$  and  $J$ . If there is a strong possibility of curve crossings (which is the case of systems, such as transition metal compounds), non-diagonal elements are needed to be computed as well. To achieve that, the spin-free CASSCF states are allowed to mix by an effective Hamiltonian already at the previous stage of the calculation, which is the MS-CASPT2 method.

As the electronic states often originate from several separate CASSCF calculations, they usually differ in the set of optimized orbitals (specifically adjusted to individual states), which enter in the subsequent RASSI calculation. Normally, this would cause computational problems, but thanks to the above cited algorithm<sup>135</sup> RASSI manages to overcome this obstacle. Very briefly, it is based on transforming two different input orbital sets  $X$  and  $Y$  of the pair of CASSCF wave functions  $\Psi_1 = \sum_{\mu} C_{\mu}^X \phi_{\mu}^X$  and  $\Psi_2 = \sum_{\nu} C_{\nu}^Y \phi_{\nu}^Y$  into biorthonormal bases  $A$  and  $B$ , i.e. those that fulfil the bi-orthonormality condition

$$\langle \phi_p^A | \phi_q^B \rangle = \delta_{pq} \quad (2.37)$$

where  $\phi_p^A$ ,  $\phi_q^B$  are CSFs or SDs built from orbitals  $\{\phi_k^A\}$ ,  $\{\phi_l^B\}$ , respectively. Thus after this operation we get  $\Psi_1 = \sum_p C_p^A \phi_p^A$  and  $\Psi_2 = \sum_q C_q^B \phi_q^B$  with the new CI expansion vectors  $C_p^A$  and  $C_q^B$ , still reproducing exactly the original wave functions. This transformation is possible for wave functions that are closed under de-excitation (i.e. it can be easily done for CAS or RAS wave functions) and it radically simplifies the calculation of the matrix elements between the states. The original CASSCF states, which may be non-orthogonal and interacting, are by solving the secular problem transformed into a set of truly orthogonal and non-interacting (eigen)states, which is of great importance when dealing with excited states. The only restriction that must be obeyed is that the same size of active orbital space and the same atomic orbital basis set have to be used for all the states.

Since RASSI is able to include more than hundred states in a calculation without greater difficulties or dramatic increase in computational costs and the accuracy of the SOC results is quite high, it is the preceding CASSCF stage of the computation (especially, the choice of the active space) that still represents a general limiting factor. In addition, in case of transition metals it should be pointed out that the situation is often complicated by the high density of electronic states. Accidentally near-degenerate states and close-lying interacting terms in these systems may result in a strong mixing of configurations and the calculations have to be conducted more carefully. The corresponding electronic spectra are usually intricate and hard to analyse theoretically. When spacings between states are comparable to errors of the CASPT2 method (0.0–0.3 eV/a few hundred meV), it appears to be questionable whether we are, in such a situation, not reaching the applicability limit of the present approach. In other words, it is the correct evaluation of relative energy of manifold electronic states and their relative order based on a reasonably chosen active space, not the inclusion of SOC alone what primarily determines the success of the computational protocol.

Further details of the method are mentioned in the literature.<sup>109,138</sup>

### 2.4.5 TD-DFT

The conventional static DFT method based on the Hohenberg–Kohn–Sham theory<sup>112,113</sup> had been restricted only to calculations of static properties for the lowest eigenstate in each symmetry class before its extension into the time-dependent domain was introduced by Runge and Gross<sup>144</sup> in 1984. Since then time-dependent density functional theory (TD-DFT) has been gradually becoming one of the most promising and efficient tools in the treatment of various many-body systems influenced by the presence of time-dependent potentials (for instance, electric or magnetic fields), including atoms, molecules, solids etc. Many articles, reviews and books on this method and associated problems have been published, e.g. References [104,145–147]. A very nice historical review of TD-DFT has been written by Casida.<sup>148</sup> Just as in the CASSCF/CASPT2 approach, applying TD-DFT to excited states is by now well-established and thus this method provides a reasonable theoretical counterpart to spectroscopic experiments. Many issues in molecular optics and electronic spectroscopy can be tackled by means of TD-DFT – namely, calculations of dynamic polarizabilities, hyperpolarizabilities, oscillator strengths and electronic excitation spectra<sup>149,150</sup> are relatively easy to handle in comparison with standard post-HF methods. Due to its feasibility and

versatility, TD-DFT has proved to achieve an impressive performance also in chemistry of transition metal complexes.<sup>1,19,26,28,29,44,151,152</sup>

As in static DFT, the wave function (time-dependent in TD-DFT case) is associated with the time-dependent electronic density, which guarantees that expectation value of any physical observable (and the related quantum mechanical operator) can be regarded as a unique functional of the (exact) electronic density. The knowledge of the exact electronic density is thus sufficient to determine any of system characteristics. In order to calculate dynamic response properties several scientists made efforts to devise a generalization of time-independent DFT to treat time-dependent external potentials, e.g. Deb and Ghosh,<sup>153</sup> Kohn<sup>154–156</sup> etc. The most famous ones are, perhaps, Runge and Gross. In their pioneering work<sup>144</sup> they laid the general mathematical foundations of TD-DFT by formulating a theorem concerning  $v$ -representable densities analogous to the first HK theorem.<sup>113</sup> This theorem postulates that the single-particle (external) potential  $v(\mathbf{r}, t)$  is uniquely determined (up to an additive spatially constant time-dependent function) by the density  $\rho(\mathbf{r}, t)$ . That means that one-to-one correspondence  $v(\mathbf{r}, t) \rightarrow \rho(\mathbf{r}, t)$ , which is obtained by solving the time-dependent Schrödinger equation with a fixed initial state  $\Psi(t_0) = \Psi_0$  and by calculating the corresponding densities  $\rho(\mathbf{r}, t)$ , is invertible, i.e. both of these relations hold true:

$$\rho(\mathbf{r}, t) = \rho[v](\mathbf{r}, t) \quad (2.38)$$

$$v(\mathbf{r}, t) = v[\rho](\mathbf{r}, t) \quad (2.39)$$

The potential is only required to be expandable into a Taylor series with respect to the time coordinate around  $t = t_0$ . If the initial state  $\Psi_0$  is a stationary (nondegenerate) ground state, then the expectation values of an operator  $\hat{O}(t)$  (in which no derivation or integration over time is present) are (unique) functionals only of the density alone, since the time-dependent phase factor of  $\Psi[\rho]$  cancels out in Eq. (2.40)

$$O(t) = \langle \Psi[\rho](t) | \hat{O}(t) | \Psi[\rho](t) \rangle \equiv O[\rho](t). \quad (2.40)$$

The second HK theorem needs to be reformulated for time-dependent systems, as the minimum principle cannot be applied and has to be replaced by the variational principle of the quantum mechanical (Dirac-Frenkel) action

$$A = \int_{t_0}^{t_1} dt \langle \Psi(t) | i\hbar \frac{\partial}{\partial t} - \hat{H}(t) | \Psi(t) \rangle \quad (2.41)$$

with the initial condition  $\Psi(t_0) = \Psi_0$ .

To get information about the evolution of a system under the influence of a time-dependent external potential, the extrema of the action integral is searched. It can be thought of as a parallel to classical mechanics where a trajectory of a system is derived from the extrema of the action  $\int_{t_0}^{t_1} dt L(t)$ ,  $L$  being the Lagrangian. Then the second theorem says that the action functional  $A[\rho]$  gives a stationary point (i.e. the Euler equation reads  $\frac{\delta A[\rho]}{\delta \rho(\mathbf{r}, t)} = 0$ ) at the exact solution of the time-dependent Schrödinger equation. In other words, it is only the true time-dependent electron density which makes the action stationary. Later, this Runge–

Gross action principle turned out not to be mathematically rigorous, since it led to a contradiction concerning the causality and symmetry properties of response functions. The inaccuracies were eliminated by defining a new action functional by van Leeuwen.<sup>145,157</sup> In 2008 Vignale justified the results derived from the original Runge–Gross principle by introducing the Runge–Gross–Vignale action principle<sup>158</sup> which uses the correct formulation of the variational principle for the time evolution of the density.

Next, Runge and Gross proposed an effective single-particle Schrödinger equation in order to obtain the density  $\rho(\mathbf{r}, t)$  for time-dependent systems.<sup>144</sup> It can be viewed as the time-dependent equivalent of the Kohn–Sham formalism and it represents the most commonly used scheme of TD-DFT calculations together with using the adiabatic approximation, explained below. The time-dependent Kohn–Sham equation is derived by minimizing the action  $A$  under the constraint (Eq. (2.43)) and has the following form (compare to the time-independent Eq. (2.28))

$$\left( -\frac{\hbar^2}{2m_e} \nabla^2 + v_{\text{eff}}^{\text{KS}}(\mathbf{r}, t) \right) \psi_i(\mathbf{r}, t) = i\hbar \frac{\partial}{\partial t} \psi_i(\mathbf{r}, t). \quad (2.42)$$

Like in the time-independent case the Kohn–Sham noninteracting reference system is defined so that the solution of Eq. (2.42), (spin-)orbitals  $\psi_i(\mathbf{r}, t)$ , return the same electron density  $\rho(\mathbf{r}, t)$  (Eq. (2.43)) as for the interacting system, assuming the effective potential  $v_{\text{eff}}^{\text{KS}}(\mathbf{r}, t)$  does exist.  $f_i$  are the (possibly fractional) orbital occupation numbers.

$$\rho(\mathbf{r}, t) = \sum_i f_i |\psi_i(\mathbf{r}, t)|^2 \quad (2.43)$$

The effective potential consists of the external  $v_{\text{ext}}(\mathbf{r}, t)$  and the self-consistent field  $v_{\text{SCF}}(\mathbf{r}, t)$ , which are set by the following relations

$$v_{\text{eff}}^{\text{KS}}(\mathbf{r}, t) = v_{\text{ext}}(\mathbf{r}, t) + v_{\text{SCF}}(\mathbf{r}, t) \quad (2.44)$$

$$v_{\text{ext}}(\mathbf{r}, t) = v_{\text{static}}(\mathbf{r}) + v_{\text{appl}}(\mathbf{r}, t) \quad (2.45)$$

$$v_{\text{SCF}}(\mathbf{r}, t) = \frac{e^2}{4\pi\epsilon_0} \int \frac{\rho(\mathbf{r}', t)}{|\mathbf{r} - \mathbf{r}'|} d\mathbf{r}' + v_{\text{xc}}(\mathbf{r}, t). \quad (2.46)$$

$v_{\text{static}}(\mathbf{r})$  represents the static external potential of the unperturbed system. A typical form is the electron-nuclear attraction  $-\frac{e^2}{4\pi\epsilon_0} \sum_I \frac{Z_I}{r_I}$ , with  $Z_I$  being the atomic number of nucleus  $I$ ,  $r_I$  being the distance between the electron and the nucleus  $I$ .  $v_{\text{appl}}(\mathbf{r}, t)$  denotes an applied time-dependent external perturbation that was switched on slowly and infinitely long ago at time  $t_0$  (for  $t < t_0$  it is considered to be constant). When interested in calculations of electronic excitations,  $v_{\text{appl}}(\mathbf{r}, t)$  is an oscillating electric field of the incident light. The self-consistent field  $v_{\text{SCF}}(\mathbf{r}, t)$  is comprised of the classical Coulombic potential between electrons and the exchange-correlation potential  $v_{\text{xc}}(\mathbf{r}, t)$  that is given by

$$v_{\text{xc}}[\rho](\mathbf{r}, t) = \frac{\delta A_{\text{xc}}[\rho]}{\delta \rho(\mathbf{r}, t)} \approx \frac{\delta E_{\text{xc}}[\rho_t]}{\delta \rho_t(\mathbf{r}, t)} = v_{\text{xc}}[\rho_t](\mathbf{r}). \quad (2.47)$$

Within the adiabatic approximation the unknown functional  $A_{\text{xc}}[\rho]$ , the exchange-correlation part of the action functional (2.41), can be replaced by the XC functional  $E_{\text{xc}}[\rho_t]$  of time-independent DFT defined above in Chapter 2.4.1, where the index  $t$  symbolizes that  $E_{\text{xc}}[\rho_t]$  is a function of density evaluated at the time  $t$ . Thus a time-dependence in  $A_{\text{xc}}[\rho]$  is eliminated and virtually a static problem is solved. The adiabatic approximation is based on the assumption the external potential varies so slowly in time that we can write

$$A_{\text{xc}} = \int_{t_0}^{t_1} E_{\text{xc}}[\rho_t] dt. \quad (2.48)$$

The disadvantage of this frequently used approximation is that it does not take into account any retardation effects. This is obvious from Eq. (2.47), in which the exchange-correlation potential is a functional only of density at the same time, thereby it is assumed to react instantaneously. Hence the information about time-spatial correlations and memory to any temporal change of the density is lost. In some cases the approximation turns out to be insufficient and thus XC functionals beyond the adiabatic approximation are needed.<sup>159</sup> However, it has been shown that the XC potentials within the adiabatic approximation have a large scope of applicability.

The time-dependent density-functional response theory (TD-DFRT), the widely used implementation of the TD-DFT equations, is based on the linear response (LR) theory,<sup>155,156,160–162</sup> which enabled to employ TD-DFT for the computation of excitation energies and oscillator strengths within the DFT framework.<sup>149,163</sup> In order to present a theoretical basis of the TD-DFRT method a density-density response function  $\chi(\mathbf{r}, t, \mathbf{r}', t')$  of the interacting system should be introduced

$$\chi(\mathbf{r}, t, \mathbf{r}', t') = \left. \frac{\delta \rho[v_{\text{ext}}](\mathbf{r}, t)}{\delta v_{\text{ext}}(\mathbf{r}', t')} \right|_{v_{\text{ext}}[\rho_0] = v_{\text{static}}}. \quad (2.49)$$

It describes the first order response of the electron density associated with a system initially in an unperturbed stationary (generally ground) state  $\Psi_0$  (corresponding to density  $\rho_0(\mathbf{r})$ ) to an applied time-dependent external field (a perturbation which was turned on slowly and adiabatically). In our case we studied the response of the GS electron density to the oscillating optical field. Then the linear density response  $\rho^{(1)}(\mathbf{r}, t)$  to this perturbation reads

$$\rho^{(1)}(\mathbf{r}, t) = \int dt' \int d\mathbf{r}' \chi(\mathbf{r}, t, \mathbf{r}', t') v_{\text{appl}}(\mathbf{r}', t'). \quad (2.50)$$

By virtue of the Runge–Gross theorem, it is computationally advantageous to reformulate the linear density response in terms of  $\chi_{\text{KS}}(\mathbf{r}, t, \mathbf{r}', t') = \left. \frac{\delta \rho[v_{\text{eff}}^{\text{KS}}](\mathbf{r}, t)}{\delta v_{\text{eff}}^{\text{KS}}(\mathbf{r}', t')} \right|_{v_{\text{eff}}^{\text{KS}}[\rho_0]}$ , the density-density response function of the noninteracting (ground-state) reference system, which is

easier to calculate (since  $\chi_{KS}$  can be readily constructed from the static unperturbed Kohn–Sham orbitals)

$$\rho^{(1)}(\mathbf{r}, t) = \int dt' \int d\mathbf{r}' \chi_{KS}(\mathbf{r}, t, \mathbf{r}', t') v_{\text{eff}}^{\text{KS}(1)}(\mathbf{r}', t'). \quad (2.51)$$

$v_{\text{eff}}^{\text{KS}(1)}$  refers to the effective potential calculated to the first order in  $v_{\text{appl}}$ . Since  $v_{\text{eff}}^{\text{KS}(1)}$  depends also on  $\rho^{(1)}$ , it results in a self-consistent scheme for the calculation of  $\rho^{(1)}$ . Then by performing the Fourier transform the time domain is transferred into the frequency domain representation, which is convenient for the calculation of excitation spectra. The response theory takes advantage of the general fact that the frequency-dependent linear response of a finite interacting system has discrete poles at exact excitation energies. Thus  $\chi_{KS}$  has poles at the Kohn–Sham eigenvalue differences  $\omega_{jk} := \varepsilon_j - \varepsilon_k$ , whereas  $\chi$  has poles at the true excitation energies  $\omega_I := E_I - E_0$  of the studied unperturbed system. The ultimate objective is to obtain the shift of  $\omega_{jk}$  towards  $\omega_I$  systematically. The complete derivation of the TD-DFRT working equations and the final form of an eigenvalue problem can be found elsewhere.<sup>155,156,159–162,164</sup>

One of the benefits of the present method is that the entire electronic excitation spectrum is obtained all at once, in a single calculation. Furthermore, the TD-DFRT is capable of handling excitations involving excited-state multiplets and assigning spin multiplicity without reference to a wave function. From the spectroscopic point of view the interesting response property is the dynamic dipole polarizability  $\alpha(\omega)$ , which implicitly contains the information on the interaction of a molecule with light. Hence the pole structure of the dynamic polarizability (Eq. (2.52)) yields spectroscopic oscillator strengths  $f_I$  (Eq. (2.53)) and vertical excitation energies  $\omega_I$ . The derivation for the mean dynamic polarizability  $\bar{\alpha}(\omega)$ ,  $f_I$  and  $\omega_I$  can be found in the literature<sup>155,156,159–162,164</sup> (atomic units are used here):

$$\bar{\alpha}(\omega) = \frac{1}{3} \text{tr} \alpha(\omega) = \sum_{I \neq 0} \frac{f_I}{\omega_I^2 - \omega^2}, \quad (2.52)$$

$$f_I = \frac{2}{3} (E_I - E_0) (|\langle \Psi_0 | \hat{x} | \Psi_I \rangle|^2 + |\langle \Psi_0 | \hat{y} | \Psi_I \rangle|^2 + |\langle \Psi_0 | \hat{z} | \Psi_I \rangle|^2) \quad (2.53)$$

where we sum over all electronic excited states,  $E_0$  and  $E_I$  are energies of the ground and excited stationary states  $\Psi_0$  and  $\Psi_I$  of the unperturbed Hamiltonian, respectively.

Like in static DFT, the success of TD-DFT calculations depends to a large extent upon a chosen approximation of the exact exchange-correlation part of the effective single-particle potential and its variation with the density, the so-called exchange-correlation kernel  $f_{xc}$  (the functional derivative of exchange-correlation potential, i.e.  $\partial v_{xc} / \partial \rho$ ). Hence great effort is put into seeking for better and more realistic and at the same time manageable approximations.

To sum up, it should be noted that the TD-DFT approach belongs to single-reference theories, i.e. only excitations given by linear combinations of singly excited configurations are involved. Within the conventional TD-DFT method only the calculation of transition energies smaller than the vertical ionization potential of a molecule is reliable due to incorrect

asymptotic behaviour of pure XC functionals (e.g. local density approximation<sup>165,166</sup> (LDA) or generalized gradient approximation (GGA)). In real systems the electron-nucleus interaction decays as  $1/r$ , where  $r$  denotes the distance between the electron and the nucleus. However, pure XC functionals decay much faster at large distances, thus underestimating this interaction, which leads to wrong predictions of higher virtual orbitals and high-lying excitations.<sup>162</sup> Furthermore, the local character of these functionals cannot correctly describe a non-local nature of CT states and much care is required with respect to a proper choice of XC functional for this type of excited states (see Chapter 3.1.2 for a detailed discussion).

Regarding the treatment of relativistic corrections within TD-DFT, the scalar relativistic effects were taken into account by employing the SR ZORA,<sup>65,71</sup> as described in Chapter 2.2.2. To incorporate SOC into our calculations we utilized the approximate SO-TD-DFT method<sup>86</sup> for closed-shell systems, as implemented in the ADF<sup>87–89</sup> program package. The lowest single-group symmetry excited states (i.e. spin-free states, only with the inclusion of the SR effects) are calculated at first and then the spin-orbit excited states (within double-group symmetry) are determined afterwards by introducing SOC as a perturbation. The composition of the final SO states in terms of parent SF states is given automatically. The spin-orbit coupling operator within the ZORA<sup>63</sup> is taken in the following form (in atomic units):

$$\hat{h}_{so} = i\sigma \left( \mathbf{p} \times \frac{c^2}{2c^2 - V} \mathbf{p} \right) \quad (2.54)$$

where the particular symbols have been already explained in Chapter 2.2.1. In order to simplify the evaluation of SO effects two approximations were proposed – (1) spin-orbit coupling between occupied and virtual spin-orbitals is neglected, and (2) the spin-orbit operator (Eq. (2.54)) acts only on the lowest several tenth single-group singlet and triplet states, i.e. the single-group excited-state space is truncated. The errors associated with both of these simplifications were checked carefully on a set of chosen systems<sup>86</sup> and it was concluded that the method represents a reasonable compromise between accuracy and cost-effectivity. Although the computational effort of this approach is not much larger than the computation of electronic excited states by means of TD-DFT within the SR ZORA, the obtained precision of SOC influenced excitation energies is more than acceptable provided that SO-TD-DFT is used appropriately within the limits of perturbation approach. Generally, it is well-known that a perturbation should be small, which implies in this case that spin-orbit coupling should not affect the radial orbital shape much. This is more or less fulfilled for  $d$  and  $f$  orbitals, but not for  $p$  orbitals, especially  $5p$  and  $6p$  orbitals. Thus the approximate SO-TD-DFT method works well for  $4d$  and lighter elements, and even for  $5d$  elements or medium-size molecules containing these atoms with the exception of electronic states where  $6p$  orbitals participate in transitions. In our systems we were mainly interested in transitions involving  $d$  orbitals which can be safely handled by the present approach.

There is also a possibility of using a more rigorous approach towards SOC treatment in closed-shell systems – TD-DFT in the relativistic two-component ZORA formulation,<sup>85</sup> as well available in the ADF software. In contrast to the approximate perturbative SO-TD-DFT method, in this technique the spin-orbit effects are included in the calculation of electronic

states from the outset and they are treated variationally. The use of double-group symmetry turns out to be computationally advantageous and helpful in the assignment of excited states. The noncollinear scheme<sup>167</sup> for the XC potential is successfully employed to deal with spin densities, thus ensuring the correct nonrelativistic limit and threefold degenerate triplet excitations. The standard ZORA Hamiltonian (Eq. (2.16)) is used with the total potential  $V$  involving the nuclear-attraction potential, the electronic-repulsion potential and the XC potential. The relativistic TD-DFT based on the two-component ZORA<sup>63,85</sup> is able to provide results with high precision, nevertheless, it is computationally much more demanding than SO-TD-DFT and its usage for medium-size transition metal complexes is rather limited.

A detailed description of both above outlined methods together with a thorough test of their applicability and further information about relativistic SO calculations of closed-shell molecules within ZORA can be found in References [64,85,86].



## Chapter 3: INDIVIDUAL PROJECTS

### 3.1 Rhenium tricarbonyl complexes with halide ligands

#### 3.1.1 Introduction

This section concerns a series of rhenium(I) tricarbonyl complexes  $[\text{ReX}(\text{CO})_3(\text{bpy})]$  ( $\text{X} = \text{Cl}, \text{Br}, \text{I}$ ;  $\text{bpy} = 2,2'$ -bipyridine) with the schematic structure illustrated in Figure 3.1.

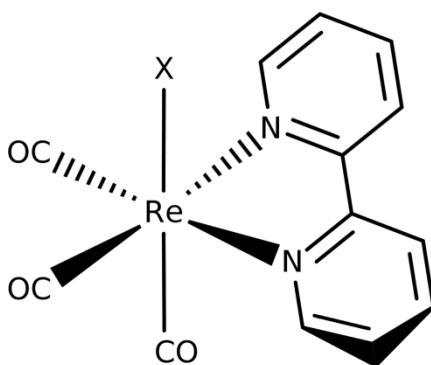


**Figure 3.1.** The general molecular structure of rhenium(I) tricarbonyl complexes with a halide.

Their DFT optimized geometries are depicted in Figure 3.2.

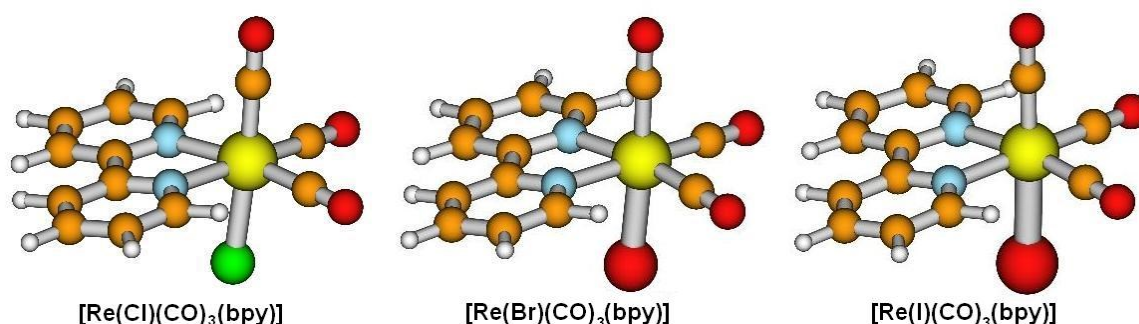


**Figure 3.2.** The geometries of rhenium(I) tricarbonyl complexes with halide ligands. Atoms are represented by the following coloured spheres of an appropriate size: yellow = rhenium (the central ion), green = chlorine, big red = bromine, the biggest red = iodine, small red = oxygen, blue = nitrogen, orange = carbon, white = hydrogen.

A rhenium (Re) atom in the coordination centre (with atomic number = 75) is a heavy, third row transition metal, which is located in the seventh group of the periodic table. Its (neutral) atomic electron shell configuration can be written as  $\text{Re}:[\text{Xe}]4f^{14}5d^56s^2$ . In  $[\text{ReX}(\text{CO})_3(\text{bpy})]$  ( $\text{X} = \text{Cl}, \text{Br}, \text{I}$ ) complexes rhenium is in oxidation state (+1) – since

a positive charge of rhenium is compensated by a negative charge of halides, the molecules are in total electroneutral. Rhenium(I) has  $d^6$  configuration and therefore Re(I) complexes are sometimes referred to as  $d^6$  complexes. All the three complexes possess a low-spin singlet (closed-shell) ground state. The central rhenium ion has a coordination number of 6, which leads to a formation of a pseudo-octahedral structure, as shown in Figures 3.1 and 3.2.

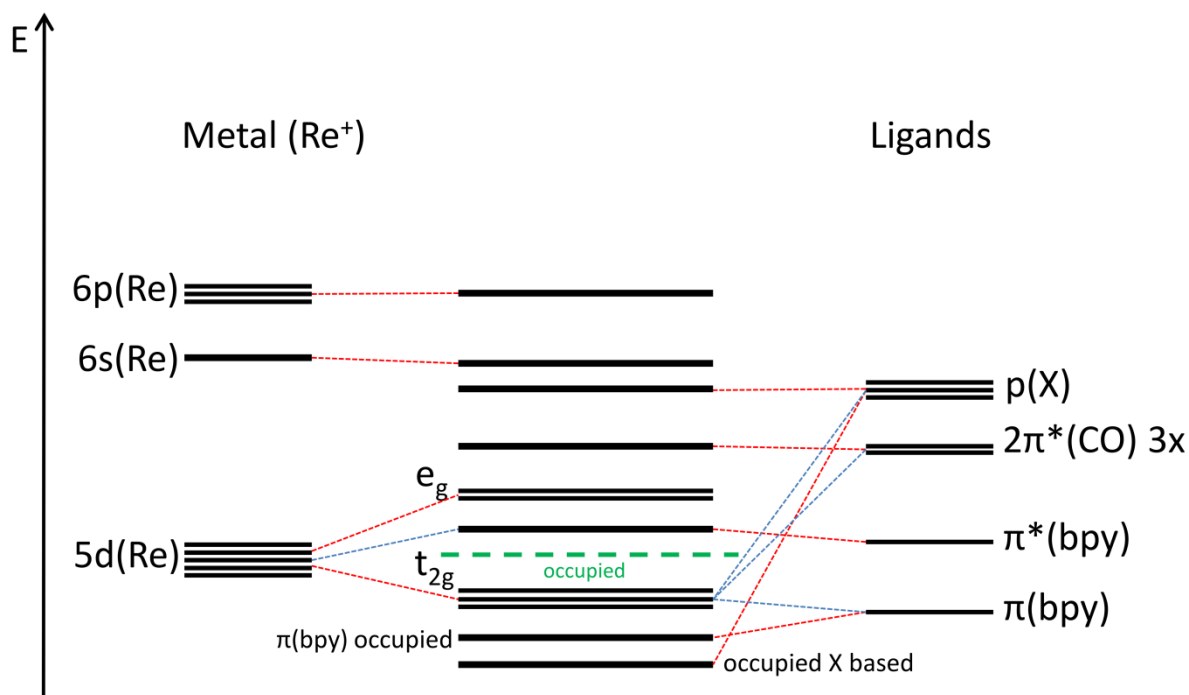


**Figure 3.3.** The schematic molecular diagram of the pseudo-octahedral [ReX(CO)<sub>3</sub>(bpy)] complex. Energy differences between individual orbitals are just roughly estimated (not obtained by a calculation) and therefore the energetics is not proportional to real system MOs – the picture serves merely as an illustration to get a basic notion about the electronic structure. For the sake of simplicity, labels for a regular octahedron are used and a formation of symmetry adapted linear combinations (SALCs) of ligand orbitals is not shown. Red and blue dashed lines indicate main and minor contributions of atomic (in case of Re, X) or molecular orbitals (CO, bpy), respectively. A green bold dashed line separates occupied and virtual orbitals for the closed-shell GS configuration.

A schematic molecular diagram including the most important orbitals on the metal and ligands is drawn in Figure 3.3. Since six ligands in the complex are not identical, a regular, highly symmetrical octahedron is deformed into a pseudo-octahedral structure. This is accompanied by a further loss of degeneracy of originally degenerate  $d$  metal orbitals (i.e. threefold degenerate  $t_{2g}$  and doubly degenerate  $e_g$  MOs are split accordingly). The resulting occupied MOs which are centred at the metal have a substantial contribution from  $\pi^*(\text{CO})$  and  $p_\pi(\text{X})$  orbitals, and to a minor extent from  $\pi(\text{diimine})$  orbitals. Another important thing is the presence of an electron-accepting  $\alpha$ -diimine ( $\text{N}^{\wedge}\text{N}$ ) ligand (a bipyridine in this case, a phenantroline in case of the second project) which is responsible for low-lying MLCT ( $d\pi^*$ ) and IL ( $\pi\pi^*$ ) excited states. Figure 3.3 will be discussed later in connection with an active space analysis.

From a methodological point of view, rhenium(I) tricarbonyl-diimine complexes with halide ligands served us as a test and validation of theoretical approaches and thus the first project will be treated in a more extensive way. Since the studied transition metal complexes have a lot in common and the similar approach to investigations were adopted for both projects, the second project will be presented more briefly.

Our motivation to study these systems by means of advanced quantum chemical methods is given by several reasons. Firstly, the experimental data are available and the direct comparison between theory and experiment could be very beneficial for both sides. For example, rhenium(I) tricarbonyl complexes were studied by femtosecond fluorescence spectroscopy.<sup>28</sup> The ultrafast intersystem crossings and their rates ( $\sim$ fs–ps time scale) were discovered, which helps to elucidate relevant photophysics of these systems. Based on the time-resolved experiments and previous (TD-)DFT calculations<sup>28,168</sup> it was revealed that one  $^1$ MLCT, two low-lying  $^3$ MLCT and one  $^3$ IL excited states participate in these ultrafast intersystem crossings and the origin of luminescence properties of these molecules can be attributed mainly to the presence of these electronic excited states.  $[\text{ReX}(\text{CO})_3(\text{bpy})]$  complexes exhibit a long-lived (ns) phosphorescence<sup>21,40,43,169</sup> which comes from the lowest MLCT triplet state. Rhenium(I) tricarbonyl complexes belong to the class of compounds for which the rich electronic-vibrational relaxation behaviour induced by the excitation of the low-lying singlet MLCT ( $\text{ReX}(\text{CO})_3 \rightarrow \text{diimine CT}$ ) state is characteristic. Among others, this involves two or three fast processes, one of them being assigned to the ISC<sup>26,28,29</sup> and the other to thermally activated nonradiative decay of the lowest triplet state.<sup>169</sup>

Secondly, the aim of this project is to analyze the influence of a halide ligand substitution, on going from chloride to iodide. Varying the coordination sphere by the presence of different axial ligands (halides in this case), energies, compositions and shapes of the resulting molecular orbitals will change. As a consequence, physical and optical characteristics of these complexes will differ.<sup>21,30</sup> One can take advantage of this fact and by a clever choice of ligands one can adjust the properties of a given complex according to desired needs. In our study we investigated a few spectral trends connected with a halide replacement and attempted to trace the effect of the increasing SOC constant of halides in a row Cl, Br, I in spectra. In this context, a relatively surprising observation concerning ISC rates in these complexes was made by Cannizzo et al.<sup>28</sup> and will be presented later.

Thirdly, more information is highly needed, since these molecules could be efficiently used in different areas of photonic applications.<sup>1,16,17</sup> Nevertheless, theoretical articles about photophysics of transition metal compounds (especially those including SOC) are still quite rare. The first studies of ISC processes come from the late 1990s and they dealt with the photodissociation dynamics of  $\text{HCo}(\text{CO})_4$  molecule,<sup>170,171</sup>  $[\text{Mn}(\text{H})(\text{CO})_3(\text{H-dab})]$  ( $\text{H-dab}$  = 1,4-diaza-1,3-butadiene) and  $[\text{Re}(\text{H})(\text{CO})_3(\text{H-dab})]$  complexes,<sup>172,173</sup> investigated by means of wavepacket propagations on *ab initio* (spin–orbit coupled) PESs calculated on the CASSCF/(MR-)CCI (multireference contracted configuration interaction) level of theory. The common to all these molecules is the finding that ISC rates influence the probabilities of directions in which the system can dissociate.

Lastly, continual progress in computational chemistry has made it feasible to employ sophisticated spin–orbit techniques. This important advance has offered the opportunity to compare directly spin-free and spin–orbit calculations. For instance, absorption spectra for a

pair of transition metal hydrides  $\text{H}_2\text{M}(\text{CO})_4$  ( $\text{M} = \text{Fe}, \text{Os}$ )<sup>174</sup> and  $\text{HM}(\text{CO})_5$  ( $\text{M} = \text{Mn}, \text{Re}$ )<sup>175</sup> were computed. It was found out that spin-orbit spectra are in better agreement with experiments than spin-free ones for all the complexes. In case of first row transition metals ( $\text{Fe}$  and  $\text{Mn}$ ), the effect of SOC is relatively minor. By contrast, third row transition metals ( $\text{Os}$  and  $\text{Re}$ ) are considerably influenced by SOC, which manifests itself in a strong mixing of excited states and increasing their density (i.e. in the same energy range more SO states can be identified when compared to original spin-free states). In a spectrum, these two features are reflected by broadening spectral bands and lowering their intensities, as well as by increasing a total number of underlying transitions. Very high SO excited-state densities were discovered for  $\text{Ir}(\text{ppy})_3$  by TD-DFT with perturbative SOC treatment.<sup>176,177</sup> As the complexes of our interest have a rhenium ion as a metal centre, it is evident that without accounting for SOC it is impossible to decipher the complicated experimental mechanism properly and interpretation of the luminescence spectra cannot be adequately reasonable. Indeed, the static DFT (optimization) approach<sup>28</sup> to calculating the main geometrical deformations associated with a transition from the electronic GS minimum to the low-lying ES minima turned out to be insufficient in an effort to find a correlation between the experimental dynamics and the calculated results. From the character of heavy metal atoms it can be easily inferred that the absence of the spin-orbit interaction in the computation is responsible for this insufficiency. Thus our calculations involved the effects of spin-orbit coupling and followed the excited-state reactive pathway within an adiabatic picture.

All in all, there are without a doubt plenty of features that remain to be revealed about the broad class of  $\text{Re}^{\text{I}}$  tricarbonyl complexes  $[\text{Re}(\text{L})(\text{CO})_3(\alpha\text{-diimine})]^n$  ( $\text{L} = \text{Cl}, \text{Br}, \text{I}$  with  $n = 0$ ;  $\text{L} = 4\text{-ethylpyridine}$ , imidazole with  $n = 1+$ ;  $\alpha\text{-diimines} = \text{bipyridine}$  and phenanthroline derivatives) and their ultrafast excited-state dynamics. Some of the complexes were subjected to spectroscopic experiments or were calculated by means of spin-free DFT and TD-DFT,<sup>1,26,28,29,44,168</sup> SOC being estimated only qualitatively.<sup>28</sup> Nevertheless, none of them have been computed by means of SO-MS-CASPT2 and SO-TD-DFT before the date of publishing our articles in 2011 and 2012. Since spin-free calculations were not able to explain experimental observations fully, the answer presumably lies exactly in spin-orbit coupling. Later, a few examples will be given to confirm this statement. For the sake of clarity, the results for the  $[\text{Re}(\text{imH})(\text{CO})_3(\text{phen})]^+$  complex, also belonging to this family of rhenium compounds, will be presented in Chapter 3.2.

One of our goals was to evaluate transition energies between the electronic ground state and several low-lying singlet and triplet electronic excited states of  $[\text{ReX}(\text{CO})_3(\text{bpy})]$  ( $\text{X} = \text{Cl}, \text{Br}, \text{I}$ ) and to determine their origin with including SOC effects on the SO-MS-CASPT2 and SO-TD-DFT level of theory. The results from both methods will be presented and at the same time discussed in the section Results and discussion. In addition, the calculated values will be compared with each other and the resulting vertical spin-free and spin-orbit theoretical absorption spectra will be investigated in conjunction with the available experimental data.

This part is based on publication<sup>27</sup> which is attached at the end of the doctoral thesis. The project was completed in cooperation with Professor Chantal Daniel from Laboratoire de Chimie Quantique at Université de Strasbourg. The related experiments were performed in London and Lausanne. Namely, the ultrafast intersystem crossings were studied by means of

femtosecond fluorescence up-conversion technique with polychromatic detection.<sup>28</sup> The UV–vis absorption spectra were recorded in different solvents (MeCN, DCM and toluene). Finally, emission lifetimes were obtained via the time-correlated single-photon counting technique. A detailed description of spectroscopic measurements can be found in References [27,28].

Recently (2015), these systems were reinvestigated by Gourlaouen and our co-worker Professor Daniel<sup>178</sup> by employing SO-TD-DFT. They optimized several lowest excited states and performed wavepacket simulations.

### 3.1.2 Computational details

The GS geometries were optimized by DFT/PBE0 (Perdew, Burke, Ernzerhof exchange and correlation functional<sup>179,180</sup>) in Gaussian<sup>106</sup> and used for subsequent calculations.<sup>27</sup> In addition, the equilibrium geometry of the lowest triplet excited state determined by means of unrestricted Kohn–Sham DFT (UKS-DFT) was utilized in SO-TD-DFT to model various characteristics of photophysics. All three molecules exhibit the  $C_s$  symmetry, which was fixed in all calculations.

Two different approaches were adopted: SO-MS-CASPT2 employing the Molcas<sup>82–84</sup> software and SO-TD-DFT using the ADF<sup>87–89</sup> program.

In case of CASSCF/MS-CASPT2, input orbitals were generated by the KS-DFT method with the B3LYP (Becke, Lee, Yang, Perdew exchange and correlation<sup>181</sup>) functional. Then the SA-CASSCF calculations were performed. Based on the information from the previous TD-DFT calculations it was decided to include the following states in the final SO calculation: the singlet ground state, four lowest singlet excited states and four lowest triplet excited states in each symmetrical representation ( $a'$  and  $a''$  of the  $C_s$  symmetry), making together 17 electronic spin-free states.

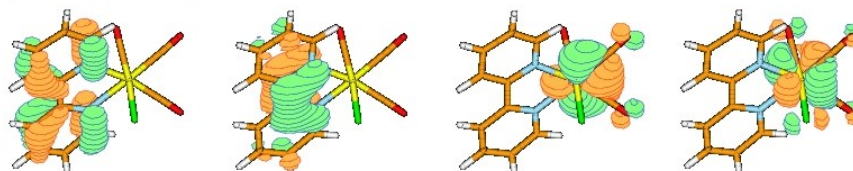
**Table 3.1.** The contraction schemes for ANO-RCC basis sets used for rhenium(I) tricarbonyl complexes with halide ligands.

Atom	Contraction scheme	Contracted to
Re	(24s, 21p, 15d, 11f, 4g, 2h)	(7s, 6p, 4d, 2f, 1g)
I	(22s, 19p, 13d, 5f, 3g)	(8s, 7p, 5d, 4f, 2g)
Br	(20s, 17p, 11d, 4f, 2g)	(6s, 5p, 3d, 2f, 1g)
Cl	(17s, 12p, 5d, 4f, 2g)	(5s, 4p, 2d, 1f)
C, N, O	(14s, 9p, 4d, 3f, 2g)	(4s, 3p, 2d, 1f)
H	(8s, 4p, 3d, 1f)	(3s, 2p, 1d)

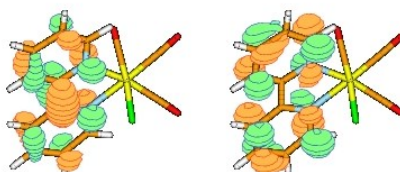
As far as the choice of a basis set is concerned, several test *ab initio* calculations with a nonrelativistic type of basis set (together with the effective core pseudopotential for a rhenium atom) for the Cl and Br complexes were executed. In case of the iodo complex it was not possible to carry out a calculation with a nonrelativistic basis set for an iodine and it was essential to take a relativistic type of basis set, which is able to introduce the SR effects (substantially pronounced by I) into a calculation per se. For these reasons the ECPs were

definitively abandoned and a greater basis set was chosen. Finally, the ANO-RCC basis sets<sup>73,74</sup> were used for all three complexes. For I and the rest of atoms, the basis with a quadruple- $\zeta$  and a triple- $\zeta$  contraction scheme was used, respectively. Table 3.1 lists the contraction schemes for particular atoms.

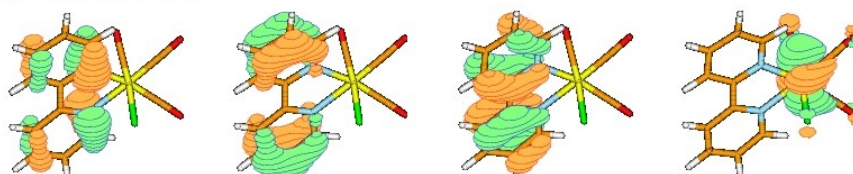
Occupied, a' symmetry:



Virtual, a' symmetry:



Occupied, a'' symmetry:



Virtual, a'' symmetry:



**Figure 3.4.** The frontier occupied and virtual molecular orbitals included in the active space at the CASSCF stage of the calculation of  $[\text{ReCl}(\text{CO})_3(\text{bpy})]$ .

The final active space for all three molecules comprised 16 electrons in 13 active orbitals (in the shorthand notation CASSCF(16,13)), including HOMO-3, HOMO-2, HOMO-1, HOMO, LUMO, LUMO+1 in the a' symmetry and HOMO-3, HOMO-2, HOMO-1, HOMO, LUMO, LUMO+1, LUMO+2 in the a'' symmetry, where HOMO and LUMO stand for the highest occupied and lowest unoccupied MOs, respectively. The  $[\text{ReCl}(\text{CO})_3(\text{bpy})]$  complex is chosen to depict the composition of the active space (Figure 3.4). By using the Cholesky decomposition<sup>182</sup> of the two-electron integral matrix the total computational effort is reduced substantially. The level shift technique was employed in the CASPT2 method to circumvent potential intruder state difficulties. The best solution was achieved for a value of level shift of  $\hat{H}_0$  being 0.15 a.u. Since the structure optimized for the electronic ground state was taken as the input for all excited states as well, nuclear relaxation effects were neglected in our calculations. Thus, only vertical (Franck–Condon) transitions were considered in this approach.

Unfortunately, no fully operational implicit solvent model was available in the Molcas package at time when the calculations were performed. Due to this fact the SO-MS-CASPT2 calculations did not take into account any solvent effects, i.e. the molecules were simulated only in vacuo. On the other hand, the TD-DFT calculations can afford to account for solvent effect corrections, and thus the conductor-like screening model model COSMO<sup>183,184</sup> (for acetonitrile, dichloromethane and toluene) was employed. In case of TD-DFT it has been found out that calculations in vacuo shift transitions substantially to lower energies and this could together with an unsuitable choice of an XC functional lead to incorrect band assignments.<sup>168,185</sup> More details illustrated by the Cl substituted complex can be found elsewhere.<sup>1</sup>

Regarding other parameters of the TD-DFT calculations, Slater type orbital (STO) basis sets (triple- $\zeta$  type with two polarization functions for Re and double- $\zeta$  type with one polarization function for the other atoms) and the PBE0 hybrid functional<sup>179,180</sup> were assessed to be the optimal solution for these transition metal complexes. In previous studies<sup>1,168</sup> it has been shown and verified that the performance of hybrid functionals is superior to pure functionals.

The right choice of an XC functional is crucial to quality of TD-DFT results and requires considerable practical experience.<sup>1</sup> Usually, the conventional TD-DFT method tends to underestimate energies of charge-transfer excitations,<sup>186</sup> in some cases even by 1–2 eV.<sup>148</sup> DFT-type methods generally work well provided that an electronic transition occurs within a single molecular site. Nevertheless, this is not fulfilled for CT excited states where the electron is transferred from a donor orbital to an acceptor orbital located at a different place of a molecule. The electrostatic interaction between spatially separated charge densities of the electron-hole pair is non-local in character and therefore all local XC functionals (i.e. all pure functionals, LDA or GGA) fail to describe CT excited states accurately. Another serious problem arises from the wrong asymptotic behaviour of these functionals (i.e. the decay is faster than  $1/r$ , where  $r$  denotes the distance between the electron and the nucleus (the hole)). On top of that, calculations might wrongly predict the energy ordering of individual excited states, since more localized states are described correctly, in contrast to high-lying CT states with long-range charge separation which are incorrectly predicted to be among the lowest ones. The solution lies in introducing the non-local HF exchange into functionals. In our calculations we used hybrid functionals<sup>181,187</sup> which present a significant improvement over local XC functionals thanks to an incorporated fraction of the HF exact exchange, namely PBE0<sup>179,180</sup> and B3LYP.<sup>181</sup> The PBE0 functional provides reliable results<sup>188,189</sup> and usually works better than B3LYP for transition metal complexes, which is the reason why it was chosen in our projects.

A special category of XC functionals that are well-suited for a long-range CT description is called the range-separated hybrid functionals<sup>190–193</sup> (RSHs) (e.g. Coulomb-attenuating method-B3LYP<sup>194</sup> (CAM-B3LYP)) which tailor (increase) the portion of exact exchange to the increasing interelectronic distance. These relatively new directions in development of the TD-DFT method were not adopted in this doctoral thesis, since at that time these XC functionals (such as CAM-B3LYP) were not implemented in the ADF software and they were not yet ready for a routine usage.

In TD-DFT, the scalar relativistic effects were introduced by SR ZORA.<sup>65,71</sup> To obtain a set of spin-orbit states, at first the lowest spin-free singlet and triplet excited states in both symmetries were determined and afterwards the spin-orbit A' and A'' excited states were calculated. Namely, 30 lowest singlet and 30 lowest triplet states were taken and subsequently 120 lowest SO states were computed. In this formalism spin-orbit coupling was treated as a perturbation.<sup>86</sup> In addition, to enable a comparison with a more advanced spin-orbit including technique, the relativistic two-component zeroth-order regular approximation<sup>85</sup> in the TD-DFT method was utilized for several lowest excited states of  $[\text{ReI}(\text{CO})_3(\text{bpy})]$ . Since the results turned out to be comparable, only the computationally less demanding approximate (perturbative) SO-TD-DFT approach was used. Moreover, a few years ago the more advanced technique was extremely computationally demanding (at that time almost not feasible for medium-size complexes containing heavy elements).

The following paragraph deals with the analysis of active space orbitals in the CASSCF step of the SO-MS-CASPT2 method. To apply an optimal active space, one should include at least all  $d$  orbitals on a metal (i.e. occupied  $t_{2g}$  and virtual  $e_g$ ),  $p_\pi$  on a halide ligand,  $\pi$  orbitals of carbonyls and of a bipyridine ligand. Unfortunately, in practice one is forced to omit some of them in order to keep a calculation feasible. In other words, the inclusion of all these orbitals into the active space is beyond limits of the current computational resources. As already discussed in the section Theoretical overview (see Chapter 2.4.2), an inadequate or insufficient composition of active space can lead for example to switching of closely-spaced MO energy levels. Namely, the LUMO in  $[\text{ReX}(\text{CO})_3(\text{bpy})]$  should correspond to  $\pi^*(\text{bpy})$  and the LUMO+1 is composed dominantly of  $d\pi$  on Re (see Figure 3.3). However, it might happen that energies of these two MOs interchange due to an incorrect active space, which in consequence changes a character of the lowest allowed excitation from MLCT to MC. MC in this case refers to the so-called  $dd$  states that are typically much higher in energy than MLCT. Because of that,  $d \rightarrow d^*$  transitions do not have to be taken into consideration in our calculations. In the worst case scenario, the calculation might produce completely unphysical results.

### 3.1.3 Results and discussion

The experimental UV-vis absorption spectra<sup>27</sup> of  $[\text{ReX}(\text{CO})_3(\text{bpy})]$  ( $\text{X} = \text{Cl}, \text{Br}, \text{I}$ ) (recorded in MeCN and DCM) are shown in Figure 3.5 and the corresponding measured values (also for toluene) are presented in Table 3.2. Three spectroscopically interesting regions are present: at 380–400 nm, 290–295 nm, and 235–245 nm. According to Rossenaar et al.<sup>43</sup> and spin-free TD-DFT calculations,<sup>28,168</sup> they were identified as  $\text{ReX}(\text{CO})_3 \rightarrow \text{bpy}^1\text{CT}$ ,  $^1\text{IL}(\pi\pi^*(\text{bpy}))$  and  $\text{Re} \rightarrow \text{CO}^1\text{MLCT}/^1\text{IL}$ , respectively. In case of iodide, one more band was detected around 223 nm, which was attributed to a higher-lying  $\text{ReX}(\text{CO})_3 \rightarrow \text{bpy}^1\text{CT}$  transition.<sup>43</sup>

Inspecting the spectra (Figure 3.5 and Table 3.2), a few trends are observed. Concerning the lowest-energy band centred at  $\sim 380$  nm, the halide ligand influences its position in the following energetic order:  $\text{Cl} \geq \text{Br} \gg \text{I}$ . The heavier the halide, the more the peak is shifted to the red; for example in MeCN the values are  $26\,954\text{ cm}^{-1}$  ( $\text{Cl}$ )  $\geq 26\,667\text{ cm}^{-1}$  ( $\text{Br}$ )  $\gg 25\,974\text{ cm}^{-1}$  ( $\text{I}$ ). The difference between the chloro and the bromo complex is much smaller



than between the bromo and the iodo complex. Next, the decreasing polarity of solvent has the same effect: MeCN > DCM > toluene, i.e. less polar solvents shift this peak towards lower energies; e.g. for  $[\text{ReCl}(\text{CO})_3(\text{bpy})]$  the values are  $26\,954\text{ cm}^{-1}$  (MeCN) >  $25\,840\text{ cm}^{-1}$  (DCM) >  $24\,814\text{ cm}^{-1}$  (toluene).

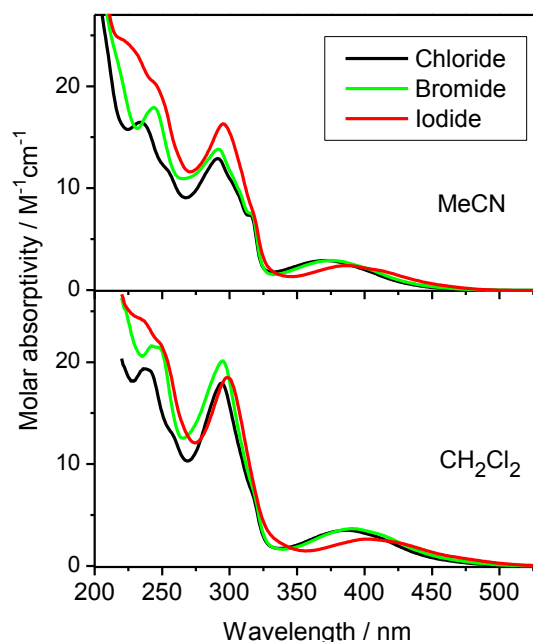


**Figure 3.5.** The experimental UV–vis absorption spectra of  $[\text{ReX}(\text{CO})_3(\text{bpy})]$  ( $X = \text{Cl}, \text{Br}, \text{I}$ ) in acetonitrile (MeCN) and dichloromethane (DCM). (adopted from Reference [27])

In order to emphasize the importance of SOC, we start with spin-free calculated data and then we proceed to spin-orbit results. Tables 3.3, 3.4 and 3.5 compile the spin-free MS-CASPT2 transition energies from the GS  $a^1A'$  to the low-lying pure singlet and triplet excited states and the associated oscillator strengths  $f$  of  $[\text{ReX}(\text{CO})_3(\text{bpy})]$  ( $X = \text{Cl}, \text{Br}, \text{I}$ ) calculated in vacuo. Hereafter the excited states are labelled by a prefix given by lower-case letters (the GS being  $a^1A'$ ), which denotes the energy order of the states of given spin multiplicity and symmetry (assuming the  $C_s$  point group). In the second and third columns of Tables 3.3, 3.4 and 3.5, the most contributing CSFs of a particular excited state (described by the main corresponding excitation) and their characters are listed. Transitions from the singlet ground state to all triplet excited states are spin-forbidden (oscillator strengths are equal to zero) in accordance with the spin selection rule.

When compared the lowest spin-free MS-CASPT2 energetic situation of the three complexes, they are quite similar in nature and slightly vary in oscillator strengths. Quantitatively, the overall trend is to shift to lower transition energies on going from Cl to I. The transitions with the strongest oscillator strengths correspond roughly to the bands observed experimentally (except of the highest-energy band at  $\sim 235\text{--}245\text{ nm}$ , which was not simulated by means of MS-CASPT2), achieving thus a reasonable agreement between theory and experiment.

**Table 3.2.** The experimental UV–vis absorption spectra of  $[\text{ReX}(\text{CO})_3(\text{bpy})]$  ( $\text{X} = \text{Cl}, \text{Br}, \text{I}$ ) in acetonitrile, dichloromethane and toluene. <sup>a</sup>Determined by a Gaussian analysis. (sh = shoulder, br = broad)

Solvent	Wavelength [nm]	Energy $[\text{cm}^{-1}]$	Molar absorptivity $[\text{M}^{-1}\cdot\text{cm}^{-1}]$
<b><math>[\text{ReCl}(\text{CO})_3(\text{bpy})]</math></b>			
MeCN	371	26 954	2 900
	315 sh	31 746	7 400
	291	34 364	12 900
	252 sh	39 683	12 100
	234	42 735	14 500
$\text{CH}_2\text{Cl}_2$	387	25 840	3 500
	316 sh	31 646	
	294	34 014	17 900
	257 sh	38 911	
	238	42 017	19 300
Toluene	403	24 814	
<b><math>[\text{ReBr}(\text{CO})_3(\text{bpy})]</math></b>			
MeCN	375	26 667	2 900
	315 sh	31 746	
	292	34 247	13 800
	244	40 984	17 900
$\text{CH}_2\text{Cl}_2$	392	25 510	3 700
	295	33 898	20 100
	245 br	40 816	21 500
Toluene	405	24 691	
<b><math>[\text{ReI}(\text{CO})_3(\text{bpy})]</math></b>			
MeCN	385	25 974	2 400
	316 sh	31 646	
	295	33 898	16 300
	244 sh	40 984	20 400
	220 sh	45 455	24 600
$\text{CH}_2\text{Cl}_2$	402	24 876	2 600
	299	33 445	18 500
	245 sh	40 816	22 400
	233 sh	42 918	24 300
Toluene	496	20 145 <sup>a</sup>	
	449	22 295 <sup>a</sup>	
	422	23 687 <sup>a</sup>	

**Table 3.3.** The spin-free MS-CASPT2 transition energies and oscillator strengths  $f$  of  $[\text{ReCl}(\text{CO})_3(\text{bpy})]$  calculated in vacuo. The energy values are given in reciprocal centimetres and as wavelengths (in nm).

State	Dominant excitation	Character	Energy [cm <sup>-1</sup> ]	Wavelength [nm]	Osc. strength
<b>Singlets</b>					
a <sup>1</sup> A"	d <sub>Re</sub> ,pCl → π* <sub>bpy</sub> (62%)	MLCT/XLCT	24 780	403	0.0058
b <sup>1</sup> A'	d <sub>Re</sub> ,pCl → π* <sub>bpy</sub> (80%)	MLCT/XLCT	25 700	389	0.0479
c <sup>1</sup> A'	d <sub>Re</sub> → π* <sub>bpy</sub> (81%)	MLCT	29 650	337	0.0005
b <sup>1</sup> A"	d <sub>Re</sub> → d <sub>Re</sub> , π* <sub>CO</sub> (68%)	MC/MLCT(CO)	31 520	317	0.0013
d <sup>1</sup> A'	d <sub>Re</sub> ,pCl → π* <sub>bpy</sub> (77%)	MLCT/XLCT	32 440	308	0.0036
e <sup>1</sup> A'	d <sub>Re</sub> → π* <sub>bpy</sub> (67%)	MLCT	33 780	296	0.0154
c <sup>1</sup> A"	d <sub>Re</sub> ,pCl → π* <sub>bpy</sub> (48%); d <sub>Re</sub> , π <sub>bpy</sub> → π* <sub>bpy</sub> (29%)	MLCT/XLCT/IL	35 306	283	0.0056
d <sup>1</sup> A"	d <sub>Re</sub> ,pCl → π* <sub>bpy</sub> (53%); π <sub>bpy</sub> → π* <sub>bpy</sub> (20%)	MLCT(/XLCT)/IL	36 465	274	0.3328
<b>Triplets</b>					
a <sup>3</sup> A"	d <sub>Re</sub> ,pCl → π* <sub>bpy</sub> (54%); π <sub>bpy</sub> → π* <sub>bpy</sub> (23%)	MLCT/XLCT/IL	24 190	413	-
a <sup>3</sup> A'	d <sub>Re</sub> ,pCl → π* <sub>bpy</sub> (49%); d <sub>Re</sub> ,pCl → π* <sub>bpy</sub> (37%)	MLCT/XLCT	26 290	380	-
b <sup>3</sup> A"	d <sub>Re</sub> ,pCl → π* <sub>bpy</sub> (25%); π <sub>bpy</sub> → π* <sub>bpy</sub> (25%)	MLCT/XLCT/IL	29 610	338	-
b <sup>3</sup> A'	d <sub>Re</sub> → π* <sub>bpy</sub> (48%); d <sub>Re</sub> → π* <sub>bpy</sub> (39%)	MLCT	30 940	323	-
c <sup>3</sup> A"	d <sub>Re</sub> → d <sub>Re</sub> , π* <sub>CO</sub> (73%)	MC/MLCT(CO)	31 540	317	-
c <sup>3</sup> A'	d <sub>Re</sub> ,pCl → π* <sub>bpy</sub> (40%); d <sub>Re</sub> ,pCl → π* <sub>bpy</sub> (27%)	MLCT/XLCT	32 410	309	-
d <sup>3</sup> A'	d <sub>Re</sub> → d <sub>Re</sub> , π* <sub>CO</sub> (72%)	MC/MLCT(CO)	34 430	290	-
d <sup>3</sup> A"	d <sub>Re</sub> → d <sub>Re</sub> , π* <sub>CO</sub> (84%)	MC/MLCT(CO)	34 470	290	-

The lowest experimental band lying around 380–400 nm is based on transitions to two low-lying MLCT/XLCT, MLCT singlet states, namely a<sup>1</sup>A" and b<sup>1</sup>A', with calculated values of 24 780 cm<sup>-1</sup> (403 nm) and 25 700 cm<sup>-1</sup> (389 nm) in  $[\text{ReCl}(\text{CO})_3(\text{bpy})]$ , 24 340 cm<sup>-1</sup> (411 nm) and 25 590 cm<sup>-1</sup> (391 nm) in  $[\text{ReBr}(\text{CO})_3(\text{bpy})]$ , 21 920 cm<sup>-1</sup> (456 nm) and 24 590 cm<sup>-1</sup> (407 nm) in  $[\text{ReI}(\text{CO})_3(\text{bpy})]$ . The latter contributes the most to this band, having a larger oscillator strength than the former. The decreasing tendency of theoretical energy values in the series Cl ≥ Br >> I reproduces (qualitatively) the experimental red shift already

discussed above (Figure 3.5). The low-lying states can be described as predominantly MLCT ( $5d_{\text{Re}} \rightarrow \pi^*(\text{bpy})$ ) in the chloro complex, with an increasing XLCT ( $p_{\pi}(\text{X}) \rightarrow \pi^*(\text{bpy})$ ) character when moving to the bromo and the iodo complex.

**Table 3.4.** The spin-free MS-CASPT2 transition energies and oscillator strengths  $f$  of  $[\text{ReBr}(\text{CO})_3(\text{bpy})]$  calculated in vacuo. The energy values are given in reciprocal centimetres and as wavelengths (in nm).

State	Dominant excitation	Character	Energy [cm <sup>-1</sup> ]	Wavelength [nm]	Osc. strength
<b>Singlets</b>					
a <sup>1</sup> A''	d <sub>Re</sub> ,p <sub>Br</sub> → π* <sub>bpy</sub> (88%)	MLCT/XLCT	24 340	411	0.0096
b <sup>1</sup> A'	d <sub>Re</sub> ,p <sub>Br</sub> → π* <sub>bpy</sub> (67%)	MLCT/XLCT	25 590	391	0.0790
c <sup>1</sup> A'	d <sub>Re</sub> → π* <sub>bpy</sub> (71%)	MLCT	29 340	341	0.0000
b <sup>1</sup> A''	d <sub>Re</sub> ,p <sub>Br</sub> → π* <sub>bpy</sub> (82%)	MLCT/XLCT	31 000	323	0.0098
d <sup>1</sup> A'	d <sub>Re</sub> ,p <sub>Br</sub> → π* <sub>bpy</sub> (65%)	MLCT/XLCT	32 535	307	0.0176
c <sup>1</sup> A''	d <sub>Re</sub> → d <sub>Re</sub> , π* <sub>CO</sub> (50%); d <sub>Re</sub> ,p <sub>Br</sub> → π* <sub>bpy</sub> (34%)	MC/MLCT(CO)/ /MLCT/XLCT	34 960	286	0.0103
d <sup>1</sup> A''	d <sub>Re</sub> ,p <sub>Br</sub> → π* <sub>bpy</sub> (46%); d <sub>Re</sub> → d <sub>Re</sub> , π* <sub>CO</sub> (36%)	MLCT/XLCT/ /MC/MLCT(CO)	36 440	274	0.0055
e <sup>1</sup> A'	d <sub>Re</sub> → π* <sub>bpy</sub> (68%)	MLCT	36 520	274	0.0013
<b>Triplets</b>					
a <sup>3</sup> A''	d <sub>Re</sub> ,p <sub>Br</sub> → π* <sub>bpy</sub> (59%)	MLCT/XLCT	22 490	445	-
a <sup>3</sup> A'	d <sub>Re</sub> ,p <sub>Br</sub> → π* <sub>bpy</sub> (88%)	MLCT/XLCT	24 370	410	-
b <sup>3</sup> A''	π <sub>bpy</sub> → π* <sub>bpy</sub> (56%); d <sub>Re</sub> ,p <sub>Br</sub> → π* <sub>bpy</sub> (20%)	IL/MLCT/XLCT	27 600	362	-
b <sup>3</sup> A'	d <sub>Re</sub> → π* <sub>bpy</sub> (89%)	MLCT	29 160	343	-
c <sup>3</sup> A''	d <sub>Re</sub> → d <sub>Re</sub> , π* <sub>CO</sub> (87%)	MC/MLCT(CO)	30 830	324	-
c <sup>3</sup> A'	d <sub>Re</sub> → d <sub>Re</sub> , π* <sub>CO</sub> (86%)	MC/MLCT(CO)	30 950	323	-
d <sup>3</sup> A'	d <sub>Re</sub> ,p <sub>Br</sub> → π* <sub>bpy</sub> (80%)	MLCT/XLCT	36 190	276	-
d <sup>3</sup> A''	d <sub>Re</sub> ,p <sub>Br</sub> → π* <sub>bpy</sub> (72%)	MLCT/XLCT	36 220	276	-

The next strong transitions in the spin-free spectrum emerge in the range ca. 275–340 nm in  $[\text{ReCl}(\text{CO})_3(\text{bpy})]$  and  $[\text{ReBr}(\text{CO})_3(\text{bpy})]$  and 290–340 nm in  $[\text{ReI}(\text{CO})_3(\text{bpy})]$ . The theoretical peak consists of transitions to several singlet states (c<sup>1</sup>A', d<sup>1</sup>A', e<sup>1</sup>A', b<sup>1</sup>A'', c<sup>1</sup>A'' and d<sup>1</sup>A''), reaching its maximum at 296 nm (e<sup>1</sup>A' for X = Cl), 307 nm (d<sup>1</sup>A' for X = Br) and 322 nm (d<sup>1</sup>A' for X = I). From that it is obvious that the maximum shifts a little bit to lower energies when changing the halide ligand from Cl to I.

It is evident from our calculations that at least two lowest excited singlet states and two lowest triplet states originate from MLCT with an XLCT contribution. The nature of the b<sup>1</sup>A'

state is given by the charge transfer from  $d_{\text{Re}}X(\text{CO})_3$  to  $\pi^*(\text{bpy})$ , as seen in Tables 3.3, 3.4 and 3.5. The halide to  $\pi^*(\text{bpy})$  contribution is significantly increased in case of the iodo complex. We have thus confirmed the conclusions of TD-DFT calculations stated in Reference [28].

**Table 3.5.** The spin-free MS-CASPT2 transition energies and oscillator strengths  $f$  of  $[\text{ReI}(\text{CO})_3(\text{bpy})]$  calculated in vacuo. The energy values are given in reciprocal centimetres and as wavelengths (in nm).

State	Dominant excitation	Character	Energy [cm <sup>-1</sup> ]	Wavelength [nm]	Osc. strength
<b>Singlets</b>					
$a^1A''$	$d_{\text{Re}} \rightarrow \pi^*_{\text{bpy}}$ (69%)	MLCT	21 920	456	0.0059
$b^1A'$	$d_{\text{Re}}, p_{\text{I}} \rightarrow \pi^*_{\text{bpy}}$ (77%)	MLCT/XLCT	24 590	407	0.0944
$b^1A''$	$d_{\text{Re}} \rightarrow d_{\text{Re}}, \pi^*_{\text{CO}}$ (64%)	MC/MLCT(CO)	29 450	339	0.0045
$c^1A'$	$d_{\text{Re}} \rightarrow \pi^*_{\text{bpy}}$ (77%)	MLCT	29 470	339	0.0010
$c^1A''$	$d_{\text{Re}} \rightarrow \pi^*_{\text{bpy}}$ (61%)	MLCT	30 050	333	0.0068
$d^1A'$	$d_{\text{Re}}, p_{\text{I}} \rightarrow \pi^*_{\text{bpy}}$ (79%)	MLCT/XLCT	31 040	322	0.0254
$e^1A'$	$d_{\text{Re}} \rightarrow \pi^*_{\text{bpy}}$ (75%)	MLCT	31 740	315	0.0002
$d^1A''$	$d_{\text{Re}}, p_{\text{I}} \rightarrow \pi^*_{\text{bpy}}$ (32%); $p_{\text{I}} \rightarrow \pi^*_{\text{bpy}}$ (17%)	MLCT/XLCT	34 230	292	0.0187
<b>Triplets</b>					
$a^3A''$	$\pi_{\text{bpy}}, d_{\text{Re}} \rightarrow \pi^*_{\text{bpy}}$ (44%); $d_{\text{Re}}, p_{\text{I}} \rightarrow \pi^*_{\text{bpy}}$ (33%)	IL/MLCT/XLCT	21 610	463	-
$a^3A'$	$d_{\text{Re}}, p_{\text{I}} \rightarrow \pi^*_{\text{bpy}}$ (83%)	MLCT/XLCT	24 185	413	-
$b^3A''$	$d_{\text{Re}}, p_{\text{I}} \rightarrow \pi^*_{\text{bpy}}$ (38%)	MLCT/XLCT	27 970	357	-
$c^3A''$	$d_{\text{Re}} \rightarrow d_{\text{Re}}, \pi^*_{\text{CO}}$ (37%); $d_{\text{Re}} \rightarrow d_{\text{Re}}, \pi^*_{\text{CO}}$ (37%)	MC/MLCT(CO)	29 290	341	-
$b^3A'$	$d_{\text{Re}} \rightarrow \pi^*_{\text{bpy}}$ (84%)	MLCT	29 350	341	-
$c^3A'$	$d_{\text{Re}}, p_{\text{I}} \rightarrow \pi^*_{\text{bpy}}$ (48%)	MLCT/XLCT	30 300	330	-
$d^3A''$	$d_{\text{Re}} \rightarrow d_{\text{Re}}, \pi^*_{\text{CO}}$ (45%); $d_{\text{Re}} \rightarrow d_{\text{Re}}, \pi^*_{\text{CO}}$ (37%)	MC/MLCT(CO)	31 000	322	-
$d^3A'$	$d_{\text{Re}} \rightarrow d_{\text{Re}}, \pi^*_{\text{CO}}$ (60%)	MC/MLCT(CO)	32 360	309	-

The spin-free TD-DFT transition energies and the associated oscillator strengths  $f$  of  $[\text{ReX}(\text{CO})_3(\text{bpy})]$  ( $X = \text{Cl}, \text{Br}, \text{I}$ ) calculated in dichloromethane (at the COSMO level) are listed in Tables 3.6, 3.7 and 3.8. The results in MeCN and toluene were also calculated. As already mentioned, the lower-case letter prefix is used for denoting the energy order of states in each symmetrical representation. MS-CASPT2 involved 16 lowest excited states and thereby simulated the spectrum in the vis and near-UV spectral regions only. The MS-CASPT2 results thus do not capture the band around 235–245 nm. On the other hand, solvent-corrected TD-DFT, where more excited singlet states are included, covered also the UV part of the spectrum (below 275 nm) as it can be seen from Tables 3.6, 3.7 and 3.8.

**Table 3.6.** The solvent-corrected (COSMO) spin-free TD-DFT transition energies and oscillator strengths  $f$  of  $[\text{ReCl}(\text{CO})_3(\text{bpy})]$  calculated in dichloromethane. The energy values are given in reciprocal centimetres and as wavelengths (in nm). Only singlet states with oscillator strengths greater than 0.005 are shown (with the exception of the lowest  $a^1A''$  state).

State	Dominant excitation	Character	Energy [cm <sup>-1</sup> ]	Wavelength [nm]	Osc. strength
<b>Singlets</b>					
$a^1A''$	$d_{\text{Re}}, p_{\text{Cl}} \rightarrow \pi^*_{\text{bpy}}$ (98%)	MLCT/XLCT	22 570	443	0.0020
$b^1A'$	$d_{\text{Re}}, p_{\text{Cl}} \rightarrow \pi^*_{\text{bpy}}$ (98%)	MLCT/XLCT	24 110	415	0.0534
$d^1A'$	$d_{\text{Re}}, p_{\text{Cl}} \rightarrow \pi^*_{\text{bpy}}$ (93%)	MLCT/XLCT	32 790	305	0.0217
$e^1A''$	$p_{\text{Cl}}, d_{\text{Re}} \rightarrow \pi^*_{\text{bpy}}$ (67%)	XLCT/MLCT	34 970	286	0.0307
$f^1A'$	$p_{\text{Cl}}, d_{\text{Re}} \rightarrow \pi^*_{\text{bpy}}$ (92%)	XLCT/MLCT	35 270	283	0.0556
$g^1A''$	$\pi_{\text{bpy}} \rightarrow \pi^*_{\text{bpy}}$ (53%); $d_{\text{Re}}, p_{\text{Cl}} \rightarrow \pi^*_{\text{bpy}}$ (30%)	IL/MLCT/XLCT	36 000	278	0.2746
$h^1A'$	$p_{\text{Cl}}, d_{\text{Re}} \rightarrow \pi^*_{\text{bpy}}$ (72%)	XLCT/MLCT	38 655	259	0.0164
$i^1A''$	$d_{\text{Re}}, p_{\text{Cl}} \rightarrow d_{\text{Re}}, \text{CO}$ (59%)	MLCT/MC	40 465	247	0.0316
$j^1A'$	$p_{\text{Cl}}, d_{\text{Re}} \rightarrow \pi^*_{\text{bpy}}$ (72%)	XLCT/MLCT	41 280	242	0.0097
$j^1A''$	$\pi_{\text{bpy}} \rightarrow \pi^*_{\text{bpy}}$ (75%)	IL	42 260	237	0.1081
<b>Triplets</b>					
$a^3A''$	$d_{\text{Re}}, p_{\text{Cl}} \rightarrow \pi^*_{\text{bpy}}$ (97%)	MLCT/XLCT	21 760	459	-
$a^3A'$	$d_{\text{Re}}, p_{\text{Cl}} \rightarrow \pi^*_{\text{bpy}}$ (93%)	MLCT/XLCT	22 510	444	-
$b^3A''$	$\pi_{\text{bpy}} \rightarrow \pi^*_{\text{bpy}}$ (78%)	IL	25 640	390	-
$b^3A'$	$d_{\text{Re}} \rightarrow \pi^*_{\text{bpy}}$ (98%)	MLCT	26 920	371	-
$c^3A'$	$d_{\text{Re}}, p_{\text{Cl}}, \rightarrow \pi^*_{\text{bpy}}$ (51%)	XLCT/MLCT	30 340	330	-
$c^3A''$	$d_{\text{Re}}, p_{\text{Cl}} \rightarrow \pi^*_{\text{bpy}}$ (77%)	XLCT/MLCT	30 490	328	-

**Table 3.7.** The solvent-corrected (COSMO) spin-free TD-DFT transition energies and oscillator strengths  $f$  of  $[\text{ReBr}(\text{CO})_3(\text{bpy})]$  calculated in dichloromethane. The energy values are given in reciprocal centimetres and as wavelengths (in nm). Only singlet states with oscillator strengths greater than 0.005 are shown (with the exception of the lowest  $a^1A''$  state).

State	Dominant excitation	Character	Energy [cm <sup>-1</sup> ]	Wavelength [nm]	Osc. strength
<b>Singlets</b>					
$a^1A''$	$d_{\text{Re}}, p_{\text{Br}} \rightarrow \pi^*_{\text{bpy}}$ (97%)	MLCT/XLCT	21 800	459	0.0012
$b^1A'$	$d_{\text{Re}}, p_{\text{Br}} \rightarrow \pi^*_{\text{bpy}}$ (97%)	MLCT/XLCT	22 990	435	0.0432
$e^1A'$	$p_{\text{Br}}, d_{\text{Re}} \rightarrow \pi^*_{\text{bpy}}$ (70%)	XLCT/MLCT	31 430	318	0.0212
$f^1A'$	$p_{\text{Br}}, d_{\text{Re}} \rightarrow \pi^*_{\text{bpy}}$ (75%)	XLCT/MLCT	32 470	308	0.0620
$f^1A''$	$\pi_{\text{bpy}} \rightarrow \pi^*_{\text{bpy}}$ (73%)	IL	35 020	286	0.2725
$j^1A'$	$p_{\text{Br}}, d_{\text{Re}} \rightarrow \pi^*_{\text{bpy}}$ (70%)	XLCT/MLCT	38 215	262	0.0351
$l^1A'$	$p_{\text{Br}}, d_{\text{Re}} \rightarrow \pi^*_{\text{bpy}}$ (85%)	XLCT/MLCT	40 090	249	0.0409
$j^1A''$	$p_{\text{Br}}, d_{\text{Re}} \rightarrow \pi^*_{\text{bpy}}$ (43%); $d_{\text{Re}} \rightarrow d_{\text{Re}}, \text{CO}$ (23%)		40 530	247	0.0596
$m^1A'$	$p_{\text{Br}}, d_{\text{Re}} \rightarrow \pi^*_{\text{bpy}}$ (89%)	XLCT/MLCT	41 630	240	0.0344
$k^1A''$	$d_{\text{Re}}, p_{\text{Br}} \rightarrow \pi^*_{\text{bpy}}$ (70%)	MLCT/XLCT/IL	41 930	239	0.1158
<b>Triplets</b>					
$a^3A''$	$d_{\text{Re}}, p_{\text{Br}} \rightarrow \pi^*_{\text{bpy}}$ (97%)	MLCT/XLCT	21 100	474	-
$a^3A'$	$d_{\text{Re}}, p_{\text{Br}} \rightarrow \pi^*_{\text{bpy}}$ (93%)	MLCT/XLCT	21 540	464	-
$b^3A''$	$\pi_{\text{bpy}} \rightarrow \pi^*_{\text{bpy}}$ (51%)	IL	24 760	404	-
$b^3A'$	$d_{\text{Re}} \rightarrow \pi^*_{\text{bpy}}$ (97%)	MLCT	26 655	375	-
$c^3A'$	$p_{\text{Br}}, d_{\text{Re}} \rightarrow \pi^*_{\text{bpy}}$ (69%)	XLCT/MLCT/IL	28 810	347	-
$c^3A''$	$p_{\text{Br}}, d_{\text{Re}} \rightarrow \pi^*_{\text{bpy}}$ (31%); $\pi_{\text{bpy}} \rightarrow \pi^*_{\text{bpy}}$ (22%)	XLCT/IL	29 890	335	-

**Table 3.8.** The solvent-corrected (COSMO) spin-free TD-DFT transition energies and oscillator strengths  $f$  of  $[\text{ReI}(\text{CO})_3(\text{bpy})]$  calculated in dichloromethane. The energy values are given in reciprocal centimetres and as wavelengths (in nm). Only singlet states with oscillator strengths greater than 0.005 are shown (with the exception of the lowest  $a^1A''$  state).

State	Dominant excitation	Character	Energy [cm <sup>-1</sup> ]	Wavelength [nm]	Osc. strength
<b>Singlets</b>					
$a^1A''$	$p_{\text{I}}, d_{\text{Re}} \rightarrow \pi^*_{\text{bpy}}$ (98%)	XLCT/MLCT	21 410	467	0.0006
$b^1A'$	$p_{\text{I}}, d_{\text{Re}} \rightarrow \pi^*_{\text{bpy}}$ (98%)	XLCT/MLCT	22 080	453	0.0231
$d^1A'$	$d_{\text{Re}}, p_{\text{I}} \rightarrow \pi^*_{\text{bpy}}$ (95%)	MLCT/XLCT	29 480	339	0.0595
$f^1A'$	$p_{\text{I}}, d_{\text{Re}} \rightarrow \pi^*_{\text{bpy}}$ (85%)	XLCT/MLCT	31 660	316	0.0248
$h^1A'$	$p_{\text{I}}, d_{\text{Re}} \rightarrow d_{\text{Re}}, \text{CO}$ (70%)	XLCT/MLCT	34 740	288	0.0161
$g^1A''$	$\pi_{\text{bpy}} \rightarrow \pi^*_{\text{bpy}}$ (76%)	IL	35 230	284	0.1900
$j^1A'$	$d_{\text{Re}}, p_{\text{I}} \rightarrow \pi^*_{\text{bpy}}$ (92%)	MLCT/XLCT	36 790	272	0.0394
$k^1A'$	$d_{\text{Re}}, p_{\text{I}} \rightarrow \pi^*_{\text{bpy}}$ (95%)	MLCT/XLCT	37 590	266	0.0410
$i^1A''$	$d_{\text{Re}}, p_{\text{I}} \rightarrow \pi^*_{\text{bpy}}$ (81%)	MLCT/XLCT	38 055	263	0.0402
$m^1A'$	$d_{\text{Re}}, p_{\text{I}} \rightarrow \pi^*_{\text{bpy}}$ (95%)	MLCT/XLCT	39 720	252	0.0394
$k^1A''$	$d_{\text{Re}}, p_{\text{Cl}} \rightarrow \pi^*_{\text{bpy}}$ (37%); $d_{\text{Re}}, p_{\text{Cl}} \rightarrow d_{\text{Re}}, \text{CO}$ (22%)	MLCT/XLCT/IL	40 310	248	0.2008
<b>Triples</b>					
$a^3A''$	$d_{\text{Re}}, p_{\text{I}} \rightarrow \pi^*_{\text{bpy}}$ (98%)	XLCT/MLCT	20 870	479	-
$a^3A'$	$d_{\text{Re}}, p_{\text{I}} \rightarrow \pi^*_{\text{bpy}}$ (98%)	XLCT/MLCT	21 025	476	-
$b^3A''$	$\pi_{\text{bpy}} \rightarrow \pi^*_{\text{bpy}}$ (51%)	IL	25 210	397	-
$b^3A'$	$d_{\text{Re}} \rightarrow \pi^*_{\text{bpy}}$ (63%)	MLCT	26 720	374	-
$c^3A'$	$d_{\text{Re}}, p_{\text{I}} \rightarrow \pi^*_{\text{bpy}}$ (54%)	MLCT	27 150	368	-
$c^3A''$	$\pi_{\text{bpy}} \rightarrow \pi^*_{\text{bpy}}$ (58%)	IL/MLCT	28 640	349	-

Figure 3.6 shows the theoretical UV-vis absorption spectra simulated by the solvent-corrected spin-free TD-DFT calculations. According to Tables 3.6, 3.7 and 3.8, the experimental peak appearing at  $\sim 290$  nm is attributed to  $^1\text{IL}$  ( $\pi\pi^*(\text{bpy})$ ) mixed with MLCT. Reversely, the intense peak around 240 nm is predominantly MLCT with IL ( $\pi\pi^*(\text{bpy})$ ) admixture. For the lowest-lying transitions the XLCT contribution increases considerably when going from the chloro to the iodo complex.<sup>27</sup> When we make a more detailed comparison of the experimental (Figure 3.5) and theoretical (Figure 3.6) spectra, the above mentioned trend concerning the effect of a halide substitution ( $\text{Cl} \rightarrow \text{I}$ ) on the lowest-energy band is reproduced by TD-DFT. Also the already discussed influence of decreasing solvent polarity on this band is present when taking into account the theoretical spectra in MeCN and toluene.<sup>27</sup> Thus it can be concluded that spin-free MS-CASPT2 and TD-DFT are in mutual qualitative agreement and both reproduce the experimental spectra in a satisfactory way.



However, in contrast to MS-CASPT2, the TD-DFT low-lying transitions tend to be more delocalized with a greater XLCT contribution, sometimes even exaggerated.<sup>1,36,37</sup>

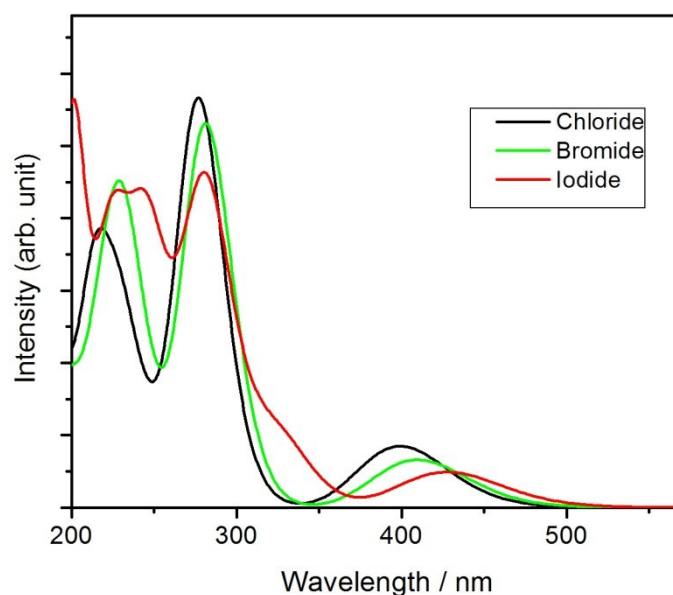


**Figure 3.6.** The theoretical UV-vis absorption spectra of  $[\text{ReX}(\text{CO})_3(\text{bpy})]$  calculated by means of spin-free TD-DFT (PBE0, COSMO/ $\text{CH}_2\text{Cl}_2$ ) (fwhm =  $4000\text{ cm}^{-1}$ ). (adopted from Reference [27])

After we have analysed the spin-free calculations, we approach to the section with the spin-orbit results. Although the spin-free theoretical spectrum provides a reasonably good interpretation of majority of experimental data, by using the spin-free theory only we are not able to explain all spectral features manifested in the absorption spectra shown in Figure 3.5. Two shoulders on the low-energy side of the lowest-energy absorption band for all the three complexes represent one of such examples. The SO treatment is also necessary for a description of emission characteristics and photophysical data. Since Figure 3.5 does not bring a desired resolution of these two weak bands, the relevant detail of the experimental spectrum for the iodo complex recorded in toluene is depicted in Figure 3.7. Based on a Gaussian analysis, two weak bands are localized at  $\sim 20\,150\text{ cm}^{-1}$  and  $\sim 22\,300\text{ cm}^{-1}$  (the main band being at  $\sim 23\,690\text{ cm}^{-1}$  ( $422\text{ nm}$ )). Their origin is not clear, but it can be assumed that their presence is connected with the existence of spin-mixed states. Close-lying singlet and triplet excited states, the possibility of their mixing and their varying character from MLCT to XLCT – that all together is presumably bound to the spin-orbit interaction. Therefore the spin-orbit theory must be employed in order to account for experimental observations not covered by the spin-free results and to acquire an in-depth understanding of the complex photophysical behaviour of transition metal complexes.

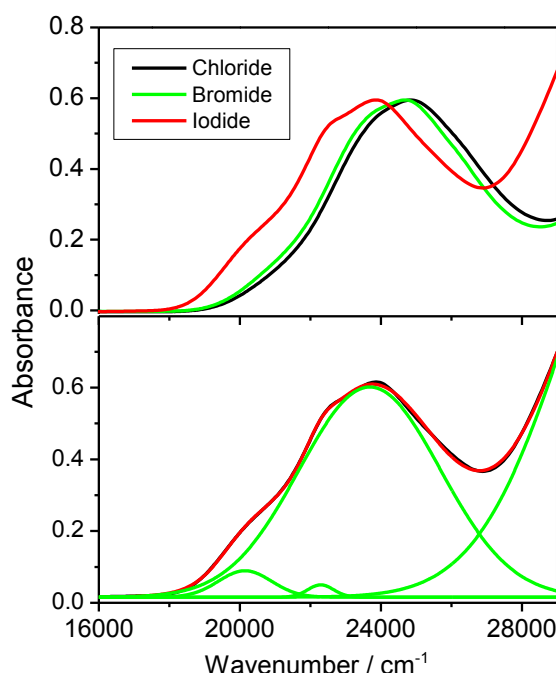


**Figure 3.7.** The experimental spectra recorded in toluene. Top: The intensity-normalized absorption spectra of  $[\text{ReX}(\text{CO})_3(\text{bpy})]$ . Bottom: Deconvoluted spectrum of the  $[\text{ReI}(\text{CO})_3(\text{bpy})]$ . Experimental spectrum in black, fitted function in red and individual Gaussians in green. Fitted parameters (max wavenumber, fwhm, relative band area): 20 150  $\text{cm}^{-1}$ , 1 500  $\text{cm}^{-1}$ , 0.047; 22 300  $\text{cm}^{-1}$ , 740  $\text{cm}^{-1}$ , 0.011; 23 690  $\text{cm}^{-1}$ , 4 010  $\text{cm}^{-1}$ , 1.000. (adopted from Reference [27])

The spin-orbit MS-CASPT2 transition energies from the ground state to the low-lying excited states of  $[\text{ReX}(\text{CO})_3(\text{bpy})]$  ( $X = \text{Cl}, \text{Br}, \text{I}$ ) calculated in vacuo and the associated oscillator strengths  $f$  are presented in Tables 3.9, 3.10 and 3.11. The SO excited states are numbered separately in both symmetries (the GS being  $1A'$ ). Table 3.12 contains the same characteristics for the solvent-corrected (COSMO/ $\text{CH}_2\text{Cl}_2$ ) SO-TD-DFT method. To distinguish the results of both methods from each other, the TD-DFT SO states are labelled by lower-case letters (the GS being  $aA'$ ). The origin of a particular spin-orbit state characterized by spin-free singlet and triplet state parentages is given in the second column in all Tables.

At first glance, it is apparent that the number of spin-orbit states compared to the spin-free situation has substantially increased – in the same energy range manifold spin-orbit states are identified, which has proven to be one of the features typical of transition metal complexes, i.e. a high density of states. In case of MS-CASPT2, 32 lowest SO excited states result from 16 lowest SF excited states. The final number of 32 SO excited states is put together from 8 singlet and  $3 \times 8$  triplet components, as mentioned in the SO-RASSI section (Chapter 2.4.4).

**Table 3.9.** The spin-orbit MS-CASPT2 transition energies and oscillator strengths  $f$  of  $[\text{ReCl}(\text{CO})_3(\text{bpy})]$  calculated in vacuo. The energy values are given in reciprocal centimetres and as wavelengths (in nm). Oscillator strengths lower than 0.00005 are omitted. Only the spin-free state contributions greater or equal to 5% are shown.

SO state	Contribution of the SO states in terms of SF states [%]	Character	Energy [ $\text{cm}^{-1}$ ]	Wavelength [nm]	Osc. strength
2A'	$a^3A''$ (79) + $b^1A'$ (18)	MLCT/XLCT/IL	23 600	424	0.0089
3A'	$a^3A''$ (84) + $a^3A'$ (11)	MLCT/XLCT/IL	23 700	422	0.0006
1A''	$a^3A''$ (85) + $a^3A'$ (12)	MLCT/XLCT/IL	23 710	422	
2A''	$a^1A''$ (79) + $a^3A'$ (18)	MLCT/XLCT	24 200	413	0.0041
4A'	$b^1A'$ (79) + $a^3A''$ (20)	MLCT/XLCT	26 060	384	0.0378
5A'	$a^3A'$ (84) + $a^3A''$ (14)	MLCT/XLCT	26 510	377	0.0001
3A''	$a^3A'$ (85) + $a^3A''$ (13)	MLCT/XLCT	26 520	377	
4A''	$a^3A'$ (80) + $a^1A''$ (19)	MLCT/XLCT	26 640	375	0.0018
6A'	$b^3A''$ (76) + $c^1A'$ (20)	MLCT/XLCT/IL	29 480	339	0.0001
7A'	$b^3A''$ (95)	MLCT/XLCT/IL	29 545	338	0.0006
5A''	$b^3A''$ (96)	MLCT/XLCT/IL	29 560	338	
8A'	$c^1A'$ (75) + $b^3A''$ (22)	MLCT	30 030	333	0.0003
9A'	$c^3A''$ (71) + $d^1A'$ (23) + $b^3A'$ (5)	MC/MLCT(CO)	31 060	322	0.0004
6A''	$b^1A''$ (74) + $c^3A'$ (23)	MC/MLCT(CO)	31 080	322	0.0009
10A'	$c^3A''$ (57) + $b^3A'$ (25) + $c^3A'$ (16)	MC/MLCT(CO)	31 150	321	
7A''	$b^3A'$ (93)	MLCT	31 160	321	0.0009
8A''	$c^3A''$ (70) + $c^3A'$ (20) + $b^3A'$ (8)	MC/MLCT(CO)	31 170	321	
9A''	$b^3A'$ (81) + $c^3A''$ (11)	MLCT	31 200	320	0.0007
11A'	$b^3A'$ (71) + $c^3A''$ (19) + $c^3A'$ (6)	MLCT	31 220	320	
10A''	$c^3A'$ (74) + $c^3A''$ (19)	MLCT/XLCT	32 720	306	
12A'	$c^3A'$ (74) + $c^3A''$ (21)	MLCT/XLCT	32 720	306	
11A''	$c^3A'$ (73) + $b^1A''$ (20)	MLCT/XLCT	32 740	305	0.0004
13A'	$d^1A'$ (70) + $c^3A''$ (24)	MLCT/XLCT	32 900	304	0.0036
14A'	$e^1A'$ (79) + $d^3A''$ (17)	MLCT	33 595	298	0.0112
12A''	$d^3A'$ (72) + $c^1A''$ (19)	MC/MLCT(CO)	34 070	293	0.0012
13A''	$d^3A'$ (52) + $d^3A''$ (42)	MC/MLCT(CO)	34 120	293	
15A'	$d^3A'$ (51) + $d^3A''$ (44)	MC/MLCT(CO)	34 120	293	
16A'	$d^3A''$ (80) + $e^1A'$ (19)	MC/MLCT(CO)	34 720	288	0.0033
17A'	$d^3A''$ (53) + $d^3A'$ (46)	MC/MLCT(CO)	34 880	287	0.0001
14A''	$d^3A''$ (53) + $d^3A'$ (46)	MC/MLCT(CO)	34 885	287	
15A''	$c^1A''$ (76) + $d^3A'$ (19)	MLCT/XLCT/IL	35 700	280	0.0323
16A''	$d^1A''$ (94)	MLCT/(XLCT)/IL	36 550	274	0.3039

**Table 3.10.** The spin-orbit MS-CASPT2 transition energies and oscillator strengths  $f$  of  $[\text{ReBr}(\text{CO})_3(\text{bpy})]$  calculated in vacuo. The energy values are given in reciprocal centimetres and as wavelengths (in nm). Oscillator strengths lower than 0.00005 are omitted. Only the spin-free state contributions greater or equal to 5% are shown.

SO state	Contribution of the SO states in terms of SF states [%]	Character	Energy [ $\text{cm}^{-1}$ ]	Wavelength [nm]	Osc. strength
1A''	$a^3A''$ (83) + $a^3A'$ (14)	MLCT/XLCT	22 010	454	
2A'	$a^3A''$ (83) + $a^3A'$ (14)	MLCT/XLCT	22 015	454	
3A'	$a^3A''$ (90) + $b^1A'$ (7)	MLCT/XLCT	22 130	452	0.0062
2A''	$a^1A''$ (50) + $a^3A'$ (46)	MLCT/XLCT	23 170	431	0.0044
4A'	$a^3A'$ (83) + $a^3A''$ (16)	MLCT/XLCT	24 655	405	
3A''	$a^3A'$ (83) + $a^3A''$ (15)	MLCT/XLCT	24 660	405	
4A''	$a^3A'$ (53) + $a^1A''$ (47)	MLCT/XLCT	25 320	395	0.0048
5A'	$b^1A'$ (86) + $a^3A''$ (9)	MLCT/XLCT	25 710	389	0.0682
6A'	$b^3A''$ (97)	IL/MLCT/XLCT	27 590	362	
5A''	$b^3A''$ (96)	IL/MLCT/XLCT	27 600	362	
7A'	$b^3A''$ (95)	IL/MLCT/XLCT	27 635	362	0.0033
6A''	$b^3A'$ (94)	MLCT	29 430	340	0.0001
7A''	$b^3A'$ (94)	MLCT	29 450	339	0.0006
8A'	$b^3A'$ (93)	MLCT	29 460	339	0.0016
9A'	$c^1A'$ (85) + $c^3A''$ (7)	MLCT	29 550	338	0.0001
10A'	$c^3A''$ (46) + $c^3A'$ (40) + $c^1A'$ (10)	MC/MLCT(CO)	30 040	333	0.0001
8A''	$c^3A'$ (50) + $b^1A''$ (43) + $c^3A''$ (5)	MC/MLCT(CO)/ /MLCT/XLCT	30 140	332	0.0034
9A''	$c^3A''$ (49) + $c^3A'$ (45) + $b^1A''$ (5)	MC/MLCT(CO)	30 180	331	0.0003
11A'	$c^3A''$ (86) + $d^1A'$ (13)	MC/MLCT(CO)	30 550	327	0.0018
10A''	$c^3A'$ (54) + $c^3A''$ (45)	MC/MLCT(CO)	31 700	315	
12A'	$c^3A'$ (54) + $c^3A''$ (45)	MC/MLCT(CO)	31 705	315	
11A''	$b^1A''$ (51) + $c^3A'$ (48)	MLCT/XLCT/ /MC/MLCT(CO)	31 870	314	0.0060
13A'	$d^1A'$ (86) + $c^3A''$ (14)	MLCT/XLCT	32 905	304	0.0153
12A''	$c^1A''$ (53) + $d^3A'$ (24) + $d^3A''$ (15) + + $d^1A''$ (8)	MC/MLCT(CO)/ /MLCT/XLCT	34 460	290	0.0027
13A''	$c^1A''$ (43) + $d^1A''$ (25) + $d^3A''$ (18) + + $d^3A'$ (13)	MC/MLCT(CO)/ /MLCT/XLCT	35 510	281	0.0107
14A'	$d^3A'$ (52) + $d^3A''$ (48)	MLCT/XLCT	35 590	281	
14A''	$d^3A'$ (97)	MLCT/XLCT	36 200	276	0.0002
15A'	$d^3A''$ (100)	MLCT/XLCT	36 250	276	
16A'	$e^1A'$ (97)	MLCT	36 760	272	0.0012
15A''	$d^3A''$ (65) + $d^3A'$ (26) + $d^1A''$ (9)	MLCT/XLCT	36 860	271	0.0006
17A'	$d^3A''$ (52) + $d^3A'$ (48)	MLCT/XLCT	36 910	271	
16A''	$d^1A''$ (56) + $d^3A'$ (40)	MLCT/XLCT/MC/ /MLCT(CO)	37 130	269	0.0014

**Table 3.11.** The spin-orbit MS-CASPT2 transition energies and oscillator strengths  $f$  of  $[\text{ReI}(\text{CO})_3(\text{bpy})]$  calculated in vacuo. The energy values are given in reciprocal centimetres and as wavelengths (in nm). Oscillator strengths lower than 0.00005 are omitted. Only the spin-free state contributions greater or equal to 5% are shown.

SO state	Contribution of the SO states in terms of SF states [%]	Character	Energy [ $\text{cm}^{-1}$ ]	Wavelength [nm]	Osc. strength
2A'	$a^3A''$ (87) + $b^1A'$ (9)	IL/MLCT/XLCT	21 085	474	0.0078
1A''	$a^3A''$ (86) + $a^3A'$ (12)	IL/MLCT/XLCT	21 100	474	
3A'	$a^3A''$ (87) + $a^3A'$ (9)	IL/MLCT/XLCT	21 110	474	0.0031
2A''	$a^1A''$ (84) + $a^3A'$ (14)	MLCT	21 400	467	0.0048
3A''	$a^3A'$ (86) + $a^3A''$ (9)	MLCT/XLCT	24 460	409	0.0002
4A'	$a^3A'$ (86) + $a^3A''$ (12)	MLCT/XLCT	24 500	408	0.0009
4A''	$a^3A'$ (85) + $a^1A''$ (11)	MLCT/XLCT	24 570	407	0.0008
5A'	$b^1A'$ (86) + $a^3A''$ (12)	MLCT//XLCT	24 930	401	0.0817
6A'	$b^3A''$ (90) + $c^3A'$ (7)	MLCT/XLCT	27 800	360	0.0001
5A''	$b^3A''$ (90) + $c^3A'$ (8)	MLCT/XLCT	27 800	360	
7A'	$b^3A''$ (93)	MLCT/XLCT	27 825	359	0.0011
6A''	$b^1A''$ (65) + $c^3A'$ (25) + $b^3A'$ (10)	MC/MLCT(CO)	28 780	347	0.0030
7A''	$c^3A''$ (77) + $c^3A'$ (14) + $b^3A''$ (6)	MC/MLCT(CO)	28 980	345	
8A'	$c^3A''$ (80) + $c^3A'$ (14) + $b^3A''$ (6)	MC/MLCT(CO)	28 980	345	0.0001
9A'	$c^3A''$ (85)	MC/MLCT(CO)	29 040	344	0.0004
8A''	$b^3A'$ (56) + $c^1A''$ (32) + $c^3A'$ (7)	MLCT	29 120	343	0.0025
10A'	$b^3A'$ (89) + $d^3A''$ (6)	MLCT	29 420	340	0.0004
9A''	$b^3A'$ (91) + $d^3A''$ (6)	MLCT	29 430	340	
11A'	$c^1A'$ (90) + $d^3A''$ (7)	MLCT	29 530	339	0.0011
10A''	$c^1A''$ (55) + $b^3A'$ (30) + $b^1A''$ (10)	MLCT	30 440	328	0.0019
12A'	$c^3A'$ (72) + $c^3A''$ (17)	MLCT/XLCT	30 780	325	0.0011
11A''	$c^3A'$ (76) + $c^3A''$ (18)	MLCT/XLCT	30 790	325	0.0001
13A'	$d^3A''$ (48) + $d^1A'$ (36) + $e^1A'$ (5) + $c^3A'$ (5)	MC/MLCT(CO)/ /MLCT/XLCT	30 920	323	0.0108
12A''	$c^3A'$ (64) + $b^1A''$ (22) + $c^1A''$ (10)	MLCT/XLCT	31 000	323	0.0034
13A''	$d^3A''$ (86) + $b^3A'$ (6)	MC/MLCT(CO)	31 080	322	0.0005
14A'	$d^3A''$ (89) + $c^1A'$ (6)	MC/MLCT(CO)	31 090	322	0.0001
15A'	$d^1A'$ (53) + $d^3A''$ (42)	MLCT/XLCT/ /MC/MLCT(CO)	31 350	319	0.0121
16A'	$e^1A'$ (86)	MLCT	32 081	312	0.0006
14A''	$d^3A'$ (87) + $d^1A''$ (11)	MC/MLCT(CO)	32 096	311	0.0020
15A''	$d^3A'$ (97)	MC/MLCT(CO)	32 411	308	
17A'	$d^3A'$ (96)	MC/MLCT(CO)	32 415	308	
16A''	$d^1A''$ (88) + $d^3A'$ (12)	MLCT/XLCT	34 521	290	0.0165

**Table 3.12.** The spin–orbit TD-DFT transition energies and oscillator strengths  $f$  of  $[\text{ReX}(\text{CO})_3(\text{bpy})]$  ( $\text{X} = \text{Cl}, \text{Br}, \text{I}$ ) calculated in dichloromethane (COSMO). The energy values are given in reciprocal centimetres and as wavelengths (in nm). Oscillator strengths lower than 0.00005 are omitted. Only the spin-free state contributions greater or equal to 5% are shown.

SO state	Contribution of the SO states in terms of SF states [%]	Character	Energy [ $\text{cm}^{-1}$ ]	Wavelength [nm]	Osc. strength
<b>X = Cl</b>					
aA''	$\text{a}^3\text{A}''$ (70) + $\text{a}^3\text{A}'$ (27)	MLCT/XLCT	21 160	473	
bA'	$\text{a}^3\text{A}''$ (70) + $\text{a}^3\text{A}'$ (27)	MLCT/XLCT	21 170	472	
cA'	$\text{a}^3\text{A}''$ (90) + $\text{b}^1\text{A}'$ (7)	MLCT/XLCT	21 430	467	0.0039
bA''	$\text{a}^1\text{A}''$ (48) + $\text{a}^3\text{A}'$ (48)	MLCT/XLCT	21 620	462	0.0009
cA''	$\text{a}^3\text{A}'$ (71) + $\text{a}^3\text{A}''$ (28)	MLCT/XLCT	22 920	436	
dA'	$\text{a}^3\text{A}'$ (71) + $\text{a}^3\text{A}''$ (28)	MLCT/XLCT	22 920	436	
dA''	$\text{a}^1\text{A}''$ (49) + $\text{a}^3\text{A}'$ (50)	MLCT/XLCT	23 250	430	0.0009
eA'	$\text{b}^1\text{A}'$ (88) + $\text{a}^3\text{A}''$ (8)	MLCT/XLCT	24 230	413	0.0472
eA''	$\text{b}^3\text{A}'$ (96)	MLCT/XLCT	25 630	390	
fA'	$\text{b}^3\text{A}''$ (99)	MLCT/XLCT	25 640	390	
gA'	$\text{b}^3\text{A}''$ (96)	MLCT/XLCT	25 650	390	0.0009
fA''	$\text{b}^3\text{A}''$ (95)	MLCT/XLCT	27 070	369	
hA'	$\text{b}^3\text{A}''$ (95)	MLCT/XLCT	27 080	369	0.0002
iA'	$\text{c}^1\text{A}'$ (96)	MLCT/XLCT	27 080	369	0.0013
<b>X = Br</b>					
aA''	$\text{a}^3\text{A}''$ (61) + $\text{a}^3\text{A}'$ (36)	XLCT/MLCT	20 240	494	
bA'	$\text{a}^3\text{A}''$ (61) + $\text{a}^3\text{A}'$ (37)	XLCT/MLCT	20 240	494	
bA''	$\text{a}^1\text{A}''$ (42) + $\text{a}^3\text{A}'$ (56)	XLCT/MLCT	20 610	485	0.0005
cA'	$\text{a}^3\text{A}''$ (84) + $\text{b}^1\text{A}'$ (14)	XLCT/MLCT	20 615	485	0.0059
cA''	$\text{a}^3\text{A}'$ (61) + $\text{a}^3\text{A}''$ (38)	XLCT/MLCT	22 210	450	
dA'	$\text{a}^3\text{A}'$ (61) + $\text{a}^3\text{A}''$ (27)	XLCT/MLCT	22 220	450	
dA''	$\text{a}^1\text{A}''$ (56) + $\text{a}^3\text{A}'$ (42)	XLCT/MLCT	22 640	442	0.0007
eA'	$\text{b}^1\text{A}'$ (81) + $\text{a}^3\text{A}''$ (14)	XLCT/MLCT	23 325	429	0.0356
eA''	$\text{b}^3\text{A}'$ (98)	XLCT/MLCT	24 770	404	
fA'	$\text{b}^3\text{A}''$ (99)	XLCT/MLCT	24 780	403	
gA'	$\text{b}^3\text{A}''$ (95)	XLCT/MLCT	24 810	403	0.0017
fA''	$\text{b}^3\text{A}''$ (95)	XLCT/MLCT	26 680	375	
gA''	$\text{b}^3\text{A}''$ (93)	XLCT/MLCT	26 690	375	0.0002
hA'	$\text{c}^1\text{A}'$ (96)	XLCT/MLCT	26 700	374	0.0006

**Table 3.12** (continued)

SO state	Contribution of the SO states in terms of SF states [%]	Character	Energy [cm <sup>-1</sup> ]	Wavelength [nm]	Osc. strength
X = I					
aA''	a <sup>3</sup> A'' (51) + a <sup>3</sup> A' (47)	XLCT/MLCT	19 160	522	
bA'	a <sup>3</sup> A'' (52) + a <sup>3</sup> A' (47)	XLCT/MLCT	19 170	521	0.0001
bA''	a <sup>3</sup> A' (55) + a <sup>1</sup> A'' (44)	XLCT/MLCT	19 410	515	0.0003
cA'	a <sup>3</sup> A'' (65) + a <sup>1</sup> A' (31)	XLCT/MLCT	19 560	511	0.0073
cA''	a <sup>3</sup> A' (48) + a <sup>3</sup> A'' (44)	XLCT/MLCT	21 920	456	
dA'	a <sup>3</sup> A' (47) + a <sup>3</sup> A'' (45)	XLCT/MLCT	22 010	454	0.0019
dA''	a <sup>1</sup> A'' (51) + a <sup>3</sup> A' (44)	XLCT/MLCT	22 200	450	0.0003
eA'	b <sup>1</sup> A' (58) + a <sup>3</sup> A'' (30)	XLCT/MLCT	22 535	444	0.0134
eA''	b <sup>3</sup> A' (84)	XLCT/MLCT	24 960	400	
fA'	b <sup>3</sup> A'' (84)	XLCT/MLCT	24 970	400	
gA'	b <sup>3</sup> A'' (94)	XLCT/MLCT	25 120	398	0.0015
gA''	b <sup>3</sup> A'' (95)	XLCT/MLCT	26 205	382	
hA'	b <sup>3</sup> A' (30) + c <sup>1</sup> A' (26) + c <sup>3</sup> A' (14)	XLCT/MLCT	26 320	380	0.0006
iA'	c <sup>3</sup> A' (40) + b <sup>3</sup> A' (36) + d <sup>1</sup> A' (6)	XLCT/MLCT	26 630	375	0.0036

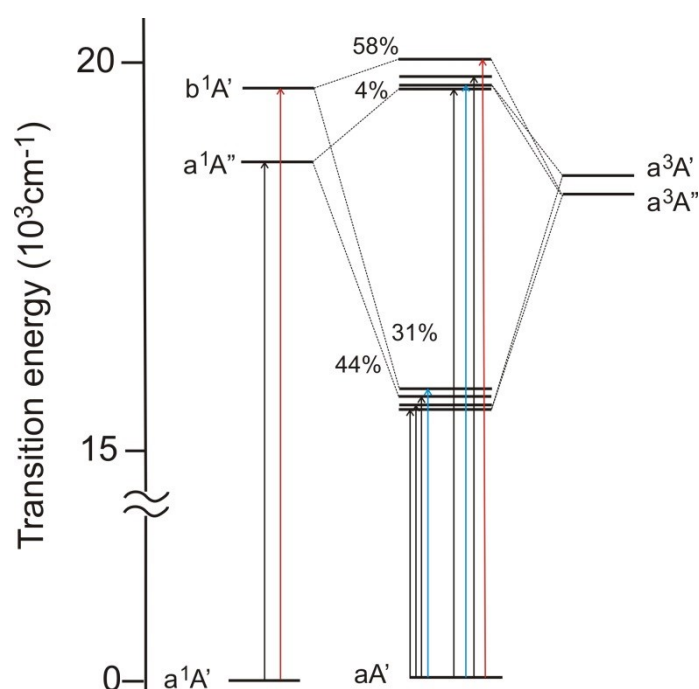


**Figure 3.8.** The correlation of the low-lying TD-DFT spin-free singlet (left column) and triplet (right column) states with the resulting spin-orbit states (in the middle) of [ReI(CO)<sub>3</sub>(bpy)] in toluene. The main spin-free contributions to a particular spin-orbit state are depicted by thin lines. Red, blue and black arrows indicate transitions with oscillator strengths larger than 0.01, 0.001–0.01 and 0.0005–0.001, respectively. Calculated by means of SO-TD-DFT (PBE0, COSMO/toluene). (adopted from Reference [27])

Figures 3.8 and 3.9 illustrate how the spin-free singlet and triplet states of  $[\text{ReI}(\text{CO})_3(\text{bpy})]$  interact via spin-orbit coupling in TD-DFT/toluene and MS-CASPT2/vacuum, respectively. These correlation diagrams show how the lowest-lying spin-free states are mixed together to form the spin-orbit states. The TD-DFT and MS-CASPT2 correlation diagrams are qualitatively comparable. The resulting SO states are clustered in two groups, separated roughly by  $\sim 4000\text{ cm}^{-1}$  (SO-TD-DFT) and  $\sim 3000\text{ cm}^{-1}$  (SO-MS-CASPT2) in energy from each other, with a high density of states inside each group. The parentage of the lowest SO states is indicated by black thin lines connecting a particular SF and SO state with a given percentage. Usually, SO-TD-DFT predicts seven SO states between the optically populated ES ( $\sim b^1A'$ ) and the GS of  $[\text{ReX}(\text{CO})_3(\text{bpy})]$ , compared to only three SF states (e.g. cf. Table 3.8 and Table 3.12). SO-MS-CASPT2 provides the same or similar results for the three complexes – e.g. see Tables 3.5 and 3.11 for  $[\text{ReI}(\text{CO})_3(\text{bpy})]$ . This is documented also in Figures 3.8 and 3.9 – we can count 7 SO states below the 8-th SO state originating predominantly from the spectroscopically allowed  $b^1A'$  state in both methods.

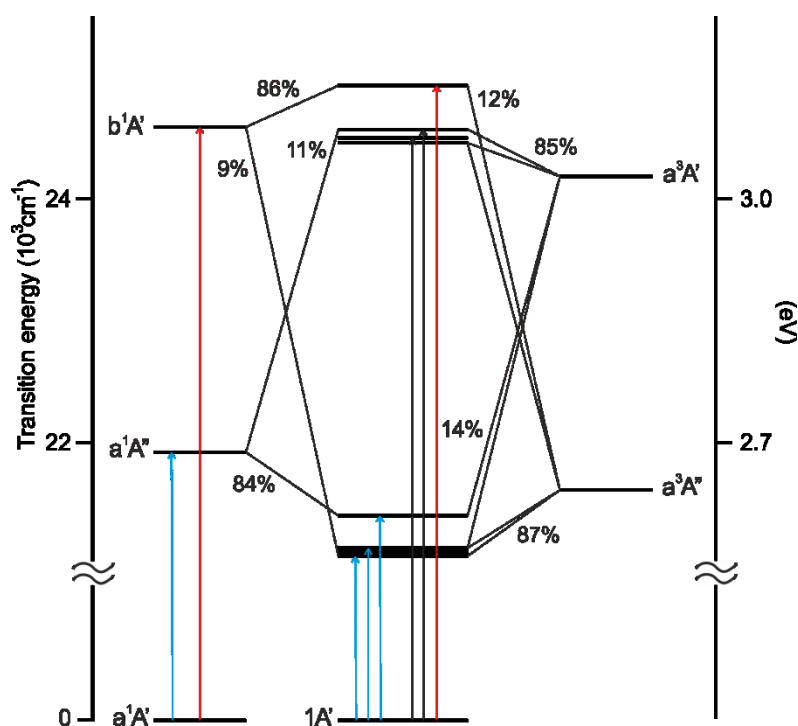


**Figure 3.9.** The correlation of the low-lying MS-CASPT2 spin-free singlet (left column) and triplet (right column) states with the resulting spin-orbit states (in the middle) of  $[\text{ReI}(\text{CO})_3(\text{bpy})]$  in vacuo. The main spin-free contributions to a particular spin-orbit state are depicted by thin lines. Red, blue and black arrows indicate transitions with oscillator strengths larger than 0.01, 0.001–0.01 and 0.0005–0.001, respectively. Calculated by means of SO-MS-CASPT2.

Due to a formation of spin-orbit states by mixing together spin-free singlet and triplet states we can observe that originally spin-forbidden “singlet-to-triplet” transitions become allowed. Already a small admixture of a spectroscopically strongly allowed spin-free singlet excited state into a spin-orbit state with a prevailing spin-free triplet origin is sufficient for getting a non-zero oscillator strength of a transition to that state. For example, in case of SO-



MS-CASPT2 the SO 2A' state is composed of 79%  $a^3A''$  and 18%  $b^1A'$  ( $f = 0.0089$ ) in the Cl complex, the SO 3A' state comprises 90%  $a^3A''$  and 7%  $b^1A'$  ( $f = 0.0062$ ) in the Br complex, and finally in the I complex the SO 2A' state is formed by 87%  $a^3A''$  and 9%  $b^1A'$  ( $f = 0.0078$ ). In case of SO-TD-DFT (Table 3.12, dichloromethane) it corresponds to the SO cA' state (90%  $a^3A''$  and 7%  $b^1A'$ ,  $f = 0.0039$ ) in the Cl complex, to the cA' state (84%  $a^3A''$  and 14%  $b^1A'$ ,  $f = 0.0059$ ) in the Br complex, and to the eA' state (30%  $a^3A''$  and 58%  $b^1A'$ ,  $f = 0.0134$ ). Singlet admixtures contribute to transition dipole moments for the transition from the singlet GS and they also make emission processes allowed. As it would be expected (since the SOC constant of the halide ligand increases with an increasing atomic number), the mixing of spin-free singlet and triplet states increases in a row  $Cl < Br < I$  for SO-TD-DFT and the transition becomes more intense (see the oscillator strengths in the brackets).

Now the SO-MS-CASPT2 absorption spectra will be described. The transition energies calculated in vacuo by this approach are overestimated by about  $1000\text{ cm}^{-1}$  when compared to the experimental values. The lowest-energy band in the  $[ReCl(CO)_3(bpy)]$  spectrum ranges from  $23\,600\text{ cm}^{-1}$  (424 nm) to  $26\,640\text{ cm}^{-1}$  (375 nm) including several weakly absorbing MLCT states. The band reaches its maximum computed at  $26\,060\text{ cm}^{-1}$  (384 nm) ( $f = 0.0378$ ), which is attributed to the 4A' state (79%  $b^1A'$  and 20%  $a^3A''$ ). In line with the experimental spectra (Table 3.2, Figure 3.5), the position of this band is moved to lower energies in the series  $Cl > Br > I$ . In the bromo complex, the maximum of the band is calculated at  $25\,710\text{ cm}^{-1}$  (389 nm) corresponding to the 5A' state (86%  $b^1A'$  and 9%  $a^3A''$ ,  $f = 0.0682$ ). In the I substituted complex, this band occurs in the region between  $21\,085\text{ cm}^{-1}$  (474 nm) and  $27\,800\text{ cm}^{-1}$  (360 nm) involving several states (predominantly of the XLCT character with MLCT contributions) with the maximum at  $24\,930\text{ cm}^{-1}$  (401 nm), which is assigned to the 5A' state (86%  $b^1A'$  and 12%  $a^3A''$ ,  $f = 0.0817$ ).

Moving to the higher-energy part of the absorption spectrum, the next band starts at  $32\,900\text{ cm}^{-1}$  (304 nm) with the maximum at  $33\,595\text{ cm}^{-1}$  (298 nm) belonging to the 14A' state (79%  $e^1A'$  and 17%  $d^3A''$ ,  $f = 0.0112$ ) in the Cl complex. In the Br complex, this feature is shifted to lower energies with the maximum calculated at  $32\,905\text{ cm}^{-1}$  (304 nm) corresponding to the 13A' state (86%  $d^1A'$  and 14%  $c^3A''$ ,  $f = 0.0153$ ). As expected, in the iodo complex the band is even more red-shifted beginning at  $29\,530\text{ cm}^{-1}$  (339 nm) with the maximum at  $31\,350\text{ cm}^{-1}$  (319 nm) (the 15A' state: 53%  $d^1A'$  and 42%  $d^3A''$ ,  $f = 0.0121$ ). The highest-energy band around 235–245 nm as seen in the experimental spectra (Figure 3.5) is not covered by the SO-MS-CASPT2 method due to the low number of calculated roots. Two strong transitions in the middle UV region at the end of the theoretical spectrum of  $[ReCl(CO)_3(bpy)]$  calculated at  $35\,700\text{ cm}^{-1}$  (280 nm) and  $36\,550\text{ cm}^{-1}$  (274 nm) are attributed to the 15A'' state (76%  $c^1A''$  and 19%  $d^3A'$ ,  $f = 0.0323$ ) and 16A'' state (94%  $d^1A''$  and 4%  $d^3A'$ ,  $f = 0.3039$ ), respectively. Both have a MLCT–IL character.

Next we move on to the analysis of the SO-TD-DFT spectra and subsequently to the comparative assessment of the results from both theoretical methods. Based on the values in Table 3.12 the theoretical spectra of all the three complexes in dichloromethane were simulated – they are depicted in Figure 3.10.

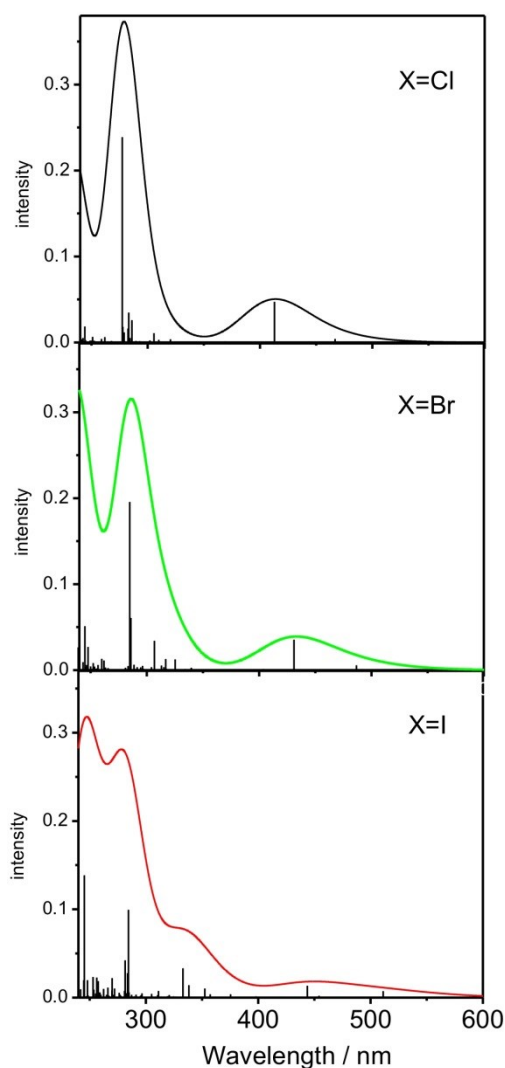


**Figure 3.10.** The theoretical UV-vis absorption spectra of  $[\text{ReX}(\text{CO})_3(\text{bpy})]$  calculated by means of SO-TD-DFT (COSMO/ $\text{CH}_2\text{Cl}_2$ ) (fwhm =  $4000\text{ cm}^{-1}$ ). (adopted from Reference [27])

As predicted by Figure 3.10, the SO-TD-DFT intensities of the lowest-energy absorption band (i.e. the oscillator strengths corresponding to the strongest transition of this band, namely to the SO  $eA'$  state in all the three complexes) follow a decreasing trend observed also experimentally (Figure 3.5) in the order Cl (88%  $b^1A'$  and 8%  $a^3A''$ ,  $f = 0.0472$ ) > Br (81%  $b^1A'$  and 14%  $a^3A''$ ,  $f = 0.0356$ ) > I (58%  $b^1A'$  and 30%  $a^3A''$ ,  $f = 0.0134$ ). This goes hand in hand with the fact that the amount of spin-free singlet  $b^1A'$  admixture decreases considerably when going from Cl to I and in consequence the oscillator strength is smaller for the I complex than for the Cl complex. In other words, the spin-mixing in this optically predominantly populated SO state is stronger with the increasing SOC constant of the halide ligand, as expected. The same assumption of the increasing SO interaction in the direction from Cl to I in connection with the increasing halide SOC constant was already predicted, based on the previous spin-free TD-DFT calculations,<sup>28</sup> which also found the relationship between increasing SOC and rising electron contribution of  $p_\pi(X)$  in the transition. On the

other hand, the SO-MS-CASPT2 calculated transitions to the lowest-energy absorption band maximum, contrary to the experiment, even become more intense on changing the halide from Cl to I: Cl (4A', 79% b<sup>1</sup>A' and 20% a<sup>3</sup>A",  $f = 0.0378$ ) < Br (5A', 86% b<sup>1</sup>A' and 9% a<sup>3</sup>A",  $f = 0.0682$ ) < I (5A', 86% b<sup>1</sup>A' and 12% a<sup>3</sup>A",  $f = 0.0817$ ). As seen in Tables 3.9, 3.10 and 3.11, the spin-mixing is quite similar for the low-lying states in all the three complexes. The larger singlet percentage for the I complex than for the Cl complex explains why the iodo complex has the larger oscillator strength for this excitation. This contradiction between SO-MS-CASPT2 and SO-TD-DFT (together with the experiment) can be to a large extent ascribed to some deficiencies of the MS-CASPT2 approach involving limitations given by the choice of the active space, a limited number of excited states included in a calculation and by neglecting solvent effects. The other important issue regards the difference between two methods consisting in the larger MLCT–XLCT mixing in case of TD-DFT which strengthens the effect of a halide ligand on the SO interaction.<sup>1,36,37</sup>

Since the highest experimental resolution was achieved in toluene (Figure 3.7), the comparison in the lowest-energy part of the spectra is performed for this solvent. The corresponding low-lying transitions and oscillator strengths for all the three complexes calculated in toluene by means of SO-TD-DFT can be found in Table S3 of Supplementary Information in Reference [27].

As already mentioned, the occurrence of two shoulders in the lowest-energy part of the experimental spectra (see the high-resolved spectrum of [ReI(CO)<sub>3</sub>(bpy)] in toluene in Figure 3.7) cannot be clarified by the calculated spin-free spectrum, whereas the theoretical spin–orbit spectrum is able to explain the origin of these weak bands. According to Table 3.11 providing the SO-MS-CASPT2 results for [ReI(CO)<sub>3</sub>(bpy)], these shoulders are attributed to the low-lying SO 2A" (467 nm), and almost degenerate 2A' and 3A' (474 nm) states. The 2A" state has a prevalent singlet a<sup>1</sup>A" character, while the 2A' and 3A' states are formed mainly by spin-free triplet states. However, they contain a small singlet participation of the b<sup>1</sup>A' state (9% and 2%, respectively – due to a value lower than 5% not shown in Table 3.11), through which the transitions become allowed. The SO-TD-DFT calculations bring qualitatively similar conclusions, also giving an explanation for the existence of the two low-energy bands. Namely, these are assigned to excitations to the SO bA" and cA' states with oscillator strengths  $f = 0.0003$  and  $f = 0.0061$ , respectively (see Table S3, Supplementary Information – Reference [27]). In the spin-free calculations the transitions to the a<sup>1</sup>A", a<sup>3</sup>A' and a<sup>3</sup>A" states, which are the main components of these spin–orbit states, are either forbidden or the oscillator strength is very small in case of the a<sup>1</sup>A" state.

Choosing [ReI(CO)<sub>3</sub>(bpy)] as an example, Figure 3.11 offers a comparison not only of the SO-TD-DFT and SO-MS-CASPT2 approaches, but also relates spin-free and spin–orbit transitions within a particular method, thus demonstrating the SO influence. The inclusion of SOC leads to several typical changes in a spectrum. We can notice a larger span of spin–orbit energies between the lowest excited and the highest calculated state, in contrast to the spin-free calculation. In addition, energies of the lowest-lying transitions in the SO framework are shifted to lower wavenumbers. Comparing the top and bottom pictures, we can clearly see that the difference between SF and SO excitations is significantly greater in case of the TD-DFT technique. Here the energy range is more broadened than in the MS-CASPT2 figure and also magnitudes of oscillator strengths become more equal, which matches better with the

experimentally observed shoulders and large widths of bands. The other effect of SOC and contrast with the spin-free spectrum can be found in overall lowering of peak intensities, which is again more pronounced in TD-DFT. This is compensated by an increased number of allowed transitions (with small, but non-zero oscillator strengths) due to a formation of spin-mixed states – the high density of close-lying states is well described by both methods.

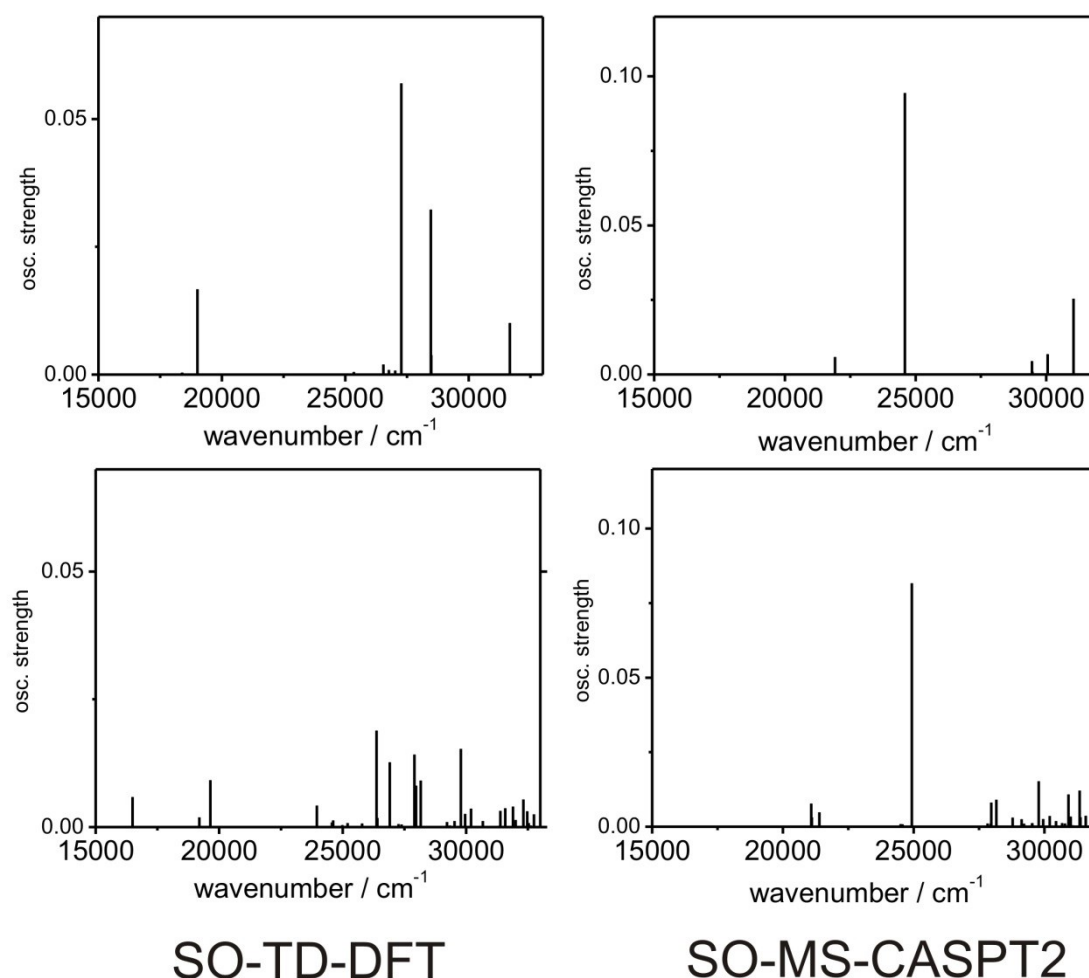


**Figure 3.11.** The comparison of calculated low-lying spin-free (top) and spin-orbit (bottom) transitions of  $[\text{ReI}(\text{CO})_3(\text{bpy})]$  by means of TD-DFT/toluene (left) and MS-CASPT2/vacuum (right). (adopted from Reference [27])

The subsequent paragraphs will be devoted to inferences and implications for photophysics of  $[\text{ReX}(\text{CO})_3(\text{bpy})]$  following from the calculated and observed character of the optically populated and lower-lying SO excited states. After we have investigated the origin, energy and intensity of the low-lying transitions, we are ready to make an attempt to deduce a mechanism of the ultrafast excited-state dynamics in terms of nonradiative and radiative deactivation pathways and participating excited states.

Based on the previous joined theoretical (spin-free) and experimental study<sup>28</sup> on  $[\text{ReX}(\text{CO})_3(\text{bpy})]$ , it was found out that the luminescence spectrum of these complexes (measured on a fs-ps time scale) is comprised of three spectral components: (1) a broad fluorescence band from the initially optically populated singlet  $b^1\text{A}'$  state at very short times

(with decay lifetimes  $\tau_1 = 85$  fs, 128 fs, 152 fs for Cl, Br, I, respectively), (2) a phosphorescence band from a higher intermediate triplet state ( $b^3A''$ ) (with decay kinetics  $\tau_2 = 340$  fs, 470 fs, 1 180 fs for Cl, Br, I, respectively), and (3) a steady-state phosphorescence spectrum from the lowest triplet  $a^3A''$  state at longer times. Moreover, a correlation between  $\tau_1$  and the ISC times to the  $b^3A''$  and  $a^3A''$  state was revealed, as well as a correlation between  $\tau_2$  and the internal conversion between both triplet states was established. Contrary to expectations, the observed ISC rates decrease with the increasing SOC between singlet and triplet states in the order  $Cl < Br \ll I$  (given by an increase of the SOC constant of the halide ligand and the admixture of the halide character to the excited states). However, there is an evident connection of ISC rates to the vibrational frequency of the Re–X stretching mode, which indicates that the driving force of ISC is mediated by a nonadiabatic coupling. Also other recent experimental studies<sup>31,32,195</sup> suggest that the lack of correlation between SOC and ISC rates can be partly explained by the assumption that it is the structural dynamics which may influence ISC rates dramatically.

In the light of the present SO calculations, especially the high density of SO states has many consequences for the photophysics of  $[ReX(CO)_3(bpy)]$ . Due to a strong mixing of states and small energetic differences between them, more than one SO state is presumably excited under irradiation and this group of vibrationally hot states go immediately ( $\leq 10$  fs) through intramolecular vibrational reorganization (IVR), which is experimentally observed as the “instantaneous” fluorescence Stokes shift.<sup>28,31,32,196</sup> The  $\tau_2$  kinetics may correspond to decay of the SO  $bA''$  ( $2A''$ ) or  $cA'$  ( $2A'$  or  $3A'$ ) states that are populated either by optical excitation (allowed due to a singlet admixture) or by ISC from  $eA'$  ( $4A'$  or  $5A'$ ). However, these assumptions should be viewed rather as qualitative explanations – it is obvious that by using the optimized GS geometry for excited states we are not able to simulate structural and electronic changes associated with the evolution of the excited system after irradiation.

Rhenium(I) complexes  $[ReX(CO)_3(bpy)]$  have been subjected to experimental investigations of the emission lifetime temperature dependence.<sup>27,197,198</sup> In view of these findings the existence of an excited state lying above the three lowest SO states (coming from ZFS of the lowest spin-free triplet (MLCT)  $a^3A''$  state) has been predicted, whose origin remains unclear. This deactivating “fourth” state undergoes a fast nonradiative decay to the ground state, which is many times faster than for the three SO states. Our SO calculations enable to identify this state satisfactorily, provided that two conditions are fulfilled: (1) the optimized lowest spin-free triplet  $a^3A''$  state geometry can be used for all the relevant SO states, and (2) the long-lived emission arises from a set of thermally equilibrated SO states obeying Boltzmann statistics. The former assumption has to be accepted in order to perform calculations. Nevertheless, it might cause some discrepancies between theory and reality, since relaxed geometries of individual SO states can obviously differ. Table 3.13 contains transition energies and oscillator strengths of the eight lowest solvent-corrected (MeCN) SO-TD-DFT states of  $[ReX(CO)_3(bpy)]$  calculated at the equilibrium  $a^3A''$  state geometry. The same labelling of SO states is used as for the other SO-TD-DFT results. As seen from Table 3.13, the ZFS of  $[ReCl(CO)_3(bpy)]$  is computed to be 8 and 133  $cm^{-1}$ , which is in good accordance with 6 and 90  $cm^{-1}$  obtained experimentally<sup>197,198</sup> in a glass (where ZFS tends to be smaller than in solution owing to a higher  $IL(\pi\pi^*)$ –MLCT mixing). Inspecting the calculated oscillator strengths of the three lowest SO states in the complexes, we see that the

lowest one ( $aA''$ ) is not emissive at all and the third one ( $cA'$ ) emits much more than the second one ( $bA'$ ) – both observations are in agreement with the experimental data.

**Table 3.13.** The solvent-corrected (COSMO/MeCN) spin-orbit TD-DFT transition energies to the low-lying excited states and oscillator strengths  $f$  of  $[\text{ReX}(\text{CO})_3(\text{bpy})]$  calculated at the optimized  $a^3A''$  state geometry. The energy values are given in reciprocal centimetres and as wavelengths (in nm). Oscillator strengths lower than 0.00005 are omitted.  $\Delta E$  denotes the energy difference between the actual state and the lowest SO excited state ( $aA''$ ).

SO state	Contribution of the SO states in terms of SF states [%]	Character	Energy [ $\text{cm}^{-1}$ ]	$\Delta E$ [ $\text{cm}^{-1}$ ]	Wavelength [nm]	Osc. strength
<b>X = Cl</b>						
$aA''$	$a^3A''$ (89) + $a^3A'$ (9)	MLCT/XLCT	15 472	0	646	
$bA'$	$a^3A''$ (89) + $a^3A'$ (9)	MLCT/XLCT	15 480	8	646	0.0001
$cA'$	$a^3A''$ (96) + $b^1A'$ (2)	MLCT/XLCT	15 605	133	641	0.0014
$bA''$	$a^1A''$ (75) + $a^3A'$ (22)	MLCT/XLCT	16 458	986	607	0.0006
$cA''$	$a^3A'$ (86) + $a^3A''$ (12)	MLCT/XLCT	18 171	2699	550	
$dA'$	$a^3A'$ (90) + $a^3A''$ (9)	MLCT/XLCT	18 172	2700	550	
$dA''$	$a^1A''$ (24) + $a^3A'$ (76)	MLCT/XLCT	18 378	2906	544	0.0002
$eA'$	$b^1A'$ (92) + $b^3A'$ (3)	MLCT/XLCT	20 440	4968	489	0.0579
<b>X = Br</b>						
$aA''$	$a^3A''$ (84) + $a^3A'$ (14)	MLCT/XLCT	15 453	0	647	
$bA'$	$a^3A''$ (84) + $a^3A'$ (14)	MLCT/XLCT	15 460	7	647	0.0001
$cA'$	$a^3A''$ (96) + $b^1A'$ (4)	MLCT/XLCT	15 642	189	639	0.0022
$bA''$	$a^1A''$ (68) + $a^3A'$ (29)	MLCT/XLCT	16 271	818	614	0.0003
$cA''$	$a^3A'$ (84) + $a^3A''$ (15)	MLCT/XLCT	18 119	2666	552	
$dA'$	$a^3A'$ (85) + $a^3A''$ (14)	MLCT/XLCT	18 120	2667	552	
$dA''$	$a^1A''$ (30) + $a^3A'$ (69)	MLCT/XLCT	18 405	2952	543	0.0002
$eA'$	$b^1A'$ (93) + $a^3A''$ (4)	MLCT/XLCT	20 078	4625	498	0.0483
<b>X = I</b>						
$aA''$	$a^3A''$ (70) + $a^3A'$ (27)	XLCT/MLCT	15 585	0	642	
$bA'$	$a^3A''$ (70) + $a^3A'$ (28)	XLCT/MLCT	15 590	5	641	0.0001
$cA'$	$a^3A''$ (85) + $a^1A'$ (13)	XLCT/MLCT	15 914	329	628	0.0045
$bA''$	$a^3A'$ (55) + $a^1A''$ (43)	XLCT/MLCT	16 130	545	620	0.0001
$cA''$	$a^3A'$ (69) + $a^3A''$ (28)	XLCT/MLCT	18 466	2881	541	
$dA'$	$a^3A'$ (68) + $a^3A''$ (27)	XLCT/MLCT	18 478	2893	541	0.0006
$dA''$	$a^1A''$ (42) + $a^3A'$ (56)	XLCT/MLCT	18 961	3376	527	0.0001
$eA'$	$b^1A'$ (77) + $a^3A''$ (13)	XLCT/MLCT	19 765	4180	506	0.0278

Moreover, the desired “fourth” state was discovered by the SO-TD-DFT calculation. It was identified as the SO  $bA''$  state with a non-zero oscillator strength (Table 3.13). It has a MLCT/XLCT character and contains a substantial singlet contribution ( $a^1A''$ , namely 75% for the Cl, 68% for the Br and 43% for the I complex) that highly likely allows for its prompt nonradiative decay to the ground state. The decreasing singlet participation in the order  $\text{Cl} >$

Br > I is responsible for slowing down of this non-emissive process, which in turn causes the increase of room-temperature emission lifetimes when going from Cl to I for a chosen temperature value (see Table 4 and Figure 8 in Reference [27]). The revelation of the low-lying SO bA" state that offers the thermally activated quenching pathway (through its thermal population) explains why the phosphorescence decay in  $[\text{ReX}(\text{CO})_3(\text{bpy})]$  depends on temperature.

The ns-lived phosphorescence is attributed mainly to the emissive SO cA' state with the largest oscillator strength among the lowest-lying SO excited states (see Table 3.13). The corresponding transition energies are  $15\,605\text{ cm}^{-1}$  for the chloro,  $15\,642\text{ cm}^{-1}$  for the bromo and  $15\,914\text{ cm}^{-1}$  for the iodo substituted complex. These values agree satisfactorily with the experimental emission band maxima (recorded in MeCN at room temperature):  $15\,450$ ,  $15\,700$  and  $15\,800\text{ cm}^{-1}$ , respectively.<sup>198</sup>

For more details about the experimentally obtained temperature dependence of the phosphorescence decay parameters and related qualitative explanations based on the SO model we refer to our article.<sup>27</sup>

## 3.2 Rhenium tricarbonyl complex with imidazole

### 3.2.1 Introduction

This part deals with the rhenium(I) tricarbonyl-diimine complex  $[\text{Re}(\text{imH})(\text{CO})_3(\text{phen})]^+$  (imH = imidazole, phen = 1,10-phenanthroline). The schematic structure is illustrated in Figure 3.12.

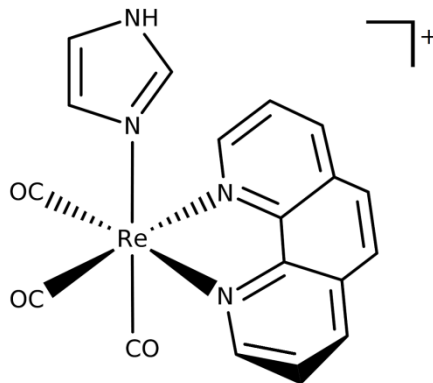


**Figure 3.12.** The molecular structure of the  $[\text{Re}(\text{imH})(\text{CO})_3(\text{phen})]^+$  complex.

In the  $[\text{Re}(\text{imH})(\text{CO})_3(\text{phen})]^+$  complex rhenium is in oxidation state (+1) – since all ligands are electroneutral, the whole molecule bears a single positive charge. The same characteristics can be applied as for the  $[\text{ReX}(\text{CO})_3(\text{bpy})]$  compounds: the complex also possesses a low-spin singlet (closed-shell) ground state, the central rhenium ion has a coordination number of 6 and the molecule takes up a shape of a pseudo-octahedral structure. Like a bipyridine in case of  $[\text{ReX}(\text{CO})_3(\text{bpy})]$ , a phenanthroline ligand acts as an electron-acceptor and participates in low-energy MLCT ( $d \rightarrow \pi^*$ ) or IL ( $\pi\pi^*$ ) transitions.

The motivation to investigate  $[\text{Re}(\text{imH})(\text{CO})_3(\text{phen})]^+$  is based to a large extent on the same reasons as in the  $[\text{ReX}(\text{CO})_3(\text{bpy})]$  case and the reader is referred to the relevant sections in the first project (Chapter 3.1.1).  $[\text{Re}(\text{imH})(\text{CO})_3(\text{phen})]^+$  has been chosen, since it embodies the main essence of the above mentioned class of  $\text{Re}^{\text{I}}$  tricarbonyl-diimine complexes.<sup>21,30,40</sup> Indeed, it is one of the key and well-studied representative<sup>95</sup> of this family – for instance, it is known for its usage in electron-transfer reactions and relaxation dynamics in Re-labelled proteins as a photosensitizer and phototrigger.<sup>19,20,199–202</sup> In addition, there are available experimental data<sup>26</sup> emerging from fluorescence up-conversion, transient absorption and picosecond TRIR spectroscopy, which are accompanied by spin-free (TD-)DFT calculations.<sup>26</sup>

The results in this section have been summarized in Reference [92], being attached at the end of the thesis. This review publication compiles various relativistic and spectroscopic features of heavy-metal complexes and presents them within SOC conceptual framework.

Very recently (summer 2016), this system was reinvestigated by Fumanal and our co-worker Professor Daniel<sup>203</sup> by employing the same two methods (SO-TD-DFT and SO-MS-CASPT2). Regarding the wave function approach, a higher and better optimized version of the Molcas software with corrected ANO-RCC basis sets has been available, which enables to incorporate solvent effects and improve our results.



### 3.2.2 Computational details

The GS geometry was optimized by DFT/PBE0<sup>179,180</sup> in Gaussian.<sup>105</sup> For the purpose of studying photophysical characteristics, also the geometry optimization of the lowest triplet state  $a^3A''$  (by means of UKS-DFT) and the lowest excited spin-free singlet state  $b^1A'$  (by TD-DFT) was carried out. The deviations of chosen bond lengths between the optimized structures of  $b^1A'$  and  $a^3A''$  states and the ground state can be found in Table A1 in Appendix A of Reference [92]. The polarizable conductor calculation model<sup>184</sup> (PCM) for dimethylformamide (DMF) was utilized for including solvent effects. Polarized triple- $\zeta$  basis sets 6-311g(d)<sup>204,205</sup> were used for first and second row atoms (H, C, N, O) and quasirelativistic ECPs and corresponding optimized set of basis functions were taken for Re.<sup>69,206</sup>  $[\text{Re}(\text{imH})(\text{CO})_3(\text{phen})]^+$  possesses the  $C_s$  symmetry, which was preserved in all calculations.<sup>92</sup>

As in the first project, two distinct methods were employed: SO-MS-CASPT2 by means of the Molcas<sup>82–84</sup> software and SO-TD-DFT using the ADF<sup>87–89</sup> program.

Regarding the CASSCF/MS-CASPT2 approach, the generating of input orbitals was done by means of KS-DFT/B3LYP.<sup>181</sup> The SA-CASSCF calculations included together 20 electronic spin-free states: the singlet ground state, five lowest singlet and five lowest triplet excited states in the first symmetrical representation  $a'$ , and four lowest singlet and five lowest triplet excited states in the second symmetrical representation  $a''$ . The ANO-RCC basis sets<sup>73,74</sup> were used for all the atoms. For Re the basis with a triple- $\zeta$  contraction scheme and for the other atoms a double- $\zeta$  contraction scheme were used, as seen from Table 3.14.

**Table 3.14.** The contraction schemes for ANO-RCC basis sets used for  $[\text{Re}(\text{imH})(\text{CO})_3(\text{phen})]^+$ .

Atom	Contraction scheme	Contracted to
Re	(24s, 21p, 15d, 11f, 4g, 2h)	(7s, 6p, 4d, 2f, 1g)
C, N, O	(14s, 9p, 4d, 3f, 2g)	(3s, 2p, 1d)
H	(8s, 4p, 3d, 1f)	(2s, 1p)

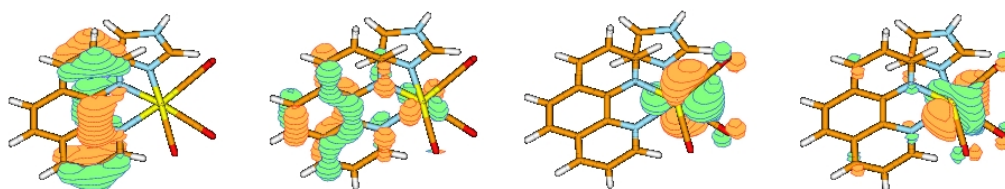
The active space was built with 18 electrons distributed in 14 active orbitals (i.e. CASSCF(18,14)), including HOMO-3, HOMO-2, HOMO-1, HOMO, LUMO, LUMO+1, LUMO+2 in the  $a'$  symmetry and HOMO-4, HOMO-3, HOMO-2, HOMO-1, HOMO, LUMO, LUMO+1 in the  $a''$  symmetry. The composition of the active space is depicted in Figure 3.13. The Cholesky decomposition<sup>182</sup> of a two-electron integral matrix was employed. A value 0.15 a.u. of level shift correction was applied in CASPT2 to avoid intruder state problems. The SO-MS-CASPT2 calculations were performed in vacuo.

In the TD-DFT calculations, STO basis sets (triple- $\zeta$  type with two polarization functions for Re and double- $\zeta$  type with one polarization function for the other atoms – core electrons were included) and the PBE0 hybrid functional<sup>179,180</sup> were used. The scalar relativistic effects were introduced by SR ZORA.<sup>65,71</sup> The double-group symmetry spin-orbit  $A'$  and  $A''$  excited states were determined by means of the approximate (perturbative) SO-TD-DFT approach.<sup>86</sup> For testing purposes, a few lowest spin-orbit excited states were calculated also by the

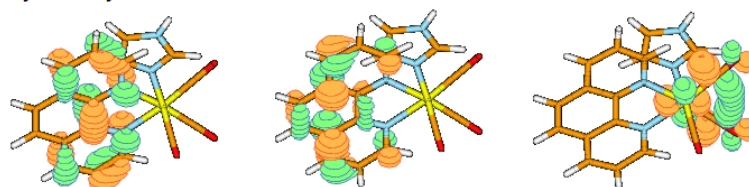
advanced SOC technique – the relativistic two-component ZORA.<sup>85</sup> Nevertheless, only the perturbative approach was followed, because the results from both methods did not differ much from each other. Solvent corrections were taken into account by employing the COSMO<sup>183</sup> model (for DMF).

Unless otherwise stated, the other computational details remain the same as for the first project.

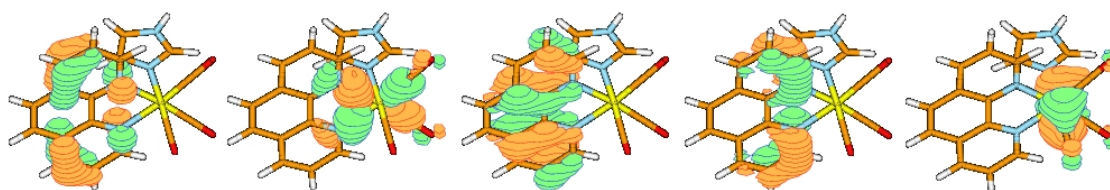
Occupied, a' symmetry:



Virtual, a' symmetry:



Occupied, a'' symmetry:



Virtual, a'' symmetry:

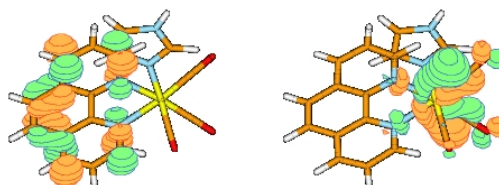


**Figure 3.13.** The frontier occupied and virtual molecular orbitals included in the active space at the CASSCF stage of the calculation of  $[\text{Re}(\text{imH})(\text{CO})_3(\text{phen})]^+$ .

### 3.2.3 Results and discussion

To be consistent with the first project, the following text will be organized in a similar manner. In the beginning, the relevant experimental data are briefly presented in order to outline what our calculations were focused on. Then we start with the spin-free description and we continue with the spin-orbit model with the aim to interpret available photophysical observations in a more accurate way. The section will be concluded with a summary of the common photophysical trends manifested in the extended family of  $\text{Re}^{\text{I}}$  tricarbonyl complexes  $[\text{Re}(\text{L})(\text{CO})_3(\alpha\text{-diimine})]^n$ . Naturally, since the complexes discussed in the first project belong to this class as well, the same or similar rules and principles retain valid also for them.

The experimental UV–vis absorption spectrum of  $[\text{Re}(\text{imH})(\text{CO})_3(\text{phen})]^+$  recorded in DMF can be found in Reference [26]. This broad spectrum exhibits a strongly absorbing region between 200–300 nm and two distinct shoulders at approximately 328 and 362 nm.

Time-resolved fluorescence spectra<sup>26</sup> were measured by the broadband femtosecond fluorescence up-conversion technique – after excitation by 400 nm laser pulses a very broad emission (fluorescence) band at ~530–540 nm emerges almost immediately (<30 fs). The fluorescence decay kinetics seems to be biexponential – it simultaneously populates two states with a ~144 fs lifetime:<sup>26</sup> (1) an intermediate one characterized by a weak broad emission (phosphorescence at ~580 nm), and (2) the lowest excited state that produces a broad emission (phosphorescence at ~590 nm). These phosphorescent states decay with a 1.5 ps<sup>26</sup> and a 120 ns lifetime,<sup>95</sup> respectively. By TRIR spectroscopy<sup>26</sup> the “major” (with a prevailing MLCT character) and “minor” (MLCT–IL character) low-lying long-lived excited states are detected for  $[\text{ReCl}(\text{CO})_3(\text{N}^{\wedge}\text{N})]$ . It appears that both of these states are populated right after optical excitation with a ratio 4:1 (for (phen)), reaching a thermal equilibrium after a few picosecond-long relaxation period. Based on time-resolved UV–vis spectroscopy<sup>26</sup> several other ps decay lifetimes of relaxation processes are evaluated. Since  $\text{Re}^{\text{I}}$  carbonyl-diimine complexes exhibit generally the temperature dependence of emission decay from the lowest excited state(s),<sup>27,169,207</sup> it can be expected that  $[\text{Re}(\text{imH})(\text{CO})_3(\text{phen})]^+$  would also possess this feature.

Table 3.15 lists the spin-free MS-CASPT2 transition energies from the GS  $a^1A'$  to the low-lying pure singlet and triplet excited states and the associated oscillator strengths  $f$  of  $[\text{Re}(\text{imH})(\text{CO})_3(\text{phen})]^+$  in vacuo. The spin-free TD-DFT results calculated in DMF are presented in Table 3.16. The excited-state labelling is the same as described in the first project. The character of a particular state in terms of the main corresponding excitation(s) is given in the second and third columns in both Tables. Singlet–triplet transitions have zero oscillator strengths in line with the spin selection rule.

From the previous spin-free DFT and TD-DFT calculations<sup>26</sup> several important findings can be drawn about  $[\text{Re}(\text{imH})(\text{CO})_3(\text{phen})]^+$  and generally about  $[\text{Re}(\text{L})(\text{CO})_3(\text{N}^{\wedge}\text{N})]^n$  complexes. They were confirmed by our spin-free TD-DFT calculations (employing a different solvent model and basis set) and a reasonable qualitative agreement was achieved with spin-free MS-CASPT2. (1) The lowest theoretically spin-allowed  $a^1A' \rightarrow a^1A'$  MLCT/LLCT transition displays very low intensity due to an unfavourable orbital overlap (documented by the calculated oscillator strength  $f = 0.0044$  via spin-free MS-CASPT2 (Table 3.15) and  $f = 0.0012$  via spin-free TD-DFT (Table 3.16)). (2) The experimental lowest-energy absorption band (lying approximately around 360 nm depending on actual ligands and solvent) can be attributed to the two lowest allowed transitions, namely  $a^1A' \rightarrow b^1A'$  and  $a^1A' \rightarrow d^1A'$ . Their oscillator strengths are  $f = 0.0432$  and  $0.0362$  (spin-free MS-CASPT2), and  $f = 0.0343$  and  $0.0839$  (spin-free TD-DFT), respectively. The characters were calculated to be MLCT/LLCT ( $\pi^*(\text{CO}) \rightarrow \pi^*(\text{phen})$ ) (according to both MS-CASPT2 and TD-DFT) and  $\text{Re}(\text{CO})_3 \rightarrow \text{N}^{\wedge}\text{N}$  MLCT with a small LLCT ( $\text{imH} \rightarrow \pi^*(\text{phen})$ ) contribution according to Reference [26]. In MS-CASPT2, the transition to the  $c^1A'$  state is the most allowed ( $f = 0.051$ ), in contrast to TD-DFT, where it has an insignificant oscillator strength. (3) Higher-lying  $^1\text{IL}$  ( $\pi\pi^*(\text{phen})$ ) transitions are responsible for intense UV bands

(around 270–280 nm in case of phen), e.g. see the  $f^1A'$  state (MS-CASPT2) or the  $h^1A'$  and  $i^1A''$  states (TD-DFT).

**Table 3.15.** The spin-free MS-CASPT2 transition energies and oscillator strengths  $f$  of  $[Re(imH)(CO_3(phen))]^+$  calculated in vacuo. The energy values are given in eV, reciprocal centimetres and as wavelengths (in nm).

State	Dominant excitation	Character	Energy [eV]	Energy [ $cm^{-1}$ ]	Wavelength [nm]	Osc. strength
<b>Singlets</b>						
$a^1A''$	$d_{Re}, \pi^*_{CO} \rightarrow \pi^*_{phen}$ (87%)	MLCT/LLCT	3.377	27237	367	0.0044
$b^1A'$	$d_{Re}, \pi^*_{CO}, \pi_{phen} \rightarrow \pi^*_{phen}$ (81%)	MLCT/LLCT(IL)	3.583	28899	346	0.0432
$c^1A'$	$d_{Re}, \pi^*_{CO} \rightarrow \pi^*_{phen}$ (83%)	MLCT/LLCT	3.723	30028	333	0.0510
$d^1A'$	$d_{Re}, \pi^*_{CO} \rightarrow \pi^*_{phen}$ (75%)	MLCT/LLCT	3.876	31262	320	0.0362
$b^1A''$	$d_{Re}, \pi^*_{CO} \rightarrow \pi^*_{phen}$ (40%); $d_{Re}, \pi^*_{CO} \rightarrow \pi^*_{phen}$ (45%)	MLCT/LLCT	4.105	33109	302	0.0144
$e^1A'$	$d_{Re} \rightarrow d_{Re}, CO$ (84%)	MC/MLCT(CO)	4.145	33432	299	0.0234
$c^1A''$	$d_{Re}, \pi^*_{CO} \rightarrow \pi^*_{phen}$ (45%); $d_{Re}, \pi^*_{CO} \rightarrow \pi^*_{phen}$ (41%)	MLCT/LLCT	4.289	34593	289	0.0053
$f^1A'$	$\pi_{phen}, d_{Re} \rightarrow \pi^*_{phen}$ (49%); $\pi_{phen} \rightarrow \pi^*_{phen}$ (24%)	MLCT–IL	4.505	36335	275	0.0599
$d^1A''$	$d_{Re}, \pi^*_{CO} \rightarrow \pi^*_{phen}$ (83%)	MLCT/LLCT	4.844	39069	256	0.0026
<b>Triplets</b>						
$a^3A''$	$\pi_{phen}, d_{Re} \rightarrow \pi^*_{phen}$ (67%)	IL/MLCT	3.223	25995	385	-
$a^3A'$	$d_{Re}, \pi^*_{CO} \rightarrow \pi^*_{phen}$ (53%); $d_{Re}, \pi^*_{CO} \rightarrow \pi^*_{phen}$ (18%)	MLCT/LLCT	3.347	26995	370	-
$b^3A''$	$d_{Re}, \pi^*_{CO}, \pi_{phen} \rightarrow \pi^*_{phen}$ (80%)	MLCT(IL/LLCT)	3.842	30988	323	-
$b^3A'$	$d_{Re}, \pi^*_{CO} \rightarrow \pi^*_{phen}$ (67%)	MLCT/LLCT	4.009	32335	309	-
$c^3A''$	$d_{Re}, CO \rightarrow d_{Re}, CO$ (41%); $d_{Re} \rightarrow d_{Re}, CO$ (34%)	MC/MLCT(CO)	4.023	32448	308	-
$c^3A'$	$d_{Re}, \pi^*_{CO} \rightarrow \pi^*_{phen}$ (54%); $d_{Re}, \pi^*_{CO} \rightarrow \pi^*_{phen}$ (23%)	MLCT/LLCT	4.060	32746	305	-
$d^3A''$	$d_{Re}, CO \rightarrow d_{Re}, CO$ (47%); $d_{Re} \rightarrow d_{Re}, CO$ (28%)	MC/MLCT(CO)	4.313	34787	288	-
$d^3A'$	$\pi_{phen}, d_{Re} \rightarrow \pi^*_{phen}$ (64%)	IL(/MLCT)	4.313	34787	288	-
$e^3A'$	$\pi_{phen} \rightarrow \pi^*_{phen}$ (54%)	IL	4.440	35811	279	-
$e^3A''$	$d_{Re} \rightarrow \pi^*_{phen}$ (41%); $\pi_{phen} \rightarrow \pi^*_{phen}$ (14%); $\pi_{phen}, d_{Re} \rightarrow \pi^*_{phen}$ (11%)	MLCT–IL	4.873	39303	254	-

**Table 3.16.** The spin-free lowest TD-DFT transition energies and oscillator strengths  $f$  of  $[\text{Re}(\text{imH})(\text{CO}_3(\text{phen}))]^+$  calculated in DMF (COSMO). The energy values are given in eV, reciprocal centimetres and as wavelengths (in nm). Only singlet transitions with oscillator strengths greater than 0.002 are shown (with the exception of the lowest  $a^1A''$  state).

State	Dominant excitation	Character	Energy [eV]	Energy [ $\text{cm}^{-1}$ ]	Wavelength [nm]	Osc. strength
<b>Singlets</b>						
$a^1A''$	$d_{\text{Re}}, \pi^*_{\text{CO}} \rightarrow \pi^*_{\text{phen}}$ (98%)	MLCT/LLCT	3.085	24879	402	0.0012
$b^1A'$	$d_{\text{Re}}, \pi^*_{\text{CO}}, \pi_{\text{phen}} \rightarrow \pi^*_{\text{phen}}$ (93%)	MLCT/LLCT	3.412	27521	363	0.0343
$d^1A'$	$d_{\text{Re}}, \pi^*_{\text{CO}}, \pi_{\text{phen}} \rightarrow \pi^*_{\text{phen}}$ (76%)	MLCT/LLCT	3.581	28885	346	0.0839
$b^1A''$	$d_{\text{Re}}, \pi^*_{\text{CO}}, \pi_{\text{phen}} \rightarrow \pi^*_{\text{phen}}$ (91%)	MLCT/LLCT	3.802	30663	326	0.0178
$g^1A'$	$\pi_{\text{imH}} \rightarrow \pi^*_{\text{phen}}$ (96%)	LLCT	4.457	35950	278	0.0241
$h^1A''$	$d_{\text{Re}}, \pi^*_{\text{CO}}, \pi_{\text{phen}} \rightarrow \pi^*_{\text{phen}}$ (61%)	MLCT/LLCT	4.739	38222	262	0.0666
$h^1A'$	$\pi_{\text{phen}} \rightarrow \pi^*_{\text{phen}}$ (80%)	IL	4.751	38316	261	0.0969
$i^1A''$	$\pi_{\text{phen}} \rightarrow \pi^*_{\text{phen}}$ (67%)	IL	4.921	39688	252	0.3277
<b>Triplets</b>						
$a^3A''$	$d_{\text{Re}}, \pi^*_{\text{CO}} \rightarrow \pi^*_{\text{phen}}$ (53%)	MLCT/LLCT	2.818	22728	440	-
$a^3A'$	$d_{\text{Re}}, \pi^*_{\text{CO}}, \pi_{\text{phen}} \rightarrow \pi^*_{\text{phen}}$ (78%)	MLCT/LLCT	3.013	24304	411	-
$b^3A''$	$d_{\text{Re}}, \pi^*_{\text{CO}}, \pi_{\text{phen}} \rightarrow \pi^*_{\text{phen}}$ (67%)	MLCT/LLCT	3.133	25271	396	-
$b^3A'$	$d_{\text{Re}}, \pi^*_{\text{CO}}, \pi_{\text{phen}} \rightarrow \pi^*_{\text{phen}}$ (51%)	MLCT/LLCT	3.430	27665	361	-
$c^3A'$	$d_{\text{Re}}, \pi^*_{\text{CO}}, \pi_{\text{phen}} \rightarrow \pi^*_{\text{phen}}$ (58%)	MLCT/LLCT	3.464	27940	358	-
$c^3A''$	$d_{\text{Re}}, \pi^*_{\text{CO}}, \pi_{\text{phen}} \rightarrow \pi^*_{\text{phen}}$ (80%)	MLCT/LLCT	3.588	28938	345	-

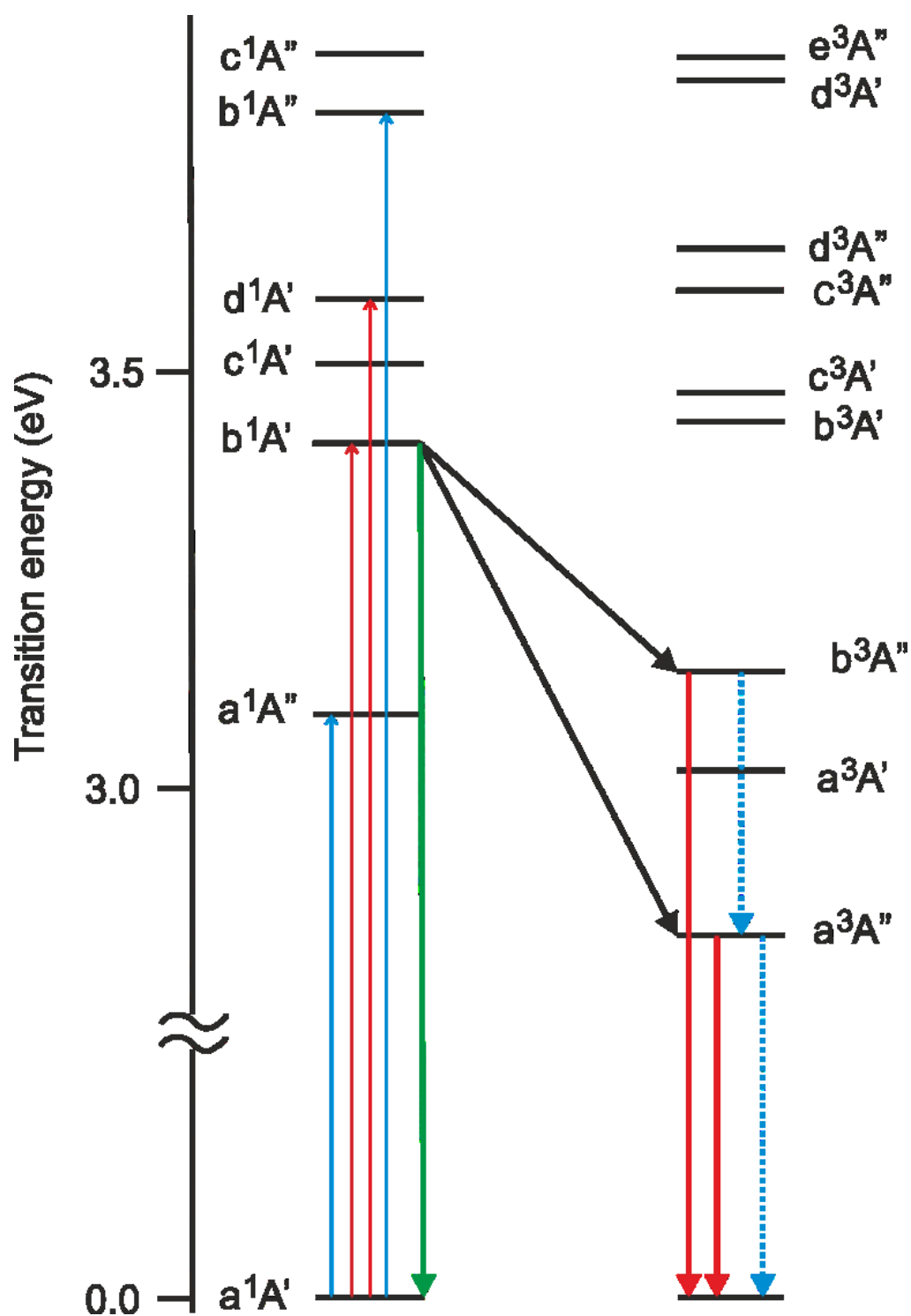


**Figure 3.14.** The spin-free model of  $[\text{Re}(\text{imH})(\text{CO})_3(\text{phen})]^+$ . Green arrow = fluorescence, black arrow = ISC, red arrow = phosphorescence, blue dotted arrow = nonradiative decay. Vibrational relaxation is not depicted. Calculated by means of spin-free TD-DFT (PBE0, COSMO/DMF). For more information see the text. (adopted from Reference [92] and modified)

On the basis of spin-free TD-DFT calculations, the straightforward and relatively simple spin-free concept was established to interpret the available experiment, schematically shown in Figure 3.14. It captures the fundamental photophysical features and explains them in a similar way as the previously proposed spin-free models of other  $\text{Re}^{\text{I}}$  carbonyl-diimine complexes.<sup>26,28,29,40</sup> It assumes that optical excitation populates the lowest spectroscopically allowed (i.e. singlet)  $\text{b}^1\text{A}'$  MLCT state, which gives rise to “instantaneous” fluorescence Stokes shift (depicted by a green arrow in Figure 3.14). The fluorescence is a consequence of ultrafast intramolecular vibrational reorganization and its decay lifetime ( $\sim 150$  fs) corresponds to ISC (black arrows) to the low-lying  $\text{a}^3\text{A}''$  MLCT state and to an intermediate triplet state (lying energetically higher than the  $\text{a}^3\text{A}''$  state), identified as the  $\text{b}^3\text{A}''$  state. Both triplet states undergo phosphorescence (red arrows) – in case of the  $\text{a}^3\text{A}''$  state it is long-lived phosphorescence with a 120 ns decay lifetime. At the same time these two states decay also nonradiatively (blue dotted arrows) – the  $\text{b}^3\text{A}''$  state decays very fast to the  $\text{a}^3\text{A}''$  state and this lowest excited state completes the hypothetical cycle by decaying to the ground state. Vibrational and solvational relaxations participate in this nonradiative energy dissipation and redistribution.

It ought to be emphasized that even the spin-free model would not have been able to cover the whole mechanism if it had not included some of SO-based processes, e.g. ISC or phosphorescence. The spin-free considerations serve as a good starting point to understand the photophysical behaviour in transition metal complexes, nevertheless, there are experimental observations which the spin-free model fails to explain satisfactorily. For instance, it is not capable of accounting for various measured time constants associated with relaxation processes during emission and absorption, or for the temperature-dependent emission decay. Another problem arises with the presence of “major” and “minor” triplet states which can be solved only with the help of the SO model that will be described later.

Before we move to a detailed analysis of the SO model, the principal results of our SOC calculations will be presented. The spin-orbit MS-CASPT2 transition energies from the ground state to the low-lying excited states of  $[\text{Re}(\text{imH})(\text{CO})_3(\text{phen})]^+$  calculated in vacuo and the associated oscillator strengths  $f$  are reported in Table 3.17. The same characteristics for the solvent-corrected (COSMO/DMF) SO-TD-DFT method are compiled in Table 3.18. The lowest SO excited states are characterized by their double-group symmetries and are numbered (SO-MS-CASPT2) or labelled by lower-case letters (SO-TD-DFT), separately in each of the two symmetries (the GS being  $1\text{A}'$  or  $\text{aA}'$ , respectively). The origin of a particular spin-orbit state based on spin-free singlet and triplet state contributions is shown in the second column in both Tables. In case of SO-MS-CASPT2 the prevailing character is roughly indicated in the third column. For both methods it can be stated that since already SF states are often mixed in terms of MLCT, LLCT or IL excitations, it is even more complicated to determine the character of SO states which are usually combinations of more than two different SF states.

**Table 3.17.** The spin-orbit MS-CASPT2 transition energies and oscillator strengths  $f$  of  $[\text{Re}(\text{ImH})(\text{CO})_3(\text{phen})]^+$  calculated in vacuo. The energy values are given in eV, reciprocal centimetres and as wavelengths (in nm). Oscillator strengths lower than 0.00005 are omitted.

SO state	Contribution of the SO states in terms of SF states [%]	Character	Energy [eV]	Energy [ $\text{cm}^{-1}$ ]	Wavelength [nm]	Osc. strength
1 1A''	$a^3A''$ (78) + $a^3A'$ (14) + $b^1A'$ (3) + $c^1A'$ (3)	IL/MLCT	3.166	25535	392	
2 2A'	$a^3A''$ (82) + $a^3A'$ (15) + $c^3A'$ (1)	IL/MLCT	3.179	25640	390	
3 3A'	$a^3A''$ (92) + $b^1A'$ (4) + $c^3A'$ (1)	IL/MLCT	3.190	25729	389	0.0060
4 2A''	$a^3A'$ (50) + $a^1A''$ (46) + $c^3A'$ (2) + $b^3A'$ (1)	MLCT/LLCT	3.266	26342	380	0.0019
5 3A''	$a^3A'$ (82) + $a^3A''$ (17)	MLCT/LLCT	3.370	27181	368	
6 4A''	$a^3A'$ (84) + $a^3A''$ (15)	MLCT/LLCT	3.370	27181	368	
7 4A'	$a^3A'$ (49) + $a^1A''$ (49) + $b^3A'$ (1)	MLCT/LLCT	3.428	27649	362	0.0024
8 5A'	$b^1A'$ (84) + $a^3A''$ (7) + $b^3A''$ (5)	MLCT/LLCT(IL)	3.591	28963	345	0.0437
9 6A'	$c^1A'$ (74) + $b^3A''$ (15) + $b^3A'$ (4) + $a^3A''$ (3) + $a^3A'$ (2)	MLCT/LLCT	3.709	29915	334	0.0364
10 5A''	$b^3A''$ (87) + $b^3A'$ (6) + $c^3A'$ (5)	MLCT(IL/LLCT)	3.824	30843	324	
11 6A''	$b^3A''$ (63) + $d^1A'$ (26) + $b^1A'$ (5)	MLCT/LLCT(IL)	3.840	30972	323	0.0010
12 7A'	$b^3A''$ (72) + $c^1A'$ (15) + $d^1A'$ (10)	MLCT(IL/LLCT)	3.865	31173	321	0.0158
13 8A'	$d^1A'$ (57) + $b^3A''$ (36) + $c^3A''$ (5)	MLCT/LLCT(IL)	3.880	31294	320	0.0191
14 -	$b^3A'$ (42) + $b^1A''$ (25) + $c^3A''$ (13) + $c^3A'$ (13) + $d^3A'$ (2)	MLCT/LLCT	3.967	31996	313	0.0021
15 -	$b^3A'$ (48) + $c^3A'$ (28) + $c^3A''$ (16) + $c^1A''$ (4) + $a^1A''$ (2)	MLCT/LLCT	3.988	32165	311	0.0002
16 -	$c^3A''$ (69) + $b^3A'$ (18) + $c^3A'$ (11) + $d^3A'$ (1)	MC/MLCT(CO)	4.009	32335	309	0.0001
17 -	$c^3A''$ (45) + $b^3A'$ (33) + $c^3A'$ (12) + $b^3A''$ (7) + $d^3A'$ (2)	MC/MLCT(CO)/ /MLCT/LLCT	4.013	32367	309	
18 -	$c^3A''$ (66) + $b^3A'$ (25) + $d^1A'$ (5) + $c^1A'$ (2) + $c^3A'$ (1)	MC/MLCT(CO)/ /MLCT/LLCT	4.033	32528	307	0.0049
19 -	$b^3A'$ (49) + $c^3A''$ (43) + $d^1A'$ (2) + $b^3A''$ (2) + $e^1A'$ (1)	MLCT/LLCT/MC/ /MLCT(CO)	4.044	32617	307	0.0012
20 -	$b^3A'$ (32) + $c^3A'$ (30) + $b^1A''$ (23) + $d^3A'$ (6) + $c^3A''$ (5)	MLCT/LLCT	4.057	32722	306	0.0055
21 -	$c^3A'$ (68) + $e^1A'$ (15) + $c^3A''$ (11) + $b^3A''$ (4)	MLCT/LLCT	4.089	32980	303	0.0008
22 -	$c^3A'$ (59) + $c^3A''$ (19) + $b^3A'$ (14) + $c^1A''$ (4) + $b^3A''$ (2)	MLCT/LLCT	4.109	33141	302	0.0001
23 -	$b^1A''$ (41) + $c^3A'$ (40) + $b^3A'$ (13) + $d^3A'$ (4)	MLCT/LLCT	4.166	33601	298	0.0060
24 -	$e^1A'$ (81) + $c^3A'$ (14) + $b^3A'$ (2) + $c^3A''$ (1)	MC/MLCT(CO)	4.167	33609	298	0.0248
25 -	$d^3A''$ (74) + $f^1A'$ (20) + $e^3A''$ (4) + $c^3A''$ (1)	MC/MLCT(CO)	4.231	34125	293	0.0108
26 -	$c^1A''$ (48) + $d^3A'$ (39) + $c^3A'$ (7) + $b^3A'$ (5) + $c^3A''$ (1)	MLCT/LLCT/IL	4.262	34375	291	0.0027
27 -	$d^3A''$ (90) + $d^3A'$ (7) + $e^3A''$ (3)	MC/MLCT(CO)	4.298	34666	288	0.0002
28 -	$d^3A''$ (99)	MC/MLCT(CO)	4.317	34819	287	0.0001



**Table 3.17** (continued)

SO state	Contribution of the SO states in terms of SF states [%]	Character	Energy [eV]	Energy [cm <sup>-1</sup> ]	Wavelength [nm]	Osc. strength
29	- d <sup>3</sup> A' (90) + d <sup>3</sup> A'' (7) + c <sup>3</sup> A'' (1)	IL(/MLCT)	4.332	34940	286	0.0008
30	- d <sup>3</sup> A' (87) + b <sup>1</sup> A'' (9) + d <sup>3</sup> A'' (1) + b <sup>3</sup> A' (1)	IL(/MLCT)	4.353	35109	285	0.0016
31	- d <sup>3</sup> A' (55) + c <sup>1</sup> A'' (41) + e <sup>3</sup> A' (1) + b <sup>3</sup> A' (1)	IL/MLCT/LLCT	4.388	35391	283	0.0014
32	- e <sup>3</sup> A' (100)	IL	4.444	35843	279	
33	- e <sup>3</sup> A' (99)	IL	4.445	35851	279	
34	- e <sup>3</sup> A' (98)	IL	4.445	35851	279	
35	- f <sup>1</sup> A' (75) + d <sup>3</sup> A'' (23) + e <sup>3</sup> A'' (2)	MLCT-IL/MC/ /MLCT(CO)	4.564	36811	272	0.0454
36	- d <sup>1</sup> A'' (100)	MLCT/LLCT	4.848	39102	256	0.0026
37	- e <sup>3</sup> A'' (100)	MLCT-IL	4.877	39335	254	
38	- e <sup>3</sup> A'' (97) + d <sup>3</sup> A'' (3)	MLCT-IL	4.897	39497	253	
39	- e <sup>3</sup> A'' (94) + f <sup>1</sup> A' (4) + d <sup>3</sup> A'' (1)	MLCT-IL	4.912	39618	252	0.0029

**Table 3.18.** The spin-orbit TD-DFT transition energies and oscillator strengths  $f$  of [Re(imH)(CO)<sub>3</sub>(phen)]<sup>+</sup> calculated in DMF. The energy values are given in eV, reciprocal centimetres and as wavelengths (in nm). Oscillator strengths lower than 0.00005 are omitted.

SO state	Contribution of the SO states in terms of SF states [%]	Energy [eV]	Energy [cm <sup>-1</sup> ]	Wavelength [nm]	Osc. strength
aA''	a <sup>3</sup> A'' (91) + a <sup>3</sup> A' (6)	2.791	22 511	444	
bA'	a <sup>3</sup> A'' (91) + a <sup>3</sup> A' (6) + c <sup>3</sup> A' (1)	2.792	22 519	444	0.0003
cA'	a <sup>3</sup> A'' (96) + b <sup>1</sup> A' (1) + c <sup>3</sup> A' (1)	2.799	22 575	443	0.0006
bA''	a <sup>3</sup> A' (60) + a <sup>1</sup> A'' (34) + c <sup>3</sup> A' (2) + b <sup>3</sup> A' (2)	2.945	23 753	421	0.0005
cA''	a <sup>3</sup> A' (82) + a <sup>3</sup> A'' (17)	2.992	24 132	414	
dA'	a <sup>3</sup> A' (76) + a <sup>3</sup> A'' (7) + b <sup>3</sup> A'' (15)	2.992	24 132	414	0.0002
dA''	a <sup>1</sup> A'' (57) + a <sup>3</sup> A' (38)	3.104	25 035	399	0.0004
eA'	b <sup>3</sup> A'' (91) + c <sup>3</sup> A' (3) + b <sup>1</sup> A' (2)	3.106	25 052	399	0.0017
eA''	b <sup>3</sup> A'' (79) + a <sup>3</sup> A' (18)	3.139	25 318	395	
fA'	b <sup>3</sup> A'' (80) + a <sup>3</sup> A' (17)	3.141	25 334	395	0.0003
gA'	b <sup>1</sup> A' (64) + b <sup>3</sup> A' (14) + c <sup>3</sup> A' (5) + c <sup>1</sup> A' (4) + c <sup>3</sup> A'' (4)	3.381	27 270	367	0.0219
fA''	b <sup>3</sup> A' (67) + c <sup>3</sup> A' (20) + d <sup>3</sup> A' (5)	3.392	27 358	366	
hA'	b <sup>3</sup> A' (57) + c <sup>3</sup> A' (23) + b <sup>1</sup> A' (6)	3.395	27 383	365	0.0026
gA''	b <sup>3</sup> A' (62) + c <sup>3</sup> A' (25) + b <sup>1</sup> A'' (5)	3.397	27 399	365	0.0009
iA'	c <sup>3</sup> A' (48) + b <sup>3</sup> A' (11) + d <sup>1</sup> A' (17) + b <sup>1</sup> A' (8) + c <sup>1</sup> A' (5)	3.471	27 995	357	0.0173
hA''	c <sup>3</sup> A' (63) + b <sup>3</sup> A' (23) + d <sup>3</sup> A' (5) + b <sup>3</sup> A'' (8)	3.473	28 012	357	
iA''	c <sup>3</sup> A' (65) + b <sup>3</sup> A' (21) + b <sup>1</sup> A'' (6)	3.476	28 036	357	0.0002
jA'	c <sup>1</sup> A' (67) + d <sup>3</sup> A' (8) + c <sup>3</sup> A' (7) + b <sup>1</sup> A' (4)	3.500	28 229	354	0.0042
kA'	d <sup>1</sup> A' (40) + d <sup>3</sup> A' (38) + b <sup>3</sup> A' (5) + b <sup>1</sup> A' (5)	3.579	28 867	346	0.0361
jA''	c <sup>3</sup> A'' (93)	3.596	29 004	345	
lA'	d <sup>1</sup> A' (30) + c <sup>3</sup> A'' (58) + c <sup>3</sup> A' (6) + c <sup>1</sup> A' (3)	3.605	29 076	344	0.0251

A direct comparison of the SF- and SO-TD-DFT UV-vis absorption spectra of  $[\text{Re}(\text{imH})(\text{CO})_3(\text{phen})]^+$  (in DMF) is depicted in Figure 3.15. The region ranging from 300 to 450 nm, i.e. the lowest experimental band extending from  $\sim 320$  to  $\sim 420$  nm, is enlarged for a better resolution. At first glance, the SF and SO spectra resemble closely each other. However, when scrutinizing the origin of bands there is a marked difference between the top and bottom panels. In case of the SO model, the number of underlying allowed transitions increases, their oscillator strengths are lowered and the final band is broadened and weakened, compared to spin-free TD-DFT, where only three intense peaks contribute to the lowest-energy band. Thus the SO model (represented among other things by a high density of states) reproduces reasonably well the broad and asymmetric shape of the experimental band. These observations concerning changes of the number and intensities of excited states in the SO treatment vs. the SF description were confirmed also by SO-MS-CASPT2 (20 SF states result in 40 SO states counting the GS – see Table 3.17). In the approximate energy range between the optically populated ES ( $\sim b^1A'$ ) and the lowest  $a^3A''$  state SO-MS-CASPT2 predicts 8 SO states, compared to only 4 SF states (see Figure 3.16). According to SO-TD-DFT even 14 SO states are localised vs. 5 SF states (see Figure 3.17). The difference between SO-MS-CASPT2 (only 8 SO states) and SO-TD-DFT (14 SO states) is caused by the fact that in case of SO-MS-CASPT2 the  $b^3A''$  state is lying significantly higher (even above the  $b^1A'$  state) and thus gives rise to higher-energy SO states lying outside the described energy interval.

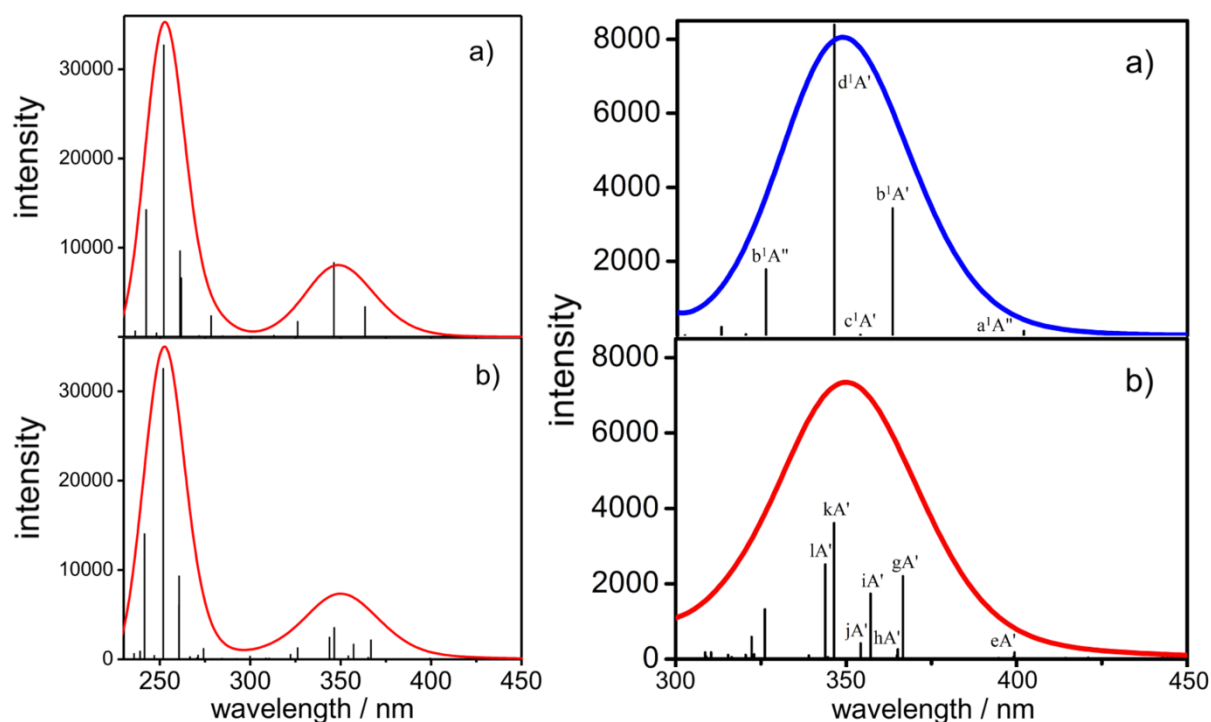


**Figure 3.15.** The theoretical UV-vis absorption spectra of  $[\text{Re}(\text{imH})(\text{CO})_3(\text{phen})]^+$  in DMF (COSMO) simulated by means of a) SF- (top) and b) SO-TD-DFT (bottom). On the right side the inset of the whole spectra depicting the lowest-energy band is shown. Black discrete lines indicate calculated electronic transitions – their height is proportional to the oscillator strength and the most significant contributions are marked by the label of the final ES. Fitted by Gaussian band-shapes assuming  $\text{fwhm} = 3000 \text{ cm}^{-1}$ .

Figure 3.16 (MS-CASPT2) and Figure 3.17 (TD-DFT) demonstrates how SF singlet and triplet states of  $[\text{Re}(\text{imH})(\text{CO})_3(\text{phen})]^+$  mix together to give rise to SO states when SOC is taken into account. The parentage of the lowest SO states is indicated by black dashed lines connecting a particular SF and SO state with a given percentage. The correlation diagrams for both methods are qualitatively comparable for the first six SO states. For higher-lying states the diagrams differ to a certain extent, which can be ascribed to the fact that the spin-free  $a^3A'$  and  $b^3A''$  states are separated much more in MS-CASPT2 than in TD-DFT.

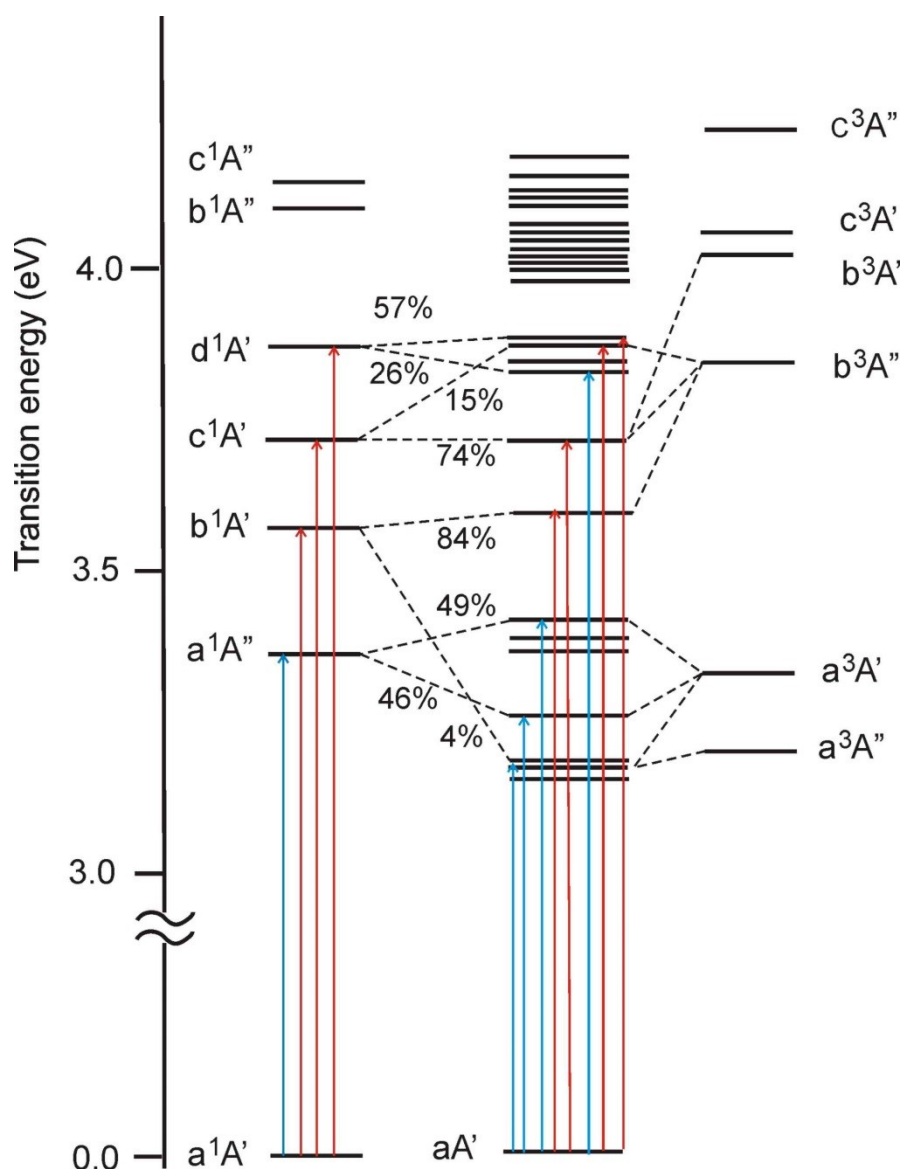


**Figure 3.16.** The correlation of MS-CASPT2 spin-free singlet (left column) and triplet (right column) states with the resulting spin-orbit states (in the middle) of  $[\text{Re}(\text{imH})(\text{CO})_3(\text{phen})]^+$  in vacuo. The main spin-free contributions to a particular spin-orbit state are depicted by dashed lines. Red, blue and black arrows indicate transitions with oscillator strengths larger than 0.01, 0.001–0.01 and 0.0005–0.001, respectively. The SO states calculated by means of SO-MS-CASPT2. (adopted from Reference [92])

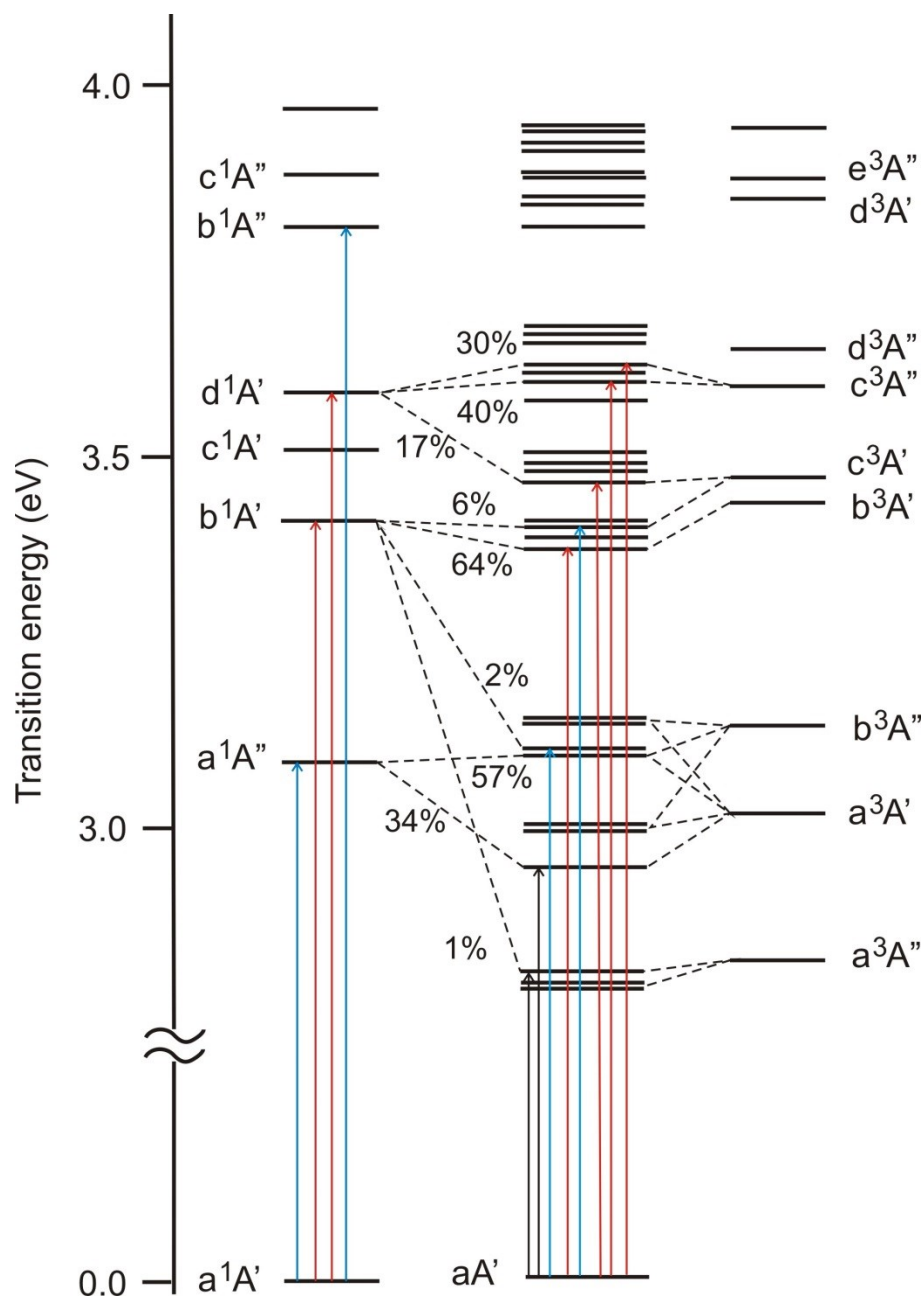


**Figure 3.17.** The correlation of TD-DFT spin-free singlet (left column) and triplet (right column) states with the resulting spin-orbit states (in the middle) of  $[\text{Re}(\text{imH})(\text{CO})_3(\text{phen})]^+$  in DMF. The main spin-free contributions to a particular spin-orbit state are depicted by dashed lines. Red, blue and black arrows indicate transitions with oscillator strengths larger than 0.01, 0.001–0.01 and 0.0005–0.001, respectively. The SO states calculated by means of SO-TD-DFT (PBE0, COSMO/DMF). (adopted from Reference [92])

Looking at the three lowest SO states (with  $A''$ ,  $A'$  and  $A'$  double-group symmetry, ordered by the increasing energy) (Tables 3.17 and 3.18), we notice that they all three stem predominantly from the spin-free  $a^3A''$  MLCT state (more than ca. 80% and more than 90% in SO-MS-CASPT2 and SO-TD-DFT, respectively). They can be viewed as three sublevels of the originally threefold degenerate multiplet split in the presence of SOC. In other words, ZFS is observed – the calculated values of  $(2A'-1A'')$  and  $(3A'-1A'')$  separation are 105 and

194 cm<sup>-1</sup> by SO-MS-CASPT2 and 8 and 64 cm<sup>-1</sup> by SO-TD-DFT. Whereas the lowest aA'' (termed 1A'' in case of SO-MS-CASPT2) has (almost) a zero oscillator strength according to both methods and does not contribute to the absorption spectrum, transitions to the other two sublevels of A' symmetry exhibit very small, but non-zero intensities (see Table 3.18). In both SO bA' and cA' states a spin-free allowed singlet admixture can be found, which is responsible for the fact that these transitions are no longer forbidden. SO-MS-CASPT2 predicts that only the highest one of the three sublevels is spectroscopically weakly allowed (due to a small contribution of the spin-free singlet b<sup>1</sup>A' state) (Table 3.17).

In accordance with the above mentioned manifestations of SOC in a spectrum, more allowed or semi-allowed transitions are present than in the spin-free model. By means of SO-TD-DFT it was calculated that the following SO states contribute to the lowest-energy absorption band of [Re(imH)(CO)<sub>3</sub>(phen)]<sup>+</sup> (right bottom panel in Figure 3.15), namely eA', gA', hA', iA', jA', kA', lA' and other higher-lying states (not shown in Table 3.18). For example, the mixed MLCT–IL eA' state is predominantly of a triplet character and only the very small b<sup>1</sup>A' admixture (2%) ensures that the transition to this state has a non-zero oscillator strength. The truly allowed transitions involve transitions to the gA' (MLCT with a small IL contribution) and iA' (MLCT–IL) states, and to the kA' and lA' states, which are intense due to substantial b<sup>1</sup>A' or/and d<sup>1</sup>A' contributions (the two most intense peaks in the spin-free spectrum (right top panel in Figure 3.15)), respectively. In case of SO-MS-CASPT2, the large oscillator strengths are observed for transitions to those SO states which contain a significant singlet character (based on the spin-free b<sup>1</sup>A', c<sup>1</sup>A' and d<sup>1</sup>A' states) – these are the 5A', 6A', 7A' and 8A' states. Note that all allowed transitions occur to states with the double-group symmetry A', which is not surprising, since the ground state possesses the same A' symmetry. Moreover, it should be pointed out that these SO states are spectroscopically allowed, although their triplet parentage could be relatively high. For instance, the 6A' state is composed of 24% triplet components.

So far, we have worked on the presumption that the optimized GS geometry can be used to approximate the geometry of all excited states (i.e. if not specified, the equilibrium GS structure was taken as the input geometry). This rather crude approximation may be justified by the fact that the Franck–Condon transitions have been assumed. However, for modelling emission characteristics and especially for studying the evolution of excited-state behaviour it is insufficient. Therefore in the following paragraphs we concentrate on the SO calculations that are based on the relaxed geometries of the lowest singlet (b<sup>1</sup>A') and triplet (a<sup>3</sup>A'') excited states and we compare the resulting SO-state diagrams to that at the optimized GS geometry. The b<sup>1</sup>A' geometry is chosen to simulate the optically populated SO state(s) and the a<sup>3</sup>A'' geometry would correspond well to the three lowest SO states.

The underlying data of the solvent-corrected (COSMO/DMF) SO-TD-DFT transition energies from the ground state (aA') to the low-lying excited states of [Re(imH)(CO)<sub>3</sub>(phen)]<sup>+</sup> and the associated oscillator strengths *f* calculated at the optimized geometries of the spin-free b<sup>1</sup>A' and a<sup>3</sup>A'' states are listed in Tables 3.19 and 3.20, respectively. The last column of both Tables contains values of Einstein spontaneous emission coefficient *A* for radiative transitions to the ground state.

**Table 3.19.** The solvent-corrected (COSMO/DMF) spin–orbit TD-DFT transition energies to the low-lying excited states and oscillator strengths  $f$  of  $[\text{Re}(\text{imH})(\text{CO})_3(\text{phen})]^+$  calculated at the optimized  $b^1A'$  geometry. The energy values are given in eV and reciprocal centimetres. Oscillator strengths lower than 0.00005 are omitted (together with Einstein spontaneous emission coefficient for this state).

SO state	Contribution of the SO states in terms of SF states [%]	Energy [eV]	Energy [ $\text{cm}^{-1}$ ]	Osc. strength	Emiss. coeff. [ $10^7 \cdot \text{s}^{-1}$ ]
aA''	$a^3A''$ (68) + $a^3A'$ (28) + $b^3A'$ (2)	2.368	19 102		
bA'	$a^3A''$ (68) + $a^3A'$ (28) + $c^1A'$ (2)	2.370	19 112	0.0010	0.024
cA'	$a^3A''$ (94) + $b^1A'$ (3) + $c^3A'$ (2)	2.407	19 417	0.0022	0.055
bA''	$a^3A'$ (78) + $a^1A''$ (19) + $b^3A'$ (3)	2.450	19 761	0.0002	0.005
cA''	$a^3A'$ (68) + $a^3A''$ (30)	2.545	20 528		
dA'	$a^3A'$ (68) + $a^3A''$ (30)	2.545	20 529	0.0001	0.003
dA''	$a^1A''$ (76) + $a^3A'$ (21)	2.694	21 730	0.0006	0.019
eA'	$b^1A'$ (45) + $b^3A''$ (36) + $b^3A'$ (13)	2.866	23 117	0.0308	1.098
eA''	$b^3A''$ (88) + $b^3A'$ (7)	2.924	23 580		
fA'	$b^3A''$ (90) + $b^3A'$ (6) + $b^1A'$ (2)	2.925	23 593	0.0019	0.071
gA'	$b^1A'$ (34) + $b^3A''$ (60) + $c^1A'$ (1)	2.959	23 862	0.0242	0.919
fA''	$b^3A'$ (84) + $c^3A''$ (6) + $c^3A'$ (4)	3.040	24 519		
gA''	$b^3A'$ (88) + $a^1A''$ (5)	3.046	24 565	0.0001	0.004
hA'	$b^3A'$ (69) + $b^1A'$ (12) + $c^1A'$ (8)	3.049	24 589	0.0100	0.403
iA'	$c^1A'$ (77) + $b^3A'$ (11) + $c^3A'$ (6)	3.159	25 480	0.0198	0.857
hA''	$c^3A'$ (82) + $b^1A''$ (10)	3.202	25 826	0.0019	0.085
iA''	$c^3A'$ (76) + $b^3A''$ (11)	3.212	25 910	0.0001	0.004
jA'	$c^3A'$ (72) + $c^1A'$ (8) + $c^3A''$ (10)	3.214	25 924	0.0029	0.130
kA'	$c^3A'$ (68) + $d^1A'$ (24)	3.303	26 640	0.0148	0.701

**Table 3.20.** The solvent-corrected (COSMO/DMF) spin–orbit TD-DFT transition energies to the low-lying excited states and oscillator strengths  $f$  of  $[\text{Re}(\text{imH})(\text{CO})_3(\text{phen})]^+$  calculated at the optimized  $a^3A''$  geometry. The energy values are given in eV and reciprocal centimetres. Oscillator strengths lower than 0.00005 are omitted (together with Einstein spontaneous emission coefficient for this state).

SO state	Contribution of the SO states in terms of SF states [%]	Energy [eV]	Energy [ $\text{cm}^{-1}$ ]	Osc. strength	Emiss. coeff. [ $10^7 \cdot \text{s}^{-1}$ ]
aA''	$a^3A''$ (94) + $a^3A'$ (3)	2.080	16 778		
bA'	$a^3A''$ (94) + $a^3A'$ (3) + $c^3A'$ (2)	2.081	16 787	0.0001	0.002
cA'	$a^3A''$ (96) + $c^1A'$ (1) + $c^3A'$ (1)	2.088	16 845	0.0005	0.009
bA''	$a^1A''$ (85) + $a^3A'$ (10)	2.252	18 167	0.0011	0.024
cA''	$a^3A'$ (92) + $a^3A''$ (4)	2.525	20 363		
dA'	$a^3A'$ (93) + $a^3A''$ (4)	2.525	20 369	0.0001	0.003
dA''	$a^3A'$ (88) + $a^1A''$ (4)	2.545	20 528	0.0002	0.006
eA'	$b^3A'$ (70) + $c^1A'$ (13) + $b^3A''$ (4)	2.827	22 802	0.0063	0.218
eA''	$b^3A'$ (80) + $b^3A''$ (11)	2.864	23 102		
fA''	$b^3A'$ (86) + $c^3A'$ (8) + $a^1A''$ (3)	2.879	23 219	0.0001	0.004
fA'	$b^1A'$ (63) + $b^3A''$ (30) + $a^3A'$ (3)	2.891	23 321	0.0015	0.054
gA''	$b^3A''$ (48) + $c^3A'$ (46)	2.913	23 492		
gA'	$c^3A'$ (52) + $b^3A''$ (32) + $b^1A'$ (11)	2.914	23 506	0.0003	0.011
hA'	$c^1A'$ (35) + $b^3A''$ (58) + $d^1A'$ (4)	2.919	23 543	0.0160	0.592
hA''	$c^3A'$ (86) + $b^3A'$ (8)	2.954	23 824	0.0002	0.008
iA'	$c^1A'$ (44) + $b^3A''$ (28) + $b^3A'$ (25)	2.979	24 026	0.0149	0.574
iA''	$b^3A''$ (40) + $c^3A'$ (47)	2.987	24 095		
jA'	$c^3A'$ (41) + $b^3A''$ (37) + $b^1A'$ (17)	2.993	24 139	0.0011	0.043
kA'	$d^1A'$ (86) + $c^1A'$ (2) + $b^3A''$ (3)	3.171	25 576	0.1032	4.503

The interrelations between the individual SO-state diagrams calculated at three different geometries of the spin-free  $a^1A'$ ,  $b^1A'$  and  $a^3A''$  states are shown in Figure 3.18.

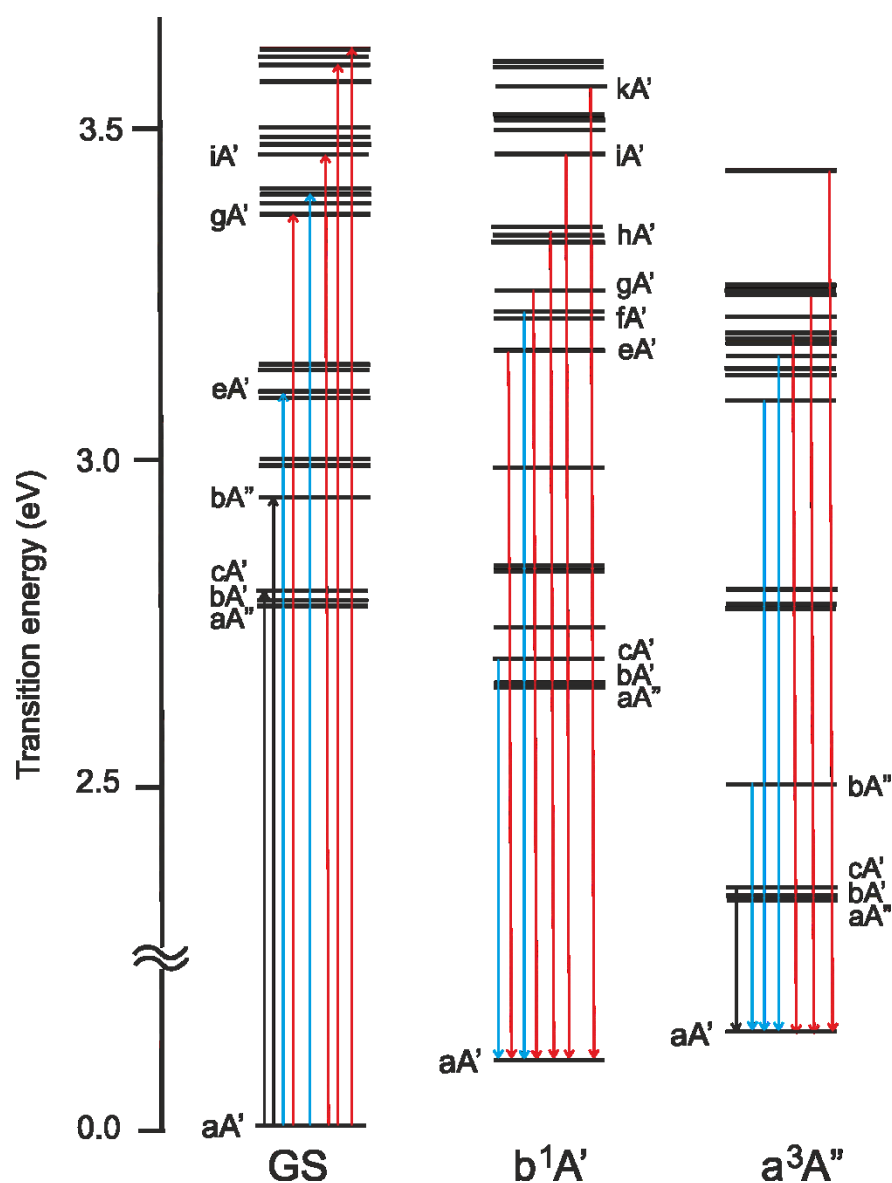


**Figure 3.18.** The comparison of individual SO states of  $[Re(imH)(CO)_3(phen)]^+$  calculated at three different optimized geometries: the spin-free ground  $a^1A'$  (left),  $b^1A'$  (middle) and  $a^3A''$  (right) states. All energies are related to the ground state at its relaxed geometry. Red, blue and black arrows indicate transitions with oscillator strengths larger than 0.01, 0.001–0.01 and 0.0005–0.001, respectively. In case of emission, transitions with Einstein coefficient  $A$  ( $10^7 \cdot s^{-1}$ ) larger than 0.1, 0.01–0.1 and 0.001–0.01 are indicated by red, blue and black upwards pointing arrows, respectively. Only the photophysically interesting SO states are marked by arrows. Calculated by means of SO-TD-DFT (PBE0, COSMO/DMF). (adopted from Reference [92])

Analyzing magnitudes of oscillator strengths in Table 3.18 it is clear that laser-pulse excitation at 400 nm ( $25\,000\text{ cm}^{-1}$ ) populates predominantly the lowest fully allowed state, i.e. the  $ga'$  MLCT state with  $f = 0.0219$  – it is in line with a large  $b^1A'$  parentage. The close-



lying SO  $eA'$ ,  $hA'$  and  $iA'$  states containing a small admixture of the  $b^1A'$  state (or other spin-free allowed states) are populated as well.

When we switch to the  $b^1A'$  geometry (which can be virtually considered as a simulation of intramolecular vibrational redistribution), we notice that all the SO excited states become stabilized in energy with the exception of the  $eA'$  state (Figure 3.18). This state loses its predominant triplet parentage and through 45%  $b^1A'$  contribution it gains substantially more intensity than at the GS geometry. The amount of the  $b^1A'$  admixture in the  $eA'$  state is even higher than in the  $gA'$  state, which is no longer the most intense transition because of 60%  $b^3A''$  contribution (in contrast to a 23% triplet character at the GS geometry – cf. Tables 3.18 and 3.19). In addition, the gap between the  $cA'$  state and the near-degenerate  $bA'$  and  $aA''$  states is enlarged, which could probably have something to do with the fact the two lowest SO states have now 28%  $a^3A'$  and 68%  $a^3A''$  content (in contrast to only 6%  $a^3A'$  and 91%  $a^3A''$  at the GS geometry) whereas the third state remains to be almost pure  $a^3A''$  in nature at all three geometries. The strongly emissive SO states ( $eA'$ ,  $gA'$ ,  $hA'$ ,  $iA'$ ,  $jA'$ ,  $kA'$ ) are predicted to lie in the region 23 117–26 640  $\text{cm}^{-1}$  (below the Franck–Condon  $gA'$  state (27 720  $\text{cm}^{-1}$ )).

Moving to the  $a^3A''$  geometry and simulating thus “intersystem crossing” to the low-lying triplet-based SO states, energies of all the SO excited states are even more stabilized. Visually examining an energy distribution of the SO states, it is apparent that they are gathered in several quite separated groups and within a group the states are densely packed – the distribution becomes rather uneven when compared to the GS and  $b^1A'$  geometries. All the three lowest SO states originate predominantly from the spin-free  $a^3A''$  state. The total calculated ZFS is 67  $\text{cm}^{-1}$ , which is of the same order as the value 42.1  $\text{cm}^{-1}$  measured<sup>197,198</sup> for  $[\text{ReCl}(\text{CO})_3(\text{phen})]$  in a low-temperature matrix. The highest one, the  $cA'$  state, is the most emissive from these three states, however, its intensity is only weak (due to a very small  $c^1A'$  admixture). The calculated energy 16 845  $\text{cm}^{-1}$  is in agreement with the experimental value of the emission band maximum (16 949  $\text{cm}^{-1} \approx 590 \text{ nm}$ ).<sup>95</sup> By contrast, the above lying  $bA''$  state is nearly three times more emissive. Its character changes from a triplet (60%  $a^3A''$  at the GS geometry) to a prevailing singlet nature (85%  $a^1A''$  at the  $a^3A''$  geometry). The highly emissive SO states ( $eA'$ ,  $fA'$ ,  $hA'$ ,  $iA'$ ,  $jA'$ ,  $kA'$ ) are located at 22 802–25 576  $\text{cm}^{-1}$ .

From the above written it is obvious that the correct SO photophysical model could be potentially created as the interplay of respective energetic segments of the three SO-state diagrams, as depicted in Figure 3.19. The SO states which participate in the excited-state dynamics of the system are de facto judged from the perspective of their best fitting structure. So we are able to interpret reasonably the main processes occurring after laser-pulse excitation of the system.

For the situation just prior to and during irradiation, the GS geometry seems to be the most adequate, since mainly the Franck–Condon  $gA'$  MLCT and the other close-lying spectroscopically allowed states are populated by optical excitation (in Figure 3.19 indicated by a pink filled circle **I**).

The  $b^1A'$  geometry suits better the situation right after excitation when ongoing IVR probably changes the molecular structure from the GS geometry towards this geometry. In addition, it is very likely that electronic energy redistribution within a group with high density of SO states (depicted by a blue filled circle **II**) takes place at the same time. This ultrafast vibrational and electronic relaxation (depicted by a black bold arrow from the circle **I**) is

accompanied by “instantaneous” fluorescence Stokes shift from 400 nm (laser pulse) to  $\sim 530$  nm ( $18\,900\text{ cm}^{-1}$ ), which is indicated by downward pointing red arrows from the group of vibrationally hot and emissive states **II**. As these SO states consist of a significant triplet character, the term “fluorescence” is strictly speaking not correct and it is more suitable to use for this emission a label “luminescence”, in this case “prompt luminescence”. The common feature<sup>26,28,29</sup> for  $\text{Re}^{\text{I}}$  carbonyl-diimine complexes is that the manifold of vibrational and electronic excitations (and relaxations) is reflected in the vast spectroscopic broadness (460–600 nm half-width) of this luminescence band (centred at  $\sim 530$  nm for  $[\text{Re}(\text{imH})(\text{CO})_3(\text{phen})]^+$ ).

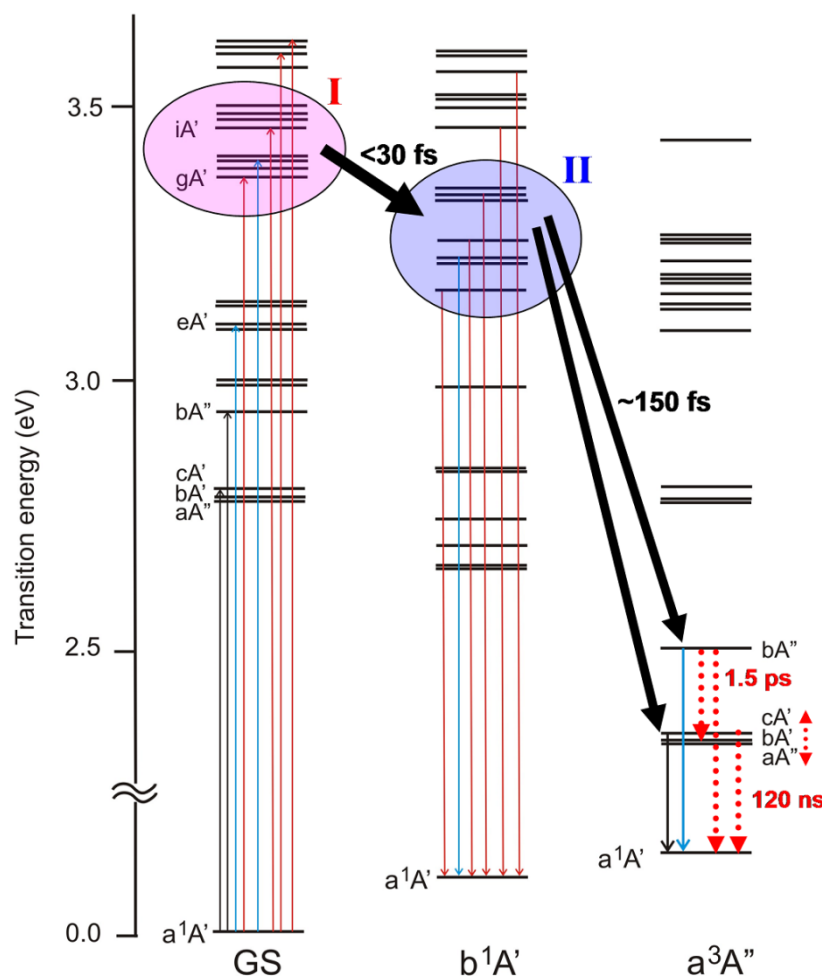


**Figure 3.19.** The spin–orbit model of  $[\text{Re}(\text{imH})(\text{CO})_3(\text{phen})]^+$ . Pink filled circle **I** = optically populated states, blue filled circle **II** = emissive states (prompt emission indicated by red thin arrows), black bold arrows = electronic and vibrational redistribution/nonradiative transition, blue and black thin arrows = emission of the four lowest SO states, red bold dotted arrow = nonradiative decay, double red bold dotted arrow = equilibration of the three lowest SO states. Vibrational relaxation is not depicted for clarity. Energies are related to the ground state at its relaxed geometry. Calculated by means of SO-TD-DFT (PBE0, COSMO/DMF). For the whole description see the text. (adopted from Reference [92])

Finally, the group of the four lowest SO excited states populated by a nonradiative transition (which is associated to the ~150 fs luminescence decay; depicted by a black bold arrow from the circle **II**) from the group **II** is best estimated by the  $a^3A''$  geometry that corresponds with the main component of these lowest SO states. The designation “nonradiative transition” should be preferred to “intersystem crossing” for analogous reasons as above – the states **II** are not pure singlets in nature. Indeed, it is the very presence of strong mixing of triplet and singlet contributions in the SO states (one of a direct consequence of SOC) that allows for the efficient transitions between particular SO states. The triplet content of the group **II** can be thought of as a “channel” through which transitions between states are facilitated. The low-lying SO states, which are thus populated, are vibrationally excited and initially they are found to be in an unequilibrated solvent arrangement, establishing rapidly the equilibrium distribution of populations among the three lowest SO states (depicted by a vertical double red dotted arrow). Based on these relaxation and solvent restructuring processes, the ps relaxation times detected experimentally by UV–vis time-resolved absorption<sup>26</sup> can be explained, whereas the spin-free model fails at this point. According to our SO model the short-lived emission (blue thin arrow) with a 1.5 ps lifetime (i.e. the phosphorescence occurring from the intermediate state in the spin-free model) is attributed to the fourth state  $bA''$  that decays nonradiatively (depicted by red bold dotted arrows) to the four lower-lying SO states including the ground state.

Another issue which cannot be clarified by the spin-free model concerns the two excited-state IR signals.<sup>26</sup> In order to attempt to identify the origin of the major and minor TRIR excited states, two different hypotheses were formulated in our SO model. They provide valuable information and a new insight into the excited-state dynamics and the temperature dependence of emission, which remains inaccessible by the spin-free approach. (1) The one possible explanation associates the major TRIR signal with the  $aA''$  and  $bA'$  states and the minor one with the  $cA'$  state with a calculated population ratio that is similar to the experimental value<sup>26</sup> 80:20 for  $[ReCl(CO)_3(phen)]$  in MeCN (for more information see Table 3 in Reference [92]). The long-lived emission (black thin arrow) (i.e. the phosphorescence with ~120 ns lifetime in the spin-free model) is assigned to the  $cA'$  state. The fourth state  $bA''$  enables the thermally activated nonradiative decay, which can be found also in other  $Re^I$  carbonyl-diimine complexes.<sup>169,207</sup> Like in the previous project of  $[ReX(CO)_3(bpy)]$ , the predominant singlet character of the  $bA''$  state at the optimized spin-free  $a^3A''$  geometry enables an efficient nonradiative decay to the ground state. Nevertheless, the differences between the IR spectra of the major and minor states are still unclear within this explanation. (2) According to the second interpretation, the major TRIR signal is attributed to all the three lowest SO  $aA''$ ,  $bA'$ ,  $cA'$  states and the minor one belongs to the  $bA''$  state, which would at its relaxed geometry lie lower than it was calculated at the  $a^3A''$  geometry. The long-lived emission is now connected with the  $bA''$  and  $cA'$  states together – these states are the most and the second most emissive among the four lowest SO states, respectively. In addition, the  $bA''$  state could also decay very efficiently nonradiatively to the ground state and thus it could act as a deactivating state when thermally populated. The same presumption can be applied to higher-lying SO states  $cA''$ ,  $dA'$ , or  $dA''$ .

It is worth mentioning that although the SO model aims to interpret also the excited-state evolution, our calculations do not involve a time domain, since MS-CASPT2 and TD-DFT (in spite of its name) are static techniques yielding only stationary electronic ground and excited states. An exact approach would consist of calculating PESs of individual SO states and investigating the regions where the surfaces cross. Perhaps a computationally a bit more accessible alternative is to perform *ab initio* nonadiabatic molecular dynamics. Unfortunately, both of these treatments are beyond limits of the current computational capacity and we have to stick to the present SO photophysical model. Simply stated, this model is based on approximating the time evolution by estimating effects of structural changes (occurring within the excited-state dynamics) on SO states. However, it should be emphasized that the geometries taken as the input were the relaxed spin-free geometries, not the relativistic ones, which may turn out to be insufficient in the whole context of SOC calculations.

Regarding SO-MS-CASPT2, an important parameter of a calculation is the number of calculated excited states – then the question arises which states have to be included into a study. As shown on a simple example of Pb dimer,<sup>109</sup> a rigorous study should comprise all physically important states in order to obtain accurate SOC results. When only lower states were included, the method provided a precise description close to the equilibrium geometry, but it was not suitable for computing the full potential curves. In our calculations we used only relaxed geometries and therefore the limited number of excited states involved in a calculation is justified for these reasons.

The above presented SO excited-state model of  $[\text{Re}(\text{imH})(\text{CO})_3(\text{phen})]^+$  is based on relativistic excited-state quantum chemical calculations that take into account SOC. Several generalizations can be extracted from this SO model, which are applicable not only to the broad class of  $\text{Re}^{\text{I}}$  carbonyl-diimine complexes, but also to many other closed-shell heavy-metal complexes. These findings are summed up in the following points:

(1) **High excited-state density and its manifestation in a spectrum.** Relative to the spin-free model, density of SO excited states is significantly increased. As a consequence, theoretical spin–orbit spectra of heavy-metal complexes differ from those calculated by the spin-free approach. Even if the spectra may look similar at first sight, at least the origin of bands is different. UV–vis absorption bands typically broaden and weaken – the higher the density of SO states and the stronger the mixing among them, the weaker the transitions are and their number increases in contrast to a spin-free spectrum, where usually less but more intense (spin-allowed) transitions are present. Since optical excitation followed by various decay and relaxation pathways can simultaneously populate a manifold of close-lying SO states, emission typically originates not from a single state but from a group of SO states, which is often reflected in the enormous spectroscopic broadness. However, in case of emission the number of emitting SO states is governed by Boltzmann population distribution. Both of these observations for absorption and emission spectra are connected to differences between oscillator strengths/Einstein spontaneous emission coefficients of individual states in the SF and SO model. Whereas spin-free oscillator strengths for transitions between singlet and triplet states are definitely zero, the situation changes when states become mixed due to SOC. Then only a small admixture of a strongly allowed singlet suffices to make a transition to/from a state with otherwise a predominant triplet parentage spectroscopically allowed. The

high density of close-lying SO states opens a possibility of populating optically more than one SO state – in addition, electronic excitation is accompanied by vibrational excitation. These states immediately undergo fast deactivation and energy redistribution processes which are realized by going down through a cascade of closely-spaced SO states (from which some can be emissive). In other words, SO excited-state PESs offer numerous electronic relaxation pathways via multiple state crossings and conical intersections between close-lying SO states that are vibronically coupled. Usually, nonradiative energy dissipation (nonradiative decay) has been attributed only to vibrational relaxation. From this new perspective, vibrational relaxation should be considered only as one of options, the second one being electronic relaxation between SO states. All these relaxation steps participate in the ultrafast excited-state dynamics and the information about them could be obtained from ultrafast experiments<sup>26,28,29</sup> (see Point 6).

**(2) A highly spin-mixed character of SO states.** The states are traditionally classified in terms of their spin multiplicity. The thing is that with an introduction of sufficiently strong SOC induced by the metal atom (and other heavier atoms) such a categorization ceases to be appropriate. To describe electronic states of transition metal complexes precisely, singlet or triplet states etc. (analogically dublet, quadruplet etc.) are no longer meaningful labels, since overwhelming majority of excited states in the SO scheme are mixed from various spin-free states, which often differ in their spin multiplicity. It is then impossible to decide about the final spin multiplicity of a given SO state. Thus the spin–orbit states should be viewed as general excited states irrespective of spin. It should be noted that the validity of assigning a spin label in complexes containing  $4d$  or  $5d$  elements was already doubted by Crosby et al.<sup>208</sup> in the 1970s. Moreover, the character of a given SO state tends to change when structural relaxation following after optical excitation is assumed. For example, the  $gA'$  state of  $[\text{Re}(\text{imH})(\text{CO})_3(\text{phen})]^+$  has a predominant singlet character at the GS geometry, whereas at the  $a^3A''$  geometry it becomes mostly triplet.

**(3) Fluorescence/phosphorescence vs. luminescence, IC/ISC vs. nonradiative transition.** Naturally, the spin-mixed character of SO states has a direct impact also on the classic photophysical processes known from Jablonski diagram (see Figure 2.2). The generalization described in the previous point washes away to some extent the differences between terms “fluorescence” – “phosphorescence” and between “internal conversion” – “intersystem crossing” as well. For instance, when hypothetically concerning equal singlet and triplet contributions to an emissive or in IC/ISC participating SO state (i.e. 50% singlet and 50% triplet origin), then there is no point in distinguishing between these categories. Instead, it would be more suitable to use universal designations and to refer to these processes as “luminescence/emission” and “nonradiative transitions between SO states”, respectively. In addition, in the former case, we distinguish between prompt and long-lived emission. Hence, in characterizing transition metal compound electronic spectra and photophysical phenomena a unified point of view ought to be preferred for such cases. However, such a strong mixing was not observed for the low-lying SO states in our systems and the prevailing singlet or triplet character was more or less preserved in majority of SO states. Therefore we can still utilize the usual terminology used among experimentalists.

(4) **The three lowest SO states.** It has been confirmed that the ZFS concept can be applied to the three lowest SO states of  $[\text{Re}(\text{imH})(\text{CO})_3(\text{phen})]^+$ . All three states originate predominantly from the lowest spin-free  $a^3A''$  triplet state (at the optimized GS and  $a^3A''$  geometries). However, this observation is not generally valid for the whole family of complexes. The states can be considered as sublevels of the  $a^3A''$  state and energy differences between them can be thus compared to experimental values of ZFS.<sup>10–12</sup> The lowest SO state is usually the least emissive (and therefore the longest-lived) and it often contains the largest percentage of a triplet character among these three sublevels. On the other hand, the third SO state is the most emissive one. Regarding higher-lying SO states, they are so strongly mixed that it is neither possible to determine a parent spin-free triplet, nor to identify all three sublevels.

(5) **Implications for photonic applications.** With the help of the SO model one can attempt to decipher complex mechanisms of deactivation pathways and various transitions between SO states, counting radiative and nonradiative processes, vibronic coupling, electronic relaxation etc. The next logical step would be to formulate selection rules which could help us to gain better control of excited-state dynamics in order to design or find materials tailored to specific and desired purposes.<sup>10–12</sup>

(6) **Ultrafast excited-state dynamics.** It is conceivable that ultrafast experiments preserve a record of SOC effects on excited-state dynamics. Time-resolved spectroscopic measurements (in the fs–ps time range) are capable of providing pertinent information (e.g. time constants) about electronic and vibrational relaxation or establishing equilibrium among the low-lying SO states. In this context, it should be mentioned that photophysical and photochemical behaviour of heavy-metal complexes characterized by their high excited-state density may also involve unforeseen features, for example a breakdown of Born-Oppenheimer approximation, a coherent population of close-lying SO states upon fs excitation or stimulated emission from higher SO states.

## Chapter 4: CONCLUSION

For a series of rhenium(I) tricarbonyl  $[\text{ReX}(\text{CO})_3(2,2'\text{-bipyridine})]$  ( $\text{X} = \text{Cl}, \text{Br}, \text{I}$ ) and  $[\text{Re}(\text{imidazole})(\text{CO})_3(1,10\text{-phenanthroline})]^+$  complexes, the energies of spin-free and spin-orbit ground and excited states and the oscillator strengths of vertical transitions were calculated. Two completely different computational approaches were adopted: the SO-MS-CASPT2 method, which uses the electronic wave function as the fundamental variable, and the SO-TD-DFT method replacing the wave function with the electron density. The electron correlation effects were included: CASSCF is able to account for the static and CASPT2 for the dynamic correlation; TD-DFT governs the amount of incorporated correlation energy by the choice of an XC functional. The scalar relativistic terms were incorporated by the basis set generation (of ANO-RCC type) for CASSCF/MS-CASPT2 or by the SR ZORA in case of TD-DFT. In the wave function formalism, SOC was added a posteriori by means of a configuration interaction model (SO-RASSI), which employs the two-component DKH transformation. In the density functional approach, SOC was treated perturbatively, following from the ZORA formulation of the spin-orbit Hamiltonian. The results from both techniques were presented, compared with each other and to available experimental data.

Herein, typical and remarkable features and trends that are common to all studied complexes will be summarized. In order to verify the necessity of considering the spin-orbit interaction explicitly in theoretical calculations, we have chosen several coordination complexes, all of them containing a central ion from third row transition metals. Our studies have proven that the relativistic SO treatment is crucial for the interpretation of photophysical data of transition metal complexes. The SOC conceptual framework is not only able to describe absorption spectra, emission characteristics and excited-state behaviour in a satisfactory way, but it also improves a quantitative agreement with the experiment and brings a physically more correct description of electronic excited states, in some cases even qualitatively different from the SF concept. Moreover, the SO model has the power to explain some of the features that cannot be captured by the SF model. SOC dramatically affects characters of individual electronic excited states and a mechanism of their deactivation and relaxation pathways. Within the SO model, electronic structures of transition metal compounds can be generally characterized by a large density of spin-orbit states which are extensively mixed from spin-free singlet and triplet states. Consequently, SOC is responsible for a change in the overall appearance of electronic spectra. Due to a different origin of the SO spectrum relative to its SF counterpart, absorption bands are weakened and broadened and also emission bands consist of transitions from several SO states. The three lowest SO states are identified as sublevels of the lowest spin-free triplet state, in line with the ZFS concept. The high density of spin-mixed states enables multiple electronic and vibrational excitation of a molecule, as well as efficient electronic relaxation of populated SO states, which is realized by going down through manifold crossings and conical intersections between closely-spaced

lower-lying SO states that are vibronically coupled. These observations have been semiquantitatively confirmed by our calculations<sup>27,92</sup> as well as by many other previous computational studies of organometallic compounds.<sup>174–177,209,210</sup>

Traditionally, the classification of electronic states and spectral properties in closed-shell molecules is based on the convention which says that excited states are either pure singlets or pure triplets. In my opinion, one of the interesting conclusions deduced from our calculations concerns the impossibility of unambiguous assigning spin multiplicity to a particular SO state. When strong SOC is introduced, majority of SO states originate from a large mixing of spin-free singlet and triplet states. Seen from this perspective, the difference between fluorescence and phosphorescence, or between internal conversion and intersystem crossing would be washed away to some extent. Therefore a unified point of view should be adopted. The information extracted from our calculations is potentially useful in gaining better control of excited-state dynamics in rhenium(I) tricarbonyl complexes. This is, in turn, vital for their various photonic applications such as OLEDs.

Regarding rhenium(I) tricarbonyl complexes with halide ligands, both spin-free and spin-orbit theoretical UV–vis spectra calculated by means of the MS-CASPT2 and TD-DFT techniques are in qualitative agreement with the experimental absorption spectra. However, only the inclusion of SOC can explain all the spectroscopic features, counting the two low-energy shoulders which are attributed to transitions to spin-mixed states and which could not be interpreted on the basis of the previous spin-free (TD-DFT) results.<sup>28,168</sup> The lowest-energy band maximum is assigned to the pure singlet  $b^1A'$  state in the SF spectrum, whereas in the SO model it is only partly of a singlet origin, namely 88% in the Cl, 81% in the Br and 58% in the I complex (SO-TD-DFT). The decreasing trend of singlet contributions corresponds well with the decreasing band maximum intensity when going from Cl to I. The experimental discovery<sup>28</sup> of ultrafast ISCs from the lowest optically predominantly populated  $^1MLCT$  state to the two emissive  $^3MLCT$  states is viewed from the SO standpoint. The fluorescence decay kinetics is found to be at least biexponential, whereby the multitude of various processes can occur after optical excitation, which is ensured by the high-density of spin-mixed states supported by our calculations. The long-lived phosphorescence comes mainly from the SO  $cA'$  state. Moreover, the temperature dependence of phosphorescence decay parameters is successfully described based on SOC considerations, revealing the occurrence of the deactivating, thermally populated SO  $bA''$  state, whose prevailing singlet character enables a nonradiative decay to the ground state. The singlet origin of the  $bA''$  state decreases in a row  $Cl > Br > I$ , which explains the increasing trend of emission lifetimes from the Cl to the I complex.

Another project concerning the  $[Re(imidazole)(CO)_3(phen)]^+$  complex aims to look into the dynamics and evolution of excited states of this system and to interpret available experimental data including ultrafast spectroscopic measurements (TRIR etc.).<sup>26</sup> On the one hand, the spin-free model consisting of the customary sets of singlet and triplet states is briefly presented. It provides a simple and reasonable description of basic photophysical behaviour induced by optical excitation, however, there are issues such as the temperature-dependent emission decay, various ps relaxation times, two different TRIR signals etc. which cannot be explained by the SF model. On the other hand, the SO model characterized by manifold spin-mixed states is developed. Three sets of SO states calculated at the optimized



geometries of three different and most significant spin-free states in the scheme are examined, putting emphasis on investigating the influence of structural changes on characters and emissivity of SO states. The SO approach is able to elucidate majority of these experimental observations, or at least to propose possible and plausible hypotheses. With the help of the SO model the principal photophysical features (i.e. prompt/long-lived emission, electronic/vibrational relaxation, nonradiative transitions, equilibration among the lowest SO states) and detected time constants can be associated with particular processes and SO states. The intermediate emission is assigned to the fourth bA" state, which could also decay nonradiatively to the ground state when thermally populated and thus could play a role in the temperature-dependent quenching of emission.

Finally, general issues related to computational methods used in these projects will be discussed. When we draw a comparison between the performances and outcomes of the SO-MS-CASPT2 and SO-TD-DFT approaches applied to our systems, one might get an overall impression that TD-DFT is a more accurate method than CASPT2, since, when compared to the experimental data, it is usually in better agreement than CASPT2. This is in apparent contradiction with a common assumption that *ab initio* methods (such as CASPT2) are of superior quality to methods based on various parametrizations and approximations (TD-DFT with a chosen functional tailored to a concrete chemical problem). At the preparatory stage of our projects the CASPT2 technique seemed to be very promising and appealing and in literature listed test applications encouraged us to use this method also for our systems. However, our initial enthusiasm eventually turned a bit sour, since our CASSCF/CASPT2 results did not live up to our great expectations. CASPT2 was not capable of describing spectral properties of the studied complexes as quantitatively as TD-DFT and as was originally expected. It can be partially ascribed to the observation that TD-DFT is very sensitive to the choice of an XC functional and once a reasonable candidate was found, TD-DFT yielded high-quality results. However, this search is a non-trivial task, in analogy to the selection of active space orbitals in CASSCF.

Another crucial issue concerns the role of a solvent. That was included only in the TD-DFT calculations. On the SO-MS-CASPT2 level of theory, isolated molecules were simulated just in vacuo, due to limitations given by the implementation of implicit solvent model in the Molcas package at that time. The direct comparison of the SO-TD-DFT results with and without solvent effect corrections has proven<sup>1</sup> that the incorporation of the actual solvent into a calculation reaches a markedly better agreement with experimental spectra. Moreover, as some of the studied transition metal complexes (such as carbonyl-diimine complexes) are strongly solvatochromic (i.e. the VIS and near-UV absorption bands are shifted to higher energies with the increasing polarity of solvent – as seen in Table 3.2), it seems to be questionable whether the vacuum-SO-MS-CASPT2 method is capable of providing a realistic insight into electronic excited states in condensed phases.

For the interpretation of absorption spectra, the equilibrium singlet GS geometry was used to determine energies and characters of all excited electronic states. On the one hand, it is a drastic approximation. On the other hand, the usage of a single common geometry for all states represents a computationally convenient and necessary solution. Furthermore, the Franck–Condon vertical transitions were considered in this doctoral thesis and thus employing of the optimized singlet GS geometry can be partly justified by the assumption that the

nuclear coordinates of the atoms constituting the complex are preserved during the transition. When we were interested in photophysical and emission data, the optimized geometries of relevant lowest-lying excited states were taken. In spite of this effort, our calculations are not able to capture all structural (and electronic) changes that are connected with transitions between different electronic states. Also, processes faster than a decay of higher excited states (e.g. ultrafast ( $\leq 10$  fs) intramolecular vibrational energy redistribution) cannot be described by the present approach.

When the literature over the last decade is checked, it is more than obvious that nowadays TD-DFT predominates in calculating excited states of medium-sized and large molecules and rivals successfully other single-reference theories, such as configuration interaction singles (CIS) and CASPT2. This can be to a large extent explained by the fact that at the CASSCF/CASPT2 level of theory we are severely restricted by the computational limits due to the size of our systems. Therefore we could not afford to improve our results by increasing the active space or to remedy basis set deficiencies by employing larger basis sets. Otherwise calculations would be too lengthy. Instead, a compromise has to be made between the feasibility of a calculation and the desired degree of accuracy.

Regarding the quality of our SO-MS-CASPT2 results, the preceding paragraphs may sound too pessimistic and critical. Hence one could ask why we did actually decide to apply the SO-MS-CASPT2 method to our systems. However, the question should be formulated in a different way – is there any better and at the same time computationally accessible approach to calculating transition metal complexes whose nature is immensely complicated and requires relativistic treatment? Firstly, there are certainly other computational alternatives (e.g. CI and CC techniques), but all of them have their pros and cons, and their usage for transition metal complexes has also its limitations. Secondly, it ought to be emphasized that the SO-TD-DFT method employing a solvent model and a suitable XC functional is able to provide a reasonable agreement and satisfactory interpretation of experimental data and it explains its wide use in the community. Thus, by means of SO-TD-DFT we have successfully developed the comprehensive SO model of excited states and their dynamics in rhenium tricarbonyl complexes. Lastly, we must stress that spin–orbit studies on these complex systems can be still considered as a bit pioneering and in this sense we did not know in advance if SO-MS-CASPT2 could perform as well, as was anticipated. Despite a lack of expected accuracy, SO-MS-CASPT2 still brings valuable information and our calculations were able to interpret the spectral and photophysical data in a qualitatively similar manner as SO-TD-DFT. To conclude, it can be stated that both theoretical approaches used in this thesis are qualitatively comparable and confirm the general SOC observations.

# BIBLIOGRAPHY

- (1) Vlček, A.; Zálaiš, S. Modeling of Charge-Transfer Transitions and Excited States in d6 Transition Metal Complexes by DFT Techniques. *Coord. Chem. Rev.* **2007**, *251* (3–4), 258–287.
- (2) Pyykko, P.; Desclaux, J. P. Relativity and the Periodic System of Elements. *Acc. Chem. Res.* **1979**, *12* (8), 276–281.
- (3) Pyykko, P. Relativistic Effects in Structural Chemistry. *Chem. Rev.* **1988**, *88* (3), 563–594.
- (4) Pyykko, P. Relativistic Effects in Chemistry: More Common Than You Thought. In *Annual Review of Physical Chemistry*; Johnson, MA and Martinez, T., Ed.; Annual Review of Physical Chemistry; Annual Reviews: 4139 El Camino Way, PO BOX 10139, Palo Alto, CA 94303-0897 USA, 2012; Vol. 63, pp 45–64.
- (5) Kober, E. M.; Meyer, T. J. An Electronic Structural Model for the Emitting MLCT Excited-States of Ru(bpy)<sub>3</sub><sup>2+</sup> and Os(bpy)<sub>3</sub><sup>2+</sup>. *Inorg. Chem.* **1984**, *23* (24), 3877–3886.
- (6) Kober, E. M.; Meyer, T. J. Concerning the Absorption-Spectra of the Ions M(bpy)<sub>3</sub><sup>2+</sup> (M=Fe,Ru,Os, bpy=2,2'-bipyridine). *Inorg. Chem.* **1982**, *21* (11), 3967–3977.
- (7) Ferguson, J.; Herren, F. A Model for the Interpretation of the Electronic-Spectra of the Complex-Ions M(bpy)<sub>2</sub><sup>3+</sup> (M=Fe,Ru,Os) in D<sub>3</sub> and C<sub>2</sub> Sites. *Chem. Phys.* **1983**, *76* (1), 45–59.
- (8) Daul, C.; Baerends, E. J.; Vernooijs, P. A Density-Functional Study of the MLCT States of [Ru(bpy)<sub>3</sub>]<sup>2+</sup> in D<sub>3</sub> Symmetry. *Inorg. Chem.* **1994**, *33* (16), 3538–3543.
- (9) Herzberg, G. *Molecular Spectra and Molecular Structure, Vol. III: Electronic Spectra and Electronic Structure of Polyatomic Molecules*; Van Nostrand: New York, 1966.
- (10) Rausch, A. F.; Homeier, H. H. H.; Yersin, H. Organometallic Pt(II) and Ir(III) Triplet Emitters for OLED Applications and the Role of Spin–Orbit Coupling: A Study Based on High-Resolution Optical Spectroscopy. *Top. Organomet. Chem.* **2010**, *29*, 193–235.
- (11) Yersin, H.; Rausch, A. F.; Czerwieniec, R.; Hofbeck, T.; Fischer, T. The Triplet State of Organo-Transition Metal Compounds. Triplet Harvesting and Singlet Harvesting for Efficient OLEDs. *Coord. Chem. Rev.* **2011**, *255* (21–22), 2622–2652.
- (12) Yersin, H.; Finkenzeller, W. J. In *Highly Efficient OLEDs with Phosphorescent Materials*; Yersin, H., Ed.; Wiley-VCH: Weinheim, Germany, 2008.
- (13) Yersin, H. *Triplet Emitters for OLED Applications. Mechanisms of Exciton Trapping and Control of Emission Properties; Topics in Current Chemistry. Transition Metal and Rare Earth Compounds*, Vol. 241.; Yersin, H., Ed.; Springer: New York, 2004.
- (14) Monat, J. E.; Rodriguez, J. H.; McCusker, J. K. Ground- and Excited-State Electronic Structures of the Solar Cell Sensitizer bis(4,4'-Dicarboxylato-2,2'-bipyridine)bis(isothiocyanato)ruthenium(II). *J. Phys. Chem. A* **2002**, *106* (32), 7399–7406.

- (15) Hagfeldt, A.; Grätzel, M. Molecular Photovoltaics. *Acc. Chem. Res.* **2000**, *33* (5), 269–277.
- (16) Lo, K. K. W. Exploitation of Luminescent Organometallic Rhenium(I) and iridium(III) Complexes in Biological Studies. *Top. Organomet. Chem.* **2010**, *29*, 115–158.
- (17) Lo, K. K.-W.; Louie, M.-W.; Zhang, K. Y. Design of Luminescent iridium(III) and rhenium(I) Polypyridine Complexes as in Vitro and in Vivo Ion, Molecular and Biological Probes. *Coord. Chem. Rev.* **2010**, *254* (21–22, SI), 2603–2622.
- (18) Lo, K. K.-W.; Tsang, K. H.-K.; Sze, K.-S.; Chung, C.-K.; Lee, T. K.-M.; Zhang, K. Y.; Hui, W.-K.; Li, C.-K.; Lau, J. S.-Y.; Ng, D. C.-M.; Zhu, N. Non-Covalent Binding of Luminescent Transition Metal Polypyridine Complexes to Avidin, Indole-Binding Proteins and Estrogen Receptors. *Coord. Chem. Rev.* **2007**, *251* (17–20), 2292–2310.
- (19) Blanco-Rodríguez, A. M.; Di Bilio, A. J.; Shih, C.; Museth, A. K.; Clark, I. P.; Towrie, M.; Cannizzo, A.; Sudhamsu, J.; Crane, B. R.; Sýkora, J.; Winkler, J. R.; Gray, H. B.; Zálíš, S.; Vlček, A. Phototriggering Electron Flow through ReI-Modified *Pseudomonas Aeruginosa* Azurins. *Chem. - A Eur. J.* **2011**, *17* (19), 5350–5361.
- (20) Shih, C.; Museth, A. K.; Abrahamsson, M.; Blanco-Rodríguez, A. M.; Di Bilio, A. J.; Sudhamsu, J.; Crane, B. R.; Ronayne, K. L.; Towrie, M.; Vlcek Jr., A.; Richards, J. H.; Winkler, J. R.; Gray, H. B. Tryptophan-Accelerated Electron Flow through Proteins. *Science* (80-. ). **2008**, *320* (5884), 1760–1762.
- (21) Kumar, A.; Sun, S. S.; Lees, A. J. Photophysics and Photochemistry of Organometallic Rhenium Diimine Complexes. *Top. Organomet. Chem.* **2010**, *29*, 1–35.
- (22) Lewis, J. D.; Moore, J. N. Cation Sensors Containing a (bpy)Re(CO)(3) Group Linked to an Azacrown Ether via an Alkenyl or Alkynyl Spacer: Synthesis, Characterisation, and Complexation with Metal Cations in Solution. *Dalt. Trans.* **2004**, No. 9, 1376–1385.
- (23) Takeda, H.; Ishitani, O. Development of Efficient Photocatalytic Systems for CO<sub>2</sub> Reduction Using Mononuclear and Multinuclear Metal Complexes Based on Mechanistic Studies. *Coord. Chem. Rev.* **2010**, *254* (3–4, SI), 346–354.
- (24) Hawecker, J.; Lehn, J. M.; Ziessel, R. Efficient Photochemical Reduction of CO<sub>2</sub> to CO by Visible-Light Irradiation of Systems Containing Re(bipy)(CO)<sub>3</sub>X or Ru(bipy)<sub>3</sub><sup>2+</sup>-CO<sub>2</sub>+ Combinations as Homogeneous Catalysts. *J. Chem. Soc. Commun.* **1983**, No. 9, 536–538.
- (25) Holten, D.; Bocian, D. F.; Lindsey, J. S. Probing Electronic Communication in Covalently Linked Multiporphyrin Arrays. A Guide to the Rational Design of Molecular Photonic Devices. *Acc. Chem. Res.* **2002**, *35* (1), 57–69.
- (26) El Nahhas, A.; Consani, C.; Blanco-Rodríguez, A. M.; Lancaster, K. M.; Braem, O.; Cannizzo, A.; Towrie, M.; Clark, I. P.; Zálíš, S.; Chergui, M.; Vlček, A. Ultrafast Excited-State Dynamics of Rhenium(I) Photosensitizers [Re(Cl)(CO)<sub>3</sub>(N,N)] and [Re(imidazole)(CO)<sub>3</sub>(N,N)]<sup>+</sup>: Diimine Effects. *Inorg. Chem.* **2011**, *50* (7), 2932–2943.
- (27) Heydová, R.; Gindensperger, E.; Romano, R.; Sýkora, J.; Vlček, A.; Zálíš, S.; Daniel, C. Spin–Orbit Treatment of UV–vis Absorption Spectra and Photophysics of

- Rhenium(I) Carbonyl–Bipyridine Complexes: MS-CASPT2 and TD-DFT Analysis. *J. Phys. Chem. A* **2012**, *116* (46), 11319–11329.
- (28) Cannizzo, A.; Blanco-Rodríguez, A. M.; El Nahhas, A.; Šebera, J.; Záliš, S.; Vlček, Jr., A.; Chergui, M. Femtosecond Fluorescence and Intersystem Crossing in Rhenium(I) Carbonyl–Bipyridine Complexes. *J. Am. Chem. Soc.* **2008**, *130* (28), 8967–8974.
- (29) Nahhas, A. El; Cannizzo, A.; Mourik, F. van; Blanco-Rodríguez, A. M.; Záliš, S.; Vlček, Jr., A.; Chergui, M. Ultrafast Excited-State Dynamics of [Re(L)(CO)3(bpy)] N Complexes: Involvement of the Solvent. *J. Phys. Chem. A* **2010**, *114* (22), 6361–6369.
- (30) Stufkens, D. J.; Vlček, A. Ligand-Dependent Excited State Behaviour of Re(I) and Ru(II) Carbonyl-Diimine Complexes. *Coord. Chem. Rev.* **1998**, *177*, 127–179.
- (31) Gawelda, W.; Cannizzo, A.; Pham, V.-T.; van Mourik, F.; Bressler, C.; Chergui, M. Ultrafast Nonadiabatic Dynamics of [FeII(bpy)3] 2+ in Solution. *J. Am. Chem. Soc.* **2007**, *129* (26), 8199–8206.
- (32) Cannizzo, A.; van Mourik, F.; Gawelda, W.; Zgrablic, G.; Bressler, C.; Chergui, M. Broadband Femtosecond Fluorescence Spectroscopy of [Ru(bpy)3]2+. *Angew. Chemie Int. Ed.* **2006**, *45* (19), 3174–3176.
- (33) Neese, F.; Petrenko, T.; Ganyushin, D.; Olbrich, G. Advanced Aspects of Ab Initio Theoretical Optical Spectroscopy of Transition Metal Complexes: Multiplets, Spin-Orbit Coupling and Resonance Raman Intensities. *Coord. Chem. Rev.* **2007**, *251* (3–4), 288–327.
- (34) Daniel, C. Electronic Spectroscopy and Photoreactivity in Transition Metal Complexes. *Coord. Chem. Rev.* **2003**, *238–239*, 143–166.
- (35) Blanco Rodríguez, A. M.; Gabrielsson, A.; Motevalli, M.; Matousek, P.; Towrie, M.; Šebera, J.; Záliš, S.; Vlček, A. Ligand-to-Diimine/Metal-to-Diimine Charge-Transfer Excited States of [Re(NCS)(CO)3(α-Diimine)] (α-Diimine = 2,2′-Bipyridine, Di- I Pr-N,N -1,4-Diazabutadiene). A Spectroscopic and Computational Study. *J. Phys. Chem. A* **2005**, *109* (23), 5016–5025.
- (36) Turki, M.; Daniel, C.; Zalis, S.; Vlcek, A.; van Slageren, J.; Stufkens, D. J. UV-Visible Absorption Spectra of [Ru(E)(E′)(CO)(2)(iPr-DAB)] (E = E′ = SnPh3 or Cl; E = SnPh3 or Cl, E′ = CH3; iPr-DAB = N,N′-Di-Isopropyl-1,4-Diaza-1,3-Butadiene): Combination of CASSCF/CASPT2 and TD-DFT Calculations. *J. Am. Chem. Soc.* **2001**, *123* (46), 11431–11440.
- (37) Gabrielsson, A.; Busby, M.; Matousek, P.; Towrie, M.; Hevia, E.; Cuesta, L.; Perez, J.; Zalis, S.; Vlcek Jr., A. Electronic Structure and Excited States of rhenium(I) Amido and Phosphido Carbonyl-Bipyridine Complexes Studied by Picosecond Time-Resolved IR Spectroscopy and DFT Calculations. *Inorg. Chem.* **2006**, *45* (24), 9789–9797.
- (38) Zalis, S.; Ben Amor, N.; Daniel, C. Influence of the Halogen Ligand on the near-UV-Visible Spectrum of [Ru(X)(Me)(CO)(2)((α-Diimine)] (X = Cl, I; Alpha-Diimine = Me-DAB, iPr-DAB; DAB=1,4-Diaza-1,3-Butadiene): An Ab Initio and TD-DFT Analysis. *Inorg. Chem.* **2004**, *43* (25), 7978–7985.
- (39) Ballhausen, C. J. *Introduction to Ligand Field Theory*; McGraw-Hill: New York, 1962.

- (40) Vlček, A. Ultrafast Excited-State Processes in Re(I) Carbonyl-Diimine Complexes: From Excitation to Photochemistry. *Top. Organomet. Chem.* **2010**, 29, 73–114.
- (41) Gamelin, D. R.; George, M. W.; Glyn, P.; Grevels, F. W.; Johnson, F. P. A.; Klotzbucher, W.; Morrison, S. L.; Russell, G.; Schaffner, K.; Turner, J. J. Structural Investigation of the Ground and Excited-States of  $\text{ClRe}(\text{CO})_3(4,4'\text{-bipyridyl})_2$  Using Vibrational Spectroscopy. *Inorg. Chem.* **1994**, 33 (15), 3246–3250.
- (42) Dattelbaum, D. M.; Omberg, K. M.; Schoonover, J. R.; Martin, R. L.; Meyer, T. J. Application of Time-Resolved Infrared Spectroscopy to Electronic Structure in Metal-to-Ligand Charge-Transfer Excited States. *Inorg. Chem.* **2002**, 41 (23), 6071–6079.
- (43) Rossenaar, B. D.; Stufkens, D. J.; Vlček Jr., A. Halide-Dependent Change of the Lowest-Excited-State Character from MLCT to XLCT for the Complexes  $\text{Re}(\text{X})(\text{CO})_3(\alpha\text{-Diimine})$  ( $\text{X} = \text{Cl}, \text{Br}, \text{I}$ ;  $\alpha\text{-Diimine} = \text{Bpy}, \text{iPr-PyCa}, \text{iPr-DAB}$ ) Studied by Resonance Raman, Time-Resolved Absorption, and Emission Spectroscopy. *Inorg. Chem.* **1996**, 35 (10), 2902–2909.
- (44) Blanco-Rodriguez, A. M.; Ronayne, K. L.; Zalis, S.; Sykora, J.; Hof, M.; Vlcek Jr., A. Solvation-Driven Excited-State Dynamics of  $[\text{Re}(\text{4-Et-Pyridine})(\text{CO})_3(2,2'\text{-Bipyridine})](+)$  in Imidazolium Ionic Liquids. A Time-Resolved Infrared and Phosphorescence Study. *J. Phys. Chem. A* **2008**, 112 (16), 3506–3514.
- (45) Blanco-Rodriguez, A. M.; Towrie, M.; Collin, J.-P.; Zalis, S.; Vlcek Jr., A. Excited-State Relaxation Dynamics of Re(I) Tricarbonyl Complexes with Macrocyclic Phenanthroline Ligands Studied by Time-Resolved IR Spectroscopy. *Dalt. Trans.* **2009**, No. 20, 3941–3949.
- (46) Alary, F.; Heully, J.-L.; Bijeire, L.; Vicendo, P. Is the (MLCT)-M-3 the Only Photoreactive State of Polypyridyl Complexes? *Inorg. Chem.* **2007**, 46 (8), 3154–3165.
- (47) Consani, C.; Premont-Schwarz, M.; ElNahhas, A.; Bressler, C.; van Mourik, F.; Cannizzo, A.; Chergui, M. Vibrational Coherences and Relaxation in the High-Spin State of Aqueous  $[\text{Fe-II}(\text{bpy})(3)](2+)$ . *Angew. Chemie-International Ed.* **2009**, 48 (39), 7184–7187.
- (48) Schrauben, J. N.; Dillman, K. L.; Beck, W. F.; McCusker, J. K. Vibrational Coherence in the Excited State Dynamics of  $\text{Cr}(\text{acac})_3$ : Probing the Reaction Coordinate for Ultrafast Intersystem Crossing. *Chem. Sci.* **2010**, 1 (3), 405–410.
- (49) Pitzer, K. S. Relativistic Effects on Chemical Properties. *Acc. Chem. Res.* **1979**, 12 (8), 272–276.
- (50) Visscher, L.; van Lenthe, E. On the Distinction between Scalar and Spin-Orbit Relativistic Effects. *Chem. Phys. Lett.* **1999**, 306 (5–6), 357–365.
- (51) Dirac, P. A. M. The Quantum Theory of the Electron. *Proc. R. Soc. London A Math. Phys. Eng. Sci.* **1928**, 117 (778), 610–624.
- (52) Dirac, P. A. M. The Quantum Theory of the Electron. Part II. *Proc. R. Soc. London A Math. Phys. Eng. Sci.* **1928**, 118 (779), 351–361.
- (53) Dylla, K. G.; Faegri Jr., K. *Introduction to Relativistic Quantum Chemistry*; Oxford University Press: New York, 2007.

- (54) Visscher, L. Fundamentals. In *Relativistic Electronic Structure Theory*; Schwerdtfeger, P., Ed.; Elsevier: Amsterdam, 2002; pp 291–331.
- (55) Saue, T. Relativistic Hamiltonians for Chemistry: A Primer. *ChemPhysChem* **2011**, *12* (17), 3077–3094.
- (56) Liu, W. Ideas of Relativistic Quantum Chemistry. *Mol. Phys.* **2010**, *108* (13), 1679–1706.
- (57) Foldy, L. L.; Wouthuysen, S. A. On the Dirac Theory of Spin 1/2 Particles and Its Non-Relativistic Limit. *Phys. Rev.* **1950**, *78* (1), 29–36.
- (58) Douglas, M.; Kroll, N. M. Quantum Electrodynamical Corrections to the Fine Structure of Helium. *Ann. Phys. (N. Y.)* **1974**, *82* (1), 89–155.
- (59) Hess, B. A. Applicability of the No-Pair Equation with Free-Particle Projection Operators to Atomic and Molecular-Structure Calculations. *Phys. Rev. A* **1985**, *32* (2), 756–763.
- (60) Wahlgren, U.; Schimmelpfennig, B.; Jusuf, S.; Stromsnes, H.; Gropen, O.; Maron, L. A Local Approximation for Relativistic Scalar Operators Applied to the Uranyl Ion and to Au-2. *Chem. Phys. Lett.* **1998**, *287* (5–6), 525–530.
- (61) Hess, B. A. Relativistic Electronic-Structure Calculations Employing a Two-Component No-Pair Formalism with External-Field Projection Operators. *Phys. Rev. A* **1986**, *33* (6), 3742–3748.
- (62) Jansen, G.; Hess, B. A. Revision of the Douglas-Kroll Transformation. *Phys. Rev. A* **1989**, *39* (11), 6016–6017.
- (63) van Lenthe, E.; Baerends, E. J.; Snijders, J. G. Relativistic Regular 2-Component Hamiltonians. *J. Chem. Phys.* **1993**, *99* (6), 4597–4610.
- (64) van Lenthe, E.; Snijders, J. G.; Baerends, E. J. The Zero-Order Regular Approximation for Relativistic Effects: The Effect of Spin-Orbit Coupling in Closed Shell Molecules. *J. Chem. Phys.* **1996**, *105* (15), 6505–6516.
- (65) van Lenthe, E.; Baerends, E. J.; Snijders, J. G. Relativistic Total-Energy Using Regular Approximations. *J. Chem. Phys.* **1994**, *101* (11), 9783–9792.
- (66) Nakajima, T.; Hirao, K. The Higher-Order Douglas-Kroll Transformation. *J. Chem. Phys.* **2000**, *113* (18), 7786–7789.
- (67) Chang, C.; Pelissier, M.; Durand, P. Regular 2-Component Pauli-like Effective-Hamiltonians in Dirac Theory. *Phys. Scr.* **1986**, *34* (5), 394–404.
- (68) Dylla, K. G.; van Lenthe, E. Relativistic Regular Approximations Revisited: An Infinite-Order Relativistic Approximation. *J. Chem. Phys.* **1999**, *111* (4), 1366–1372.
- (69) Andrae, D.; Haussermann, U.; Dolg, M.; Stoll, H.; Preuss, H. Energy-Adjusted Abinitio Pseudopotentials for the 2nd and 3rd Row Transition-Elements. *Theor. Chim. Acta* **1990**, *77* (2), 123–141.
- (70) Stevens, W. J.; Krauss, M.; Basch, H.; Jasien, P. G. Relativistic Compact Effective Potentials and Efficient, Shared-Exponent Basis-Sets for the 3rd-Row, 4th-Row, and

- 5th-Row Atoms. *Can. J. Chem. Can. Chim.* **1992**, 70 (2), 612–630.
- (71) van Lenthe, E.; Ehlers, A.; Baerends, E.-J. Geometry Optimizations in the Zero Order Regular Approximation for Relativistic Effects. *J. Chem. Phys.* **1999**, 110 (18), 8943–8953.
- (72) Cao, X.; Dolg, M. Relativistic Pseudopotentials. In *Relativistic methods for chemists*; Barysz, M and Ishikawa, Y., Ed.; Challenges and Advances in Computational Chemistry and Physics; Springer: PO BOX 17, 3300 AA Dordrecht, Netherlands, 2010; Vol. 10, pp 215–277.
- (73) Roos, B. O.; Lindh, R.; Malmqvist, P.-Å.; Veryazov, V.; Widmark, P.-O. New Relativistic ANO Basis Sets for Transition Metal Atoms. *J. Phys. Chem. A* **2005**, 109 (29), 6575–6579.
- (74) Roos, B. O.; Lindh, R.; Malmqvist, P.-Å.; Veryazov, V.; Widmark, P.-O. Main Group Atoms and Dimers Studied with a New Relativistic ANO Basis Set. *J. Phys. Chem. A* **2004**, 108 (15), 2851–2858.
- (75) Veryazov, V.; Widmark, P.-O.; Roos, B. O. Relativistic Atomic Natural Orbital Type Basis Sets for the Alkaline and Alkaline-Earth Atoms Applied to the Ground-State Potentials for the Corresponding Dimers. *Theor. Chem. Accounts Theory, Comput. Model. (Theoretica Chim. Acta)* **2004**, 111 (2–6), 345–351.
- (76) Kaltsoyannis, N. Relativistic Effects in Inorganic and Organometallic Chemistry. *J. Chem. Soc. Dalt. Trans.* **1997**, No. 1, 1–12.
- (77) Bethe, H.; Salpeter, E. *Quantum Mechanics of One- and Two-Electron Atoms*; Springer: Berlin, 1957.
- (78) Schaefer III, H. F. *Applications of Electronic Structure Theory*; Plenum Press: New York, 1977.
- (79) Hess, B. A.; Marian, C. M.; Wahlgren, U.; Gropen, O. A Mean-Field Spin-Orbit Method Applicable to Correlated Wavefunctions. *Chem. Phys. Lett.* **1996**, 251 (5–6), 365–371.
- (80) Cotton, F. A. *Chemical Applications of Group Theory*, 3rd edn.; Wiley-Interscience: New York, 1991.
- (81) Salthouse, J. A.; Ware, M. J. *Point Group Character Tables and Related Data*; Cambridge University Press: London, 1972.
- (82) Aquilante, F.; De Vico, L.; Ferré, N.; Ghigo, G.; Malmqvist, P.-A.; Neogrády, P.; Pedersen, T. B.; Pitonák, M.; Reiher, M.; Roos, B. O.; Serrano-Andrés, L.; Urban, M.; Veryazov, V.; Lindh, R. MOLCAS 7: The next Generation. *J. Comput. Chem.* **2010**, 31 (1), 224–247.
- (83) URL: <http://www.molcas.org>.
- (84) Veryazov, V.; Widmark, P.-O.; Serrano-Andrés, L.; Lindh, R.; Roos, B. O. 2MOLCAS as a Development Platform for Quantum Chemistry Software. *Int. J. Quantum Chem.* **2004**, 100 (4), 626–635.



- (85) Wang, F.; Ziegler, T.; van Lenthe, E.; van Gisbergen, S.; Baerends, E. J. The Calculation of Excitation Energies Based on the Relativistic Two-Component Zeroth-Order Regular Approximation and Time-Dependent Density-Functional with Full Use of Symmetry. *J. Chem. Phys.* **2005**, *122* (20), 204103.
- (86) Wang, F.; Ziegler, T. A Simplified Relativistic Time-Dependent Density-Functional Theory Formalism for the Calculations of Excitation Energies Including Spin-Orbit Coupling Effect. *J. Chem. Phys.* **2005**, *123* (15), 154102.
- (87) te Velde, G.; Bickelhaupt, F. M.; Baerends, E. J.; Fonseca Guerra, C.; van Gisbergen, S. J. A.; Snijders, J. G.; Ziegler, T. Chemistry with ADF. *J. Comput. Chem.* **2001**, *22* (9), 931–967.
- (88) ADF2010, SCM. Theoretical Chemistry, Vrije Universiteit: Amsterdam, The Netherlands.
- (89) Guerra, C. F.; Snijders, J. G.; te Velde, G.; Baerends, E. J. Towards an Order-N DFT Method. *Theor. Chem. Acc.* **1998**, *99* (6), 391–403.
- (90) Obara, S.; Itabashi, M.; Okuda, F.; Tamaki, S.; Tanabe, Y.; Ishii, Y.; Nozaki, K.; Haga, M. Highly Phosphorescent Iridium Complexes Containing Both Tridentate Bis(benzimidazolyl)-Benzene or -Pyridine and Bidentate Phenylpyridine: Synthesis, Photophysical Properties, and Theoretical Study of Ir-Bis(benzimidazolyl)benzene Complex. *Inorg. Chem.* **2006**, *45* (22), 8907–8921.
- (91) Siddique, Z. A.; Yamamoto, Y.; Ohno, T.; Nozaki, K. Structure-Dependent Photophysical Properties of Singlet and Triplet Metal-to-Ligand Charge Transfer States in copper(I) Bis(diimine) Compounds. *Inorg. Chem.* **2003**, *42* (20), 6366–6378.
- (92) Baková, R.; Chergui, M.; Daniel, C.; Vlček Jr., A.; Zális, S. Relativistic Effects in Spectroscopy and Photophysics of Heavy-Metal Complexes Illustrated by Spin-orbit Calculations of [Re(imidazole)(CO)<sub>3</sub>(phen)]<sup>+</sup>. *Coord. Chem. Rev.* **2011**, *255* (7–8), 975–989.
- (93) JABŁOŃSKI, A. Efficiency of Anti-Stokes Fluorescence in Dyes. *Nature* **1933**, *131* (3319), 839–840.
- (94) URL: [http://www.shsu.edu/chm\\_tgc/chemilumdir/JABLONSKI.html](http://www.shsu.edu/chm_tgc/chemilumdir/JABLONSKI.html).
- (95) Connick, W. B.; DiBilio, A. J.; Hill, M. G.; Winkler, J. R.; Gray, H. B. Tricarbonyl(1,10-phenanthroline)(imidazole)rhenium(I): A Powerful Photooxidant for Investigations of Electron Tunneling in Proteins. *Inorganica Chim. Acta* **1995**, *240* (1–2), 169–173.
- (96) Bhasikuttan, A. C.; Suzuki, M.; Nakashima, S.; Okada, T. Ultrafast Fluorescence Detection in Tris(2,2'-bipyridine)ruthenium(II) Complex in Solution: Relaxation Dynamics Involving Higher Excited States. *J. Am. Chem. Soc.* **2002**, *124* (28), 8398–8405.
- (97) Vlcek, A.; Farrell, I. R.; Liard, D. J.; Matousek, P.; Towrie, M.; Parker, A. W.; Grills, D. C.; George, M. W. Early Photochemical Dynamics of Organometallic Compounds Studied by Ultrafast Time-Resolved Spectroscopic Techniques. *J. Chem. Soc. Trans.* **2002**, No. 5, 701–712.

- (98) Schoonover, J. R.; Strouse, G. F. Time-Resolved Vibrational Spectroscopy of Electronically Excited Inorganic Complexes in Solution. *Chem. Rev.* **1998**, 98 (4), 1335–1355.
- (99) Kuimova, M. K.; Alsindi, W. Z.; Dyer, J.; Grills, D. C.; Jina, O. S.; Matousek, P.; Parker, A. W.; Portius, P.; Sun, X. Z.; Towrie, M.; Wilson, C.; Yang, J. X.; George, M. W. Using Picosecond and Nanosecond Time-Resolved Infrared Spectroscopy for the Investigation of Excited States and Reaction Intermediates of Inorganic Systems. *Dalt. Trans.* **2003**, No. 21, 3996–4006.
- (100) Bredenbeck, J.; Helbing, J.; Hamm, P. Labeling Vibrations by Light: Ultrafast Transient 2D-IR Spectroscopy Tracks Vibrational Modes during Photoinduced Charge Transfer. *J. Am. Chem. Soc.* **2004**, 126 (4), 990–991.
- (101) Perić, M.; Engels, B.; Peyerimhoff, S. D. *Quantum Mechanical Structure Calculations with Chemical Accuracy*; Langhoff, S. R., Ed.; Kluwer Academic Publishers: Dordrecht, The Netherlands, 1995.
- (102) Roos, B. O.; Fülcher, M. P.; Malmqvist, P.-A.; Merchán, M.; Serrano-Andrés, L. Theoretical Studies of Electronic Spectra of Organic Molecules. In *Quantum Mechanical Electronic Structure Calculations with Chemical Accuracy*; Langhoff, S. R., Ed.; Kluwer Academic Publishers: Dordrecht, The Netherlands, 1995; pp 357–438.
- (103) Stanton, J. F.; Bartlett, R. J. The Equation of Motion Coupled-Cluster Method. A Systematic Biorthogonal Approach to Molecular Excitation Energies, Transition Probabilities, and Excited State Properties. *J. Chem. Phys.* **1993**, 98 (9), 7029–7039.
- (104) Onida, G.; Reining, L.; Rubio, A. Electronic Excitations: Density-Functional versus Many-Body Green's-Function Approaches. *Rev. Mod. Phys.* **2002**, 74 (2), 601–659.
- (105) Frisch, M. J.; Trucks, G. W.; Schlegel, H. B.; Scuseria, G. E.; Robb, M. A.; Cheeseman, J. R.; Scalmani, G.; Barone, V.; Mennucci, B.; Petersson, G. A.; Nakatsuji, H.; Caricato, M.; Li, X.; Hratchian, H. P.; Izmaylov, A. F.; Bloino, J.; Zheng, G.; Sonnenberg, J. L.; Hada, M.; Ehara, M.; Toyota, K.; Fukuda, R.; Hasegawa, J.; Ishida, M.; Nakajima, T.; Honda, Y.; Kitao, O.; Nakai, H.; Vreven, T.; Montgomery Jr., J. A.; Peralta, J. E.; Ogliaro, F.; Bearpark, M.; Heyd, J. J.; Brothers, E.; Kudin, K. N.; Staroverov, V. N.; Kobayashi, R.; Normand, J.; Raghavachari, K.; Rendell, A.; Burant, J. C.; Iyengar, S. S.; Tomasi, J.; Cossi, M.; Rega, N.; Millam, J. M.; Klene, M.; Knox, J. E.; Cross, J. B.; Bakken, V.; Adamo, C.; Jaramillo, J.; Gomperts, R.; Stratmann, R. E.; Yazyev, O.; Austin, A. J.; Cammi, R.; Pomelli, C.; Ochterski, J. W.; Martin, R. L.; Morokuma, K.; Zakrzewski, V. G.; Voth, G. A.; Salvador, P.; Dannenberg, J. J.; Dapprich, S.; Daniels, A. D.; Farkas, O.; Foresman, J. B.; Ortiz, J. V.; Cioslowski, J.; Fox, D. J. Gaussian 09, Revision A.02. Wallingford, CT 2009.
- (106) Frisch, M. J.; Trucks, G. W.; Schlegel, H. B.; Scuseria, G. E.; Robb, M. A.; Cheeseman, J. R.; Scalmani, G.; Barone, V.; Mennucci, B.; Petersson, G. A.; Nakatsuji, H.; Caricato, M.; Li, X.; Hratchian, H. P.; Izmaylov, A. F.; Bloino, J.; Zheng, G.; Sonnenberg, J. L.; Hada, M.; Ehara, M.; Toyota, K.; Fukuda, R.; Hasegawa, J.; Ishida, M.; Nakajima, T.; Honda, Y.; Kitao, O.; Nakai, H.; Vreven, T.; Montgomery Jr., J. A.; Peralta, J. E.; Ogliaro, F.; Bearpark, M.; Heyd, J. J.; Brothers, E.; Kudin, K. N.; Staroverov, V. N.; Kobayashi, R.; Normand, J.; Raghavachari, K.; Rendell, A.; Burant, J. C.; Iyengar, S. S.; Tomasi, J.; Cossi, M.; Rega, N.; Millam, J. M.; Klene, M.; Knox,

- J. E.; Cross, J. B.; Bakken, V.; Adamo, C.; Jaramillo, J.; Gomperts, R.; Stratmann, R. E.; Yazyev, O.; Austin, A. J.; Cammi, R.; Pomelli, C.; Ochterski, J. W.; Martin, R. L.; Morokuma, K.; Zakrzewski, V. G.; Voth, G. A.; Salvador, P.; Dannenberg, J. J.; Dapprich, S.; Daniels, A. D.; Farkas, O.; Foresman, J. B.; Ortiz, J. V.; Cioslowski, J.; Fox, D. J. Gaussian 09, Revision A.01. Wallingford, CT 2009.
- (107) Roos, B. O.; Taylor, P. R.; Siegbahn, P. E. M. A Complete Active Space SCF Method (CASSCF) Using a Density Matrix Formulated Super-CI Approach. *Chem. Phys.* **1980**, *48* (2), 157–173.
- (108) Finley, J.; Malmqvist, P.-Å.; Roos, B. O.; Serrano-Andrés, L. The Multi-State CASPT2 Method. *Chem. Phys. Lett.* **1998**, *288* (2–4), 299–306.
- (109) Roos, B. O.; Malmqvist, P.-Å. Relativistic Quantum Chemistry: The Multiconfigurational Approach. *Phys. Chem. Chem. Phys.* **2004**, *6* (11), 2919–2927.
- (110) Hartree, D. R. The Wave Mechanics of an Atom with a Non-Coulomb Central Field. Part I. Theory and Methods. *Math. Proc. Cambridge Philos. Soc.* **1928**, *24* (1), 89–110.
- (111) Fock, V. Näherungsmethode Zur Lösung Des Quantenmechanischen Mehrkörperproblems. *Zeitschrift für Phys.* **1930**, *61* (1–2), 126–148.
- (112) Kohn, W.; Sham, L. J. Self-Consistent Equations Including Exchange and Correlation Effects. *Phys. Rev.* **1965**, *140* (4A), A1133–A1138.
- (113) Hohenberg, P.; Kohn, W. Inhomogeneous Electron Gas. *Phys. Rev.* **1964**, *136* (3B), B864–B871.
- (114) Parr, R. G.; Yang, W. *Density-Functional Theory of Atoms and Molecules*; Oxford University Press: New York, 1989.
- (115) Roos, B. O. The Complete Active Space Self-Consistent Field Method and Its Applications in Electronic Structure Calculations. In *Advances in Chemical Physics; Ab Initio Methods in Quantum Chemistry*; Lawley, K. P., Ed.; John Wiley & Sons, Ltd.: Chichester, England/New York, 1987; p 399.
- (116) Knowles, P. J.; Werner, H.-J. An Efficient Second-Order MC SCF Method for Long Configuration Expansions. *Chem. Phys. Lett.* **1985**, *115* (3), 259–267.
- (117) Malmqvist, P. A.; Rendell, A.; Roos, B. O. The Restricted Active Space Self-Consistent-Field Method, Implemented with a Split Graph Unitary Group Approach. *J. Phys. Chem.* **1990**, *94* (14), 5477–5482.
- (118) Roos, B. The Complete Active Space SCF Method in a Fock-Matrix-Based Super-CI Formulation. *Int. J. Quantum Chem.* **1980**, *17*, 175–189.
- (119) Roos, B. O.; Andersson, K.; Fülcher, M. P.; Malmqvist, P.-Å.; Serrano-Andrés, L.; Pierloot, K.; Merchán, M. Multiconfiguration Perturbation Theory: Applications in Electronic Spectroscopy. In *Advances in Chemical Physics: New Methods in Computational Quantum Mechanics*; Prigogine, I., Rice, S. A., Eds.; John Wiley & Sons, Ltd.: New York, 1996; pp 219–332.
- (120) Andersson, K.; Malmqvist, P. A.; Roos, B. O.; Sadlej, A. J.; Wolinski, K. Second-Order Perturbation Theory with a CASSCF Reference Function. *J. Phys. Chem.* **1990**,

- 94 (14), 5483–5488.
- (121) Andersson, K.; Malmqvist, P.-Å.; Roos, B. O. Second-Order Perturbation Theory with a Complete Active Space Self-Consistent Field Reference Function. *J. Chem. Phys.* **1992**, 96 (2), 1218–1226.
- (122) Wolinski, K.; Pulay, P. Generalized Møller–Plesset Perturbation Theory: Second Order Results for Two-Configuration, Open-Shell Excited Singlet, and Doublet Wave Functions. *J. Chem. Phys.* **1989**, 90 (7), 3647–3659.
- (123) Wolinski, K.; Sellers, H. L.; Pulay, P. Consistent Generalization of the Møller-Plesset Partitioning to Open-Shell and Multiconfigurational SCF Reference States in Many-Body Perturbation Theory. *Chem. Phys. Lett.* **1987**, 140 (3), 225–231.
- (124) Roos, B. O.; Linse, P.; Siegbahn, P. E. M.; Blomberg, M. R. A. A Simple Method for the Evaluation of the Second-Order-Perturbation Energy from External Double-Excitations with a CASSCF Reference Wavefunction. *Chem. Phys.* **1982**, 66 (1–2), 197–207.
- (125) Levy, B.; Berthier, G. Generalized Brillouin Theorem for multiconfigurational SCF Theories. *Int. J. Quantum Chem.* **1968**, 2 (2), 307–319.
- (126) Brillouin, L. La Méthode Du Champ Self-Consistent. *Actual. Sci. Ind.* **1933**, 71.
- (127) Møller, C.; Plesset, M. S. Note on an Approximation Treatment for Many-Electron Systems. *Phys. Rev.* **1934**, 46 (7), 618–622.
- (128) Andersson, K.; Roos, B. O. Multiconfigurational Second-Order Perturbation Theory: A Test of Geometries and Binding Energies. *Int. J. Quantum Chem.* **1993**, 45 (6), 591–607.
- (129) Ghigo, G.; Roos, B. O.; Malmqvist, P.-Å. A Modified Definition of the Zeroth-Order Hamiltonian in Multiconfigurational Perturbation Theory (CASPT2). *Chem. Phys. Lett.* **2004**, 396 (1–3), 142–149.
- (130) Roos, B. O.; Andersson, K. Multiconfigurational Perturbation Theory with Level Shift — the Cr2 Potential Revisited. *Chem. Phys. Lett.* **1995**, 245 (2–3), 215–223.
- (131) Roos, B.; Andersson, K.; Fulscher, M.; Serrano Andres, L.; Pierloot, K.; Merchán, M.; Molina, V. Applications of Level Shift Corrected Perturbation Theory in Electronic Spectroscopy. *J. Mol. Struct.* **1996**, 388, 257–276.
- (132) Malrieu, J.; Heully, J.; Zaitsevskii, A. Multiconfigurational 2nd-Order Perturbative Methods - Overview and Comparison of Basic Properties. *Theor. Chim. Acta* **1995**, 90 (2–3), 167–187.
- (133) Zaitsevskii, A.; Malrieu, J.-P. Multi-Partitioning Quasidegenerate Perturbation Theory. A New Approach to Multireference Møller-Plesset Perturbation Theory. *Chem. Phys. Lett.* **1995**, 233 (5–6), 597–604.
- (134) Malmqvist, P.-Å.; Roos, B. O. The CASSCF State Interaction Method. *Chem. Phys. Lett.* **1989**, 155 (2), 189–194.
- (135) Malmqvist, P. A. Calculation of Transition Density Matrices by Nonunitary Orbital

- Transformations. *Int. J. Quantum Chem.* **1986**, 30 (4), 479–494.
- (136) Fagerli, H.; Schimmelpfennig, B.; Gropen, O.; Wahlgren, U. Spin-Orbit Effects in the PtH<sub>2</sub><sup>+</sup> Ion. *J. Mol. Struct. THEOCHEM* **1998**, 451 (1–2, SI), 227–235.
- (137) Karlstrom, G.; Malmqvist, P. A. An Abinitio Study of Aqueous Fe(2<sup>+</sup>)-Fe(3<sup>+</sup>) Electron-Transfer. *J. Chem. Phys.* **1992**, 96 (8), 6115–6119.
- (138) Malmqvist, P. Å.; Roos, B. O.; Schimmelpfennig, B. The Restricted Active Space (RAS) State Interaction Approach with Spin–orbit Coupling. *Chem. Phys. Lett.* **2002**, 357 (3–4), 230–240.
- (139) Shavitt, I. Graph Theoretical Concepts for Unitary Group Approach to Many-Electron Correlation Problem. *Int. J. Quantum Chem.* **1977**, No. Y-11, 131–148.
- (140) Shavitt, I. Matrix Element Evaluation in the Unitary Group Approach to the Electron Correlation Problem. *Int. J. Quantum Chem.* **1978**, 12 (12), 5–32.
- (141) Marian, C. M.; Wahlgren, U. A New Mean-Field and ECP-Based Spin-Orbit Method. Applications to Pt and PtH. *Chem. Phys. Lett.* **1996**, 251 (5–6), 357–364.
- (142) Schimmelpfennig, B. AMFI - An Atomic Mean Field Integral Program. University of Stockholm: Stockholm, Sweden 1996.
- (143) Christiansen, O.; Gauss, J.; Schimmelpfennig, B. Spin-Orbit Coupling Constants from Coupled-Cluster Response Theory. *Phys. Chem. Chem. Phys.* **2000**, 2 (5), 965–971.
- (144) Runge, E.; Gross, E. K. U. Density-Functional Theory for Time-Dependent Systems. *Phys. Rev. Lett.* **1984**, 52 (12), 997–1000.
- (145) van Leeuwen, R. Key Concepts in Time-Dependent Density-Functional Theory. *Int. J. Mod. Phys. B* **2001**, 15 (14), 1969–2023.
- (146) Burke, K.; Petersilka, M.; Gross, E. K. U. A Hybrid Functional for the Exchange-Correlation Kernel in Time-Dependent Density Functional Theory. In *Recent Advances in Density-Functional Methods*; Fantucci, P., Bencini, A., Eds.; World Scientific: Singapore, 2002; Vol. III, pp 67–79.
- (147) Laurent, A. D.; Jacquemin, D. TD-DFT Benchmarks: A Review. *Int. J. Quantum Chem.* **2013**, 113 (17), 2019–2039.
- (148) Casida, M. E. Time-Dependent Density-Functional Theory for Molecules and Molecular Solids. *J. Mol. Struct. THEOCHEM* **2009**, 914 (1–3), 3–18.
- (149) Jamorski, C.; Casida, M. E.; Salahub, D. R. Dynamic Polarizabilities and Excitation Spectra from a Molecular Implementation of Time-Dependent Density-Functional Response Theory: N<sub>2</sub> as a Case Study. *J. Chem. Phys.* **1996**, 104 (13), 5134–5147.
- (150) Bauernschmitt, R.; Ahlrichs, R. Treatment of Electronic Excitations within the Adiabatic Approximation of Time Dependent Density Functional Theory. *Chem. Phys. Lett.* **1996**, 256 (4–5), 454–464.
- (151) Charlot, M. F.; Pellegrin, Y.; Quaranta, A.; Leibl, W.; Aukauloo, A. A Theoretical Investigation into the Photophysical Properties of Ruthenium Polypyridine-Type Complexes. *Chem. Eur. J.* **2006**, 12 (3), 796–812.

- (152) Rosa, A.; Ricciardi, G.; Gritsenko, O.; Baerends, E. J. Excitation Energies of Metal Complexes with Time-Dependent Density Functional Theory. In *Principles and applications of density functional theory in inorganic chemistry I*; Structure and Bonding; Springer-Verlag Berlin: Heidelberger Platz 3, D-14197 Berlin, Germany, 2004; Vol. 112, pp 49–115.
- (153) Deb, B. M.; Ghosh, S. K. Schrödinger Fluid Dynamics of Many-Electron Systems in a Time-Dependent Density-Functional Framework. *J. Chem. Phys.* **1982**, *77* (1), 342–348.
- (154) Chakravarty, S.; Fogel, M. B.; Kohn, W. Dynamic Response of Inhomogeneous Fermi Systems. *Phys. Rev. Lett.* **1979**, *43* (11), 775–778.
- (155) Gross, E. K. U., Kohn, W. Time-Dependent Density-Functional Theory. *Adv. QUANTUM Chem.* **1990**, *21*, 255–291.
- (156) Gross, E.; Kohn, W. Local Density-Functional Theory of Frequency-Dependent Linear Response. *Phys. Rev. Lett.* **1985**, *55* (26), 2850–2852.
- (157) van Leeuwen, R. Causality and Symmetry in Time-Dependent Density-Functional Theory. *Phys. Rev. Lett.* **1998**, *80* (6), 1280–1283.
- (158) Vignale, G. Real-Time Resolution of the Causality Paradox of Time-Dependent Density-Functional Theory. *Phys. Rev. A* **2008**, *77* (6), 62511.
- (159) Gross, E. K. U.; Dobson, J. F.; Petersilka, M. Density Functional Theory of Time-Dependent Phenomena. In *Density functional theory II*; Topics in Current Chemistry; Springer-Verlag Berlin: Heidelberger Platz 3, W-1000 Berlin 33, Germany, 1996; Vol. 181, pp 81–172.
- (160) Petersilka, M.; Gossmann, U.; Gross, E. Excitation Energies from Time-Dependent Density-Functional Theory. *Phys. Rev. Lett.* **1996**, *76* (8), 1212–1215.
- (161) Casida, M. E. Time-Dependent Density-Functional Response Theory For Molecules. In *Recent Advances in Density Functional Methods*; Chong, D. P., Ed.; World Scientific: Singapore, 1995; pp 155–192.
- (162) Casida, M. E. *Recent Developments and Applications of Modern Density Functional Theory*; Seminario, J. M., Ed.; Theoretical and Computational Chemistry; Elsevier, 1996; Vol. 4.
- (163) Stratmann, R. E.; Scuseria, G. E.; Frisch, M. J. An Efficient Implementation of Time-Dependent Density-Functional Theory for the Calculation of Excitation Energies of Large Molecules. *J. Chem. Phys.* **1998**, *109* (19), 8218–8224.
- (164) Gross, E. K. U.; Ullrich, C. A.; Gossmann, U. J. Density Functional Theory of Time-Dependent Systems. In *Density functional theory*; Gross, E. K. U. and Dreizler, R., Ed.; NATO Advanced Science Institutes Series, Series B, Physics; Plenum Press DIV Plenum Publishing Corp: 233 Spring ST, New York, NY 10013, 1995; Vol. 337, pp 149–171.
- (165) Slater, J. C. *Quantum Theory of Molecular and Solids*; McGraw-Hill: New-York, 1974.
- (166) Vosko, S. H.; Wilk, L.; Nusair, M. Accurate Spin-Dependent Electron Liquid

- Correlation Energies for Local Spin-Density Calculations - A Critical Analysis. *Can. J. Phys.* **1980**, 58 (8), 1200–1211.
- (167) van Wullen, C. Spin Densities in Two-Component Relativistic Density Functional Calculations: Noncollinear versus Collinear Approach. *J. Comput. Chem.* **2002**, 23 (8), 779–785.
- (168) Vlček, A.; Zális, S. Comments on “Theoretical Studies of Ground and Excited Electronic States in a Series of Halide Rhenium(I) Bipyridine Complexes”<sup>†</sup>. *J. Phys. Chem. A* **2005**, 109 (12), 2991–2992.
- (169) Worl, L. A.; Duesing, R.; Chen, P.; Ciana, L. Della; Meyer, T. J. Photophysical Properties of Polypyridyl Carbonyl Complexes of rhenium(I). *J. Chem. Soc. Dalt. Trans.* **1991**, No. S, 849–858.
- (170) Heitz, M.-C.; Ribbing, C.; Daniel, C. Spin-Orbit Induced Radiationless Transitions in Organometallics: Quantum Simulation of the Intersystem Crossing Processes in the Photodissociation of HCo(CO)<sub>4</sub>. *J. Chem. Phys.* **1997**, 106 (4), 1421–1428.
- (171) Daniel, C.; Heitz, M.-C.; Manz, J.; Ribbing, C. Spin-orbit Induced Radiationless Transitions in Organometallics: Quantum Simulation of the 1E→3A<sub>1</sub> Intersystem Crossing Process in HCo(CO)<sub>4</sub>. *J. Chem. Phys.* **1995**, 102 (2), 905–912.
- (172) Guillaumont, D.; Daniel, C. Photodissociation and Electronic Spectroscopy of Mn(H)(CO)<sub>3</sub>(H-DAB) (DAB = 1,4-Diaza-1,3-Butadiene): Quantum Wave Packet Dynamics Based on Ab Initio Potentials. *J. Am. Chem. Soc.* **1999**, 121 (50), 11733–11743.
- (173) Bruand-Cote, I.; Daniel, C. Photodissociation and Electronic Spectroscopy of [Re(H)(CO)<sub>3</sub>(H-Dab)] (H-dab=1,4-Diaza-1,3-Butadiene): Quantum Wavepacket Dynamics Based on Ab Initio Potentials. *Chem. - A Eur. J.* **2002**, 8 (6), 1361–1371.
- (174) Vallet, V.; Strich, A.; Daniel, C. Spin-orbit Effects on the Electronic Spectroscopy of Transition Metal Dihydrides H<sub>2</sub>M(CO)<sub>4</sub> (M=Fe, Os). *Chem. Phys.* **2005**, 311 (1–2), 13–18.
- (175) Brahim, H.; Daniel, C.; Rahmouni, A. Spin-Orbit Absorption Spectroscopy of Transition Metal Hydrides: A TD-DFT and MS-CASPT2 Study of HM(CO)<sub>5</sub> (M = Mn, Re). *Int. J. Quantum Chem.* **2012**, 112 (9), 2085–2097.
- (176) Nozaki, K. Theoretical Studies on Photophysical Properties and Mechanism of Phosphorescence in [Fac-Ir(2-phenylpyridine)(3)]. *J. CHINESE Chem. Soc.* **2006**, 53 (1, SI), 101–112.
- (177) Jansson, E.; Minaev, B.; Schrader, S.; Ågren, H. Time-Dependent Density Functional Calculations of Phosphorescence Parameters for Fac-tris(2-Phenylpyridine) Iridium. *Chem. Phys.* **2007**, 333 (2–3), 157–167.
- (178) Gourlaouen, C.; Eng, J.; Otsuka, M.; Gindensperger, E.; Daniel, C. Quantum Chemical Interpretation of Ultrafast Luminescence Decay and Intersystem Crossings in Rhenium(I) Carbonyl Bipyridine Complexes. *J. Chem. Theory Comput.* **2015**, 11 (1), 99–110.
- (179) Adamo, C.; Barone, V. Toward Reliable Density Functional Methods without

- Adjustable Parameters: The PBE0 Model. *J. Chem. Phys.* **1999**, *110* (13), 6158–6170.
- (180) Perdew, J. P.; Burke, K.; Ernzerhof, M. Generalized Gradient Approximation Made Simple. *Phys. Rev. Lett.* **1996**, *77* (18), 3865–3868.
- (181) Becke, A. D. Density-Functional Thermochemistry .3. The Role of Exact Exchange. *J. Chem. Phys.* **1993**, *98* (7), 5648–5652.
- (182) Koch, H.; de Meras, A. S.; Pedersen, T. B. Reduced Scaling in Electronic Structure Calculations Using Cholesky Decompositions. *J. Chem. Phys.* **2003**, *118* (21), 9481–9484.
- (183) Klamt, A.; Schüürmann, G. COSMO: A New Approach to Dielectric Screening in Solvents with Explicit Expressions for the Screening Energy and Its Gradient. *J. Chem. Soc., Perkin Trans. 2* **1993**, No. 5, 799–805.
- (184) Tomasi, J.; Mennucci, B.; Cammi, R. Quantum Mechanical Continuum Solvation Models. *Chem. Rev.* **2005**, *105* (8), 2999–3093.
- (185) Yang, L.; Ren, A.; Feng, J.; Liu, X.; Ma, Y.; Zhang, M. Theoretical Studies of Ground and Excited Electronic States in a Series of Halide Rhenium(I) Bipyridine Complexes. *Society* **2004**, *109* (I), 6797–6808.
- (186) Dreuw, A.; Weisman, J. L.; Head-Gordon, M. Long-Range Charge-Transfer Excited States in Time-Dependent Density Functional Theory Require Non-Local Exchange. *J. Chem. Phys.* **2003**, *119* (6), 2943–2946.
- (187) Becke, A. D. A New Mixing of Hartree-Fock and Local Density-Functional Theories. *J. Chem. Phys.* **1993**, *98* (2), 1372–1377.
- (188) Adamo, C.; Barone, V. Inexpensive and Accurate Predictions of Optical Excitations in Transition-Metal Complexes: The TDDFT/PBE0 Route. *Theor. Chem. Acc.* **2000**, *105* (2), 169–172.
- (189) Guillemales, J. F.; Barone, V.; Joubert, L.; Adamo, C. A Theoretical Investigation of the Ground and Excited States of Selected Ru and Os Polypyridyl Molecular Dyes. *J. Phys. Chem. A* **2002**, *106* (46), 11354–11360.
- (190) Tawada, Y.; Tsuneda, T.; Yanagisawa, S.; Yanai, T.; Hirao, K. A Long-Range-Corrected Time-Dependent Density Functional Theory. *J. Chem. Phys.* **2004**, *120* (18), 8425–8433.
- (191) Peverati, R.; Truhlar, D. G. Performance of the M11 and M11-L Density Functionals for Calculations of Electronic Excitation Energies by Adiabatic Time-Dependent Density Functional Theory. *Phys. Chem. Chem. Phys.* **2012**, *14* (32), 11363–11370.
- (192) Iikura, H.; Tsuneda, T.; Yanai, T.; Hirao, K. A Long-Range Correction Scheme for Generalized-Gradient-Approximation Exchange Functionals. *J. Chem. Phys.* **2001**, *115* (8), 3540–3544.
- (193) Vydrov, O. A.; Scuseria, G. E. Assessment of a Long-Range Corrected Hybrid Functional. *J. Chem. Phys.* **2006**, *125* (23), 234109.
- (194) Yanai, T.; Tew, D. P.; Handy, N. C. A New Hybrid Exchange-Correlation Functional



- Using the Coulomb-Attenuating Method (CAM-B3LYP). *Chem. Phys. Lett.* **2004**, *393* (1–3), 51–57.
- (195) Bressler, C.; Milne, C.; Pham, V.-T.; ElNahhas, A.; van der Veen, R. M.; Gawelda, W.; Johnson, S.; Beaud, P.; Grolimund, D.; Kaiser, M.; Borca, C. N.; Ingold, G.; Abela, R.; Chergui, M. Femtosecond XANES Study of the Light-Induced Spin Crossover Dynamics in an Iron(II) Complex. *Science* (80-. ). **2009**, *323* (5913), 489–492.
- (196) Chergui, M. On the Interplay between Charge, Spin and Structural Dynamics in Transition Metal Complexes. *Dalt. Trans.* **2012**, *41* (42), 13022–13029.
- (197) Striplin, D. .; Crosby, G. . Photophysical Investigations of rhenium(I)Cl(CO)<sub>3</sub>(phenanthroline) Complexes. *Coord. Chem. Rev.* **2001**, *211* (1), 163–175.
- (198) Striplin, D. R.; Crosby, G. A. Nature of the Emitting 3MLCT Manifold of rhenium(I) (Diimine) (CO) <sub>3</sub>Cl Complexes. *Chem. Phys. Lett.* **1994**, *221* (5–6), 426–430.
- (199) Belliston-Bittner, W.; Dunn, A. R.; Nguyen, Y. H. L.; Stuehr, D. J.; Winkler, J. R.; Gray, H. B. Picosecond Photoreduction of Inducible Nitric Oxide Synthase by rhenium(I)-Diimine Wires. *J. Am. Chem. Soc.* **2005**, *127* (45), 15907–15915.
- (200) Blanco-Rodriguez, A. M.; Busby, M.; Gradinaru, C.; Crane, B. R.; Di Bilio, A. J.; Matousek, P.; Towrie, M.; Leigh, B. S.; Richards, J. H.; Vlcek, A.; Gray, H. B. Excited-State Dynamics of Structurally Characterized [Re-I(CO)(3)(phen)(HisX)](+) (X=83,109) Pseudomonas Aeruginosa Azurins in Aqueous Solution. *J. Am. Chem. Soc.* **2006**, *128* (13), 4365–4370.
- (201) Di Bilio, A. J.; Crane, B. R.; Wehbi, W. A.; Kiser, C. N.; Abu-Omar, M. M.; Carlos, R. M.; Richards, J. H.; Winkler, J. R.; Gray, H. B. Properties of Photogenerated Tryptophan and Tyrosyl Radicals in Structurally Characterized Proteins Containing rhenium(I) Tricarbonyl Diimines. *J. Am. Chem. Soc.* **2001**, *123* (13), 3181–3182.
- (202) Blanco-Rodriguez, A. M.; Busby, M.; Ronayne, K.; Towrie, M.; Gradinaru, C.; Sudhamsu, J.; Sykora, J.; Hof, M.; Zalis, S.; Di Bilio, A. J.; Crane, B. R.; Gray, H. B.; Vlcek Jr., A. Relaxation Dynamics of Pseudomonas Aeruginosa Re-I(CO)(3)(alpha-diimine)(HisX)(+) (X=83, 107, 109, 124, 126)Cu-II Azurins. *J. Am. Chem. Soc.* **2009**, *131* (33), 11788–11800.
- (203) Fumanal, M.; Daniel, C. Description of Excited States in [Re(Imidazole)(CO)(3)(Phen)](+) Including Solvent and Spin-Orbit Coupling Effects: Density Functional Theory versus Multiconfigurational Wavefunction Approach. *J. Comput. Chem.* **2016**, *37* (27), 2454–2466.
- (204) Krishnan, R.; Binkley, J. S.; Seeger, R.; Pople, J. A. Self-Consistent Molecular-Orbital Methods .20. Basis Set for Correlated Wave-Functions. *J. Chem. Phys.* **1980**, *72* (1), 650–654.
- (205) Curtiss, L. A.; McGrath, M. P.; Blaudeau, J. P.; Davis, N. E.; Binning, R. C.; Radom, L. Extension of Gaussian-2 Theory to Molecules Containing 3rd-Row Atoms Ga-Kr. *J. Chem. Phys.* **1995**, *103* (14), 6104–6113.
- (206) Martin, J. M. L.; Sundermann, A. Correlation Consistent Valence Basis Sets for Use with the Stuttgart-Dresden-Bonn Relativistic Effective Core Potentials: The Atoms Ga-Kr and In-Xe. *J. Chem. Phys.* **2001**, *114* (8), 3408–3420.

- 
- (207) Wallace, L.; Jackman, D. C.; Rillema, D. P.; Merkert, J. W. Temperature-Dependent Emission Properties of rhenium(I) Tricarbonyl Complexes Containing Alkyl-Substituted and Aryl-Substituted Phenanthrolines as Ligands. *Inorg. Chem.* **1995**, *34* (21), 5210–5214.
- (208) Crosby, G. A.; Hipps, K. W.; Elfring, W. H. Appropriateness of Assigning Spin Labels to Excited-States of Inorganic Complexes. *J. Am. Chem. Soc.* **1974**, *96* (2), 629–630.
- (209) Minaev, B.; Minaeva, V.; Ågren, H. Theoretical Study of the Cyclometalated Iridium(III) Complexes Used as Chromophores for Organic Light-Emitting Diodes. *J. Phys. Chem. A* **2009**, *113* (4), 726–735.
- (210) Matsushita, T.; Asada, T.; Koseki, S. Relativistic Study on Emission Mechanism in Palladium and Platinum Complexes. *J. Phys. Chem. A* **2006**, *110* (49), 13295–13302.

## LIST OF ATTACHED PUBLICATIONS

Radka Heydová, Etienne Gindensperger, Roberta Romano, Jan Sýkora, Antonín Vlček, Jr., Stanislav Zális, and Chantal Daniel (2012). **Spin-orbit Treatment of UV-vis Absorption Spectra and Photophysics of Rhenium(I) Carbonyl-Bipyridine Complexes: MS-CASPT2 and TD-DFT Analysis.** *The Journal of Physical Chemistry A*, 116(46), 11319-11329. <http://doi.org/10.1021/jp305461z>

Radka Baková, Majed Chergui, Chantal Daniel, Antonín Vlček Jr., and Stanislav Zális (2011). **Relativistic effects in spectroscopy and photophysics of heavy-metal complexes illustrated by spin-orbit calculations of [Re(imidazole)(CO)<sub>3</sub>(phen)]<sup>+</sup>.** *Coordination Chemistry Reviews*, 255(7-8), 975-989. <http://doi.org/10.1016/j.ccr.2010.12.027>

## **ATTACHED PUBLICATIONS**